



**UNIVERSITÀ
DEGLI STUDI
DI PADOVA**

Sede Amministrativa

UNIVERSITÀ DEGLI STUDI DI PADOVA

Sede Consorzata

UNIVERSITÀ DEGLI STUDI DI BOLOGNA

DIPARTIMENTO DI INGEGNERIA INDUSTRIALE

SCUOLA DI DOTTORATO DI RICERCA IN INGEGNERIA INDUSTRIALE

INDIRIZZO IN MECCATRONICA E SISTEMI INDUSTRIALI

XXV CICLO

**Design, Control and Management of
Renewable Energy Plants and Technologies**

“Progettazione, Controllo e Gestione di Impianti e Tecnologie per le Energie Rinnovabili”

Direttore della Scuola: Chiar.mo Prof. PAOLO COLOMBO

Coordinatore d’indirizzo: Chiar.mo Prof. ALBERTO TREVISANI

Supervisore: Chiar.mo Prof. EMILIO FERRARI

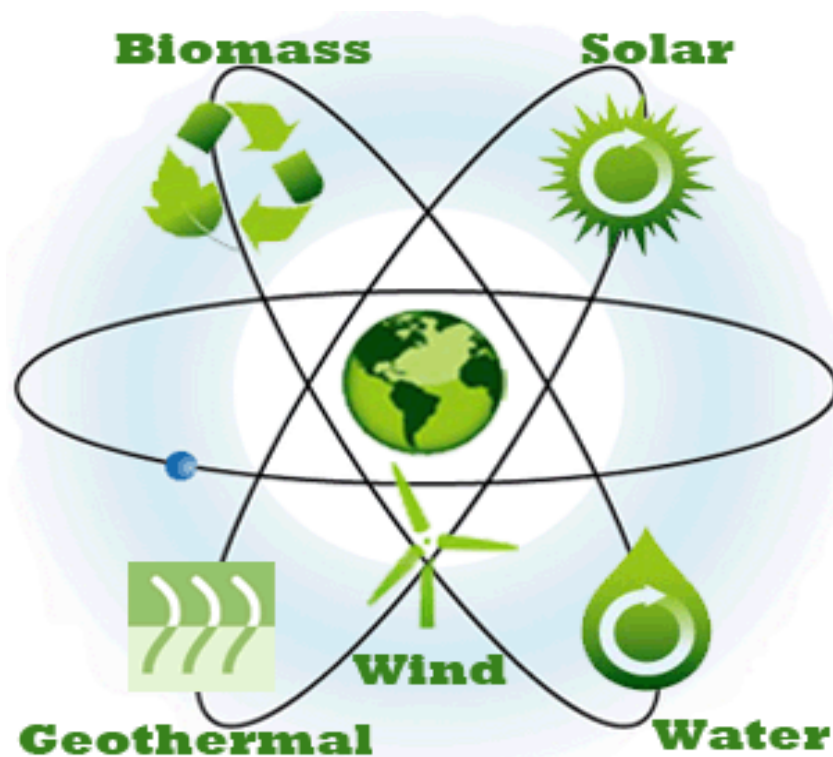
Dottorando: MARCO BORTOLINI

— 31 Gennaio 2013 —

Design, Control and Management of Renewable Energy Plants and Technologies

by

Marco Bortolini



Submitted in fulfillment of the requirements
for the Degree of Doctor of Philosophy

*University of Padua – University of Bologna
Doctoral School of Industrial Engineering*

—

January 31, 2013

Abstract

Nowadays, and even more in the next decades, the availability and easy-access to energy sources represent a crucial asset for the world development and the progress of people and nations. At the same time, the depletion of natural resources, together with the increase of the anthropic activity impact on the Earth ecosystem and climate, force communities and institutions, at all levels, to discuss and actuate different approaches to achieve the social and economic growth, based on the so-called *sustainable development pattern*. In such a scenario, renewable energy sources, i.e. solar, wind, hydro, biomass, geothermal, etc., certainly play a key role to join progress and attention to the environmental issues.

The present Ph.D. dissertation focuses on such topics investigating strategies, methods and innovative approaches for the effective design, control and management of renewable energy plants and technologies.

Specifically, the energy scenario is investigated from a global point of view proposing studies and optimization models highlighting the relevance and the potential impact of the major energy sources, both renewable and conventional. Such sources represent the elements of a big puzzle, i.e. the energy mix, in which their economic and environmental strengths should be emphasized minimizing the associated negative impacts and weaknesses.

Among renewable sources, solar energy is of primary importance for availability, diffusion and potential impact. The present Ph.D. dissertation particularly investigates such a source presenting models, methods and prototypes to increase its relevance in the energy mix. The fundamentals of solar energy, together with innovative approaches to estimate the solar radiation components, are provided. Furthermore, the pioneering concentrating solar sector is deeply focused presenting the design, development and preliminary field-test of a bi-axial Fresnel solar photovoltaic/thermal (PV/T) concentrating prototype. Possible solar tracking strategies and control algorithms are, then, investigated describing a customized semi-automatic motion control platform, developed in LabView™ programming environment. Finally, the last section, proposes an effective approach for the design of a solar simulator, the most frequently adopted device in solar optic laboratory tests.

In conclusion, the present Ph.D. dissertation describes effective strategies for the renewable energy spread, considering their performances and their potential impact to achieve the ambitious challenge of a sustainable *living planet*.

Sommario

Oggi, ed in misura crescente nei prossimi decenni, la disponibilità e facilità di accesso alle fonti energetiche rappresenta un fattore determinante per lo sviluppo mondiale ed il progresso di popoli e nazioni. Parallelamente a ciò, il progressivo sfruttamento delle risorse naturali, unito all'aumento dell'impatto delle attività antropiche sull'ecosistema terrestre e sul clima, impongono a comunità ed istituzioni, ad ogni livello, un ripensamento e l'attuazione di differenti strategie per garantire lo sviluppo sociale ed economico attraverso il ricorso ad approcci basati sul concetto di *sviluppo sostenibile*. In questo contesto, le fonti energetiche rinnovabili, i.e. solare, eolica, idroelettrica, da biomasse, geotermica, ecc., assumono certamente un ruolo determinante per coniugare progresso ed attenzione alle tematiche ambientali.

La presente Tesi di Dottorato si incentra su queste tematiche approfondendo strategie, metodi ed approcci innovativi per l'efficace progettazione, controllo e gestione di impianti e tecnologie per le energie rinnovabili.

Nel dettaglio, lo scenario d'insieme delle fonti energetiche è analizzato con logica di sistema ed orientamento all'ottimizzazione globale proponendo studi e modelli che evidenzino l'importanza ed il potenziale delle principali risorse, rinnovabili e non, come elementi di un grande mosaico, i.e. il mix energetico globale, nel quale le potenzialità economiche ed ambientali di ogni risorsa sono enfatizzate minimizzando, nel contempo, gli impatti negativi e le rispettive debolezze.

Tra le possibili fonti rinnovabili, la fonte solare assume primaria importanza per disponibilità, diffusione ed impatto potenziale. La presente Tesi di Dottorato analizza, in dettaglio, questa risorsa energetica presentando modelli, metodi ed impianti sviluppati per accrescere l'incidenza di questa risorsa nel mix energetico. Gli elementi ed aspetti fondamentali, insieme ad approcci innovativi per la stima delle componenti della radiazione solare, sono presentati nell'elaborato. Successivamente, l'innovativo settore della concentrazione solare è analizzato, in dettaglio, anche attraverso l'illustrazione delle scelte progettuali, lo sviluppo e la campagna sperimentale preliminare di un concentratore solare fotovoltaico/termico (PV/T) a lenti di Fresnel ed inseguimento biassiale. Nel seguito, vengono approfondite possibili strategie per l'inseguimento biassiale ed algoritmi di controllo, implementati in una piattaforma semi-automatizzata sviluppata in ambiente di programmazione grafica LabView™. L'ultima sezione propone, infine, un approccio per la progettazione di un simulatore solare, un dispositivo spesso adottato nei test di ottica solare.

In conclusione, la presente Tesi di Dottorato, descrive una molteplicità di strategie orientate alla diffusione delle energie rinnovabili, con attenzione alle performance ed all'impatto potenziale che esse hanno verso il raggiungimento dell'obiettivo ambizioso di un sostenibile *living planet*.

Acknowledgments

After my three years as a Ph.D. student, I firmly believe that the continuous support of a large group of excellent women and men is essential to develop my research path, leading to the results discussed in the present dissertation. This is the time to express my gratitude to them.

First of all, my best and sincere thank to Professor Emilio Ferrari, my Ph.D. Supervisor, for his clever guidance in introducing me to this challenging activity and for all his valuable advices. At the same time, a special gratitude and appreciation to Professor Mauro Gamberi, a really exceptional person and professor, for driving me during the research path, introducing new topics and point of views and for his constant support with useful suggestions. Many thanks because he is able to improve my weaknesses, to emphasize my strengths and to make me more “mechanical” than I was able even to imagine in the beginning.

I would like to express my very special gratitude to all the Industrial Mechanical Plants research group of the Department of Industrial Engineering - Alma Mater Studiorum University of Bologna. It is a great honor to collaborate with you-all. I would like to acknowledge Professor Arrigo Pareschi, Professor Alberto Regattieri, Professor Riccardo Manzini and Professor Cristina Mora for their humanity and willingness, their impressive competences and because they are always ready for “an advice” and for supporting me.

It was a great honor and luck to share both the happy and hard work days with a group of valuable colleagues and friends. Riccardo, my Ph.D. best “classmate”. He shared with me this path since the first day. Giulia, Alessandro G. and Alessandro C. that joined the group in the next years. Thank you all! ... and sorry for all the times I bored you with “the rules” and “the bureaucracy stuffs”. Thanks also to Giorgia, Andrea, Giovanni and Marco, the “Vicenza and Padova Ph.D. students”, for all the information they provide to Riccardo and me and for their friendliness.

A grateful thank to the Fondazione Studi Universitari di Vicenza for its financial support.

I cannot forget to acknowledge Professor Daniel M. Kammen and Dr. Solomon Abebe Asfaw for their support during my visit to the Renewable and Appropriate Energy Laboratory at the University of California, Berkeley. I am really grateful to them and to all the Lab group for the fruitful discussions we had and for their interesting suggestions.

Finally, and most important, I would like to thank all my family: Eros and Marisa, my parents, Arvedo, Isolina, Mario, Silvana, Giancarlo, Amelia and Lorenzo.

Thanks to Raffaella and her family, Franco, Antonella, Giulio, Debora and Alessandro.

Marco Bortolini

Table of Contents

ABSTRACT	I
SOMMARIO	III
ACKNOWLEDGEMENTS	V
TABLE OF CONTENTS	VII
LIST OF FIGURES	XI
LIST OF TABLES	XV
1. INTRODUCTION	1
1.1 Dissertation outline	5
References	8
Web - references	9
2. ENERGY NETWORK PLANNING	11
<i>General LP model for energy network economic optimization and solar PV plant economic assessment</i>	
2.1 LP model for the energy network design	12
2.1.1 Model outlook, parameters and decisional variables	13
2.1.2 Objective function	16
2.1.3 Constraints	18
2.1.4 Comments and developments	19
2.2 Economic assessment of PV plants in Europe	21
2.2.1 Performance cost model	22
2.2.2 Input, parameters and scenarios	26
2.2.2.1 <i>National PV sector key-elements</i>	27
2.2.3 Results and discussion	29
References	36
Legislation references	39
3. SOLAR RENEWABLE SOURCE	41
<i>Fundamentals and models for solar radiation prediction</i>	
3.1 Solar energy radiation	42
3.1.1 Extraterrestrial irradiance	42
3.1.2 Horizontal celestial coordinate system	44
3.1.2.1 <i>Numerical example (part I)</i>	47
3.1.3 Effect of Earth atmosphere on the incident radiation	49
3.2 Solar radiation models	50
3.2.1 TOA radiation model	51
3.2.1.1 <i>Numerical example (part II)</i>	54
3.2.2 Solar radiation models inside Earth atmosphere	56
3.2.2.1 <i>Weather and solar radiation databases</i>	56

3.2.2.2 Correlation models and parameters	57
3.2.2.3 Key Performance Indicators - (KPIs)	60
3.3 Diffuse fraction correlations	61
3.3.1 Integrated procedure for model development	61
3.3.2 Multi-location model for the diffuse fraction prediction	64
3.3.2.1 Step #1 - Model geographical context	64
3.3.2.2 Step #2 - Adopted climatologic predictors	66
3.3.2.3 Step #3 - Adopted correlation functions	66
3.3.2.4 Step #4 - Data collection	66
3.3.2.5 Step #5 - Quality control procedure and data filtering	68
3.3.2.6 Step #6 - Best fit curve coefficients	70
3.3.2.7 Step #7 - Performance assessment	76
3.3.2.8 Step #8 - Seasonality	78
3.3.2.9 Step #9 - Model validation against independent datasets	83
3.3.3 Technical note	84
References	85
Web - references	89
4. CONCENTRATING SOLAR SECTOR	91
<i>Available technologies and the current scenario</i>	
<hr/>	
4.1 Solar concentrating principle	92
4.2 Solar reflection plants	94
4.2.1 Parabolic trough systems	94
4.2.2 Parabolic dishes	95
4.2.3 Solar towers	96
4.2.4 Linear Fresnel reflectors	97
4.2.5 Perspectives of solar reflection plants	97
4.3 Solar refraction plants	98
4.4 Concentrating photovoltaic systems	100
4.4.1 CPV solar cells	100
4.4.2 Cell cooling and heat recovery	101
4.5 Smart-grid concept and distributed generation	102
References	104
Web - references	108
5. CONCENTRATING PV/T PROTOTYPE	109
<i>Bi-axial Fresnel solar cogenerator for the distributed production of power and heat</i>	
<hr/>	
5.1 Purposes and prototype overview	110
5.1.1 Prototype general features	110
5.2 Plant structural module	113
5.3 Solar collector	114
5.4 Solar receivers	115
5.4.1 Multi-junction solar cells: fundamentals	116
5.4.2 Receiver layout	118
5.5 Hydraulic cooling circuit	118
5.6 Electronic variable load	120
5.7 Sun tracking system	121
5.8 Real-time motion control and monitoring system	125
5.8.1 Power supply unit	125
5.8.2 Motion control unit	126

5.8.3 Environmental monitoring unit	127
5.8.4 Operative condition monitoring unit	128
5.9 Manufacturing cost analysis	129
5.10 Preliminary field-tests	131
6. STRATEGIES AND PLATFORM FOR CONCENTRATING SOLAR PLANT CONTROL	135
<i>Approaches for solar tracking and an integrated LabView™ control unit</i>	
<hr/>	
6.1 Solar tracking strategies	136
6.1.1 Literature review	136
6.1.2 Proposed solar tracking strategies	139
6.1.2.1 Main control loop	139
6.1.2.2 Day-time solar tracking approach	141
6.1.2.3 Forward loop bi-axial control strategy	142
6.1.2.4 Feedback bi-axial control strategy	143
6.1.2.5 Hybrid bi-axial control strategy	145
6.2 LabView™ platform for PV/T prototype control	147
6.2.1 Command & control panel	147
6.2.2 Geo-coordinates & time panel	148
6.2.3 Alarm panel	149
6.2.4 Sensors & setpoint panel	150
6.2.5 Environmental condition panel	151
6.2.6 Cooling circuit panel	152
6.2.7 Field-data acquisition procedure	152
6.2.8 Data saving and download	153
6.3 Solar tracking strategy field-test	155
6.4 MPP tracking algorithms	156
6.4.1 Perturb & observe algorithm	158
6.4.2 Incremental conductance algorithm	159
6.4.3 LabView™ simulation of perturb & observe algorithm	161
References	163
7. CONCENTRATING SOLAR SIMULATOR	169
<i>Ray-tracing model and Monte Carlo simulation for the solar simulator reflector design</i>	
<hr/>	
7.1 Solar simulator overview	170
7.2 Ray-tracing model	172
7.2.1 Analytic model	174
7.2.2 Model parameters: summary	178
7.2.3 Performance indices	179
7.3 Realistic case study	180
7.3.1 Results and discussion	181
7.3.2 Future developments	186
References	187
Web - reference	188
8. CONCLUSIONS	189
<hr/>	
8.1 Future developments	190

List of Figures

Figure 1.1. Percentage of population with access to electricity.	2
Figure 1.2. Global energy consumption split by primary sources.	2
Figure 1.3. World CO ₂ emissions by sector in 2009	3
Figure 1.4. Renewable power capacities installed, in 2010, in major Earth regions.	4
Figure 1.5. Ph.D. dissertation outline.	7
<hr/>	
Figure 2.1. Energy network overall structure.	13
Figure 2.2. Flow chart of the proposed PV system analysis.	22
Figure 2.3. Incentive vs. no-incentive scenarios for the eight countries and residential rooftop plants.	29
Figure 2.4. Incentive vs. no-incentive scenarios for the eight countries and industrial rooftop plants.	30
Figure 2.5. Sensitivity analysis of cash outflows.	31
Figure 2.6. Impact of % _{sold} on NPV, residential rooftop plants.	32
Figure 2.7. Impact of % _{sold} on NPV, industrial rooftop plants.	32
Figure 2.8. Impact of the irradiance level, I_r , on NPV and country typical ranges.	33
Figure 2.9. Impact of financial parameters on PV plant profitability.	34
Figure 2.10. PV system cost trend from 2001 to 2012.	35
<hr/>	
Figure 3.1. Standard spectral irradiance curve of the Sun.	42
Figure 3.2. Dependence of TOA solar radiation on time of the year.	43
Figure 3.3. Solar Altitude and Azimuthal angle in HCCS.	44
Figure 3.4. Equation of time, waveform.	46
Figure 3.5. Numerical example, solar altitude waveforms for summer and winter solstices.	48
Figure 3.6. Numerical example, azimuthal angle waveforms for summer and winter solstices.	48
Figure 3.7. Atmosphere attenuation phenomena and components of solar radiation.	50
Figure 3.8. TOA radiation model – horizontal surface.	51
Figure 3.9. TOA radiation model – tilted surface.	53
Figure 3.10. Numerical example, daily TOA irradiance curves for horizontal surfaces.	55
Figure 3.11. Numerical example, daily TOA incident energy varying the surface slope.	55
Figure 3.12. Numerical example, month daily TOA incident energy for five tilted surfaces.	56
Figure 3.13. Map of the 44 considered EU weather stations.	64
Figure 3.14. WRDC database. Example of the available data.	67
Figure 3.15. (K, K_d) couples, example for year 2007.	67
Figure 3.16. Quality control procedure. The scatter envelope.	68
Figure 3.17. Second degree annual correlation function, year 2004.	71
Figure 3.18. Third degree annual correlation function, year 2004.	71
Figure 3.19. Fourth degree annual correlation function, year 2004.	71
Figure 3.20. Logistic annual correlation function, year 2004.	72
Figure 3.21. Second degree annual correlation function, year 2005.	72
Figure 3.22. Third degree annual correlation function, year 2005.	72
Figure 3.23. Fourth degree annual correlation function, year 2005.	73
Figure 3.24. Logistic annual correlation function, year 2005.	73
Figure 3.25. Second degree annual correlation function, year 2006.	73
Figure 3.26. Third degree annual correlation function, year 2006.	74
Figure 3.27. Fourth degree annual correlation function, year 2006.	74

Figure 3.28. Logistic annual correlation function, year 2006.	74
Figure 3.29. Second degree annual correlation function, year 2007.	75
Figure 3.30. Third degree annual correlation function, year 2007.	75
Figure 3.31. Fourth degree annual correlation function, year 2007.	75
Figure 3.32. Logistic annual correlation function, year 2007.	76
Figure 3.33. Waveform comparison among years, annual scenario.	78
Figure 3.34. Waveform comparison among years, summer scenario.	80
Figure 3.35. (K, K_d) couples for 2005 summer scenario.	80
Figure 3.36. Waveform comparison among years, winter scenario.	82
Figure 3.37. Effect of seasonality, comparison of the long-term models.	83
<hr/>	
Figure 4.1. Reflection of solar radiation through parabolic mirror.	93
Figure 4.2. Refraction of solar radiation through Fresnel lens.	93
Figure 4.3. Parabolic trough system, example.	94
Figure 4.4. Parabolic trough solar plant for power production.	95
Figure 4.5. Parabolic dish, example.	95
Figure 4.6. Solar tower, example,	96
Figure 4.7. Linear Fresnel reflector, example.	97
Figure 4.8. Biconvex converging lens.	98
Figure 4.9. Equivalent Fresnel of a plano-convex lens.	99
Figure 4.10. Solar PV cell classification.	100
<hr/>	
Figure 5.1. Concentrating PV/T prototype, front view.	111
Figure 5.2. Concentrating PV/T prototype, back view.	111
Figure 5.3. Plant structural module: the support base.	113
Figure 5.4. Plant structural module: the pillar and the horizontal shaft.	114
Figure 5.5. Solar collector: Al frame, detail.	115
Figure 5.6. Solar collector: frames integration.	115
Figure 5.7. Triple-junction solar cell layout, example.	117
Figure 5.8. PV cell layout.	117
Figure 5.9. PV cell spectral response.	117
Figure 5.10. Solar receiver, heat exchanger.	118
Figure 5.11. Heat exchanger, fluid inlet and outlets.	118
Figure 5.12. Hydraulic cooling circuit scheme.	119
Figure 5.13. Hydraulic cooling circuit, key elements inside the protection box.	120
Figure 5.14. I-V and P-V curves, example.	120
Figure 5.15. Electronic variable load for MPP tracking.	121
Figure 5.16. Zenithal tracking mechanism.	122
Figure 5.17. Azimuthal tracking mechanism.	122
Figure 5.18. Vertical shaft, inside the pillar, for Azimuthal motion transmission.	123
Figure 5.19. Solar collimator integrated to the solar collector.	123
Figure 5.20. Light sensors, picture and polar characteristic curve.	124
Figure 5.21. Light sensor electrical acquisition circuit.	124
Figure 5.22. Hardware control board.	125
Figure 5.23. Motion control unit circuit.	126
Figure 5.24. Weather station integrating the pyranometer, the air temperature thermometer and the anemometer.	127
Figure 5.25. Pyrheliometer for direct solar irradiation measurement.	128
Figure 5.26. Prototype function cost analysis.	130
Figure 5.27. Global radiation and direct fraction profiles on July 23, 2012.	131
Figure 5.28. Obtained I-V and P-V curves for a single TJ-PV solar cell integrated to the prototype.	132

Figure 5.29. Secondary optics, plate glass prism, example.	133
<hr/>	
Figure 6.1. Main control loop, flow-chart.	140
Figure 6.2. On-off controller operating principle.	141
Figure 6.3. Scheme of a solar collimator, sensors for shadow detection.	143
Figure 6.4. Feedback control strategy, flow-chart for the Azimuthal axis of motion.	144
Figure 6.5. Hybrid control strategy, flow-chart of the switching procedure.	145
Figure 6.6. Best tracking strategy as a function of M_s ,	146
Figure 6.7. LabView™ platform, command & control panel.	148
Figure 6.8. LabView™ platform, geo-coordinates & time panel.	149
Figure 6.9. LabView™ platform, alarm panel.	150
Figure 6.10. LabView™ platform, sensors & setpoint panel.	151
Figure 6.11. LabView™ platform, environmental condition panel.	151
Figure 6.12. LabView™ platform, cooling circuit panel.	152
Figure 6.13. Field-data acquisition procedure, example.	154
Figure 6.14. Misalignment measurement strategy.	155
Figure 6.15. Forward loop strategy shadow.	155
Figure 6.16. Feedback strategy shadow.	155
Figure 6.17. P-V curves for different irradiance levels.	157
Figure 6.18. Perturb & observe algorithm.	158
Figure 6.19. incremental conductance algorithm.	160
Figure 6.20. Perturb & observe algorithm, LabView™ simulation.	161
Figure 6.21. Effect on the PV cell electrical parameters of the environmental condition change.	161
<hr/>	
Figure 7.1. High flux solar simulator, example.	170
Figure 7.2. Small scale commercial solar simulator.	170
Figure 7.3. 3D layout and components.	170
Figure 7.4. Geometric properties of parabolic and ellipsoidal surfaces.	171
Figure 7.5. Ray-tracing model, flow-chart.	173
Figure 7.6. Ray-tracing model Cartesian coordinate system and notations.	174
Figure 7.7. High flux emitting source, structure and notations.	180
Figure 7.8. Radiative flux map for the best scenario.	181
Figure 7.9. Correlation between the reflector length and global transfer efficiency for the two values of σ_{err} .	183
Figure 7.10. Correlation between the ellipsoid eccentricity and the global transfer efficiency.	185
Figure 7.11. Purchased ellipsoidal reflector.	186
<hr/>	

List of Tables

Table 2.1. Model parameters and notations.	16
Table 2.2. Model decisional variables.	15
Table 2.3. Values for the performance cost model input parameters.	26
Table 2.4. Country economic and financial data: electricity price, tax level and inflation (year 2012).	27
Table 2.5. FIT for France [€/kWh].	27
Table 2.6. FIT for Germany [€/kWh].	28
Table 2.7. FIT for Italy [€/kWh].	28
Table 2.8. United Kingdom PV system incentives [€/kWh].	29
<hr/>	
Table 3.1. Numerical example, sunrise and sunset parameters for summer and winter solstices.	48
Table 3.2. Recommended average days for each month.	52
Table 3.3. Classification of frequently adopted predictors.	58
Table 3.4. Coordinates of the 44 considered EU weather stations.	65
Table 3.5. Data for scatter envelope lower and upper curves calculation, year 2007.	69
Table 3.6. Quality control procedure results.	69
Table 3.7. Best fit curve coefficients for the annual scenario.	70
Table 3.8. Performance assessment for the annual scenario - KPIs.	77
Table 3.9. Best fit curve coefficients for the summer scenario.	79
Table 3.10. Performance assessment for the summer scenario - KPIs.	79
Table 3.11. Best fit curve coefficients for the winter scenario.	81
Table 3.12. Performance assessment for the winter scenario - KPIs.	81
Table 3.13. Model validation. Comparative analysis for check sites, year 2007.	83
<hr/>	
Table 5.1. Features of the adopted Fresnel lenses.	114
Table 5.2. Energy band gap of the most commonly adopted semi-conductors.	116
Table 5.3. PV cell electrical features.	118
Table 5.4. Features of the four adopted environmental condition sensors.	128
Table 5.5. Prototype production cost analysis.	130
Table 5.6. Combined heat and power tests.	132
<hr/>	
Table 6.1. Review and classification of active STS.	138
<hr/>	
Table 7.1. Key features of the emitting source shape. Refer to Figure 7.7. for notations.	180
Table 7.2. Tested configurations for the ellipsoidal reflector.	181
Table 7.3. Multi-scenario analysis results. Twenty best and worst scenarios.	182
Table 7.4. Dependence of η on the L and σ_{err} values.	184
<hr/>	

1. Introduction

The United Nations Millennium Development Goal Report collects eight goals that all the 191 member states of the United Nations agreed to try to achieve by the year 2015 to spread an equitable and inclusive global growth. The panel includes (United Nations, 2011):

- ✓ to eradicate extreme poverty and hunger;
- ✓ to achieve universal primary education;
- ✓ to promote gender equality and empower women;
- ✓ to reduce child mortality;
- ✓ to improve maternal health;
- ✓ to combat HIV/AIDS, malaria and other diseases;
- ✓ to ensure environmental sustainability;
- ✓ to develop a global partnership for development.

As stated by the Secretary-General of the United Nations, energy lies at the heart of all these efforts and the decisions on how to produce, distribute and consume energy profoundly influence the ability to eradicate poverty worldwide (United Nations, 2010). Clean, efficient, affordable and reliable energy services are indispensable for global prosperity. Particularly, the developing countries need to expand access to reliable and modern energy services if they are to reduce poverty and improve the health of their citizens, while developed countries, who mostly require energy, need to mark a turning point to both their energy consumption levels and associated environmental impacts.

Nowadays, between two and three billion people are totally excluded from modern energy services, about 1.6 billion have no access to electricity and up to a billion more have access, only, to unreliable electricity networks. The distribution of this phenomenon is not uniform worldwide. Africa, Asia and South America present the worst scenarios (see Figure 1.1) with a percentage higher than 50% of population without access to electricity. The major troubles occur in the rural areas where four out of five of the people without available electric energy live and where traditional biomass are still used for cooking and heating by 2.4 billion people.

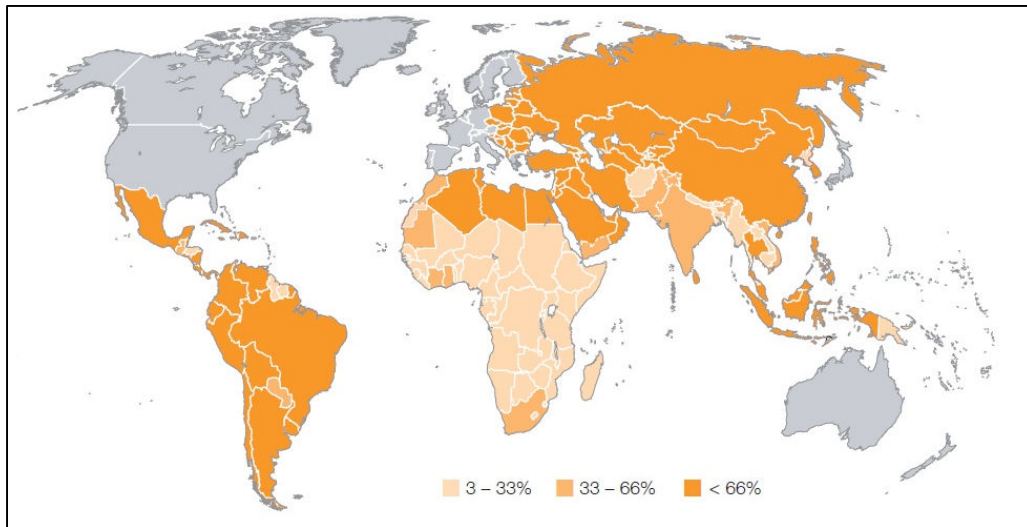


Figure 1.1. Percentages of population with access to electricity (United Nations - Energy, 2005).

Despite the large percentage of the population who still have no access to modern energy sources, the global demand for this key resource grows rapidly through recent years and presents an increasing trend for the next future. In particular, data from the International Energy Agency (IEA) show an increase of energy consumption between 1973 and 2005 of about 80.2% (from 4,676Mtoe to 8,428Mtoe), while the expected trend until 2030 highlights a further increase to 16,790Mtoe, if no mitigation strategies will be adopted (IEA, 2010). Furthermore, considering fuels/primary sources adopted to produce energy, a key role is still played by fossil fuels, e.g. coal, natural gas, oil. Figure 1.2 presents percentage data of the global energy consumption, split by primary source. The 81% of the consumed energy comes from fossil fuels, while renewable sources account for, approximately, the 16%. The figure depicts also the incidence of each renewable source in composing the whole renewable mix.

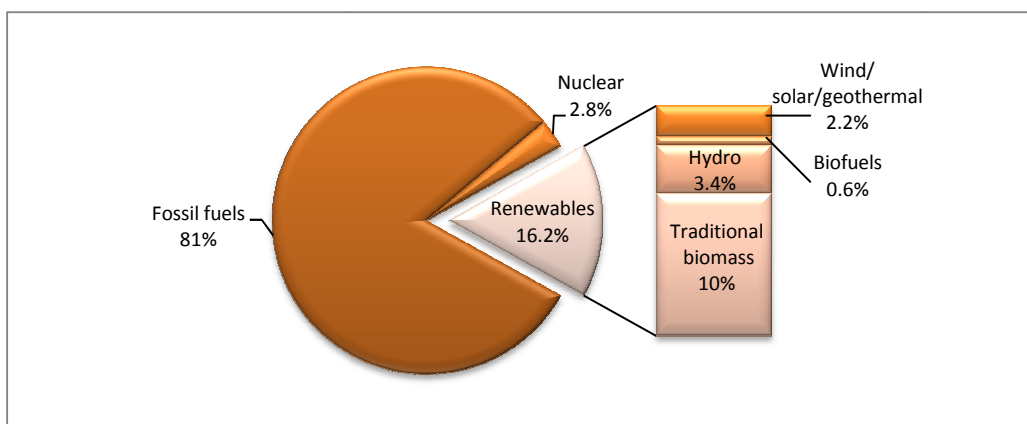


Figure 1.2. Global energy consumption split by primary sources (REN21, 2011).

From the environmental point of view, the current impact of the fossil fuels on the energy mix generates a heavy incidence of the energy sector, i.e. production, distribution and energy consumption, on the total amount of the emitted greenhouse gasses (GHG) and

pollutant agents. Figure 1.3 presents data about the world CO₂ emissions by sector, measured in 2009.

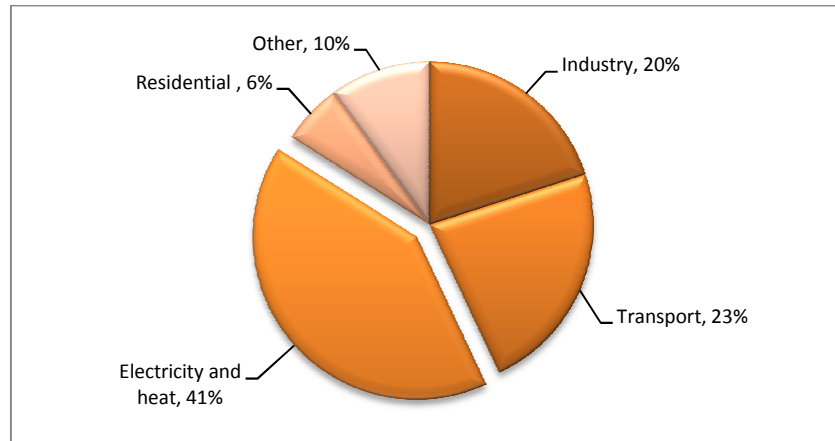


Figure 1.3. World CO₂ emissions by sector in 2009 (IEA, 2011).

Electricity and heat generation is, by far, the largest producer of carbon dioxide emissions especially due to the large use of coal, the most carbon-intensive among fossil fuels. As example, Australia, China, India, Poland and South Africa still produce between 68 and 94% of their energy through the combustion of coal.

The current scenario, shortly introduced and further investigated in the reminder of this dissertation, forces to globally face the energy issues driving the change to a more sustainable development of this sector. Particularly, the Advisory Group on Energy and Climate Change (AGECC), the highest-level board at the United Nation on this field, points out two key and complementary goals to be achieved by 2030:

- ✓ to ensure universal access to modern energy services, that means providing, at least, the basic minimum threshold of modern energy services for both consumption and productive uses to the 2-3 billion people now excluded. Modern sources of energy include fuels such as natural gas, liquid petroleum gas, diesel, biofuels and technologies enabling a cleaner and more efficient delivery and consumption of both traditional and renewable sources;
- ✓ to reduce the global energy intensity by 40 per cent. Global energy intensity measures the quantity of *traditional* energy required per unit of economic activity or output. This parameter is directly correlated to the so-called carbon-intensity and the environmental impact of the considered activity or output.

According to AGECC, these ambitious challenges are achievable partly due to technology innovations in plants, devices and the renewable energy diffusion and partly due to a shift of international priorities toward clean energy issues.

The role of renewable energies as low-carbon sources and the potential positive impact of their inclusion in the global energy mix are recognized from both scientists and institutions. Several analyses and surveys focus on the current status and potential development of renewable energy sources in different countries, geographic regions and under a wide set of conditions and strategic scenarios. As example, Winkler (2005), Arif Ozgur (2008), Baltas & Dervos (2012), Sivek et al. (2012), Tsuchiya (2012) present overviews about renewable energy perspectives in South Africa, Turkey, Greece, the Czech Republic and Japan, while Bradbrook (1996), Jacobsson & Johnson (2000) and Wüstenhagen & Menichetti (2012) propose different frameworks about opportunities offered by renewable sources suggesting strategies and development paths for their actuation.

The potential offered by renewable fonts is, theoretically, enormous. Particularly, the available annual energy from these sources is of about 3.9×10^9 PJ/year for solar, 9.4×10^4 PJ/year for wind and 9.96×10^5 PJ/year for geothermal energy (Quaschnig, 2005). Obviously, physical and natural constraints limit the convertible amount of energy. Considering the current scenario, the following Figure 1.4 summarizes data about the installed power capacities for the major Earth regions, in late 2010, considering renewable sources, excluding hydro.

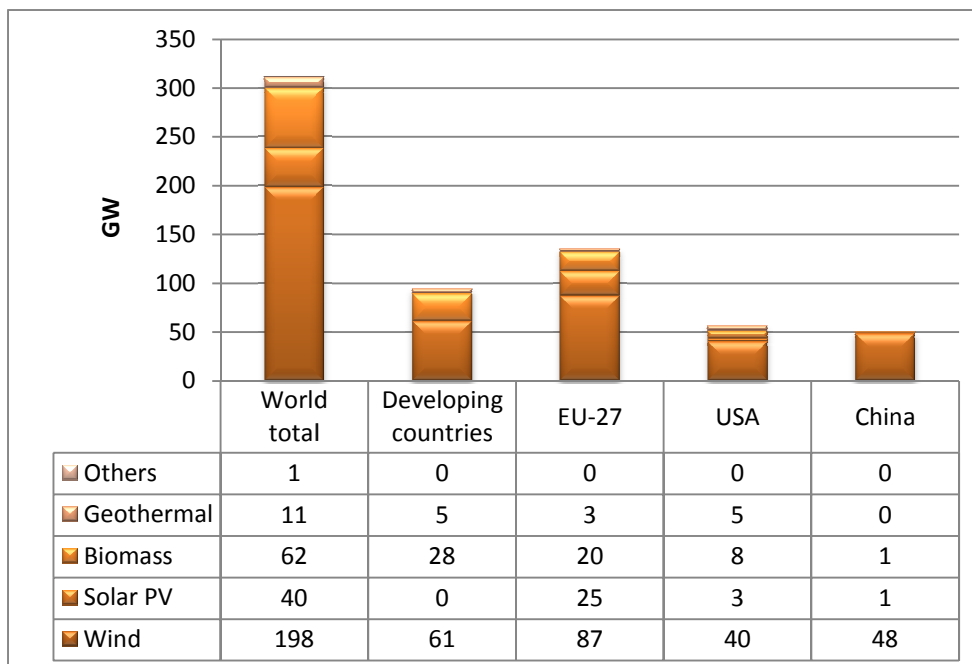


Figure 1.4. Renewable power capacities installed, in 2010, in major Earth regions [GW]. (REN21, 2011)

Efforts in the research and development of models and technical solutions able to convert energy from renewable sources to useful electric and/or thermal power, increasing the penetration of such sources in the global energy mix, are expected and promoted by both national and international institutions (European Commission, 2010, REN21, 2011, United Nations, 2010, United Nations, 2011, World Bank 2009, World Bank, 2011).

The present Ph.D. dissertation investigates these topics from a quantitative and industrial perspective describing models, approaches and the full design and development of a concentrating solar prototype for heat and power cogeneration. An overview of the energy primary source scenario and the associated possible synergies and opportunities is, firstly, presented through both an integrated dynamic optimization cost model and the description of a feasibility study focusing on solar photovoltaic (PV) plants. After that, the solar source is deeply investigated highlighting the background about its high-potential, innovative models and analyses about the prediction of solar radiation flux, representing a basic input for the design of solar energy plants. Furthermore, the concentrating solar PV and thermal sector is focused reviewing existing plant solutions. The description of the design, development and field-test phases of a bi-axial Fresnel lens solar photovoltaic/thermal (PV/T) concentrating prototype is, then, provided giving full details about the functional modules, their integration to the plant and the final installation and run. The monitoring and bi-axial motion control strategies are particularly investigated through the design of a customized semi-automatic control platform, developed adopting LabView™ graphic programming environment. Finally, the study of an auxiliary device to assess tests on the multi-junction solar PV cells adopted in concentrating PV systems is described.

The following paragraph concludes the introduction providing the detailed outline of the present Ph.D. dissertation.

1.1 Dissertation outline

This preliminary chapter introduces the relevance of energy issues in the current global scenario highlighting the strategic orientations to strength access to energy sources and to spread renewable energies and their incidence in the world energy mix. A basic set of aggregated data quantitatively supports the description. In accordance with the introduced topics, the reminder of the present Ph.D. dissertation is organized as follows.

- ✓ **Chapter 2** presents a general dynamic linear programming (LP) optimization cost model for the global design of a production/distribution energy network (focused on the electricity supply issues), including both traditional and renewable sources and the major operative and financial cost drivers. The model highlights the relevance of solar energy as a renewable and low-carbon source. Consequently, the current impact and potential profitability of investments in solar PV plants is investigated with particular reference to small/medium size solutions;

-
- ✓ **Chapter 3** focuses on the solar source describing, at first, the fundamentals of theory. The estimation of solar radiation and of its fractions, i.e. direct, diffuse and reflected components, is, then, investigated presenting a multi-location model for the prediction of solar radiation that overcomes the models and approaches proposed by past and recent literature. Goal of this chapter is answering the crucial question: *“What’s the amount of available solar radiation for a given location or region?”*. The answer to such a question is the key input for both the design and the profitability analysis of solar energy plants;
 - ✓ **Chapter 4** shortly introduces the peculiarities of solar concentration systems and reviews technologies for both PV and thermal concentration. The chapter also provides an overview and classification of the existing plants and introduces the developed solar prototype fully described in the next chapter;
 - ✓ **Chapter 5** aim is to present the bi-axial Fresnel lens solar photovoltaic/thermal (PV/T) concentrating prototype. This research activity is included to a co-financed project whose aim is the study of micro-systems and innovative technologies for solar energy cogeneration. In this context, a *“general to detail”* approach is followed to present the plant, so that a global description precedes a detailed illustration of the five integrated functional modules, i.e. support structure, solar collector and receivers, cooling and heat recovery circuit, bi-axial solar tracker, remote control platform and devices. In this section the physical components and structure, i.e. the hardware, are described while the monitoring and motion control strategies, i.e. the software, are investigated in Chapter 6. Finally, details about the prototype manufacturing costs and the preliminary plant field-test outcomes are presented;
 - ✓ **Chapter 6** presents strategies for bi-axial motion control. Azimuthal and solar altitude solar coordinates are considered suggesting both a forward loop and feedback control approach to track the Sun during day-time, i.e. from sunrise to sunset, together with an original hybrid strategy integrating the previous two. Sunset switch off, or in the event of a danger condition, and restart before sunrise are, also, properly managed. The proposed strategies are implemented in a customized semi-automatic platform, developed with LabView™ graphical programming language, integrating, also, the interfaces for monitoring and performance analysis. Details about the platform are provided together with the outcomes of a set of field-tests assessed to validate the proposed approaches when applied to the prototype;
 - ✓ **Chapter 7** analyses the design of a small-scale concentrating solar simulator, a frequently adopted auxiliary device to test, in a controlled environment, the optic

and energetic properties of multi-junction solar cells. The main components are introduced focusing on the effective design of the reflector through a Monte Carlo simulation ray-tracing approach. This research activity, partially parallel to the previous ones, allows to study a small plant to test commercial and prototypal solar cells to be integrated in concentrating plants, like the studied and described prototype;

- ✓ **Chapter 8** concludes the present dissertation providing final remarks about the developed research activities and proposing suggestions for further improvements of models, approaches and prototypes.

Figure 1.5 illustrates the dissertation outline presenting the key concepts and their division through the chapters.

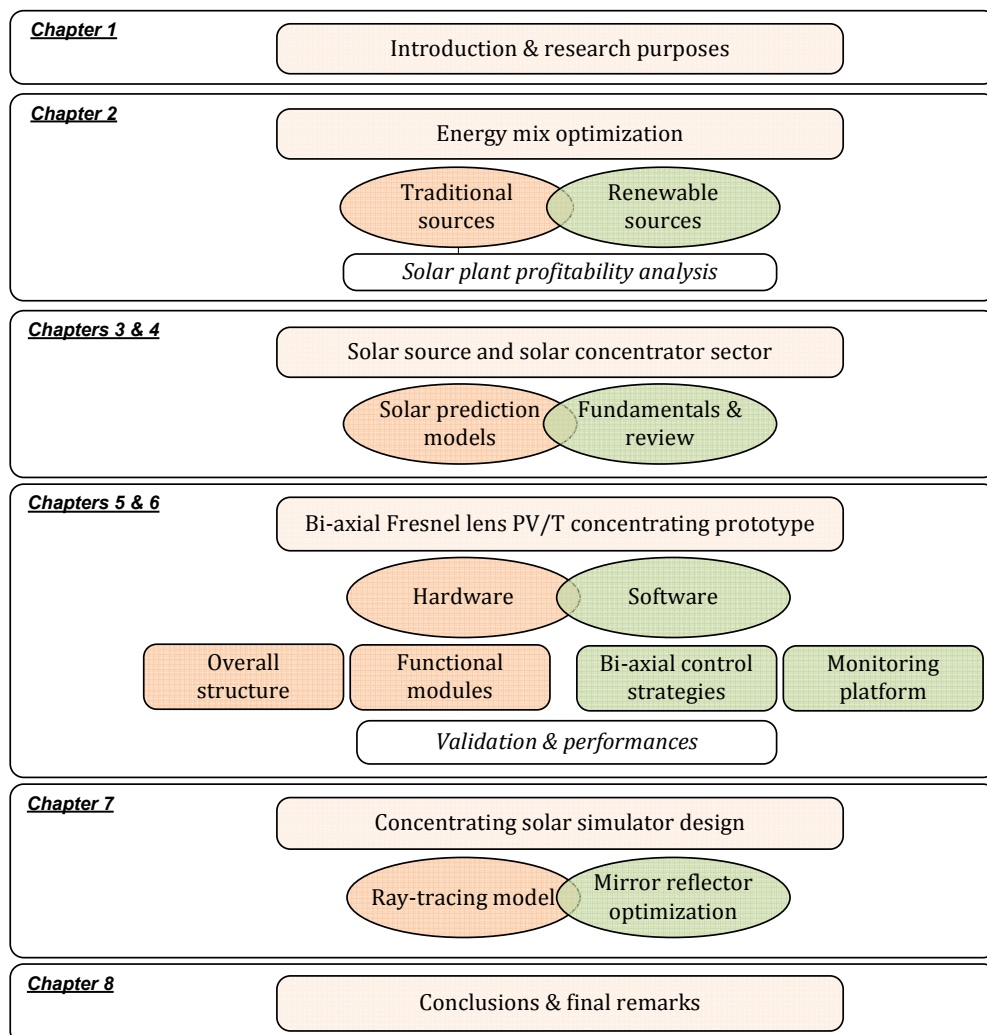


Figure 1.5. Ph.D. dissertation outline.

References

- Arif Ozgur, M., (2008). Review of Turkey's renewable energy potential. *Renewable Energy* 33:2345-2356.
- Baltas, A.E., Dervos, A.N., (2012). Special framework for the spatial planning & the sustainable development of renewable energy sources. *Renewable Energy* 48:358-363.
- Bradbrook, A.J., (1996). The development of a legislative framework for renewable energy and energy conservation. *Renewable Energy* 8(1):107-116.
- International Energy Agency (IEA), (2010). *Key World energy Statistics*. OECD/IED ed. Paris, France.
- International Energy Agency (IEA), (2011). *CO₂ Emissions from Fuel Combustion - Highlights*. OECD/IED ed. Paris, France.
- Jacobsson, S., Johnson, A., (2000). The diffusion of renewable energy technology: an analytical framework and key issues for research. *Energy Policy* 28:625-640.
- Quaschnig, V., (2005). *Understanding Renewable Energy Systems*. Earthscan ed. London, UK.
- Sivek, M., Kavina, P., Jirásek, J., Malečková, V., (2012). Factors influencing the selection of the past and future strategies for electricity generation in the Czech Republic. *Energy Policy* 48:650-656.
- Tsuchiya, H., (2012). Electricity supply largely from solar and wind resources in Japan. *Renewable Energy* 48:318-325.
- United Nations (UN), (2011). *The Millennium Development Goals Report 2011*. Lois Jensen ed., New York, USA.
- Winkler, H., (2005). Renewable energy policy in South Africa: policy options for renewable electricity. *Energy Policy* 33:27-38.
- World Bank, (2009). *Beyond Bonn – World Bank Group Progress on Renewable Energy and Energy Efficiency in Fiscal 2005-2009*. The World Bank Group ed. Washington D.C., USA.

Wüstenhagen, R., Menichetti, E., (2012). Strategic choices for renewable energy investment: conceptual framework and opportunities for further research. *Energy Policy* 40:1-10.

Web - references

European Commission, (2010). *Energy 2020 – A strategy for competitive, sustainable and secure energy*. Brussels, Belgium. Available on line:

<http://eur-lex.europa.eu/LexUriServ/LexUriServ.do?uri=COM:2010:0639:FIN:EN:PDF>

Renewable Energy Policy Network for the 21st Century (REN21), (2011). *Renewables 2011 – Global Status Report*. Paris, France. Available on line:

http://www.ren21.net/Portals/97/documents/GSR/REN21_GSR2011.pdf

United Nations (UN), (2010). *Energy for a Sustainable Future. The Secretary-General's Advisory Group on Energy and Climate Change (AGECC) – Summary report and recommendations*. New York, USA. Available on line:

[http://www.un.org/wcm/webdav/site/climatechange/shared/Documents/AGECC%20summary%20report\[1\].pdf](http://www.un.org/wcm/webdav/site/climatechange/shared/Documents/AGECC%20summary%20report[1].pdf)

United Nations – Energy (UN-Energy), (2005). *The Energy Challenge for Achieving the Millennium Development Goals*. New York, USA. Available on line:

http://www.un-energy.org/sites/default/files/share/une/un-enrg_paper.pdf

World Bank, (2011). *Promotion of New Clean Energy Technologies and the World Bank Group – Background paper for the World Bank Group Energy Sector Strategy*. Washington D.C., USA. Available on line:

http://siteresources.worldbank.org/INTESC/Resources/Clean_tech_background_paper.pdf

2. *Energy network planning*

General LP model for energy network economic optimization and solar PV plant economic assessment

The idea that renewable energy sources, and solar energy among them, are able to fully replace the fossil fuels in the global energy mix in the near future is, rather, utopian. On the contrary, working to increase their incidence and for their pervasive spread close to the traditional energy sources is a priority to decrease the negative impact of fossil fuels on the environment and to start a virtuous cycle in the energy supply sector.

The energy network planning represents a crucial issue to investigate. Defining the energy sources, their mix and the fluxes through the grid is crucial for both the effective energy supply and to give to each energy plant its correct *position* in an integrated and systemic energy grid.

In this chapter the energy network planning issue is discussed presenting a LP economic optimization cost model. The focus is on electricity supply and distribution. The proposed analytic model is general, i.e. it does not focus on any specific geographical area, but it can be adapted and further applied to specific contexts for the systematic energy network and mix design. It, also, represents a general framework to support the identification of the renewable source role highlighting the current scenario and possible perspectives.

The second part of the chapter focuses on the solar renewable source and provides an economic assessment of solar PV plants for the European area. The analysis investigates the technical and economic sustainability of such plants in their life-time and it points out the key elements to make them economically profitable.

In conclusion, the general purpose of this chapter is to provide the context that justifies the importance to study the solar source and plants. Starting from a high level economic analysis and a strategic point of view the relevance of the contributions proposed in the following chapters becomes evident.

2.1 LP model for the energy network design

The relevance of energy networks, or energy grids, to guarantee a pervasive distribution of such a crucial primary source is stressed by past and recent studies (Dong et al., 2012). At the same time, electric energy represents the most multi-purpose energy carrier in modern global economy and therefore primarily linked to human and economic development (Bazmi & Zahedi, 2011). Consequently, the interest is developing models and approaches for the electric energy network design and optimization increased a lot. The energy grid represents the logic connection between the power production systems and the energy demand points and its design deals with a wide set of different decisional issues:

- ✓ source point location;
- ✓ energy mix definition;
- ✓ dispatching strategies selection;
- ✓ energy grid configuration;
- ✓ energy flux definition;
- ✓ etc.

The impact of the energy network design on the energy source mix, the demand satisfaction and the energy cost for final consumers is critic.

In such a context, renewable energies represent an important energy primary source and renewable energy power plants need to be included at the production level of the energy networks, together with traditional fossil fuel power systems.

The adoption of analytic optimization models to face such issues represents an effective strategy to prevent bad decisions coming from informal and short-sighted approaches even if the model development and application is a hard process. According to such a way of tackling the energy network design, the literature proposes several models and methods. Several of them are based on operation research algorithms and optimization models. As example, Bounovas et al. (2011) propose both a framework and an optimization model for energy supply chain design, while Lam et al. (2010) introduce an innovative approach to face the optimization of a regional energy supply chain including the renewable sources. Furthermore, Papapostolou et al. (2011) focus on the optimization of the energy supply chain for a specific renewable source, i.e. biofuels. Bouzembrak et al. (2011) enlarge the optimization targets proposing a multi-objective green supply chain network design approach, while Nelson et al. (2012) consider the western North American scenario introducing a high-resolution modeling for the power system low-cost and low-carbon optimization. Finally, Bazmi & Zahedi (2011) recently review the topic highlighting the key role played by optimization modeling techniques in power generation and supply.

In the following an integrated and dynamic, i.e. time dependent, LP optimization cost model for the electric energy network design is proposed and commented. It includes the key nodes of the grid, i.e. energy power systems, distribution grid, demand points, and it considers a pool of energy sources, including renewable energies. The model belongs to the so-called *location & allocation* (LAP) class of optimization problems.

The model formulation is general, i.e. it does not focus on any specific geographical area, even if it can be adapted and further applied to specific contexts for the systematic energy network and mix design. The appliance of the model to a particular geographic context is not among the purposes of the present Ph.D. dissertation. The proposed model represents a general analytic framework to contextualize the efforts in solar energy conversion models and systems presented in the following chapters.

Finally, the LP model described in the following paragraphs is based on the topics studied at the *Renewable and Appropriate Energy Laboratory* (RAEL) of the *University of California, Berkeley*, as a foreign Visiting Scholar in January-April 2012.

2.1.1 Model outlook, parameters and decisional variables

The model faces the long-term strategic design of an energy network considering a 3-level grid structure. The electricity, modeled as a continuous flux of energy, flows from the power plants, through the grid, to reach the demand points. The overall structure of the grid is Figure 2.1.

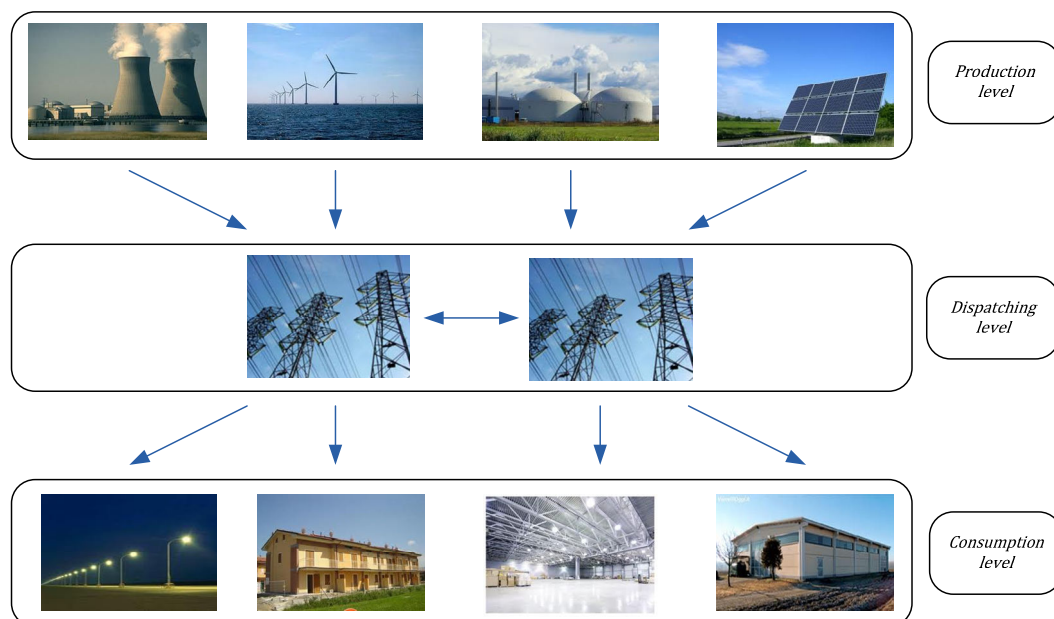


Figure 2.1. Energy network overall structure.

The production and consumption levels represent the origin and the destination of the energy fluxes. The possibility of local self-consumption, i.e. the producer and the consumer are in the same position and they consume the energy they self-produce, is considered reducing the amount of the energy demand, i.e. the energy absorbed from the grid.

The long-term strategic planning horizon allows to include in the model not only the existing power plants and transmission lines, i.e. the grid connections, but also future expansions and new projects for both such infrastructures. The hypothesis below the model is to consider the future plants and connections that have already passed their feasibility study so that their technical and economic features are known together with the expected online year and life-time.

The model parameters, i.e. the data feeding the model, and decisional variables, i.e. the model output, refer to the following nine entities:

- ✓ **Existing plants.** The existing plants belong to the production level and include all the electric energy power plants already online at the beginning of the analysis. Their capacity is assumed to be fixed. Furthermore, they cannot be decommissioned before the end of their life-time;
- ✓ **Future plants (projects).** The future plants represent the options to increase the energy producers. Among them, the model selects the most convenient future investments. Each future plant has a maximum installing capacity, a predetermined online year and life-time and, similarly to the existing plants, a set of investment and annual operative costs;
- ✓ **Existing connections.** The existing connections represent the current state of the distribution electric grid. Their transmission capacity is assumed to be fixed and they cannot be decommissioned before the end of their life-time;
- ✓ **Future connections (projects).** The future connections enlarge the distribution grid increasing its capacity and providing new connections between the geographical areas. The opportunity to install such projects is assessed by the model through proper decisional variables;
- ✓ **Demand points.** Each demand point requires electric energy. The dynamic profile of the energy demand is considered through a set of *samples*. Each sample provides the cumulative energy demand for a specific period of time that belongs to a specific year;

- ✓ **Sources.** The sources represent the set of renewable and traditional primary fonts feeding the electric energy power plants, e.g. biomass, coal, gas, oil, solar, water, wind, etc. For the sake of simplicity, each plant is supposed to require one primary source, only;
- ✓ **Geographical areas.** The geographical areas provide the spatial structure to the model. Each plant and demand point belongs to a geographical area, while each connection allows the electricity flux between two areas. Finally, more plants, demand points or, even, a mix of both can be located in the same geographical area;
- ✓ **Time points.** The time points define the demand temporal resolution. For each demand point and time point a single value of the electric energy demand is considered;
- ✓ **Years.** The years allow to consider the temporal distribution of the investments and rising costs composing the model objective function. Such an entity is used to discount the cash flows and to include the renewable source ratio, i.e. the annual percentage of energy produced from renewable sources.

The next Table 2.1 focuses on the model parameters and presents a list of them organized according to the introduced entities. Details about the adopted notations are, also, provided.

Furthermore, considering the introduced indices, a list of the model decisional variables is in Table 2.2. They refer both to the power plants and the transmission connections and they deal with the project installed capacities, produced and distributed energy.

Table 2.2. Model decisional variables.

Decisional variables		
$I_{C_{sy}}$	Future plant installed capacity	in MW s in FP y in YS
En_{th}	Existing plant produced energy	in MWh t in EP h in TP
En_{sh}	Future plant produced energy	in MWh s in FP h in TP
$I_{C_{my}}$	Future transmission line installed capacity	in MW m in FC y in YS
En_{kh}	Existing transmission line dispatched energy	in MWh k in EC h in TP
En_{mh}	Future transmission line dispatched energy	in MWh m in FC h in TP

Table 2.1. Model parameters and notations.

Existing plants			Future plants (projects)		
Index: t			Index: s		
Set: EP			Set: FP		
co_t	Plant area	in AR	co_s	Plant area	in AR
st_t	Source type	in SO	st_s	Source type	in SO
cp_t	Installed capacity	in MW	cp_s	Maximum capacity	in MW
η_t	Composite outage	in $[0,1]$	η_s	Composite outage	in $[0,1]$
e_t	Earliest online year	in YS	e_s	Earliest online year	in YS
lt_t	Plant life-time	in years	lt_s	Plant life-time	in years
χ_t	Annual capacity factor	in $[0,1]$	χ_s	Annual capacity factor	in $[0,1]$
i_t	Investment cost	in €/MW	i_s	Investment cost	in €/MW
f_t	Annual fix cost	in €/MW	f_s	Annual fix cost	in €/MW
v_t	Annual variable cost	in €/MWh	v_s	Annual variable cost	in €/MWh
u_t	Decommissioning cost	in €/MW	u_s	Decommissioning cost	in €/MW
b_t	Base-load plant	boolean	b_s	Base-load plant	boolean
Existing Connections			Future Connections (projects)		
Index: $k = (b, q)$			Index: $m = (b, q)$		
Set: $EC \subseteq AR \times AR$			Set: $FC \subseteq AR \times AR$		
cp_k	Installed capacity	in MW	cp_m	Maximum capacity	in MW
η_k	Transmission losses	in $[0,1]$	η_m	Transmission losses	in $[0,1]$
e_k	Earliest online year	in YS	e_m	Earliest online year	in YS
lt_k	Line life-time	in years	lt_m	Line life-time	in years
i_k	Investment cost	in €/MW	i_m	Investment cost	in €/MW
f_k	Annual fix cost	in €/MW	f_m	Annual fix cost	in €/MW
v_k	Annual variable cost	in €/MWh	v_m	Annual variable cost	in €/MWh
u_k	Decommissioning cost	in €/MW	u_m	Decommissioning cost	in €/MW
Demand points			Sources		
Index: p			Index: j		
Set: DP			Set: SO		
co_p	Demand point area	in AR	r_j	Renewable	boolean
d_{ph}	Demand entity	in MWh h in TP	c_{jy}	Source cost	in €/MWh y in YS
Time points			Years		
Index: h			Index: y		
Set: TP			Set: YS		
yr_h	Year	in YS	α_y	Discount factor	positive real
dr_h	Time-point duration	in hours	φ_{ay}	% energy from renewable sources	in $[0,1]$ a in AR
Geographical areas					
Index: a					
Set: AR					

2.1.2 Objective function

The model objective function considers the discounted global cost of the energy network as the result of the sum of the rising fix and variable costs, the fuel costs and the investment outflows for the grid enlargement and the inclusion of the future projects. Its analytic expression is provided in the following.

$$\phi = \sum_{t \in EP} i_t \cdot cp_t \cdot \alpha_{e_t} + \sum_{s \in FP} \sum_{y \in YS} i_s \cdot Ic_{sy} \cdot \alpha_y + \quad (2.1)$$

$$\sum_{k \in EC} i_k \cdot cp_k \cdot \alpha_{e_k} + \sum_{m \in FC} \sum_{y \in YS} i_m \cdot Ic_{my} \cdot \alpha_y + \quad (2.2)$$

$$\sum_{t \in EP} \sum_{\substack{y \in YS \\ e_t \leq y \leq e_t + lt_t}} f_t \cdot cp_t \cdot \alpha_y + \sum_{s \in FP} \sum_{y \in YS} f_s \cdot \sum_{\substack{y_1 \in YS \\ y_1 \leq y}} Ic_{sy_1} \cdot \alpha_y + \quad (2.3)$$

$$\sum_{k \in EC} \sum_{\substack{y \in YS \\ e_k \leq y \leq e_k + lt_k}} f_k \cdot cp_k \cdot \alpha_y + \sum_{m \in FC} \sum_{y \in YS} f_m \cdot \sum_{\substack{y_1 \in YS \\ y_1 \leq y}} Ic_{my_1} \cdot \alpha_y + \quad (2.4)$$

$$\sum_{t \in EP} u_t \cdot cp_t \cdot \alpha_{e_t + lt_t + 1} + \sum_{s \in FP} u_s \cdot \sum_{y \in YS} Ic_{sy} \cdot \alpha_{e_s + lt_s + 1} + \quad (2.5)$$

$$\sum_{k \in EC} u_k \cdot cp_k \cdot \alpha_{e_k + lt_k + 1} + \sum_{m \in FC} u_m \cdot \sum_{y \in YS} Ic_{my} \cdot \alpha_{e_m + lt_m + 1} + \quad (2.6)$$

$$\sum_{t \in EP} \sum_{h \in TP} v_t \cdot En_{th} \cdot \alpha_{yr_h} + \sum_{s \in FP} \sum_{h \in TP} v_s \cdot En_{sh} \cdot \alpha_{yr_h} + \quad (2.7)$$

$$\sum_{k \in EC} \sum_{h \in TP} v_k \cdot En_{kh} \cdot \alpha_{yr_h} + \sum_{m \in FC} \sum_{h \in TP} v_m \cdot En_{mh} \cdot \alpha_{yr_h} + \quad (2.8)$$

$$\sum_{j \in SO} \sum_{y \in YS} c_{jy} \cdot \left(\sum_{\substack{t \in EP \\ st_t = j}} \sum_{\substack{h \in TP \\ yr_h = y}} En_{th} + \sum_{\substack{s \in FP \\ st_s = j}} \sum_{\substack{h \in TP \\ yr_h = y}} En_{sh} \right) \cdot \alpha_y \quad (2.9)$$

In particular:

- ✓ Eq. 2.1 considers the investments for existing plants and future projects. The former addend is a sunk cost because it refers to investments already made, i.e. it does not depend on the decisional variables, while the latter is proportional to the installed power capacity. The model assumes the outflows for the existing plants to occur during their earliest online year, i.e. the discount factor is α_{e_t} , where e_t is the aforementioned earliest online year;
- ✓ Eq. 2.2 is similar to the previous equation and focuses on the existing connections and future projects;
- ✓ Eq. 2.3 computes the fix costs for the power plants. The two addends are similar to those in Eq. 2.1 and the previous considerations remain valid;
- ✓ Eq. 2.4 refers to the fix costs for the transmission connections and it follows the previous considerations;

- ✓ Eq. 2.5 and Eq. 2.6 compute the plant and connection decommissioning costs. The model assumes such outflows to occur during the first year after the end of the plant life-time;
- ✓ Eq. 2.7 computes the variable costs for energy production. For each year, they are proportional to the produced electricity;
- ✓ Eq. 2.8. includes the variable dispatching costs. They depend on the amount of electricity flowing through each connection line;
- ✓ Eq. 2.9. introduces the energy source costs for energy production. For each year, the produced electricity is grouped by the energy source it comes from to compute the related cost. Both the existing plants and the future projects are considered.

2.1.3 Constraints

The following set of constraints completes the proposed LP model.

$$\min \phi \quad (2.10)$$

subject to:

$$\sum_{\substack{k=(b,q) \in EC \\ q=a}} En_{kh} + \sum_{\substack{m=(b,q) \in EC \\ q=a}} En_{mh} - \sum_{\substack{k=(b,q) \in EC \\ b=a \wedge q \neq a}} En_{kh} - \sum_{\substack{m=(b,q) \in EC \\ b=a \wedge q \neq a}} En_{mh} = \sum_{\substack{p \in DP \\ c_o_p = a}} d_{ph} \quad a \in AR, h \in TP \quad (2.11)$$

$$\sum_{\substack{t \in EP \\ c_o_t = a}} En_{th} + \sum_{\substack{s \in FP \\ c_o_s = a}} En_{sh} = \sum_{\substack{k=(b,q) \in EC \\ b=a}} En_{kh} \cdot (1 + \eta_k) + \sum_{\substack{m=(b,q) \in FC \\ b=a}} En_{mh} \cdot (1 + \eta_m) \quad a \in AR, h \in TP \quad (2.12)$$

$$\sum_{\substack{t \in EP \\ r_{st}=1}} \sum_{\substack{h \in TP \\ y r_h = y}} En_{th} + \sum_{\substack{s \in FP \\ r_{st}=1}} \sum_{\substack{h \in TP \\ y r_h = y}} En_{sh} \geq \varphi_{ay} \cdot \left(\sum_{\substack{t \in EP \\ y r_h = y}} \sum_{\substack{h \in TP \\ y r_h = y}} En_{th} + \sum_{\substack{s \in FP \\ y r_h = y}} \sum_{\substack{h \in TP \\ y r_h = y}} En_{sh} \right) \quad a \in AR, y \in YS \quad (2.13)$$

$$\sum_{y \in YS} Ic_{sy} \leq cp_s \quad s \in FP \quad (2.14)$$

$$Ic_{sy} = 0 \quad s \in FP, y \in YS \wedge (y < e_s \vee y > e_s + lt_s) \quad (2.15)$$

$$\sum_{y \in YS} Ic_{my} \leq cp_m \quad m \in FC \quad (2.16)$$

$$Ic_{my} = 0 \quad m \in FP, y \in YS \wedge (y < e_m \vee y > e_m + lt_m) \quad (2.17)$$

$$En_{th} = 0 \quad t \in EP, h \in TP \wedge (y r_h < e_t \vee y r_h > e_t + lt_t) \quad (2.18)$$

$$En_{th} = cp_t \cdot dr_h \cdot (1 - \eta_t) \cdot \chi_t \quad t \in EP \wedge b_t = 1, h \in TP \wedge (e_t \leq y r_h \leq e_t + lt_t) \quad (2.19)$$

$$En_{th} \leq cp_t \cdot dr_h \cdot (1 - \eta_t) \cdot \chi_t \quad t \in EP \wedge b_t = 0, h \in TP \wedge (e_t \leq yr_h \leq e_t + lt_t) \quad (2.20)$$

$$En_{sh} = 0 \quad s \in FP, h \in TP \wedge (yr_h < e_s \vee yr_h > e_s + lt_s) \quad (2.21)$$

$$En_{sh} = \sum_{\substack{y \in YS \\ y \leq yr_h}} Ic_{sy} \cdot dr_h \cdot (1 - \eta_s) \cdot \chi_s \quad s \in FP \wedge b_s = 1, h \in TP \wedge (e_s \leq yr_h \leq e_s + lt_s) \quad (2.22)$$

$$En_{sh} \leq \sum_{\substack{y \in YS \\ y \leq yr_h}} Ic_{sy} \cdot dr_h \cdot (1 - \eta_s) \cdot \chi_s \quad s \in FP \wedge b_s = 0, h \in TP \wedge (e_s \leq yr_h \leq e_s + lt_s) \quad (2.23)$$

$$En_{kh} = 0 \quad k \in EC, h \in TP \wedge (yr_h < e_k \vee yr_h > e_k + lt_k) \quad (2.24)$$

$$En_{kh} \leq cp_k \cdot dr_h \cdot (1 - \eta_k) \quad k \in EC, h \in TP \wedge (e_k \leq yr_h \leq e_k + lt_k) \quad (2.25)$$

$$En_{mh} = 0 \quad m \in FC, h \in TP \wedge (yr_h < e_m \vee yr_h > e_m + lt_m) \quad (2.26)$$

$$En_{mh} \leq \sum_{\substack{y \in YS \\ y \leq yr_h}} Ic_{my} \cdot dr_h \cdot (1 - \eta_m) \quad m \in FC, h \in TP \wedge (e_m \leq yr_h \leq e_m + lt_m) \quad (2.27)$$

$$Ic_{sy}, En_{th}, En_{sh}, Ic_{my}, En_{kh}, En_{mh} \geq 0 \quad s \in FP, y \in YS, t \in EP, h \in TP, m \in FC, k \in EC \quad (2.28)$$

Eq. 2.10 minimizes the objective function. Eq. 2.11 guarantees the complete electricity supply to all the demand points located in each geographical area. In Eq. 2.12 the balance of energy flows is fixed so that all the produced energy flows through the grid to reach the demand points. For each year and geographical area, the following Eq. 2.13 forces to produce at least a fraction φ_{ay} of electricity from renewable sources. Eq. 2.14 to Eq. 2.17 force not to exceed the maximum plant and connection capacity and set to zero the installed capacity for all years out of the plant life-time. Eq. 2.18 to Eq. 2.20 consider the energy produced from the existing plants. It must be null out of the plant-life (Eq. 2.18). It is equal to the nominal capacity for base-load plants (Eq. 2.19), while, for non base-load plants it must not exceed the nominal capacity (Eq. 2.20). Eq. 2.21 to Eq. 2.23 are similar and they refer to the future plants. In such equations the considered installed capacity is the cumulate value of Ic_{sy} for all the past years, i.e. all the years before yr_h . Eq. 2.24 to Eq. 2.27 set the same constraints for the existing and future connections. No base-load connections exist. Finally, Eq. 2.28 guarantees the consistence to the decisional variables.

2.1.4 Comments and developments

The proposed LP model for the design of an energy network including a pool of existing and future plants and connections represents a framework to face the energy grid planning issues through a systematic and integrated approach. Its main strength is the global

point of view including all the entities involved in the production, distribution and consumption of the electric energy. Looking for a global minimum of cost allows to take advantage of the existing synergies, e.g. the economies of scale, the benefits coming from locating a specific plant in a favorable site, the reduction of the transmission lengths and costs, etc. As in the logistics for goods the global network optimization does not come from the join of local optima.

Furthermore, the proposed model supports a rational definition of the energy source mix for the considered context. The energy fractions include both conventional and renewable sources. Each energy source is selected to feed the plants considering the convenience of such a choice so that the best locations are considered, e.g. windy and sunny locations, primary source proximity, etc. In addition, for the most of the renewable sources, e.g. solar and wind, a great opportunity is from the null cost of the source. For such sources the last term of the objective function is, generally, equal to zero. Finally, considering the set of the introduced constraints, only Eq. 2.13 explicitly forces the use of renewable sources to meet the lower bound expressed by φ_{ay} . This equation is introduced to model the constraints actually in force to spread the adoption of renewable primary sources of energy. In Chapter 1 details are provided for the European context. Except for the constraints forced by legislations this version of the model does not introduce other external benefits for energy produced from renewable sources even if, in some contexts, incentive policies are, actually, present. Given an operative context, changes in the model are feasible to introduce such elements before the model run.

Several aspects can be introduced to refine the proposed model and to fit it to a specific geographical context. The following list reviews some of the possible developments:

- ✓ the demand profiles are assumed deterministic. A model introducing statistic distributions of the demand entity for each demand point and time point is possible;
- ✓ the demand requests are rigid. Nowadays, the most recent energy supply contracts introduce ranges for the energy shift and shed especially during demand peaks making the energy grid reactive, i.e. the *demand response* and *smart grid* paradigms. The inclusion of such issues to the model is among the possible developments;
- ✓ some national legislations and/or international plans force not only a minimum of energy produced from renewable sources but they fix upper limits to the atmosphere emissions and they introduce costs and politics to manage the emission authorizations, e.g. EU gas emission trading schemes. Further constraints to the proposed model can be introduced in such a direction;

- ✓ the incentive politics for energy self-consumption and net metering can be included to the model both as negative cost fluxes, i.e. opportunity costs, and as constraints to the produced and distributed energy.

The proposed optimization model introduces an effective approach for energy network management providing the framework for renewable energy spread, sustainable development and the integration between renewable and conventional sources in the energy mix.

The present Ph.D. dissertation focuses on solar renewable source investigating its potential and perspectives. The following paragraph matches the electric energy production issues to the solar renewable source studying the economic feasibility of PV solar plants. An analysis for the technical and economical assessment of PV systems in the European area is proposed with the main purpose to highlight the conditions most affecting the economic feasibility of PV systems in eight relevant European countries. The obtained results are of interest to point out the trend of the opportunities for future investments in solar PV plants and, generally, to understand the potential of such a renewable source.

2.2 Economic assessment of PV plants in Europe

This paragraph focuses on the economic assessment of PV plants, introducing a performance cost model, based on the net present value (NPV) and payback (PB) capital budget indices, to quantify the net cash flows through the plant life-time and evaluate their economic sustainability. The analysis is based on Bortolini et al. (2013) and matches a set of parameters affecting the plant performances, i.e. technical, environmental, economic and financial parameters, with the purpose to highlight those which are the most critical. Furthermore, the national legislations and incentive schemes for supporting the PV sector are reviewed and included to the model. Eight relevant European countries are investigated, i.e. France, Germany, Greece, Italy, Spain, The Netherlands, Turkey and United Kingdom. The final goal deals with a critical analysis of the PV sector to point out the opportunities it offers together with the criticalities and improvements that are, still, required.

The proposed model overcomes the wide set of existing literature studies including, in a unique model, a multi-country and multi-parameter analysis considering both the country peculiarities and the technical, environmental and economic conditions of several PV plant configurations. The major of the literature contributions focus on single country analyses. As example, Bernal-Augustin & Dufo-Lopez (2006), Fernandez-Infantes et al. (2006) and Hernández et al. (2008) present detailed economic studies on PV systems for Spain, while Hammond et al. (2012) focus on the United Kingdom context. Furthermore,

Focacci (2009) reviews the PV sector for Italy, Audenaert et al. (2010) propose an economic evaluation of grid connected PV systems in Flanders, Belgium, and Šály et al. (2006) review the status and conditions of PVs in Slovakia. Outside the European area, several contributions refer to the US, China and other developed countries, e.g. Becerra-López & Golding (2008), Fthenakis et al. (2009), Zhang et al. (2012), or, even, to developing countries belonging to the Sun-belt area where the potential of solar energy is higher than elsewhere. As example, Diarra & Akuffo (2002) focus on Mali, Al-Salaymeh et al. (2010) consider PV systems located in Jordan, Ghoneim et al. (2002) investigate the scenario for Kuwait, Mitscher & Rüter (2012) focus on the Brazilian region, while, finally, Nässén et al. (2002) propose an assessment of solar PVs in northern Ghana. Furthermore, a parallel research field develops comparisons among countries considering single aspects of the PV energy sector. Several works discuss the national incentive policies highlighting similarities and differences among current legislations (Reiche & Bechberger, 2004, Rowlands, 2005, Campoccia et al., 2007 & 2009, Di Dio et al., 2007, Barbose et al., 2008), while other studies evaluate the trend of PV costs with a long-term horizon correlating the past trends to the current state of the art of the manufacturing technologies (EurObserv'ER, 2007-2012).

2.2.1 Performance cost model

Figure 2.2 shows the *flow-chart* of the proposed approach for PV system analysis highlighting the considered technical, environmental, economic and financial data included in the model together with the analysis steps.

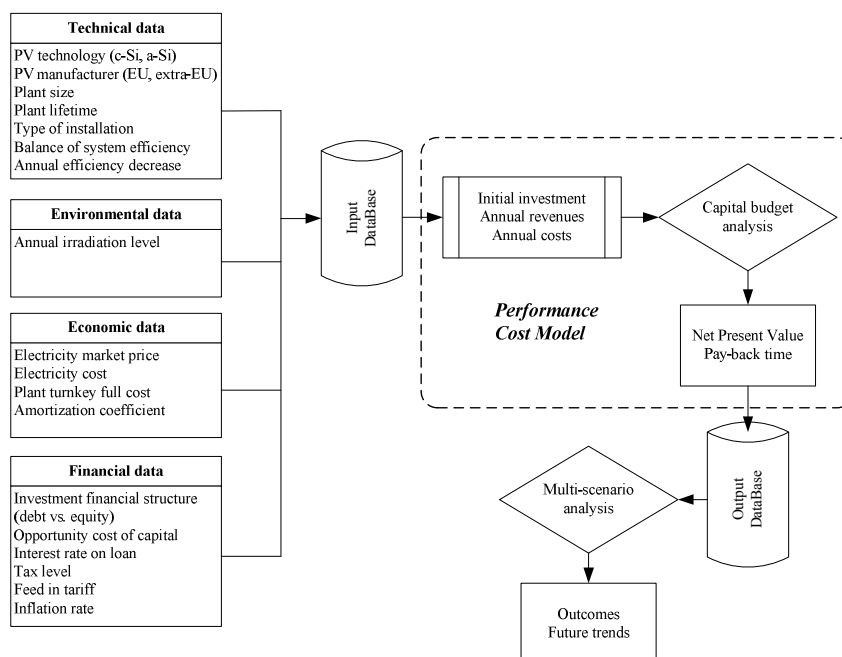


Figure 2.2. Flow chart of the proposed PV system analysis.

Starting from the input data, the performance cost model calculates the entity of the initial investment and the annual revenues and costs for each developed scenario. Such data allow to compute the NPV and PB justifying the economic feasibility of the analyzed configuration. Eq. 2.29 defines the analytic expression for NPV, while Eq. 2.30 considers the PB, i.e. the minimum number of years necessary to return on the investment.

$$NPV = -C_0 + \sum_{j=1}^n \frac{R_j - C_j}{(1+OCC)^j} \quad (2.29)$$

$$-C_0 + \sum_{j=1}^{PB} \frac{R_j - C_j}{(1+OCC)^j} = 0 \quad (2.30)$$

where:

- ✓ C_0 is the cost of the initial investment, for residential plants VAT is, already, included [€];
- ✓ R_j is the revenue for year j [€/year];
- ✓ C_j is the operative outflow for year j [€/year];
- ✓ OCC is the Opportunity Cost of Capital [%];
- ✓ n is the estimated plant lifetime [year].

The initial investment, C_0 , includes all the plant installation costs and the land purchase if the PV system is non-integrated.

$$C_0 = c_{module} \cdot kWp + c_{land} \cdot S \quad (2.31)$$

where:

- ✓ kWp is the nominal plant size [kWp];
- ✓ c_{land} is the land cost [€/m²], 0 for integrated PV systems;
- ✓ S is the ground requested area calculated as a function of the nominal plant size and the module conversion efficiency [m²].

and c_{module} is the specific installation cost of the PV system [€/kWp] obtained through a market research for both European and extra European manufactures and considering the two most frequently adopted silicon cell technologies, i.e. amorphous (a-Si) and crystalline (c-Si) solar cells. The following correlation functions between PV installation cost and its rated power express the market survey outcomes.

$$c_{module}^{EU cSi} = 2828.7 \cdot kWp^{-0.128} \quad (2.32)$$

$$c_{module}^{Extra\ EU\ cSi} = 2539.9 \cdot kWp^{-0.139} \quad (2.33)$$

$$c_{module}^{EU\ aSI} = 2356.4 \cdot kWp^{-0.114} \quad (2.34)$$

$$c_{module}^{Extra\ EU\ aSI} = 2115.8 \cdot kWp^{-0.126} \quad (2.35)$$

The operative outflow for the generic year j is as follows.

$$C_j = C^{OM\&I} \cdot (1 + g)^{j-1} + C_j^D + C_j^I + C_j^T \quad (2.36)$$

where:

- ✓ $C^{OM\&I}$ is the annual operation and maintenance outflow [€/year];
- ✓ g is the inflation rate [%];
- ✓ C_j^D is the annual outflow for the interest paid to finance the investment [€/year];
- ✓ C_j^I is the outflow due to inverter substitution for year j , for residential plants VAT is, already, included [€/year];
- ✓ C_j^T is the annual tax cost for year j , 0 if net cash flow is negative and for all residential installations [€/year].

The interest paid to finance the investment, C_j^D , occurs for non totally private equity financed investments and it is calculated through the straight line depreciation approach as in Eq. 2.37.

$$C_j^D = r \cdot \left[\varphi \cdot C_0 - \sum_{k=1}^{j-1} \left(\frac{(1+r)^k \cdot r}{(1+r)^{n-1}} \cdot \varphi \cdot C_0 - C_k^D \right) \right] \quad (2.37)$$

where:

- ✓ r is the money interest rate on loan [%];
- ✓ φ is the loan percentage [%].

Furthermore, the inverter substitution cost, C_j^I , is a common expenditure during PV plant lifetime. In the present model, a market research drives the computation of such a cost. Eq. 2.38 expresses the inverter substitution cost as a function of the plant size, while Eq. 2.39 is the best fit curve correlating the inverter specific cost to its rated power. The last equation comes from the aforementioned market survey.

$$C_j^I = c_{inverter} \cdot kWp \quad (2.38)$$

$$c_{inverter} = 0.0325 \cdot kWp^2 + 196,25 \cdot kWp + 350.95 \quad (2.39)$$

Finally, the amount of the annual tax cost, C_j^T , is expressed in Eq. 2.40 adopting the Earning Before Tax (EBT) approach.

$$C_j^T = [R_j - C^{OM\&I} \cdot (1 + g)^{j-1} - C_j^D - C_j^I - A] \cdot t \quad (2.40)$$

where:

- ✓ $A = \frac{(1+OCC)^a \cdot OCC}{(1+OCC)^a - 1} \cdot c_{module} \cdot kWp$ is the plant amortization rate, supposed constant [€/year];
- ✓ a is the plant amortization length [year];
- ✓ t is the corporate tax level [%].

The revenues R_j , which increase the plant NPV, come from both energy self-consumption and the national grid sell of the produced energy. In the first case, users do not buy electricity from the grid, while in the latter the benefits come either from the incentives, if provided, or from energy selling. The following Eq. 2.41 introduces the annual revenue expression for the generic year j .

$$R_j = R_j^S \cdot \%_{sold} + R_j^C \cdot (1 - \%_{sold}) \quad (2.41)$$

where:

- ✓ $\%_{sold}$ is the percentage of the produced energy sold to the grid [%];
- ✓ $R_j^C = E_c \cdot (1 + g)^{j-1} \cdot E_p \cdot [1 - (j - 1) \cdot \eta_d]$ is the cost saving due to energy self-consumption for year j [€/year];
- ✓ R_j^S is the energy selling revenue for year j [€/year] with
 - $R_j^S = i \cdot E_p \cdot [1 - (j - 1) \cdot \eta_d]$ if a national FIT is provided;
 - $R_j^S = E_{mp} \cdot (1 + g)^{j-1} \cdot E_p \cdot [1 - (j - 1) \cdot \eta_d]$ otherwise (no FIT);
- ✓ E_c is the electricity price for energy bought from the grid [€/kWh];
- ✓ i is the FIT [€/kWh];
- ✓ E_{mp} is the electricity price for energy sold to the grid [€/kWh];
- ✓ η_d is the yearly efficiency system decrease [%];

and the expression for the annual produced energy, E_p , is in the following Eq. 2.42

$$E_p = I_r \cdot kWp \cdot \eta_{BOS} \quad (2.42)$$

where:

- ✓ I_r is the annual global irradiation level [kWh/kWp·year];
- ✓ η_{BOS} is the balance of system efficiency [%].

2.2.2 Input parameters and scenarios

The introduced model is adopted to develop a multi-country and multi-parameter analysis to study the conditions most affecting the profitability of PV systems in the considered countries. Several configurations come from a specific setting of the introduced parameters, while varying such parameters the comparison among different configurations becomes possible. Particularly, nineteen independent parameters need to be defined to fix each scenario. In Table 2.3 and associated Table 2.4, the boundary conditions for such parameters are presented.

Table 2.3. Values for the performance cost model input parameters.

Parameter	Adopted values
Technical data	
kWp	3, 20, 50, 100, 1000kWp for industrial PV plants 3-6-9-12-15kWp for residential PV plants
n	20 years
$\%_{sold}$	0%, 50%, 100%
η_d	1%
η_{BOS}	85%
Environmental data	
I_r	from 800 to 1800kWh/kWp·year, step 50kWh/kWp·year
Economic data	
a	10 years
c_{land}	9€/m ² for non-integrated PV plants, 0€/m ² for integrated PV plants
c_{module}	function of kWp, manufacturer and PV technology (see Eq. 2.32 to Eq. 2.35)
$c^{OM\&I}$	equal to 1% of C_0
$c_{inverter}$	function of kWp (see Eq. 2.39), 0 for $j \neq 7$ and 14 (inverter replacement occurs two times during plant lifetime)
E_c	according to the next Table 2.4, columns 3 and 4
E_{mp}	according to Table 2.4, column 2
Financial data	
g	according to Table 2.4, column 7
i	according to national schemes reviewed in the next Section 2.2.2.1
OCC	3%, 6%
r	3%, 4%, 5%, 6%, 7%, 8%, 9%, 10%
t	according to Table 2.4, column 5
φ	0%, 50%, 100%

Table 2.4. Country economic and financial data: electricity price, tax level and inflation (year 2012).

Country	Electricity prices [€/kWh]			Tax levels		Annual inflation rate
	Energy sold to the market	Energy bought from the grid (industry)	Energy bought from the grid (residential)	Corporate tax	Value added tax (VAT)	
France	0.0449	0.1340	0.2781	33.33%	19.60%	2.30%
Germany	0.0623	0.1188	0.1403	29.51%	19.00%	2.50%
Greece	0.0774	0.1565	0.2164	25.00%	23.00%	3.10%
Italy	0.0483	0.1261	0.2154	31.40%	21.00%	2.90%
Spain	0.0535	0.0763	0.1478	30.00%	18.00%	3.10%
The Netherlands	0.0448	0.1149	0.1676	25.00%	19.00%	2.50%
Turkey	0.0472	0.1181	0.2202	20.00%	18.00%	6.50%
United Kingdom	0.0740	0.0790	0.1220	24.00%	20.00%	2.40%

2.2.2.1 National PV sector key-elements

In the following, details about the incentive schemes for the eight considered countries are proposed. Data refers to year 2012 and are from official legislation sources (a full list in the Reference section).

France: The French government supports PV sector through the Feed in Tariff (FIT) scheme of Table 2.5. Incentives are for 20 years and residential plants benefit of a, further, 7% VAT reduction calculated on the PV installation turnkey cost.

Table 2.5. FIT for France [€/kWh].

Plant type	Residential	Industrial
Integrated systems < 9kWp	0.3539	0.2136
Integrated systems 9kWp-36kWp	0.3096	-
Simplified integrated systems 0-36kWp	-	0.1842
Simplified integrated 36kWp-100kWp	-	0.1750
Non integrated systems	0.1051	0.1051

Germany: German government applies a FIT to PV systems for 20 years. The FIT decreases every year due to a fixed reduction rate function of the previous year installed capacity. For PV systems installed in 2012, the decrease rate is of 15% (Table 2.6).

Greece: Greece applies a FIT to energy from PV systems with installed electrical capacity lower than 1MWp. The FIT is for 20 years for non-integrated and building integrated systems over 10kWp and of 25 years for building integrated systems up to 10kWp. FIT grants 0.250€/kWh for building integrated systems up to 10kWp. For non-

integrated and building integrated systems with rated power lower than 100kWp the FIT is of 0.225€/kWh, while it decreases to 0.180€/kWh for higher power plants.

Table 2.6. FIT for Germany [€/kWh].

Plant type	FIT	Additional FIT based on self-consumption ratio	
		< 30%	> 30%
Integrated systems < 30kWp	0.244	< 30%	0.105
		> 30%	0.142
Integrated systems 30 kWp-100kWp	0.232	< 30%	0.094
		> 30%	0.130
Integrated systems 100kWp-1MWp	0.220	< 30%	0.081
		> 30%	0.118
Integrated systems > 1MWp	0.184	-	-
Non integrated systems	0.179	-	-

Italy: Since August 2012, a new incentive scheme is in force in Italy. As in Table 2.7, an overall FIT for production and sale of PV energy and a premium tariff for self-consumption are introduced. Furthermore, a FIT increase of 10% is applicable if more than 60% of the investment is from EU producers, excluding the labor cost. Italian legislation, also, provides a 10% VAT reduction to any PV installation.

Table 2.7. FIT for Italy [€/kWh].

Plant size	Integrated systems		Non-integrated systems	
	FIT	Premium tariff	FIT	Premium tariff
1kWp-3kWp	0.208	0.126	0.201	0.119
3kWp -20kWp	0.196	0.114	0.189	0.107
20kWp-200kWp	0.175	0.093	0.168	0.086
200kWp-1000kWp	0.142	0.060	0.135	0.053
1000kWp-5000kWp	0.126	0.044	0.120	0.038
> 5000kWp	0.119	0.037	0.113	0.031

Spain: In Spain, the current FIT for PV systems is of 0.289€/kWh for building integrated systems with rated power lower than 20kWp, 0.204€/kWh for building integrated systems with rated power between 20kWp and 2MWp and 0.135€/kWh for non-integrated systems.

The Netherlands: During 2011, the Dutch government promoted the production of renewable energy through the Sustainable Energy Incentive Scheme Plus (SDE+) providing a 15 years FIT of 0.120€/kWh. From 2012, Dutch government cuts all incentives to energy production from PV systems.

Turkey: FIT in Turkey are for 20 years and equals to 0.100€/kWh for PV systems commissioned before the end of 2015. A FIT increase of 0.052€/kWh is applicable if plant components are manufactured in Turkey.

United Kingdom: FIT scheme to support PV systems with rated power lower than 50MWp is in Table 2.8. FIT is granted for 25 years.

Table 2.8. United Kingdom PV system incentives [€/kWh].

Plant size	FIT
< 4kWp	0.260
4kWp-10kWp	0.210
10kWp-50kWp	0.188
50kWp-200kWp	0.160
> 250kWp	0.105

2.2.3 Results and discussion

Firstly, the impact of national support schemes and FIT to promote the PV sector is investigated. Residential and industrial plants are studied separately due to differences in the legislations actually in force. Figure 2.3 and Figure 2.4 propose the obtained results, while in the figure captions the values of the parameters assumed constant are provided in brackets.

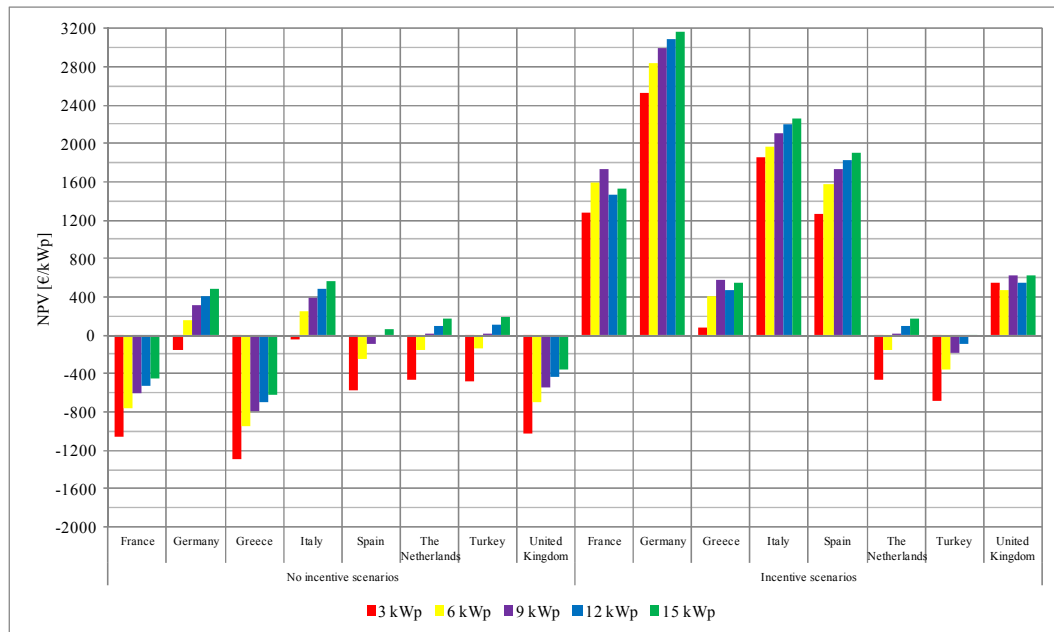


Figure 2.3. Incentive vs. no-incentive scenarios for the eight countries and residential rooftop plants

(c_{module} according to Eq.7, $I_r = 1400\text{kWh/kWp}\cdot\text{year}$, $OCC = 3\%$, $\varphi = 0\%$, $\%_{sold} = 50\%$).

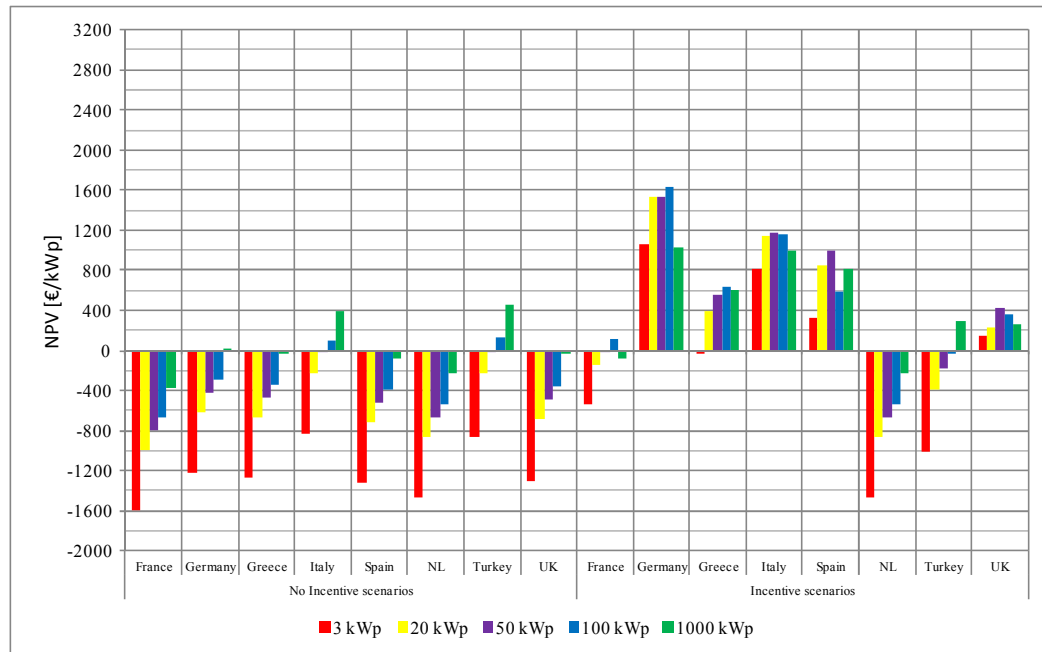


Figure 2.4. Incentive vs. no-incentive scenarios for the eight countries and industrial rooftop plants (c_{module} according to Eq.7, $I_r = 1400\text{kWh/kWp-year}$, $OCC = 3\%$, $\varphi = 0\%$, $\%_{sold} = 50\%$).

Results highlight the key role still played by the national support policies. Incentive scenarios outperform no-incentive scenarios for all plant sizes and countries, except for The Netherlands, in which results are the same due to the absence of national FIT, and Turkey due to the concurrent low level of the FIT and the high inflation rate rising the electric energy cost through years. For several scenarios the benefit introduced by the FIT marks the difference between convenient, i.e. $NPV > 0$, and non-convenient, i.e. $NPV < 0$, investments. Furthermore, a positive correlation between the NPV and the plant size is registered for all no-incentive scenarios, while, if incentives are provided, such a trend is not always experienced due to the progressive reduction of the FIT with the plant size increase. Figure 2.4 clearly justifies this evidence. Finally, the comparison between the two graphs points out the higher support introduced by national incentive schemes to residential plants toward industrial applications. As example, for Germany, Italy and Spain the NPVs for the first plant group are higher than 50% respect to the industrial plants, even if the PV plant sizes are lower and scale phenomena exist.

Although the annual revenues depend on the electricity prices, E_{mp} and E_c , and the self-consumption ratio, $(1 - \%_{sold})$, the negative cash flows are function of several cost drivers. Consequently, a sensitivity analysis is of interest. Average results, among all scenarios, are summarized in Figure 2.5.

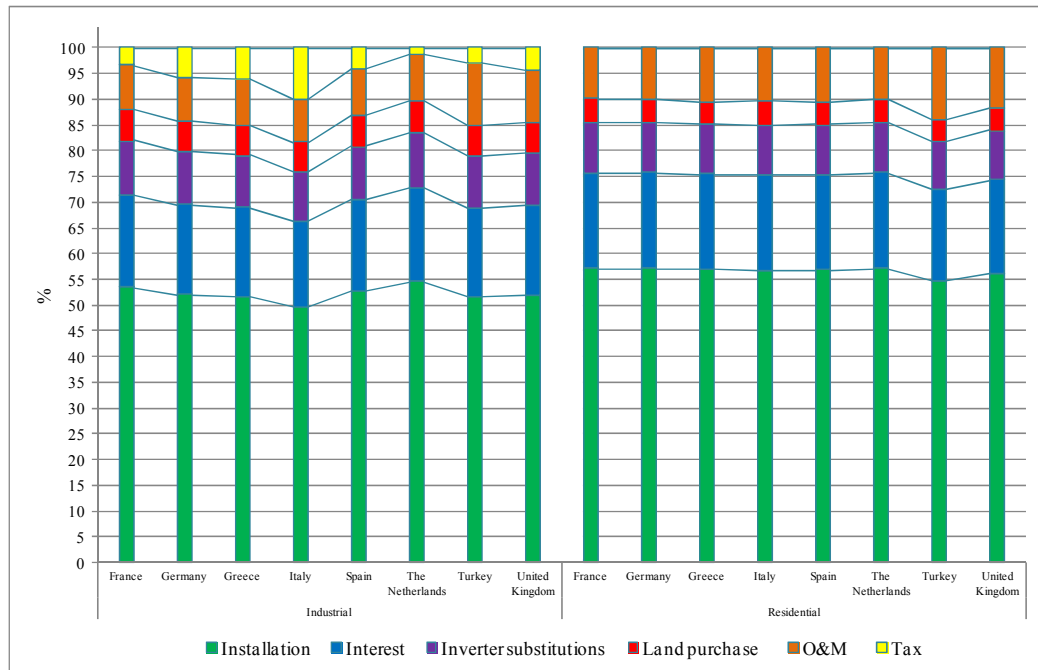
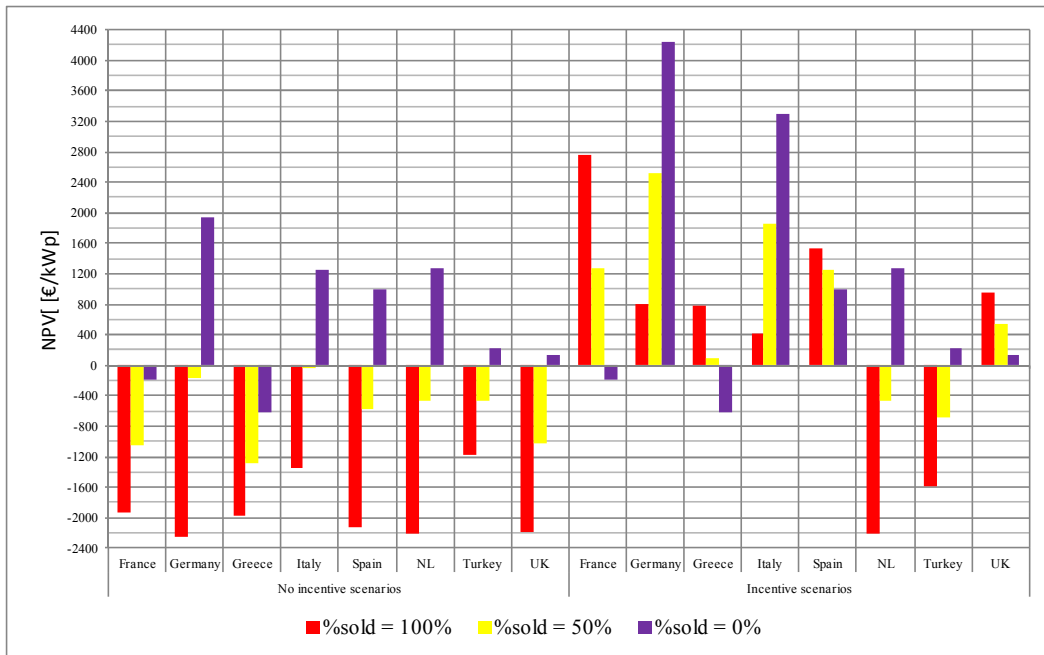


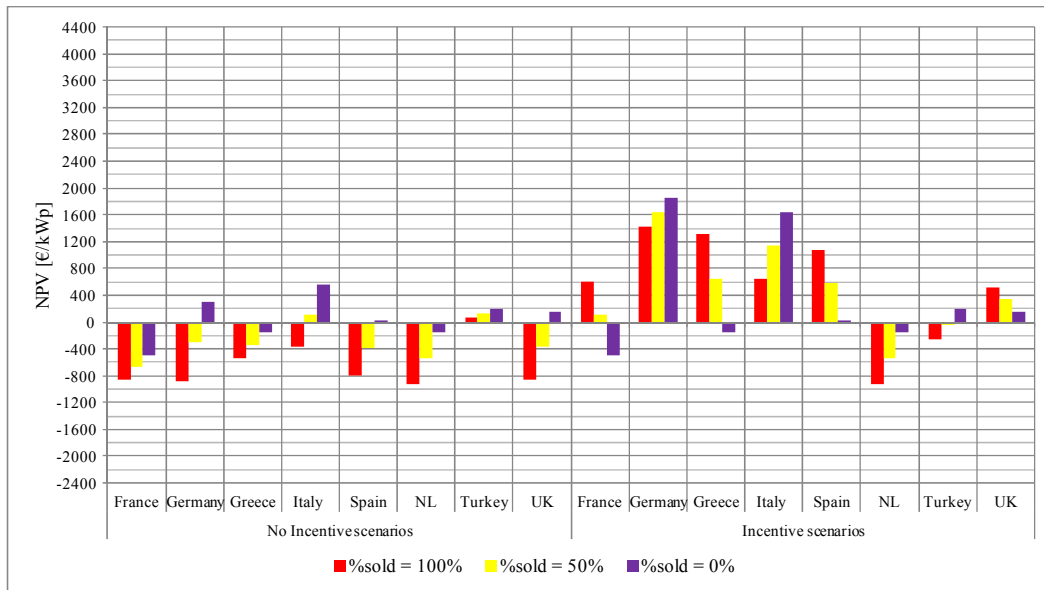
Figure 2.5. Sensitivity analysis of cash outflows.

The installation, interest on debt and land purchase drivers are all related to outcomes directly connected to the initial investment, necessary to install and start up the plant, even if the cash flows occur during the whole system lifetime. The percentage impact of such drivers on the total outcomes is between 75% and 80% and few differences exist among the eight countries. Consequently, the major of the outflows required to install and manage a PV system are during the first time-periods of the investment. Furthermore, for industrial plants, four out of six drivers present the same values because of the hypothesis, behind the proposed analysis, of adopting the same PV technologies for all countries. Differences, in the residential scenario outflows, are due to the VAT levels, specific to each country.

A third relevant outcome of the analysis is the impact of the ratio between the self-consumed and market sold electricity, i.e. the previously introduced $\%_{sold}$ parameter. A comparison among the eight countries is in Figure 2.6 and Figure 2.7 for residential and industrial installations, respectively.

Figure 2.6. Impact of $\%_{sold}$ on NPV, residential rooftop plants

(c_{module} according to Eq.7, $kWp = 3kWp$, $I_r = 1400kWh/kWp\text{-year}$, $OCC = 3\%$, $\varphi = 0\%$).

Figure 2.7. Impact of $\%_{sold}$ on NPV, industrial rooftop plants

(c_{module} according to Eq.7, $kWp = 100kWp$, $I_r = 1400kWh/kWp\text{-year}$, $OCC = 3\%$, $\varphi = 0\%$).

For no incentive scenarios, $\%_{sold} = 0\%$ is a necessary condition to generate positive NPVs, i.e. convenient investments. On the other side, in presence of national supports to the PV sector, results vary among countries mainly due to peculiarities in the legislations in force. Two sets of countries, presenting opposite trends, are identified. On one side, Germany, Italy and Turkey encourage the self-consumption of the produced energy, i.e. $\%_{sold} = 0\%$ scenarios outperform $\%_{sold} = 50\%$ and $\%_{sold} = 100\%$ scenarios, while, on the other side, France, Greece, Spain and United Kingdom, spread the exchange of the PV energy

to the electricity market through favourable tariffs and/or tax breaks. Such evidences are coherent to the review proposed in previous Section 2.2.2.1. Finally, the described trends are more evident for the residential scenarios, i.e. Figure 2.6.

Considering the incidence of the environmental conditions on the NPV and PB, the irradiation level significantly impacts on the plant profitability. For each country, power size and system installation type, i.e. residential and industrial, a lower economic limit to I_r exists to mark the difference between convenient and non-convenient investments. Figure 2.8 presents such results for typical scenarios together with the range of the measured irradiance levels for the country locations in which the 90% of the built-up areas are situated. The red dashed line identifies the convenience and non-convenience regions.

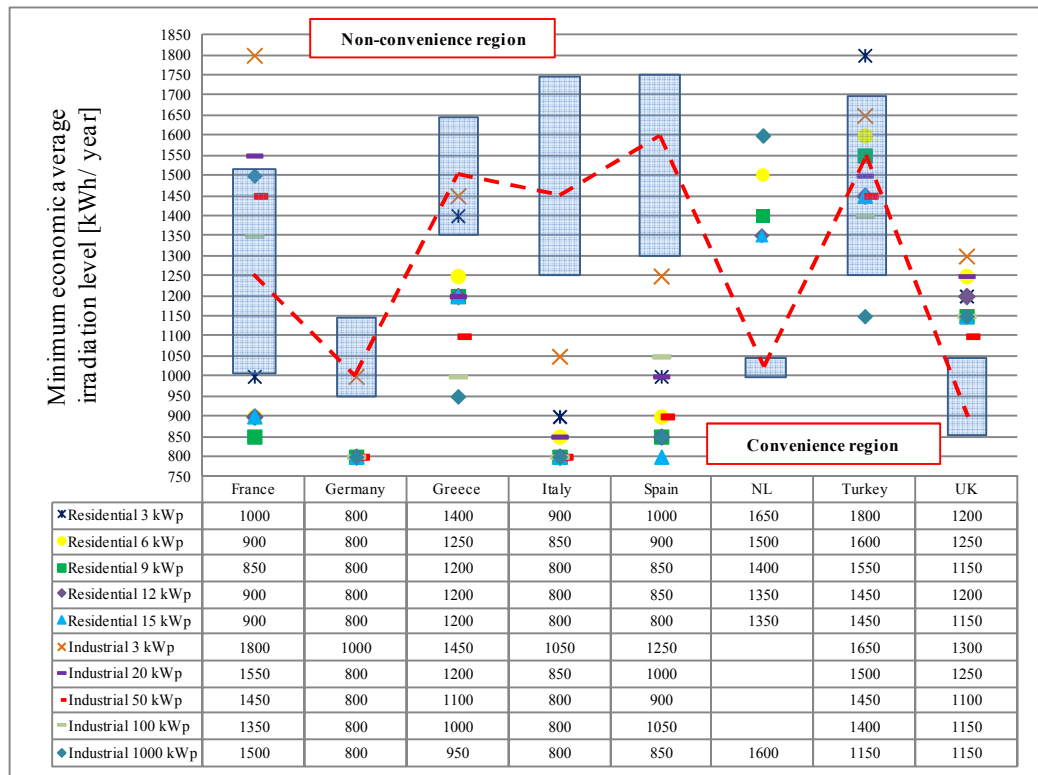


Figure 2.8. Impact of the irradiance levels, I_r , on NPV and country typical ranges

(c_{module} according to Eq.7, $OCC = 3\%$, $\varphi = 0\%$, $\%_{sold} = 50\%$).

The most of the economic lower limits for all the eight countries, except for The Netherlands and United Kingdom, fall in the convenience region, i.e. the correspondent investments present $NPV > 0$. About the two exceptions: for The Netherlands by replacing $\%_{sold} = 50\%$ to $\%_{sold} = 0\%$, i.e. totally self-consumed electric energy, the economic limits, for all scenarios, decrease and fall in the convenience region. For United Kingdom, favourable results are for $\%_{sold} = 100\%$ due to the current FIT level promoting the market exchange of energy, as shown in previous Figure 2.6 and Figure 2.7.

The last group of parameters potentially affecting the PV plant profitability are related to the financial structure of the investment to build and run the system. Particularly, two major parameters, belonging to such a group, are the loan percentage, φ , i.e. the percentage of the investment financed through debt, and the opportunity cost of capital, OCC , adopted to discount the net cash flows. A sensitivity analysis for the two aforementioned parameters belongs to the proposed analysis. The key results are in Figure 2.9.

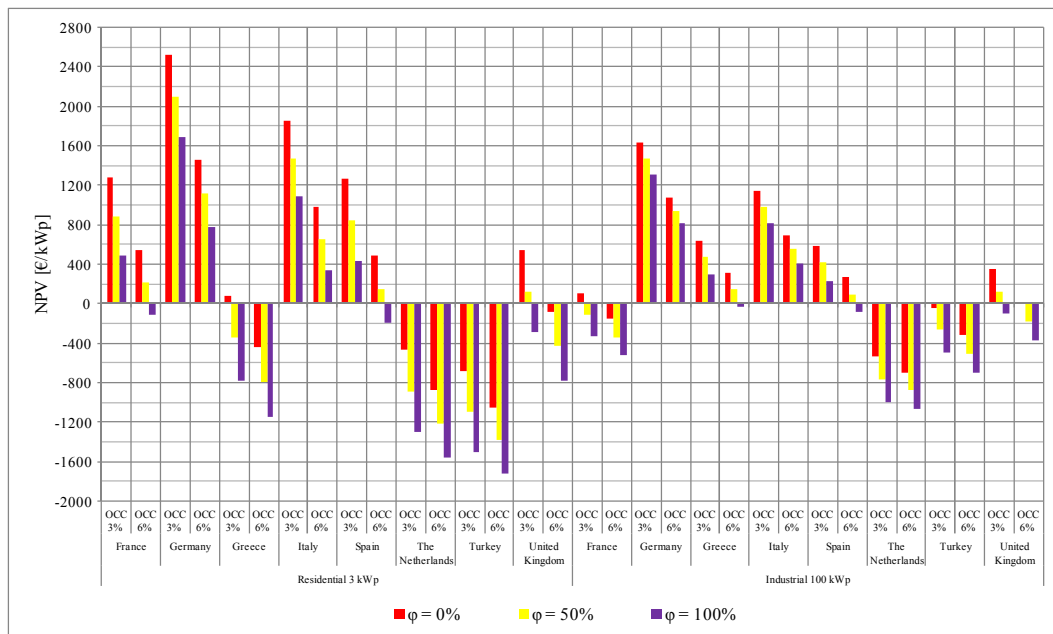


Figure 2.9. Impact of financial parameters on PV plant profitability
(c_{module} according to Eq.7, $I_r = 1400\text{kWh/kWp-year}$, $r = 4\%$, $\%_{sold} = 50\%$).

A negative correlation between φ , OCC and the NPV exist. The higher such parameters, the lower the NPV is. This trend is experienced for all countries, plant sizes and installation features so that, a relevant conclusion, is the independence of the financial structure of the investment from the country peculiarities and plant features, i.e. total equity investments and low values of the opportunity cost of capital are, always, preferable. For some scenarios, e.g. United Kingdom, the increase of the OCC from 3% to 6% generates the switch from positive to negative values of the NPV. Furthermore, the PB is, also, affected by the financial structure of the investment. Considering the sole convenient scenarios, $\varphi = 0\%$ configurations present an average PB of 9.3 years for residential plants and 7.7 years for industrial plants, while for no private equity financed investments the PB rises to 13.8 years for residential installations and 11.0 years for industrial plants. Furthermore, given the same investment financial structure, the lower PB for industrial plants toward residential installations is due to the lower initial investment (see previous Figure 2.5) and the fiscal benefit introduced by the plant amortization during the first years of the plant lifetime, i.e. C_f^T is low due to the high values of the amortization rate A .

The impact on NPV of the cell technologies, i.e. a-Si vs. c-Si, and module manufacturers, i.e. European vs. extra European, is also considered in the multi-country and multi-parameter analysis. The proposed results refer to a-Si cells produced by extra European manufacturers, i.e. Eq. 2.35. Considering the other alternatives, i.e. Eq. 2.32 to Eq. 2.34, costs generally rise of an approximately constant value generating a NPV decrease included in the range 200÷400€/kWp, while the differentials among the scenarios do not significantly change. At last, the gap between rooftop, i.e. integrated, and ground PV plants, i.e. non integrated, is positive. The land purchase costs and the lower support offered by national schemes to non integrated systems generate worse performances for the last plant group. Several non integrated scenarios are not convenient at all, while, if $NPV > 0$, the average gap between the two installation configurations is close to 25.9%.

Final remarks deal with the future perspective of the PV sector. At first, the spread of PV systems is still linked to energy policies adopted by national governments and institutions even if the increase of the electricity cost, the module efficiency and the parallel decrease of the PV system installation costs may lead PV systems to the grid parity. The decreasing trend of PV system installation costs (Figure 2.10), represents a favourable condition to ensure the future feasibility of the solar source in the European area despite some uncertainties in energy policies, e.g. Germany, Italy and Spain, still exist.

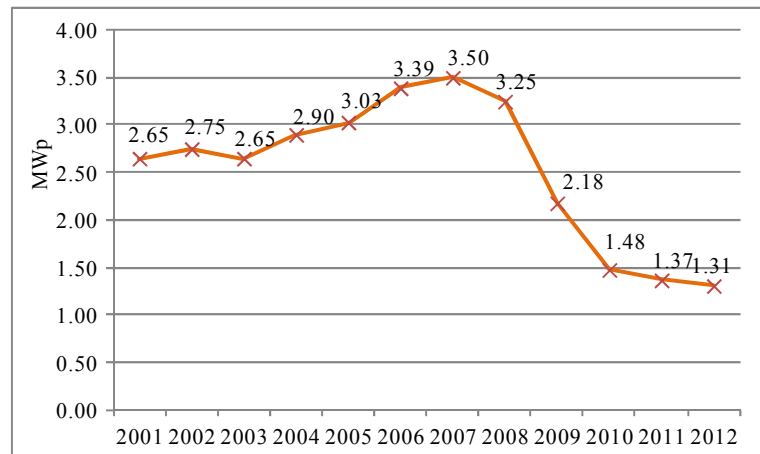


Figure 2.10. PV system cost trend from 2001 to 2012.

In conclusion, from a global point of view, the proposed models for energy network planning and PV plant economic assessment point out the relevance of the solar renewable source and encourage its inclusion in the energy mix. However, improvements are required to increase the plant technical performances and economic sustainability. Research on such a topic is encouraged. The next chapters of the present Ph.D. dissertation discuss the solar source peculiarities and propose innovative contributions to the aforementioned issues.

References

Al-Salaymeh, A., Al-Hamamre, Z., Sharaf, F., Abdelkader, M.R., (2010). Technical and economical assessment of the utilization of photovoltaic systems in residential buildings: the case of Jordan. *Energy Conversion and Management* 51:1719-1726.

Audenaert, A., Boeck, L.D., Cleyn, S.D., Lizin, S., Adam, J.F., (2010). An economic evaluation of photovoltaic grid connected systems (PVGCS) in Flanders for companies: a generic model. *Renewable Energy* 35:2674-2682.

Barbose, G., Wiser, R., Bolinger, M., (2008). Designing PV incentive programs to promote performance: a review of current practice in the US. *Renewable and Sustainable Energy Reviews* 12:960-998.

Bazmi, A.A., Zahedi, G., (2011). Sustainable energy systems: role of optimization modeling techniques in power generation and supply - a review. *Renewable and Sustainable Energy Reviews* 15:3480-3500.

Becerra-López, H.R., Golding, P., (2008). Multi-objective optimization for capacity expansion of regional power-generation systems: Case study of far west Texas. *Energy Conversion and Management* 49:1433-1445.

Bernal-Agustin, J.L., Dufo-Lopez, R., (2006). Economical and environmental analysis of grid connected photovoltaic system in Spain. *Renewable Energy* 31:1107-1128.

Bortolini, M., Gamberi, M., Graziani, A., Mora, C., (2013). Multi-country and multi-parameter analysis for the technical and economical assessment of photovoltaic systems in the European Union area. *Energy Conversion and Management* [under review].

Bounovas, V., Papadopoulos, A.I., Seferlis, P., Voutetakis, S., (2011). Energy supply chain optimization under demand variation and emission constraints. *Chemical Engineering Transactions* 25:1043-1048.

Bouzembrak, Y., Allaoui, H., Goncalves, G., Bouchriha, H., (2011). A multi-objective green supply chain network design. *Proceedings of the 4th International Conference on Logistics* 358-361.

Campoccia, A., Dusonchet, L., Telaretti, E., Zizzo, G., (2007). Feed-in tariffs for grid-connected PV systems: the situation in the European community. Proceedings of 2007 IEEE Lausanne Powertech 1981-1986.

Campoccia, A., Dusonchet, L., Telaretti, E., Zizzo, G., (2009). Comparative analysis of different supporting measures for the production of electrical energy by solar PV and wind systems: four representative European cases. *Solar Energy* 83:287-297.

Diarra, D.C., Akuffo, F.O., (2002) Solar photovoltaic in Mali: potential and constraints. *Energy Conversion and Management* 43:151-163.

Di Dio, V., Favuzza, S., La Caseia, D., Miceli, R., (2007). Economical incentives and systems of certification for the production of electrical energy from renewable energy resources. Proceeding of 2007 International Conference on Clean Electrical Power 277-282.

Dong, M., He, F., Wei, H., (2012). Energy supply chain design optimization for distributed energy systems. *Computer and Industrial Engineering* 63:546-552.

EurObserv'ER (2007). Photovoltaic energy barometer 2007 - EurObserv'ER Systèmes solaires, *Le journal des énergies renouvelables* 178:49-70.

EurObserv'ER (2009). Photovoltaic energy barometer 2009 - EurObserv'ER Systèmes solaires, *Le journal des énergies renouvelables* 190:72-102.

EurObserv'ER (2010). Photovoltaic energy barometer 2010 - EurObserv'ER Systèmes solaires, *Le journal des énergies renouvelables* 196:128-160.

EurObserv'ER (2011). Photovoltaic energy barometer 2011 - EurObserv'ER Systèmes solaires, *Le journal des énergies renouvelables* 202:144-171.

EurObserv'ER (2012). Photovoltaic energy barometer 2012 - EurObserv'ER Systèmes solaires, *Le journal des énergies renouvelables* 7:108-131.

Fernandez-Infantes, A., Contreras, J., Bernal-Agustín, J.L., (2006). Design of grid connected PV system considering electrical, economical and environmental aspect: a practical case. *Renewable Energy* 31:2042-2062.

Focacci, A., (2009). Residential plants investment appraisal subsequent to the new supporting photovoltaic economic mechanism in Italy. *Renewable and Sustainable Energy Reviews* 13:2710-2715.

Fthenakis, V., Mason, J.E., Zweibel, K., (2009). The technical, geographical, and economic feasibility for solar energy to supply the energy needs of the US. *Energy Policy* 37:387-399.

Ghoneim, A.A., Al-Sahan, A.Y., Abdullah, A.H., Economic analysis of photovoltaic-powered solar domestic hot water systems in Kuwait. *Renewable Energy* 25:81-100.

Hernández, J.C., Medina, A., Jurado, F., (2008). Impact comparison of PV system integration into rural and urban feeders. *Energy Conversion and Management* 49:1747-1765.

Hammond, G.P., Harajli, H.A., Jones, C.I., Winnett, A.B., (2012). Whole systems appraisal of a UK Building Integrated Photovoltaic (BIPV) system: energy, environmental, and economic evaluations. *Energy policy* 40:219-230.

Lam, H.L., Verbanov, P.S., Klemeš, J.J., (2010). Optimisation of regional energy supply chains utilising renewables: P-graph approach. *Computer and Chemical Engineering* 34:782-792.

Mitscher, M., Rüther, R., (2012). Economic performance and policies for grid-connected residential solar photovoltaic systems in Brazil. *Energy Policy* 49:688-694.

Nässén, J., Evertsson, J., Andersson, B.A., (2002). Distributed power generation versus grid extension: an assessment of solar photovoltaics for rural electrification in Northern Ghana. *Progress in Photovoltaics: Research and Applications* 10:495-510.

Nelson, J., Johnston, J., Mileva, A., Fripp, M., Hoffman, I., Petros-Good, A., Blanco, C., Kammen, D.M., (2012). High-resolution modeling of the western North American power system demonstrates low-cost and low-carbon futures. *Energy Policy* 43:436-447.

Papapostolou, C., Kondili, E., Kaldellis, J.K., (2011). Development and implementation of an optimisation model for biofuels supply chain. *Energy* 36:6019-6026.

Reiche, D., Bechberger, M., (2004). Policy differences in the promotion of renewable energies in the EU member states. *Energy Policy* 32:843-849.

Rowlands, I.H., (2005). Envisaging feed-in tariffs for solar photovoltaic electricity: European lessons for Canada. *Renewable and Sustainable Energy Reviews* 9:51-68.

Šály, V., Ružinský, M., Baratka, S., (2006). Photovoltaics in Slovakia - status and conditions for development within integrating Europe. *Renewable Energy* 31:865-875.

Zhang, D., Chai, Q., Zhang, X., He, J., Yue, L., Dong, X., Wu, S., (2012). Economical assessment of large-scale photovoltaic power development in China. *Energy* 40:370-375.

Legislation references

French legislation, Arrêté du 4 mars 2011 fixant les conditions d'achat de l'électricité produite par les installations utilisant l'énergie radiative du soleil telles que visées au 3° de l'article 2 du décret 2000-1196 du 6 décembre 2000.

German legislation, EEG Gesetz für den Vorrang Erneuerbarer Energien (Erneuerbare-Energien-Gesetz), 2009 (last amended on 01/01/2012).

Greece Legislation, Renewable Energy Legislation, Law 3581/2010 amending the law 3468/2006, Generation of Electricity using Renewable Energy Sources and High-Efficiency Cogeneration of Electricity and Heat and Miscellaneous Provisions.

Italian Legislation, Incentivation of electricity production from solar photovoltaic plants, Decreto Ministeriale 05/05/2011.

Italian Legislation, Incentivation of electricity production from solar photovoltaic plants, Decreto Ministeriale 05/07/2012.

Legal sources on renewable energy (Res-Legal). Available on line:

<http://www.res-legal.de/>

Spanish legislation, Real Decreto 1565/2010, de 19 de noviembre, por el que se regulan y modifican determinados aspectos relativos a la actividad de producción de energía eléctrica en régimen especial, R.D. 1565 19/11/2010.

Spanish legislation, C 14/2010, de 23 de diciembre, por el que se establecen medidas urgentes para la corrección del déficit tarifario del sector eléctrico, R.D. 14 23/12/2010.

Turkish legislation, Law on utilization of renewable energy sources for the purpose of generating electrical energy, Law n. 5436, 10/05/2005, Amended by Law 6094, 29/12/2010.

Turkish legislation, Law 6094/2010 amending the Law 5436/2005, Law on utilization of renewable energy sources for the purpose of generating electrical energy.

3. *Solar renewable source*

Fundamentals and models for solar radiation prediction

In this chapter the solar renewable source is focused. Starting from a background of the fundamentals about solar energy, radiation components and the horizontal celestial coordinate system, the strategies to measure or predict the available solar radiation on an horizontal and tilted plane are considered. Analytical models to calculate both the extraterrestrial radiation, i.e. top of atmosphere (TOA), and the available radiation on the Earth surface, together with its fractions, i.e. direct, diffuse and reflected components, are discussed, highlighting the parameters most affecting the levels of the available radiation.

Among them, the geographical coordinates, i.e. latitude, longitude and altitude, of the collection location affect the amount of the available solar energy. Consequently, a wide set of the models proposed by past and recent literature are *location-dependent* with an evident lack of applicability to locations different from the considered sites. To overcome such a weakness an innovative multi-location approach to estimate the solar radiation components in the EU area is proposed and, then, validated through a consistent dataset from the World Radiation Data Center (WRDC).

3.1 Solar energy radiation

Solar radiation is the energy irradiated by the Sun in all directions. Basically, the Sun is a hot sphere of gasses heated by nuclear fusion reactions at its center (Quaschnig, 2003). Its diameter is of about $1.39 \cdot 10^9 \text{m}$ and the average distance toward the Earth is of $1.495 \cdot 10^{11} \text{m}$. Finally, its effective blackbody temperature is of 5777K, while internal temperatures, i.e. the temperatures of the region where fusion reactions occur, are estimated in the range 8 to 40 million Kelvin degrees with a matter density 100 times higher than water (Duffie & Beckman, 2006).

3.1.1 Extraterrestrial radiation

Solar radiation consists of electromagnetic waves emitted in all directions from the Sun surface. Several studies in physics and astronomy investigate both the intensity and the spectral distribution of the solar radiation (Ball, 2005, Seghouani 2006, Kiselman et al., 2011). Considering extraterrestrial radiation, i.e. neglecting the attenuation effects caused by Earth atmosphere, the average energy per unit of time reaching a 1m^2 surface located at mean Earth-Sun distance is, approximately, constant and corresponds to the so-called solar constant, I_{sc} , equal to 1366.1W/m^2 (Gueymard, 2004, Jiang, 2009, Li et al., 2011). The solar constant represents the mean value of the irradiation spectral distribution, function of the wavelength. Figure 3.1 presents the standard spectral irradiance curve at mean Earth-Sun distance proposed by the World Radiation Center (WRC).

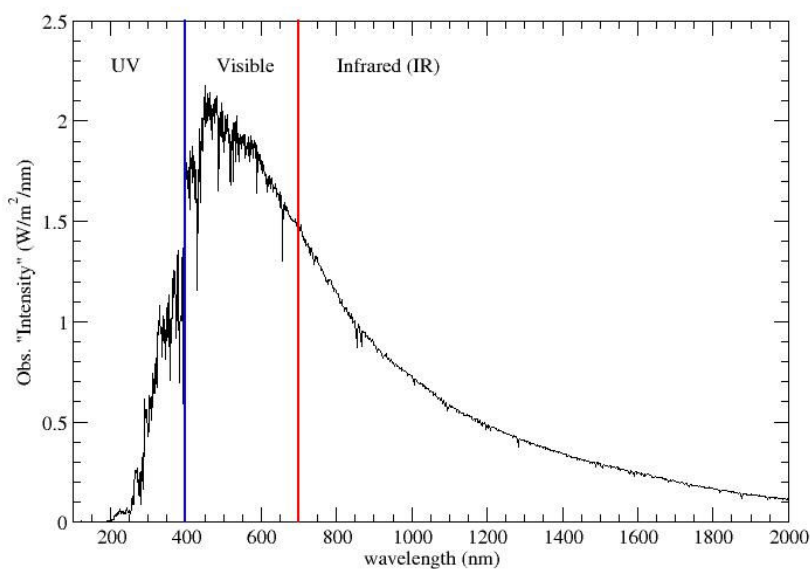


Figure 3.1. Standard spectral irradiance curve of the Sun.

Furthermore, the radiation reaching the Earth TOA, I_n , depends, quadratically, on the distance between the Sun and the Earth, d_n , and it is estimated for each day of the year, $n = 1, \dots, 365$, as in Eq. 3.1 (Spencer, 1971).

$$r = \frac{I_n}{I_{sc}} = \frac{d_{sc}^2}{d_n^2} = 1 + 0.033 \cos \left(2\pi \cdot \frac{n}{365} \right) \quad (3.1)$$

where $d_{sc} = 1.495 \cdot 10^{11} \text{m}$ is the mean distance Sun-Earth. Eq. 3.2 provides a more accurate expression for r (Duffie & Beckman, 2006).

$$r = 1.00011 + 0.034221 \cos B + 0.00128 \sin B + 0.000719 \cos 2B + 0.000077 \sin 2B \quad (3.2)$$

where $B = (n - 1) \cdot 2\pi/365$.

The dependence of r on the day of the year is due to the eccentricity of the Earth orbit, causing a cyclical variation of d_n . The graph of Figure 3.2 depicts the waveforms of the previous Eq. 3.1 and Eq. 3.2.

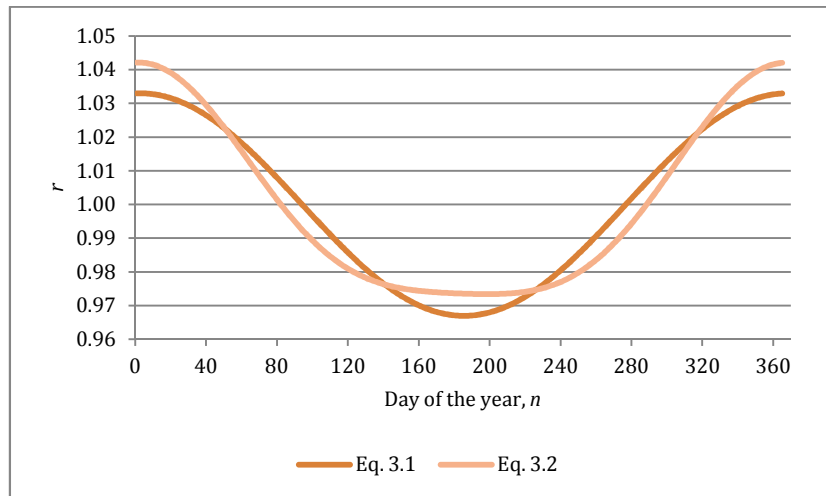


Figure 3.2. Dependence of TOA solar radiation on time of year.

According to Eq. 3.2 the minimum TOA irradiation level, I_n , is of 1328.76W/m^2 , while the maximum level is of 1422.40W/m^2 . The range of variation is equal to $\pm 3\%$ around the mean value, I_{sc} .

To calculate the available solar radiation inside the Earth atmosphere on ground, i.e. on a horizontal plane, or on a tilted surface both the direction of the Sun rays and the effects of the atmosphere need to be considered. The next paragraph introduces the horizontal celestial coordinate system (HCCS), a frequently adopted coordinate system to identify the celestial body positions and trajectories.

3.1.2 Horizontal celestial coordinate system

Basically, the level of solar radiation on a surface inside the Earth atmosphere is affected by the geographical position of the surface and the time of the day (Benford & Bock, 1939). The HCCS introduces a consistent set of angles and sign conventions to univocally describe the relative position and trajectories of celestial bodies.

In HCCS, the observer local horizon is the fundamental plane to compute angles. The coordinate system is fixed to the Earth, not to stars, so that celestial position depends both on the observer location on Earth and the time of the day. The local horizon divides the sky into the upper hemisphere, where objects are visible, and the lower hemisphere, where objects cannot be seen since the Earth is in the way. The pole of the upper hemisphere is the so-called Zenith, while the pole of the lower hemisphere is the Nadir. Two angular coordinates univocally identify the position of a generic celestial body.

- ✓ **Solar altitude**, *Alt*, representing the angle between the object and the local horizon. It is also called, elevation, because it identifies the elevation of the celestial body above the observer horizon. Solar altitude varies between 0° , i.e. celestial body lies on the horizon plane, and 90° , i.e. celestial body is at Zenith. The solar altitude complementary angle is the Zenithal angle, $\theta = 90^\circ - Alt$;
- ✓ **Azimuthal angle**, *Az*, representing the displacement from South of the projection of the celestial body position on the observer horizon plane. *Az* range is $[-180^\circ, 180^\circ]$ with 0° due South, displacements east of South are, conventionally, negative, while displacements west of South are positive.

HCCS is also called Altitude/Azimuthal (*Alt/Az*) system because of the two angles adopted to identify all the celestial bodies. Solar radiation level depends on the Sun position. In the following, the Sun will be the only considered celestial body. According to HCCS, apparent Sun motion toward Earth is described through the solar altitude and azimuthal angle values during the whole day and, particularly, from sunrise to sunset (Figure 3.3).

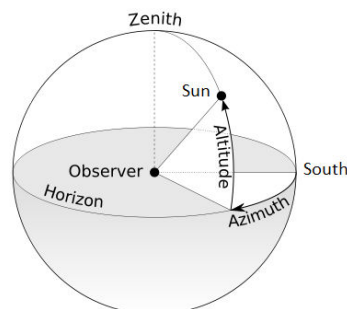


Figure 3.3. Solar altitude and Azimuthal angle in HCCS.

Several useful equations are introduced to analytically correlate such angles to the local observer coordinates and the time of the day. Before reviewing them, the following other angles and temporal parameters need to be introduced.

- ✓ **Latitude**, ϕ , representing the angular location of a generic point on Earth, north or south of the Equator, with $-90^\circ \leq \phi \leq 90^\circ$, $\phi = 0^\circ$ in correspondence of the Equator, positive values for north-located points and negative values for south-located points;
- ✓ **Longitude**, L , representing the East-West position of a generic point on Earth, with $-180^\circ \leq L \leq 180^\circ$, $L = 0^\circ$ in correspondence of the Prime Meridian which passes through the Royal Observatory in Greenwich, United Kingdom, positive values eastward and negative values westward;
- ✓ **Solar declination**, δ , representing the angular position of the Sun at solar noon with respect to the plane of the Equator, with $-23.45^\circ \leq \delta \leq 23.45^\circ$ and positive values for north-oriented angles;
- ✓ **Hour angle**, ω , representing the angular displacement of the Sun from the local meridian due to rotation of the Earth on its axis, with 15° rotation per hour (or, equivalently, $\frac{\pi}{12}$ radians) negative values before noon, positive values after noon;
- ✓ **Solar time**, t , in hours, representing the temporal parameter based on the apparent angular motion of the Sun across the sky, so that, at solar noon the Sun crosses the observer local meridian.

Cooper (1969), firstly proposes an useful expression for the solar declination approximation.

$$\delta = 23.45 \sin \left(2\pi \cdot \frac{284+n}{365} \right) \quad (3.3)$$

while, in the next years, several other and more accurate equations are obtained (Spencer, 1971, Angus & Muneer, 1993, Mihelić-Bogdanić et al., 1996, Ryuji et al., 1997).

According to the introduced definition, the expression for the hour angle, ω , in radians, is as follows.

$$\omega = (12 - t) \cdot \frac{\pi}{12} \quad (3.4)$$

Finally, the solar time, t , differs from the standard time, t_{std} , adopted in all the current civil contexts, due to the last two addends of Eq. 3.5.

$$t = t_{std} + \frac{4 \cdot (L - L_{std})}{60} + \frac{E}{60} \quad (3.5)$$

where the first addend is the standard, i.e. civil, time, the second addend computes the effect of the different longitude between the considered location and the standard meridian for the

local time zone. Four minutes are added or subtracted per each degree. Finally, the third addend is the so-called equation of time and introduces a further corrective factor because of the difference between the apparent solar time and the mean, i.e. regular, solar time (Müller, 1995). In such a context, the following expression for the equation of time (the result is in minutes) is considered:

$$E = 9.87 \sin \left(4\pi \cdot \frac{n-81}{365} \right) - 7.67 \sin \left(2\pi \cdot \frac{n-1}{365} \right) \quad (3.6)$$

The equation of time waveform is represented in the next Figure 3.4.

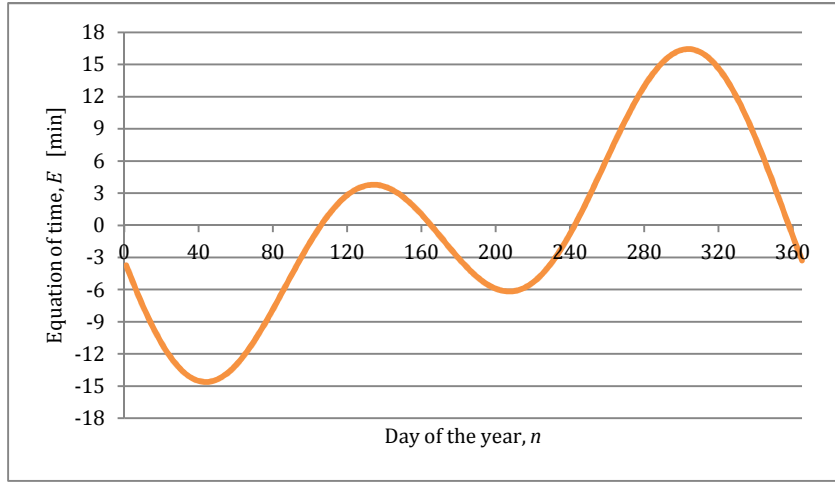


Figure 3.4. Equation of time, waveform.

The previous parameters allow to calculate the values of the two basic angles of the HCCS. Both of them are time dependent, i.e. they are a function of the declination and hour angle, and location dependent, i.e. they are a function of the latitude and longitude. Considering a horizontal surface, Eq. 3.7 is a wide adopted equation for the solar altitude computation (Duffie & Beckman, 2006, Wenham et al., 2007).

$$\sin Alt = \cos \phi \cdot \cos \omega \cdot \cos \delta + \sin \phi \cdot \sin \delta \quad (3.7)$$

Different equations are proposed by the literature correlating the azimuthal angle to geographical and temporal parameters. Duffie & Beckman (2006) calculate the cosine of the azimuthal angle through Eq. 3.8.

$$\cos Az = \frac{\sin Alt \cdot \sin \phi - \sin \delta}{\cos Alt \cdot \cos \phi} \quad (3.8)$$

while Wenham et al. (2007) propose the following expression

$$\cos Az = \frac{\cos \phi \cdot \sin \delta - \sin \phi \cdot \cos \delta \cdot \cos \omega}{\cos Alt} \quad (3.9)$$

A further expression for Az is from the Photovoltaic Geographical Information System (PVGIS).

$$\cos Az = \frac{\sin\phi \cdot \cos\delta \cdot \cos\omega - \cos\phi \cdot \sin\delta}{\sqrt{(\cos\delta \cdot \sin\omega)^2 + (\sin\phi \cdot \cos\delta \cdot \cos\omega - \cos\phi \cdot \sin\delta)^2}} \quad (3.10)$$

A long sequence of trigonometric equivalences allows to obtain each of the three expressions from any of the other two so that their equivalence is demonstrated.

Finally, the previous equations allow to calculate the analytic expressions for the sunrise and the sunset hour angle, i.e. ω_{sr} and ω_{ss} , solar time, i.e. t_{sr} and t_{ss} , and solar azimuth, i.e. Az_{sr} and Az_{ss} . Basically, when the Sun rises and sets it lies on the observer horizon plane and, consequently, the solar altitude angle is null. Previous Eq. 3.7, when $\sin Alt = 0$, becomes

$$\cos\omega_{sr/ss} = -\tan\phi \cdot \tan\delta \quad (3.11)$$

while, from Eq. 3.4,

$$t_{sr/ss} = 12 - \frac{\omega_{sr/ss}}{15} \quad (3.12)$$

Finally, from Eq. 3.8,

$$\cos Az_{sr/ss} = -\frac{\sin\delta}{\cos\phi} \quad (3.13)$$

The HCCS, together with the introduced equations, are crucial to identify the position of the Sun during day-time and they are frequently adopted to develop the Sun tracking strategies for bi-axial motion control. Details and an extensive description of them is provided in Chapter 6.

A numerical example, applying the HCCS equations, is in the next subsection. Some of the adopted assumptions, e.g. the considered location, are representative of the developed solar PV/T prototype operative conditions (see Chapter 5).

3.1.2.1 Numerical example (part I)

The present example focuses on the city of Bologna, northern Italy, and studies the values and trends of the parameters defined before. The location latitude is $\phi = 44.5136^\circ$ north and the longitude is $L = 11.3184^\circ$ east. Two days of the year are considered: the summer and winter solstices, i.e. June 21st, $n = 172$, and December the 21st, $n = 355$, representing the longest and shortest daylight days.

Applying Eq. 3.3, the solar declination is

$$\delta_{\text{June 21}} = 23.45 \sin\left(2\pi \cdot \frac{284+172}{365}\right) = 23.45^\circ \quad (3.14)$$

and

$$\delta_{\text{December 21}} = 23.45 \sin\left(2\pi \cdot \frac{284+355}{365}\right) = -23.45^\circ \quad (3.15)$$

At the solstices the solar declination assumes the maximum and minimum values.

Eq. 3.11 to 3.13 allow to study the solar coordinates of sunrise and sunset. The results for the two considered days and Bologna location are in Table 3.1.

Table 3.1. Numerical example, sunrise and sunset parameters for summer and winter solstices.

	June 21 st	December 21 st
$\omega_{sr/ss}$	$\mp 115.24^\circ$	$\mp 64.76^\circ$
t_{sr}	4.32h	7.68h
t_{ss}	19.68h	16.32h
$Az_{sr/ss}$	$\pm 123.92^\circ$	$\pm 56.08^\circ$

Considering daylight hours, Figure 3.5 and Figure 3.6 present the waveforms of the solar altitude and the azimuthal angle coordinates.

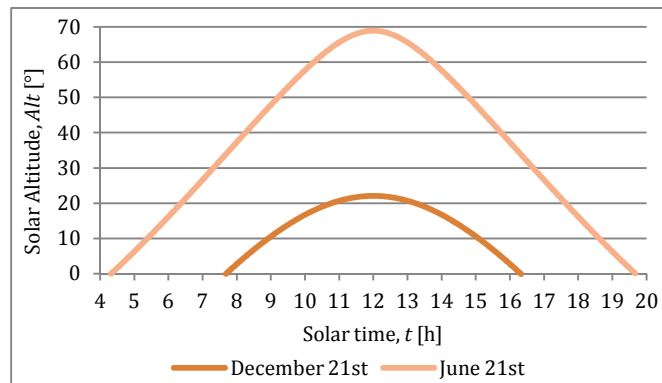


Figure 3.5. Numerical example, solar altitude waveforms for summer and winter solstices.

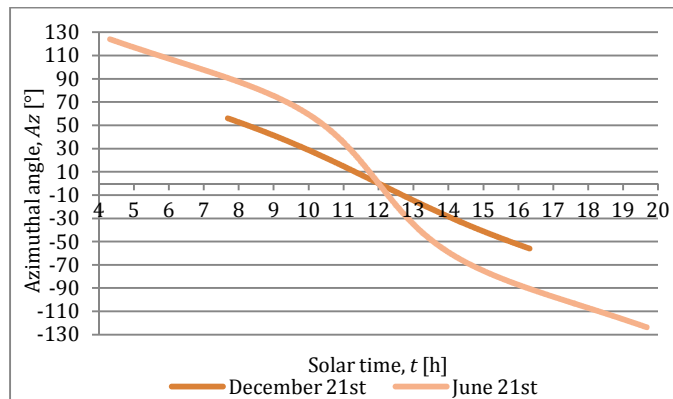


Figure 3.6. Numerical example, azimuthal angle waveforms for summer and winter solstices.

During winter days, the Sun is low in the sky, i.e. at winter solstice noon $Alt = 22.03^\circ$, while the maximum solar altitude values is of 68.94° at summer solstice noon. Such values are location dependent and decrease with the latitude, moving from Equator to Poles. Azimuthal angle presents a comparable behavior with a higher range of variation during summer daytime, i.e. 247.84° at the summer solstice, and a lower range of variation during winter daytime, i.e. 112.16° at the winter solstice. This is mainly due to the different length of the day and the different distance between the Sun and the Earth in the two seasons. Specific daytime angular displacements are equal to $16.13^\circ/h$ at the summer solstice and $12.99^\circ/h$ at the winter solstice for the azimuthal angle and $4.49^\circ/h$ at summer solstice and $2.55^\circ/h$ at winter solstice for the solar altitude.

3.1.3 Effect of Earth atmosphere on the incident radiation

Although radiation from the Sun surface is reasonably constant and no significant distortions occur until TOA, by the time it reaches the Earth surface solar radiation is highly variable owing to absorption and scattering phenomena caused by the presence of the terrestrial atmosphere. Several studies investigate such an issue, focusing on the causes and correlated effects (Lu & Khalil, 1996, Goody, 2002). Iqbal (1983) reviews atmospheric attenuation of solar radiation proposing two groups of major phenomena.

- ✓ Scattering of radiation caused by the interaction with air molecules, water and dust present in the atmosphere. Various efforts analytically study such interaction including the temporary meteorological conditions, e.g. the presence of clouds (Moon, 1940, Fritz, 1958, Thekaekara, 1974);
- ✓ Absorption of radiation in the atmosphere by ozone, vapor and carbon dioxide. Particularly, the first molecule significantly captures ultraviolet rays, i.e. $\lambda < 0.29\mu m$, while vapor and CO_2 affect the bands of the infrared, i.e. $\lambda > 2.5\mu m$. Reasonably, from the viewpoint of terrestrial applications of solar energy, only the radiation of wavelengths between $0.29\mu m$ and $2.5\mu m$ needs to be considered (Duffie & Beckman, 2006).

Furthermore, the global solar radiation incident on the Earth surface does not follow an univocal trajectory from TOA to the ground. Considering a generic target surface, three components are distinguished.

- ✓ **Direct component**, also called beam component, represents the fraction of solar radiation coming straight from the Sun and not subjected to any deviation or distortion phenomena;

- ✓ **Diffuse component** includes the fraction of solar radiation scattered from the sky and from the surroundings and not directly incident on the target surface;
- ✓ **Reflected component** is the solar radiation fraction incident on the target surface after the reflection from Earth ground, sea and/or other artificial surfaces. It depends on the so-called local Albedo and needs to be considered in presence of tilted target surfaces.

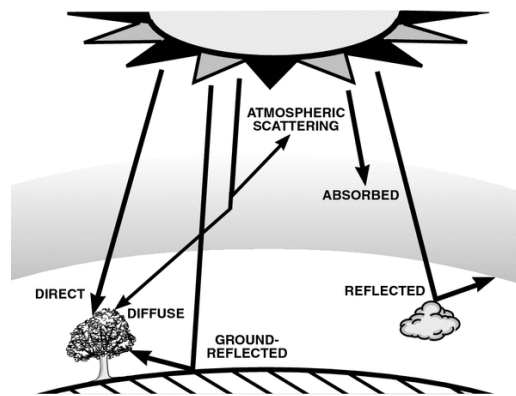


Figure 3.7. Atmosphere attenuation phenomena and components of solar radiation.

3.2 Solar radiation models

Solar radiation model purpose is to provide useful equations to predict solar radiation levels if no experimental data are available (Jamil Ahmad & Tiwari, 2010). Such models allow to calculate or estimate the solar radiation levels both on TOA and surfaces of any orientation located inside the atmosphere. For the latter case, models to estimate the direct, diffuse and reflected components are, further, necessary for a wide set of applications. Such models are, generally, expressed as analytic equations correlating the solar radiation, or its components, to one or several parameters dependent on the location and/or the climatologic conditions, e.g. hours of Sun, cloudiness, air temperature, humidity level, etc. Despite an analytic close form model is obtainable to compute TOA radiation, probabilistic approaches need to be used to estimate solar radiation inside Earth atmosphere. This is due to the uncertainty introduced by the atmosphere attenuation phenomena described in previous Section 3.1.3.

Starting from the TOA radiation, the following paragraphs focus such models, describing the related equations and providing the conditions whereas their application is feasible and results reliable.

3.2.1 TOA radiation model

TOA radiation model estimates the available solar radiation on a generic surface neglecting the attenuation effects caused by the Earth atmosphere. Useful parameters are the average irradiance level, in W/m^2 , the daily and monthly mean daily energy radiation, both in Wh/m^2 .

Basically, the parameter I_n , introduced in Section 3.1.1, expresses the incident radiation on a surface orthogonal to ray direction. Such a surface is called A_1 in the next Figure 3.8.

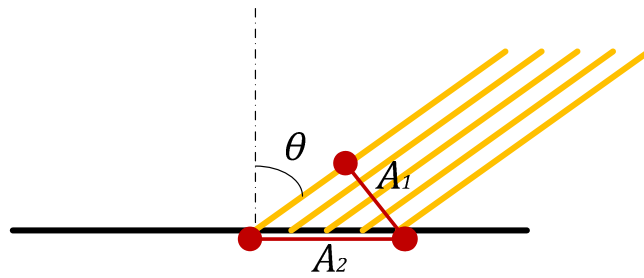


Figure 3.8. TOA radiation model – horizontal surface.

Considering the horizontal surface A_2 , irradiated as A_1 , the next identity follows.

$$I_0 \cdot A_2 = I_n \cdot A_1 \quad (3.16)$$

where I_0 is the average specific irradiation on the horizontal surface, in W/m^2 . Furthermore,

$$I_0 = I_n \cdot \frac{A_1}{A_2} = I_n \cdot \cos\theta \quad (3.17)$$

where θ is the zenithal angle. Consequently, the higher θ , the lower the irradiation level is. For $\theta = 90^\circ$, i.e. the Sun lies on the horizon, the TOA irradiation is null, while when the Sun is exactly at Zenith, i.e. it is orthogonal to the observer plane, the irradiation is maximized.

Combing Eq. 3.17 to previous Eq. 3.7,

$$I_0 = I_n (\cos\phi \cdot \cos\omega \cdot \cos\delta + \sin\phi \cdot \sin\delta) \quad (3.18)$$

representing the final expression for the specific incident radiation on the horizontal plane.

Furthermore, to calculate the daily TOA incident solar energy radiation, H_0 , the incident irradiation needs to be integrated between sunrise and sunset.

$$H_0 = \int_{t_{sr}}^{t_{ss}} I_0 dt \quad (3.19)$$

To find the integral, u-substitution method is applied, making the substitution

$$\omega = (12 - t) \cdot \frac{\pi}{12} \quad \Rightarrow \quad dt = -\frac{12}{\pi} d\omega \quad (3.20)$$

so that Eq. 3.19 becomes

$$H_0 = \int_{\omega_{sr}}^{\omega_{ss}} -\frac{12}{\pi} I_0 d\omega = \frac{12}{\pi} \int_{\omega_{ss}}^{\omega_{sr}} I_0 d\omega \quad (3.21)$$

Considering the expression of I_0 provided in Eq. 3.18 and solving the integral, the final expression is

$$H_0 = \frac{24}{\pi} I_n (\cos\phi \cdot \sin\omega_{sr} \cdot \cos\delta + \omega_{sr} \cdot \sin\phi \cdot \sin\delta) \quad (3.22)$$

if ω_{sr} is in radians or, equivalently,

$$H_0 = \frac{24}{\pi} I_n \left(\cos\phi \cdot \sin\omega_{sr} \cdot \cos\delta + \frac{\pi}{180} \omega_{sr} \cdot \sin\phi \cdot \sin\delta \right) \quad (3.23)$$

if ω_{sr} is in degrees.

Finally, an accepted and easy-use approach to compute the monthly mean daily solar energy radiation, i.e. a representative monthly value for the average daily solar radiation, is to adopt the previous Eq. 3.22 or Eq. 3.23 and to consider the so-called average day of the month to compute the required parameters. Such standard day is the day of each month with the value of the solar declination closest to the average monthly value of the solar declination. The following Table 3.2 provides the recommended average days for each month of the year and the correspondent values of the solar declination.

Table 3.2. Recommended average days for each month.

	<i>Avg day</i>	<i>n</i>	δ
January	17	17	-20.9°
February	16	47	-13.0°
March	16	75	-2.4°
April	15	105	9.4°
May	15	135	18.8°
June	11	162	23.1°
July	17	198	21.2°
August	16	228	13.5°
September	15	258	2.2°
October	15	288	-9.6°
November	14	318	-18.9°
December	10	344	-23.0°

The previously introduced TOA radiation model focuses on a horizontal target surfaces. Considering a tilted surfaces, the model needs to be modified considering the slope of the incident target area (Nijmeh & Mamlook, 2000). Figure 3.9 shows a tilted surface, south/north oriented. β is the tilt angle.

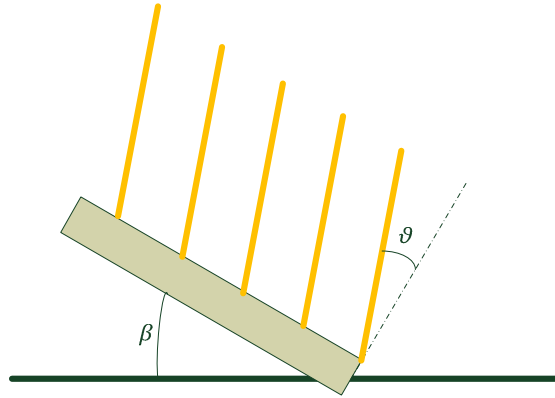


Figure 3.9. TOA radiation model – tilted surface.

In such a context, the angle the rays create with the normal direction to the surface, ϑ , is not equal to the zenithal angle of the location, as for horizontal targets. In the northern hemisphere, it is the zenithal angle of a virtual location with an artificial latitude β degrees lower than ϕ , according to Eq. 3.24, obtained from Eq. 3.7.

$$\cos\vartheta = \cos(\phi - \beta) \cdot \cos\omega \cdot \cos\delta + \sin(\phi - \beta) \cdot \sin\delta \quad (3.24)$$

For the southern hemisphere, Eq. 3.24 is modified replacing $\phi - \beta$ by $\phi + \beta$ according to the sign conventions on ϕ and δ .

$$\cos\vartheta = \cos(\phi + \beta) \cdot \cos\omega \cdot \cos\delta + \sin(\phi + \beta) \cdot \sin\delta \quad (3.25)$$

The correspondent expressions for the average specific TOA irradiation, in W/m^2 , are

$$I_{\beta} = I_n \cos\vartheta = I_n (\cos(\phi - \beta) \cdot \cos\omega \cdot \cos\delta + \sin(\phi - \beta) \cdot \sin\delta) \quad (3.26)$$

for the northern hemisphere and

$$I_{\beta} = I_n \cos\vartheta = I_n (\cos(\phi + \beta) \cdot \cos\omega \cdot \cos\delta + \sin(\phi + \beta) \cdot \sin\delta) \quad (3.27)$$

for the southern hemisphere.

Similarly to H_0 final expressions, daily TOA incident solar energy radiation is, for the northern hemisphere,

$$H_{\beta} = \frac{24}{\pi} I_n (\cos(\phi - \beta) \cdot \sin\omega_{sr} \cdot \cos\delta + \omega_{sr} \cdot \sin(\phi - \beta) \cdot \sin\delta) \quad (3.28)$$

if ω_{sr} is in radians or, equivalently,

$$H_{\beta} = \frac{24}{\pi} I_n \left(\cos(\phi - \beta) \cdot \sin\omega_{sr} \cdot \cos\delta + \frac{\pi}{180} \omega_{sr} \cdot \sin(\phi - \beta) \cdot \sin\delta \right) \quad (3.29)$$

if ω_{sr} is in degrees, and

$$H_{\beta} = \frac{24}{\pi} I_n (\cos(\phi + \beta) \cdot \sin\omega_{sr} \cdot \cos\delta + \omega_{sr} \cdot \sin(\phi + \beta) \cdot \sin\delta) \quad (3.30)$$

or

$$H_{\beta} = \frac{24}{\pi} I_n \left(\cos(\phi + \beta) \cdot \sin\omega_{sr} \cdot \cos\delta + \frac{\pi}{180} \omega_{sr} \cdot \sin(\phi + \beta) \cdot \sin\delta \right) \quad (3.31)$$

for the southern hemisphere.

Finally, the so-called geometric factor R_b expresses the ratio of the incident radiation on the tilted surface to that on the correspondent horizontal surface.

$$R_b = \frac{H_{\beta}}{H_0} \quad (3.32)$$

It represents a key parameter to calculate the TOA daily radiation on the tilted surface of a solar collector from data of the solar radiation referring to the horizontal surface. In fact, the most commonly available data are hourly and daily radiation on the horizontal surface, whereas the need is for radiation on the plane of the collector. Hottel & Woertz (1942) firstly propose an useful method and monograms to predict H_{β} given H_0 and the standard values for R_b . Later on, Whillier (1965) revises previous study extending its geographical and temporal range of applicability.

TOA radiation level represents, for all the terrestrial applications, an upper benchmark on the available solar radiation, to be scaled due to the Earth atmosphere attenuation phenomena.

3.2.1.1 Numerical example (part II)

Considering the same geographical location and days of the year of the *Numerical example (part I)* paragraph, the daily TOA irradiance levels are calculated and represented applying Eq. 3.18 and Eq. 3.26.

Considering a horizontal surfaces, the next Figure 3.10 depicts the TOA irradiance levels, I_0 , between sunrise and sunset, for the summer and winter solstice days. Similar curves are for any other days of the year and for tilted surfaces.

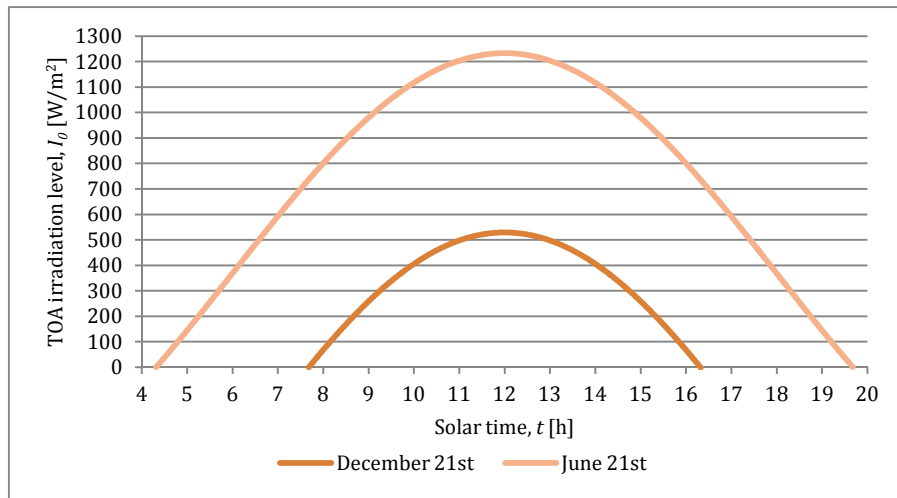


Figure 3.10. Numerical example, daily TOA irradiance curves for horizontal surfaces.

With such hypotheses, the daily TOA incident solar energy radiation is the following.

$$H_{0, \text{June } 21} = 11,641.08 \text{ Wh/m}^2 \quad H_{0, \text{December } 21} = 29,78.33 \text{ Wh/m}^2 \quad (3.33)$$

while, Figure 3.11 shows the trends of H_β varying the surface slope in the range $[0,90]$ degrees.

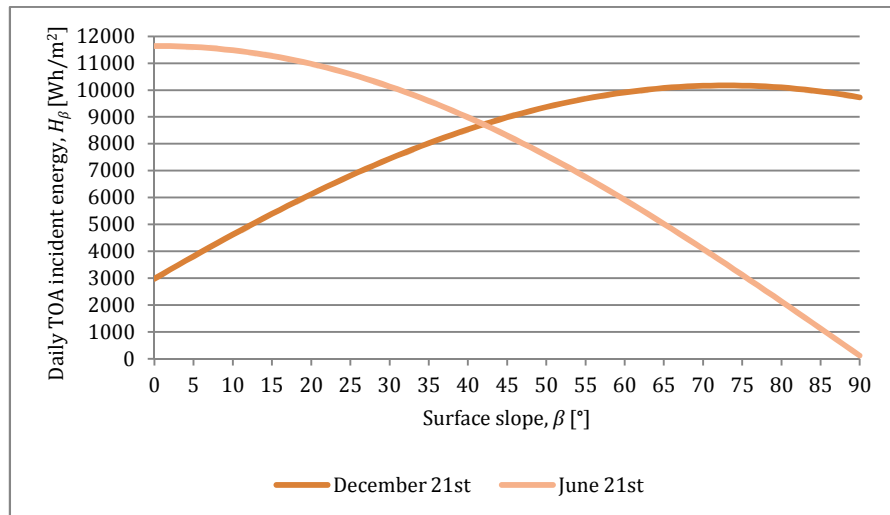


Figure 3.11. Numerical example, daily TOA incident energy varying the surface slope.

During winter, the available daily TOA incident solar energy is always lower than during summer. Furthermore, in winter, when the solar altitude is lower (see Figure 3.5) the higher values of the incident solar energy are for high tilt surfaces, e.g. 75° – 80° . On the contrary, during summer, horizontal and low tilt surfaces allow to collect the higher amount of solar energy because the Sun is closer to Zenith. Coherently, the values of R_b are, generally, higher than one during winter and lower than one in summer.

Finally, adopting the recommended average days listed in Table 3.2, the month daily TOA incident solar energy is calculated. Figure 3.12 shows the trends for such a parameter and five surfaces of ascending tilt angle, i.e. $\beta = 0, 15, 30, 45, 60$ degrees.

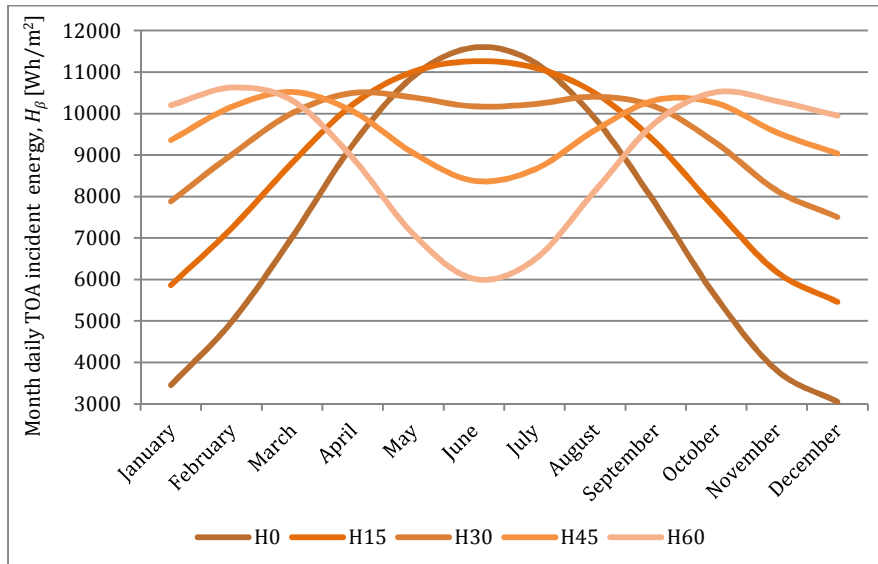


Figure 3.12. Numerical example, month daily TOA incident energy for five tilted surfaces.

3.2.2 Solar radiation models inside Earth atmosphere

Models to predict the solar radiation inside Earth atmosphere provide useful information for the solar plant design and profitability analysis. They focus on the estimation of the irradiation at ground level where solar plants are installed. As introduced in previous paragraphs, solar radiation models inside Earth atmosphere are probabilistic, i.e. stochastic, to take into account the atmosphere attenuation effects. Particularly, the most of the proposed models are correlation models developed and validated considering the historical data, measured, in the past years, by weather stations located worldwide. Consequently, the availability of complete and reliable databases of the historical climatic parameters is crucial to predict the trend of solar radiation. Such an aspect is, firstly, discussed.

3.2.2.1 Weather and solar radiation databases

In the recent years, demand for databases of high quality weather observations has intensified (Gibbas & Gilbert, 2005). In response to this need, governments, academic institutions and businesses made efforts to improve the quality and access to such databases. The US and the EU are the world regions who mostly improved their weather services collecting, through agencies like the National Oceanic and Atmospheric Administration (NOAA) and the European Environmental Agency (EEA), a huge amount of data about

weather conditions with a high geographical and temporal resolution. Efforts in the digitalization and the creation of easy-access conditions are, further, done. Several platforms and web services are developed. For the US context see, as example, Glahn & Ruth (2003) or Steiner et al. (2005), while, for the EU context, a recent project is the European Climate Assessment Dataset project (ECA&D). The major collected data refer to the local temperature and range of variation, the wind speed and direction, the precipitations, i.e. rain and snow on ground, the pressure level and the solar irradiation.

Focusing on the solar radiation data, the following aspects are important to database understand and use:

- ✓ time of the measurements;
- ✓ type of the measurements, i.e. instantaneous (punctual) vs. integrated (hourly, daily, etc.);
- ✓ measured parameter, e.g. global, direct, diffuse radiation;
- ✓ instrument used for the measure;
- ✓ receiving surface orientation, e.g. horizontal, fix slope, normal to direct radiation, etc.

The most of the radiation data available worldwide are for horizontal surfaces and the refer to hourly and daily global irradiation. Solar radiation components are not measured systematically, e.g. in Italy the national weather stations do not collect such data and very few data are available for years before 1990.

Useful and reliable data sources for solar radiation are from the World Radiation Data Center (WRDC), sponsored by the World Meteorological Organization (WMO), the National Climatic Data Center (NCDC), sponsored by the NOAA, and the Commission of the European Communities (CEC) periodically publishing the European Solar Radiation Atlas. In the following, the first source is considered.

3.2.2.2 Correlation models and parameters

Generally, solar correlation models are equations as in Eq. 3.34

$$Y = \varphi(X_1, \dots, X_i, \dots, X_n) \quad (3.34)$$

where the dependent variable Y quantifying the solar irradiance is correlated to one or more parameters, X_i , i.e. the so-called climatologic parameters or predictors, through the correlating function, φ . Consequently, to define solar correlation models two steps need to be faced:

- ✓ the selection of the most effective climatologic parameters, X_i ;
- ✓ the selection and computation of the correlation function, φ .

Reindl et al. (1990) propose an useful list of predictors for the diffuse fraction estimation. The most of them are adopted, also, for the estimation of global irradiance as stated in Badescu et al. (2012) that, also, enlarge such a list. Particularly, the authors classify the predictors in five groups as in Table 3.3.

Table 3.3. Classification of frequently adopted predictors.

Astronomical	Geographical	Meteorological (surface)	Meteorological (column integrated)	Quantities related to atmospheric turbidity
Time of the year	Latitude	Surface air pressure	Reduced ozone vertical path-length	Angstrom wavelength exponent
Solar time	Longitude	Air temperature	Total NO ₂ vertical path-length	Angstrom turbidity
Sun declination	Altitude	Dry-bulb temperature	Precipitable water	Aerosol single-scattering Albedo
Zenith angle	Ground Albedo	Air relative humidity		Linke turbidity
Solar constant		Wind speed		Unsworth-Monteith broadband turbidity
Clearness index		Cloudiness		Aerosol optical depth
Air mass		Hours of Sun		Visibility

The choice of the parameters to include to the models is not univocal. Different contexts, i.e. locations, could require different predictors due to differences in the degree of correlation with solar radiation. Furthermore, the adoption of a specific parameter requires the availability of historical data to feed the correlation model and to compute the function φ . If no data are available for one or more predictors such parameters are unusable. Frequently adopted parameters are the clearness index, the solar altitude, the ambient temperature and the relative humidity (Reindl et al., 1990, Jamil Ahmad & Tiwari, 2010, Badescu et al., 2012). Finally, the number of the predictors included in the analysis is directly related to the complexity of the model. Generally, the higher the number of predictors, the lower the applicability is. Furthermore, the increase of the independent variable number does not automatically and directly increase the accuracy of the models. The majority of the proposed models consider no more than three parameters, while a large group of them are single-predictor.

The selection and computation of the correlation function, φ , i.e. the second step of the process, is further split in two sequential phases. The former is the definition of the analytic expression of the correlation function, the latter is the computation of the coefficients of such function. For these phases, similarly to the previous step, no univocal approach exists. Furthermore, both the function expression and the coefficient values are

strongly dependent on the number and nature of the selected predictors. Polynomial functions of ascending degree are the most frequently adopted expressions since the first introduced models, e.g. Liu & Jordan (1960), while, recently, several other expressions are introduced, e.g. exponential, logarithmic, logistic, sinusoidal, etc. A full discussion and comparison of such expressions is provided in past and recent reviews about solar correlation models (Akinoglu, 1991, Ulgen & Hepbasli, 2004, Bakirci, 2009, Jamil Ahmad & Tiwari, 2011, Khatib et al., 2012, Badescu et al., 2012).

The computation of the coefficient values for the selected correlation function is generally developed through regression statistic analyses. An effective approach is the so-called least square data fitting method, firstly introduced by Carl Friedrich Gauss in 1795. Basically, the goal is to minimize the sum of squared residuals, i.e. the difference between an observed value and the fitted value provided by the model, given a set of historical observed data. Analytically, given a set of N couples (Y_i, \hat{Y}_i) of observed and predicted the sum of the squared residuals to be minimized is as follows.

$$S = \sum_{i=1}^N (Y_i - \hat{Y}_i)^2 \quad (3.35)$$

The minimum of the sum of squares is obtainable by setting the gradient to zero. If the considered model, i.e. the analytic expression of φ , contains m parameters, i.e. coefficients, the same number of gradient equations occur.

$$\frac{\partial S}{\partial \alpha_j} = 2 \sum_{i=1}^N (Y_i - \hat{Y}_i) \frac{\partial (Y_i - \hat{Y}_i)}{\partial \alpha_j} = 0 \quad j = 1, \dots, m \quad (3.36)$$

where α_j is the j^{th} parameter of φ . Full discussion about this method, variants, solving procedures and applications is provided in several books and papers (see, as e.g., Björck, 1997, Hsu, 1998).

Eq. 3.35 and Eq. 3.36 highlight that the computation of the correlation function parameters through the least square method requires observed data to calculate the residuals. This aspect has a general impact on the whole procedure. To develop solar correlation models for the prediction of solar radiation, or its fractions, inside Earth atmosphere the following data are necessary;

- ✓ the historical values for the chosen predictors, i.e. the model independent variables;
- ✓ the historical values of the solar radiation or its fractions, i.e. the model dependent variable.

This necessity justifies the growth of weather and solar radiation databases, collecting historical data, spread by national and international institutions and shortly reviewed in previous section.

An extensive review of the large set of solar radiation models proposed by the literature in the recent past is not the main focus of the present dissertation. Several papers focus on such an aspect and, also, Bortolini et al. (2011 and 2013) propose an overview of such models.

In the following, the most frequently adopted statistic key performance indicators (KPIs) to evaluate the level of fit of the model with the observed data are presented before focusing on diffuse fraction prediction proposing an integrated procedure for model development and an innovative multi-location approach for the horizontal diffuse fraction prediction in the EU area.

3.2.2.3 Key Performance Indicators – (KPIs)

Statistical performance indicators are the most frequently adopted KPIs to measure the accuracy of solar radiation models (Yorokohlu & Celik, 2006) even if, non conventional statistical procedures are, sometimes, applied (Lin et. al, 1999, Bellocchi et al., 2002).

A list of KPIs is in the following and it considers a set of N couples of (Y_i, \hat{Y}_i) values. (high) and (low) labels refer to the expected values for best performing the correlation between the model and the observed values.

- ✓ Mean absolute error (*MAE*) – (low)

$$MAE = \frac{1}{N} \sum_{i=1}^N \text{abs}(Y_i - \hat{Y}_i) \quad (3.37)$$

- ✓ Mean absolute percentage error (*MAPE*) – (low)

$$MAPE = \frac{1}{N} \sum_{i=1}^N \text{abs}\left(\frac{Y_i - \hat{Y}_i}{Y_i}\right) \quad (3.38)$$

- ✓ Root mean squared error (*RMSE*) – (low)

$$RMSE = \sqrt{\frac{1}{N} \sum_{i=1}^N (Y_i - \hat{Y}_i)^2} \quad (3.39)$$

- ✓ Regression coefficient (R^2) – (high, i.e. close to one)

$$R^2 = 1 - \frac{\sum_{i=1}^N (Y_i - \hat{Y}_i)^2}{\sum_{i=1}^N (Y_i - \bar{Y})^2} \quad (3.40)$$

where

$$\bar{Y} = \frac{1}{N} \sum_{i=1}^N Y_i \quad (3.41)$$

✓ t-statistics (t_{stat}) (Stone, 1993) – (low)

$$t_{stat} = \sqrt{\frac{(N-1)MBE^2}{RMSE^2 - MBE^2}} \quad (3.42)$$

where the mean bias error (MBE) is defined as

$$MBE = \frac{1}{N} \sum_{i=1}^N (Y_i - \hat{Y}_i) \quad (3.43)$$

3.3 Diffuse fraction correlations

Great attention is paid in the recent past to models predicting solar radiation components. This is mainly due to the lack of field data for a lot of locations worldwide. Differently from global irradiance, commonly measured by pyranometers in all weather stations, the solar radiation components require further instruments, e.g. pyrhemometers for the direct component, and dedicated measurement protocols. Consequently, field measures are rare and models predicting the distribution of the global irradiance among its components, i.e. the direct, diffuse and, if present, reflected components, received a growing interest.

3.3.1 Integrated procedure for model development

An effective procedure to develop diffuse fraction correlation models includes the following steps.

1. Selection of the geographical context of the analysis;
2. Selection of the climatologic predictors;
3. Selection of the correlation function expression;
4. Collection of historical data;
5. Analysis of the data through quality control procedures;
6. Computation of the function best fit coefficients;
7. Performance assessment through KPIs;
8. Analysis of the impact of seasonality on the developed model;
9. Model validation against independent datasets.

The first step defines the geographical boundaries of the analysis and represents a strategic phase of the process. The selection of the geographical context of the analysis is directly correlated to the geographical context of applicability of the obtained model and results. Basically, single-location and multi-location models exist. The former focuses on an unique location, generally a city area, while the latter merges data from several locations. Very few of the models proposed by the literature are multi-location. Frequently, feasibility tests to check the applicability of single-location models to regions different from those considered to model development are discussed. Rarely models are developed from databases with solar data from different regions. A relevant contribution of the present dissertation is the definition of a multi-location model for the EU geographical area.

The selection of the climatologic predictors, X_i , needs to join accuracy and applicability as discussed in Section 3.2.2.2. Models for the diffuse fraction prediction often include the clearness index as the main predictor. Such a parameter is defined as follows:

$$K = \frac{H}{H_0} \quad (3.44)$$

where H is the measured daily ground global solar radiation and H_0 is the daily TOA radiation defined in previous Eq. 3.22 and Eq. 3.23. Its theoretical range of variation is [0,1]. Single predictor models include only this parameter in the correlation function, while in multi predictor models few, i.e. one to three, further parameters are added, e.g. the solar altitude, the ambient temperature, the relative humidity, etc. The proposed multi-location model is single predictor and it considers the clearness index as the independent variable.

The correlation function expression is generally polynomial, exponential, logistics or sinusoidal. Among these, the first group is the most frequently adopted due to simplicity and effectiveness. Furthermore, multi-scenario analyses compare different expressions to outline the most suitable curves. In the developed model second, third and fourth degree polynomial functions and the logistic function are considered and compared.

The adopted data generally include historical values of several years in the recent past. The source is, sometimes, a weather station, installed by the researchers developing the model, if a single location model is developed. Otherwise, data are from the databases of public institutions or international research centers (see Section 3.2.2.1). Furthermore, annual and long-term models are developed. This aspect concerns the way the data are used, i.e. non merging or merging different year of data. The former allows the comparison among annual trends, postponing the definition of long-term model formulation, merging annual models, if the annual waveforms are comparable. The latter does not allow to highlight such differences among years. For this approach, the higher number of data adopted to develop the model could increase the fitting performances even if the compensation of annual peculiarities occur. The proposed multi-location model considers four years of historical

data from the WRDC database, from 2004 to 2007, and it develops and compares annual models, i.e. it follows the first of the two aforementioned approaches.

The accuracy of the correlation models is heavily affected by the quality of the raw data used to develop them. The solar radiation datasets frequently present inconsistencies due to systematic and casual bias generated both by problems in the equipments and faults in the measurement procedures (Geiger et al., 2002, Younes et al., 2006, Journée & Bertrand., 2011). The literature suggests to systematically check the raw data proposing several quality control procedures to filter them and to identify the so-called outliers, i.e. atypical data incorporating inconsistencies or abnormalities that need to be inquired or excluded from the analysis (Muneer & Munawwar, 2006). Different filtering strategies allow to identify the outliers. In the proposed multi-location model the standard deviation procedure based on the concept of scatter envelope introduced by Claywell et al. (2005) is adopted.

The computation of the best fit coefficients follows the least squares data fitting method. The proposed model is coherent with this standard.

Performance assessment is developed considering one or more of the KPIs described in Section 3.2.2.3.

Seasonal climate variations affect the level and distribution of the solar radiation at the ground level. During winter time the large amount of the incident radiation is diffuse radiation, while during summer the clear-sky days are higher so that a higher fraction of the global irradiance is direct. Basically, such seasonal differences are compensated in annual models, while seasonal models, i.e. models developed including data of a specific period of the year, clearly highlight the seasonal effects. The proposed multi-location model includes annual, summer and winter scenarios.

Performance assessment is different from model validation. The former of such steps analytically quantifies the fitting level of the model with the data chosen to develop it, the latter studies the applicability of the model considering different time periods and/or locations. Independent datasets are necessary to validate solar models preventing the so-called overlapping phenomenon (Munawwar & Muneer, 2007). In the proposed multi-location model historical data from different locations are used to validate the obtained correlation functions.

The described procedure for solar correlation model development represents a synthesis of the methods and approaches proposed by different literature studies. No study integrates all the steps together, especially for multi-location contexts. The proposed multi-location model develops such integration.

3.3.2 Multi-location model for the diffuse fraction prediction

This section describes, following the nine introduced steps, the developed model for the estimation of the daily diffuse fraction of solar radiation on the horizontal plane at ground level. The contents follow the study summarized in Bortolini et al. (2011 and 2013).

3.3.2.1 Step #1 – Model geographical context

The developed model is multi-location. Data are from 44 weather stations, located in 11 EU countries. Table 3.4 lists such locations providing the latitude and longitude coordinates for each of them. According to HCCS conventions, longitude negative values refer to weather stations west-located respect to the Prime Meridian. Figure 3.13 shows the considered locations on a map. Each dot represents a weather station. Three locations, in italics in Table 3.4 and with highlighted large dots in Figure 3.13, are used to validate the proposed model, i.e. Step #9. Such locations are called *check sites* in the following. Consequently, the developed multi-location model considers data from 41 of the 44 locations.

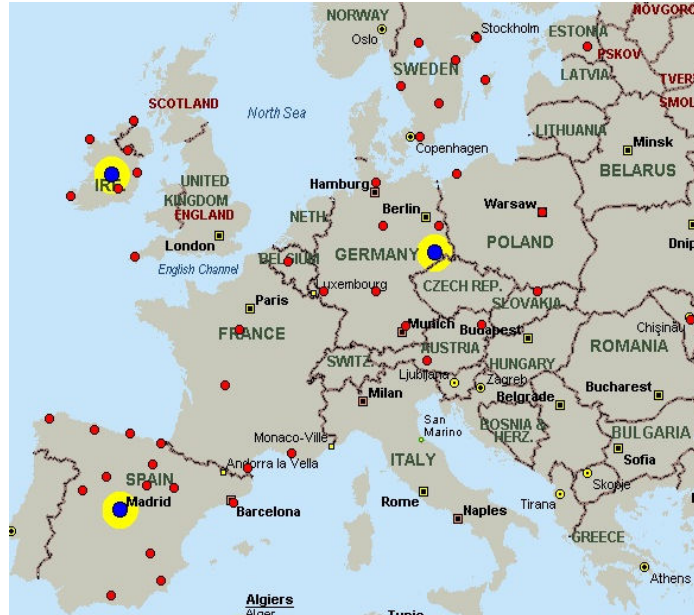


Figure 3.13. Map of the 44 considered EU weather stations.

Among the considered locations, none of them are in the Italian territory. This is due to the lack of data for the solar radiation fractions. In Italy, the available data are, only, about the global irradiance on the horizontal surface. In the future, the availability of such data allows to extend to Italy the set of the considered locations.

Table 3.4. Coordinates of the 44 considered EU weather stations.

Location	Country	Latitude [degrees]	Longitude [degrees]
Wien/Hohe warte	Austria	48.25	16.35
Sonnblick	Austria	47.05	12.95
Uccle	Belgium	50.80	4.35
Tartu/toravere	Estonia	58.25	26.47
Hamburg	Germany	53.97	10.00
Braunschweig	Germany	52.30	10.45
Lindenberg	Germany	52.22	14.12
<i>Dresden/klotzsche</i>	<i>Germany</i>	<i>51.13</i>	<i>13.75</i>
Wuerzburg	Germany	49.77	9.97
Trier	Germany	49.75	6.67
Weihenstephan	Germany	48.40	11.70
Malin head C.	Ireland	55.37	-7.33
Belmullet	Ireland	54.23	-10.00
Clones	Ireland	54.18	-7.23
Dublin	Ireland	53.43	-6.25
<i>Birr</i>	<i>Ireland</i>	<i>53.08</i>	<i>-7.88</i>
Kilkenny	Ireland	52.67	-7.27
Valentia obs	Ireland	51.93	-10.25
Kishinev	Moldova	47.00	28.82
Kolobrzeg	Poland	54.18	15.58
Warszawa	Poland	52.28	20.97
Zakopane	Poland	49.30	19.95
Moscow	Russia	55.75	37.57
Santander	Spain	43.47	-3.82
La coruna	Spain	43.37	-8.42
Oviedo	Spain	43.35	-5.87
San Sebastian	Spain	43.30	-2.05
Zaragoza	Spain	41.67	-1.07
Valladolid	Spain	41.65	-4.77
Salamanca	Spain	40.95	-5.92
<i>Madrid</i>	<i>Spain</i>	<i>40.45</i>	<i>-3.72</i>
Valencia	Spain	39.48	-0.38
Ciudad real	Spain	38.98	-3.92
Badajoz	Spain	38.88	-7.02
Murcia	Spain	38.00	-1.17
Granada/Armillia	Spain	37.13	-3.63
Karlstad	Sweden	59.37	13.47
Stockholm	Sweden	59.35	18.07
Norrkoping	Sweden	58.58	16.25
Goteborg	Sweden	57.70	12.00
Visbyaerolog. Stn	Sweden	57.67	18.35
Vaxjo/Kronoberg	Sweden	56.93	14.73
Lund	Sweden	55.72	13.22
Camborne	UK	50.22	-5.32

3.3.2.2 Step #2 – Adopted climatologic predictors

The proposed model is single predictor. The clearness index, defined in previous Eq. 3.44, is correlated to the diffuse fraction of solar radiation incident to the horizontal plane. Such a parameter is defined according to Eq. 3.45

$$K_d = \frac{H_d}{H} \quad (3.45)$$

where H_d is the daily diffuse radiation on the horizontal plane, in Wh/m^2 , and H the global radiation at the ground level. Its theoretical range of variation is $[0,1]$.

3.3.2.3 Step #3 – Adopted correlation functions

The proposed model considers and compares four different analytic functions, correlating the diffuse fraction K_d to the clearness index K . In particular, three polynomial functions of ascending degree and the logistic function are considered. Their analytic expressions are in Eq. 3.46 to Eq. 3.49.

$$\hat{K}_d = a + bK + cK^2 \quad (3.46)$$

$$\hat{K}_d = a + bK + cK^2 + dK^3 \quad (3.47)$$

$$\hat{K}_d = a + bK + cK^2 + dK^3 + eK^4 \quad (3.48)$$

$$\hat{K}_d = \frac{a}{1 + b \exp(cK)} \quad (3.49)$$

Notation \hat{K}_d indicates an expected value of the daily diffuse fraction on the horizontal plane, while K_d represents the observed value. The introduced parameters a, b, c, d, e are calculated applying the least square data fitting method in the next Step #6.

3.3.2.4 Step #4 – Data collection

The considered data are collected by the WRDC in the four year period from 2004 to 2007. The database collects hourly, daily and monthly global and diffuse radiation levels for a wide set of locations worldwide. Figure 3.14 proposes a snapshot of the database graphical interface for the first of the considered locations, i.e. Wien/Hohe warte site, and for year 2007. Similar graphs are for all the other years and locations together with the correspondent tables with analytic values. A preliminary quality control of the proposed values is assessed by the WRDC to avoid the major inconsistencies. A further check through the quality control procedure described in the Step #5 is implemented.

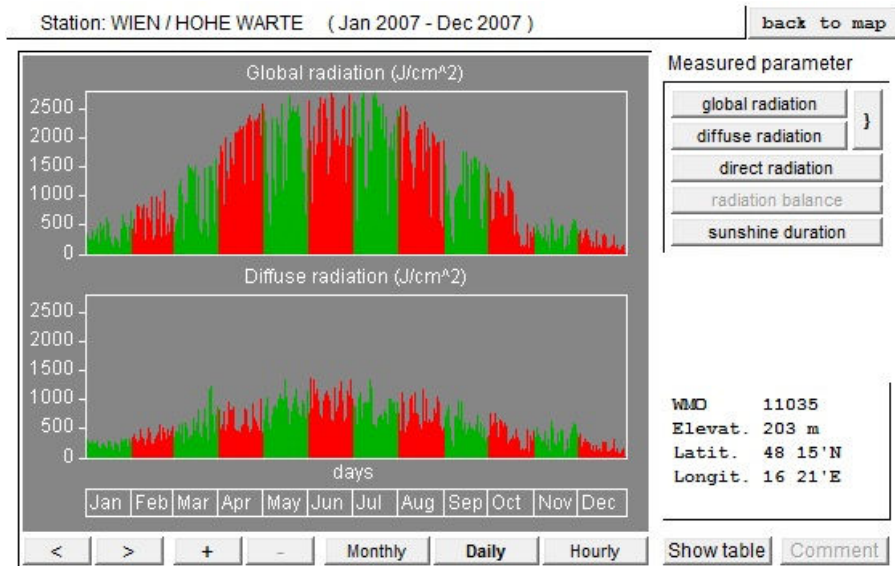


Figure 3.14. WRDC database. Example of the available data.

Querying the WRDC database, the daily observed values of H_d and H are extracted and the diffuse fraction K_d is calculated. Furthermore, the knowledge of H and the computation of H_0 allows to calculate the value of the clearness index correspondent to each value of K_d so that, for each day of the four considered years and for each of the 44 locations, the couples (K, K_d) are known. Figure 3.15 represents such couples for the 41 locations considered for multi-location model development and year 2007.

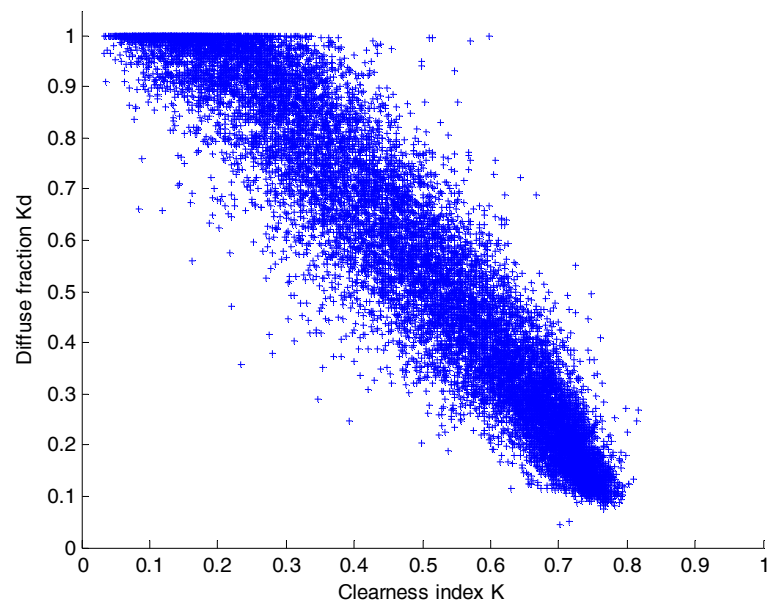


Figure 3.15. (K, K_d) couples, example for year 2007.

The goal of the study is to define the best fit curve interpolating such data.

3.3.2.5 Step #5 – Quality control procedure and data filtering

To check and filter the collected raw data the standard deviation procedure, based on the concept of scatter envelope introduced by Claywell et al. (2005), is adopted.

Figure 3.16 shows an example of scatter envelope on a diffuse fraction-clearness index graph. Each point represents a couple (K, K_d) , while the scatter envelope is the region limited by the two dashed curves, i.e. the lower and the upper curves. The scatter envelope is the region where the most of the data is expected. If no anomalies occur, low values of the clearness index are associated to high values of the diffuse fraction and vice-versa. Reasonably, the outlier data, out of the scatter envelope, need to be inquired.

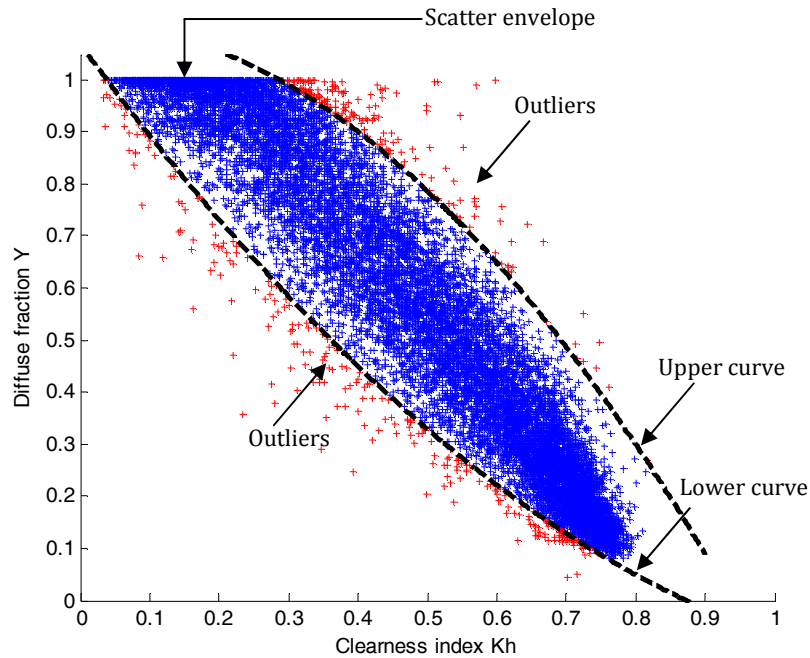


Figure 3.16. Quality control procedure. The scatter envelope.

The lower and the upper curves are defined according to the following standard deviation procedure. For each year between 2004 and 2007, all couples of daily (K, K_d) observed values are considered. Data for the three check sites are excluded because they do not contribute to the multi-location correlation function definition but they are used to the *ex-post* validation of the whole approach. Preliminarily, the couples for which K and/or K_d fall out of the $[0,1]$ range are neglected. Remaining data are divided into ten equal bands, based on their clearness index values. For each band, b , the mean value \bar{K}_{db} of the measured daily diffuse fraction on the horizontal plane and the standard deviation σ_b are computed. The considered scatter envelope includes the values falling in the $\pm 2\sigma_b$ range. Consequently, the lower curve $f_{low}(K)$ comes from the interpolation of the ten couples of values $(\bar{K}_b, \bar{K}_{db} - 2\sigma_b)$ where \bar{K}_b is the median value of the band b . Similarly, the upper curve $f_{up}(K)$ is the best-fit curve for the ten couples $(\bar{K}_b, \bar{K}_{db} + 2\sigma_b)$. For both the curves a second degree

polynomial interpolating function is adopted. All the data out of the scatter envelope are the outliers. The following Eq. 3.50 expresses the condition of acceptance for a generic couple of values (K, K_d).

$$f_{low}(K) \leq K_d \leq f_{up}(K) \quad (3.50)$$

The following example, based on 2007 values, clarifies the adopted procedure. Table 3.5 introduces the most relevant parameters necessary to calculate the scatter envelope.

Table 3.5. Data for scatter envelope lower and upper curves calculation, year 2007.

K band b	# data	\bar{K}_b	σ_b	\bar{K}_{db}	$\bar{K}_{db} - 2\sigma_b$	$\bar{K}_{db} + 2\sigma_b$
0.0-0.1	337	0.9856	0.0351	0.05	0.9153	1.0558
0.1-0.2	1366	0.9654	0.0532	0.15	0.8591	1.0717
0.2-0.3	1666	0.8979	0.0932	0.25	0.7115	1.0843
0.3-0.4	1674	0.7722	0.1246	0.35	0.5230	1.0214
0.4-0.5	1722	0.6244	0.1207	0.45	0.3831	0.8657
0.5-0.6	1959	0.4753	0.1101	0.55	0.2550	0.6956
0.6-0.7	2653	0.3089	0.0910	0.65	0.1269	0.4909
0.7-0.8	2324	0.1804	0.0587	0.75	0.0629	0.2978
0.8-0.9	6	0.1874	0.0613	0.85	0.0647	0.3100
0.9-1.0	0	-	-	-	-	-

Particularly, the last three columns include the data necessary for the interpolation and the curve definition. The obtained lower and upper curve equations are the following.

$$f_{low}(K) = 1.0680 - 1.8180K + 0.6814K^2 \quad (3.51)$$

$$f_{up}(K) = 1.1120 - 0.0383K - 1.2200K^2 \quad (3.52)$$

Previous Figure 3.16 graphically represents this example. 437 values, equal to the 3.19% of the available data, are out of the scatter envelope and represent the outliers excluded from the analysis. Table 3.6 summarizes the results obtained applying the quality control procedure to each of the four annual datasets.

Table 3.6. Quality control procedure results.

Year	# available data	# outliers	% outliers
2004	16,763	1,571	9.37
2005	13,128	1,481	11.28
2006	13,650	639	4.98
2007	13,707	437	3.19

Differences in the available data number are mainly due to lack of information in the WRDC database. In 2006 and 2007, the incidence of the outliers is significantly lower than in the previous two years. A possible reason for such an evidence is the increase of the quality in

the measurement processes and a more accurate analysis of the collected data implemented by the WRDC excluding a wide set of incoherent values. Finally, stochastic and casual phenomena always affect the measured data. The analysis of the data from several years allows to partially compensate these differences, increasing the range of applicability of the obtained results. The proposed approach follows such a direction as discussed in the next sections presenting the obtained results.

3.3.2.6 Step #6 – Best fit curve coefficients

For each of the four years the four correlating expressions, proposed in Eq. 3.46 to Eq. 3.49, are adopted to interpolate the (K, K_d) values falling in the scatter envelope, i.e. the values without anomalies and incoherencies. In this step the annual scenario is focused. Data for the 41 considered locations are analyzed together calculating the best fit coefficients for the four correlation expressions, i.e. the coefficients a, b, c, d, e . The obtained results are summarized in Table 3.7.

Table 3.7. Best fit curve coefficients for the annual scenario.

Year	2004				2005			
Function	Eq. 3.46	Eq. 3.47	Eq. 3.48	Eq. 3.49	Eq. 3.46	Eq. 3.47	Eq. 3.48	Eq. 3.49
a	1.1068	1.0098	1.0624	1.0756	1.1069	0.9872	1.0777	1.0720
b	-0.7948	0.1815	-0.5632	0.0452	-0.8218	0.4002	-0.9120	0.0451
c	-0.6474	-3.2379	-0.0030	6.1991	-0.5904	-3.8346	1.8890	6.1638
d		1.9962	-3.4491			2.4911	-7.0899	
e			3.1182				5.4318	
Year	2006				2007			
Function	Eq. 3.46	Eq. 3.47	Eq. 3.48	Eq. 3.49	Eq. 3.46	Eq. 3.47	Eq. 3.48	Eq. 3.49
a	1.0908	0.9622	0.9824	1.0567	1.0956	0.9959	0.9292	1.0594
b	-0.6238	0.6713	0.3764	0.0337	-0.6588	0.3271	1.2978	0.0351
c	-0.8512	-4.3064	-2.9931	6.5757	-0.8160	-3.4225	-7.7557	6.5610
d		2.6747	0.4234			1.9999	9.4594	
e			1.3075				-4.3502	

The obtained best fit curves are in Figure 3.17 to Figure 3.32. Each figure refers to a specific function expression and year.

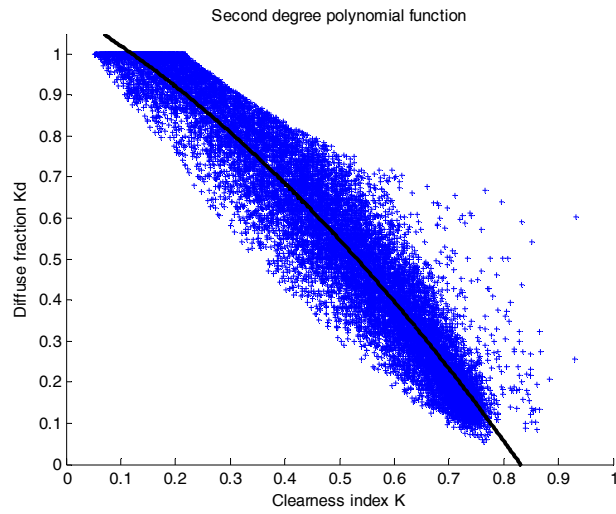


Figure 3.17. Second degree annual correlation function, year 2004.

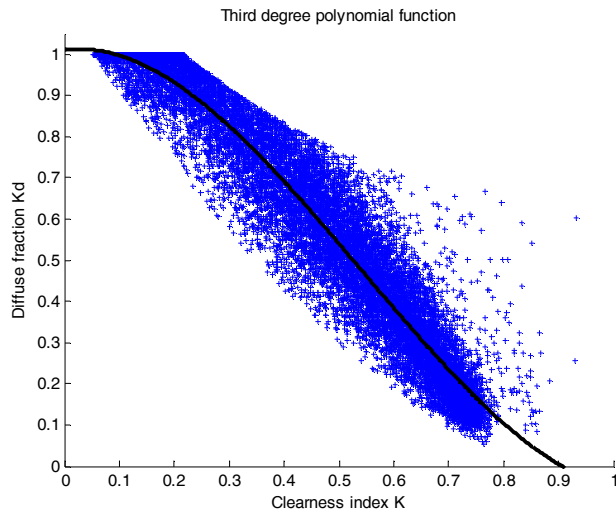


Figure 3.18. Third degree annual correlation function, year 2004.

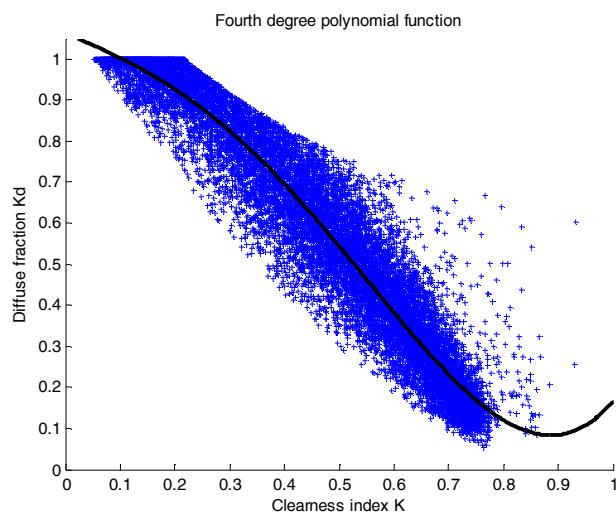


Figure 3.19. Fourth degree annual correlation function, year 2004.

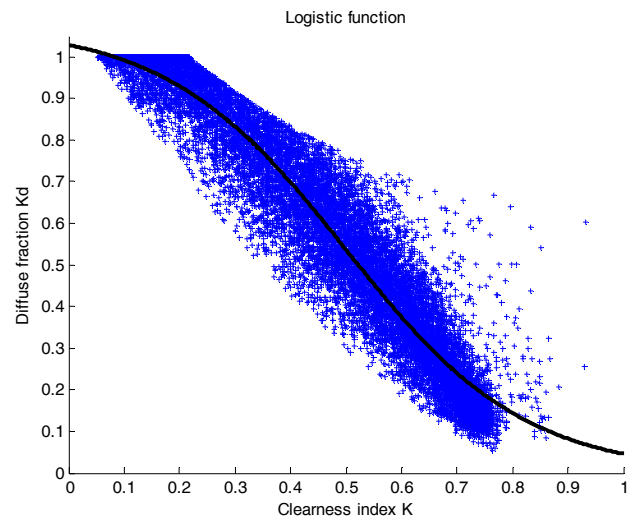


Figure 3.20. Logistic annual correlation function, year 2004.

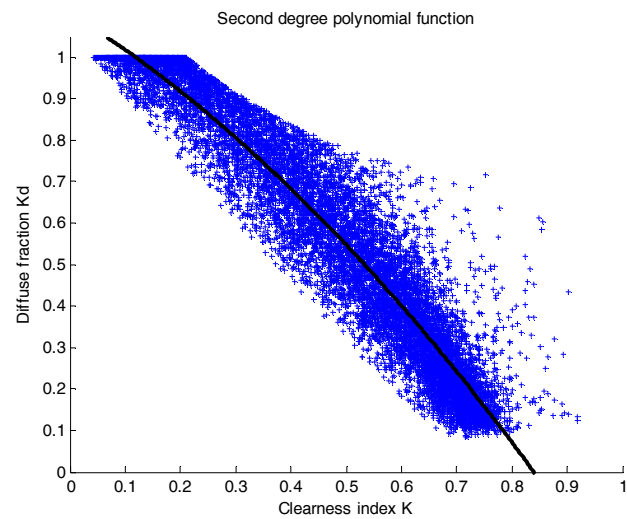


Figure 3.21. Second degree annual correlation function, year 2005.

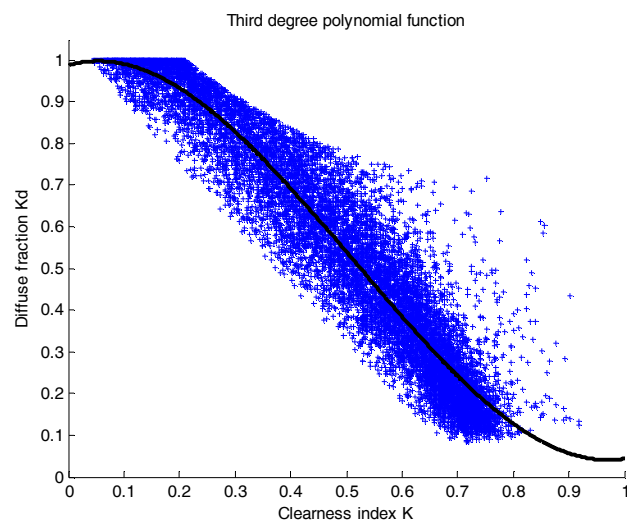


Figure 3.22. Third degree annual correlation function, year 2005.

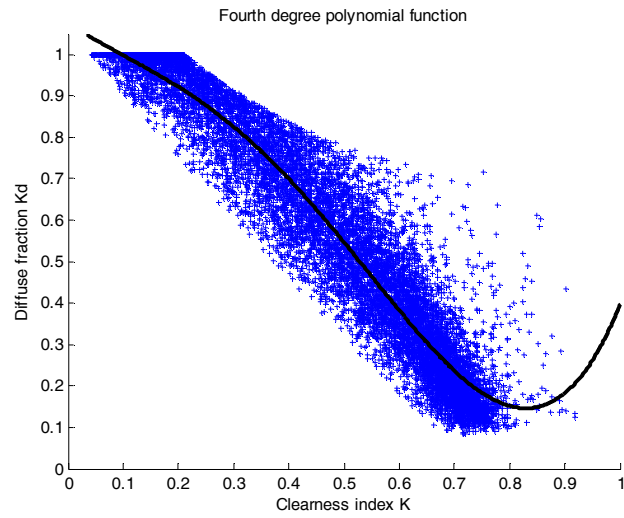


Figure 3.23. Fourth degree annual correlation function, year 2005.

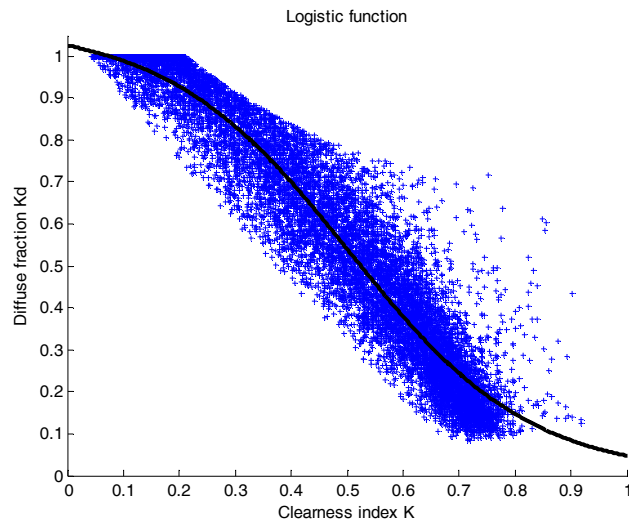


Figure 3.24. Logistic annual correlation function, year 2005.

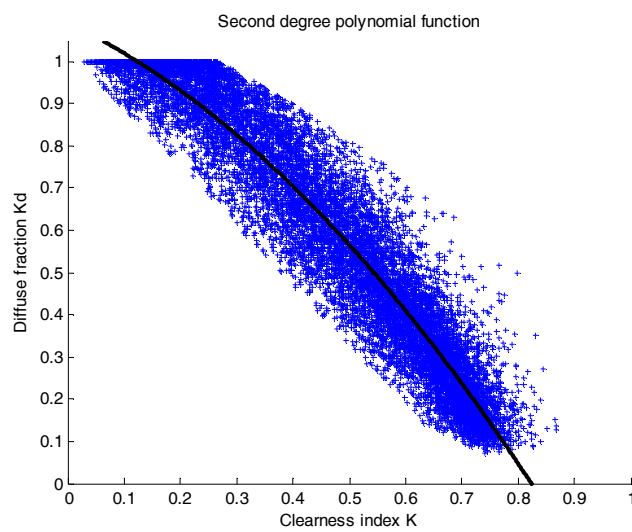


Figure 3.25. Second degree annual correlation function, year 2006.

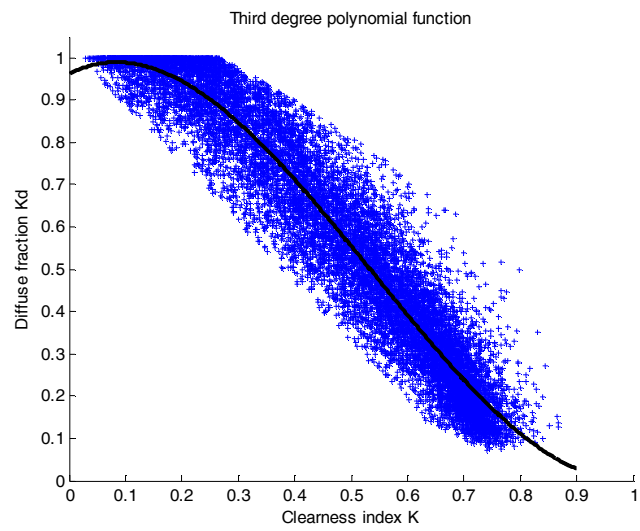


Figure 3.26. Third degree annual correlation function, year 2006.

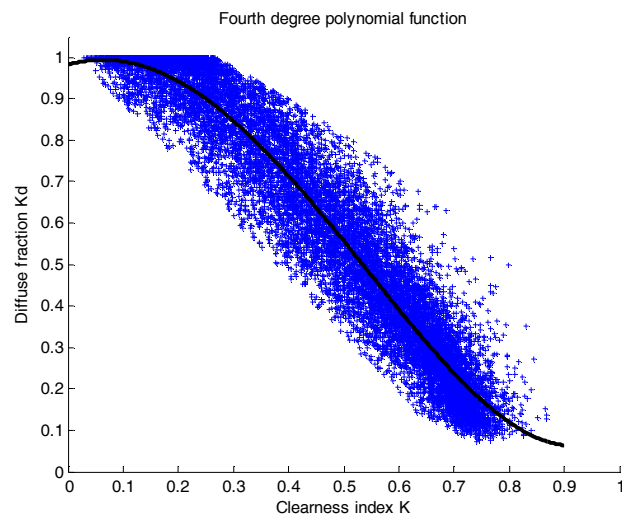


Figure 3.27. Fourth degree annual correlation function, year 2006.

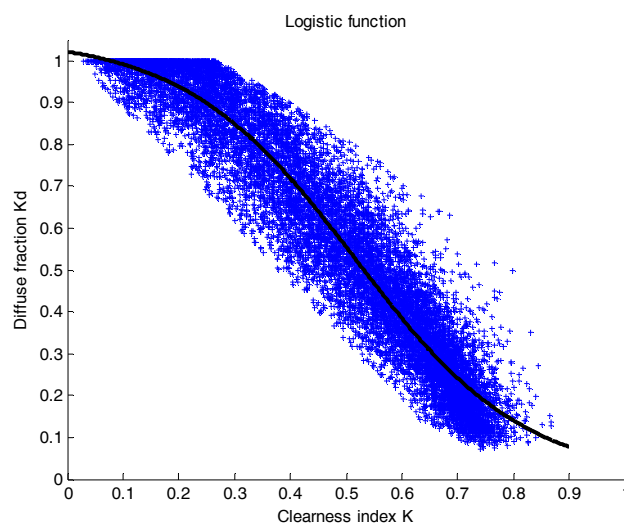


Figure 3.28. Logistic annual correlation function, year 2006.

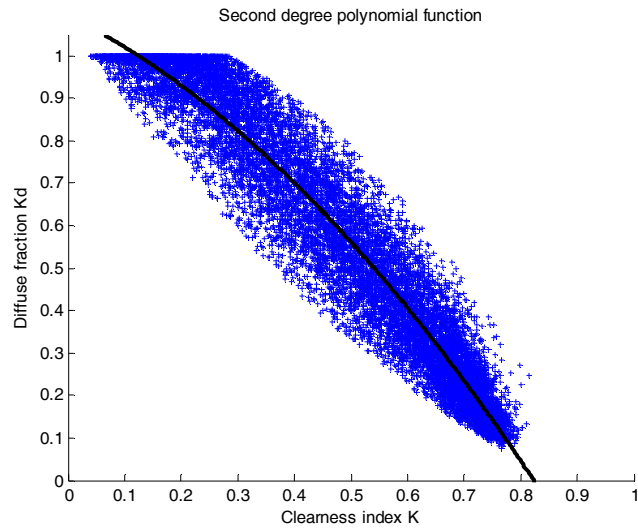


Figure 3.29. Second degree annual correlation function, year 2007.

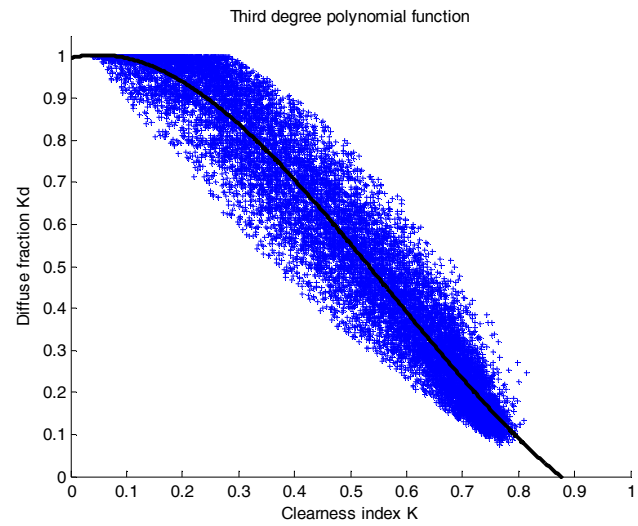


Figure 3.30. Third degree annual correlation function, year 2007.

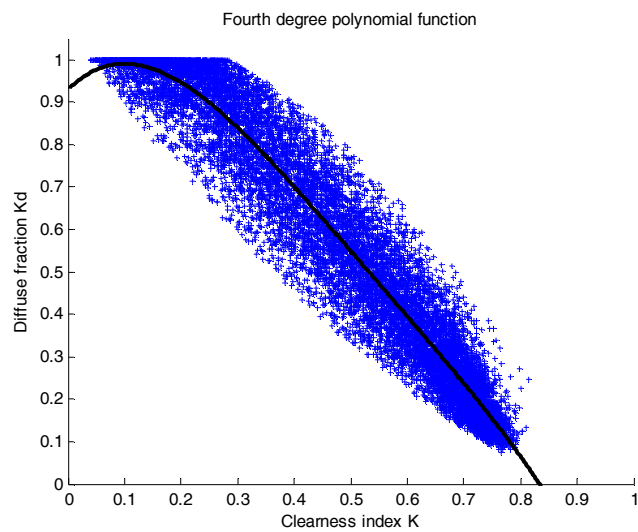


Figure 3.31. Fourth degree annual correlation function, year 2007.

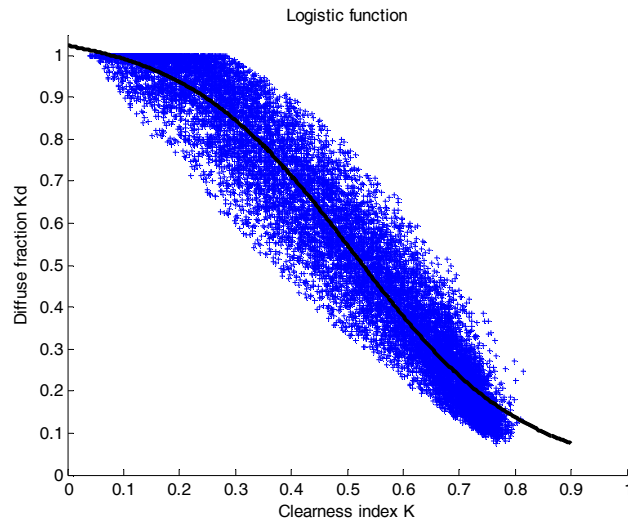


Figure 3.32. Logistic annual correlation function, year 2007.

The most of the available observed data, i.e. the blue markers in the figures above, presents clearness index values lower than 0.8. This is due to the systematic scattering and absorption phenomena of the Earth atmosphere always reducing the global radiation incident to the ground level. As a consequence, the obtained waveforms are little significant in the range $[0.8,1]$ of K and their trends can be unexpected as occurs in Figure 3.19 and Figure 3.23. The high degrees of freedom of the fourth degree polynomial curve together with the high sparseness of the observed data for years 2004 and 2005 explain such anomalous trend.

Furthermore, the top left region of the clearness index – diffuse fraction graphs is, also, little significant due to the few observed data falling in such a region. Few times no radiation reaches the ground level, i.e. $K = 0$. That is the reason because all the curves cross the y-axis for values different to one and for some of them, e.g. Figure 3.31, an unexpected local maximum occurs.

In the range $[0.1,0.8]$ of the clearness index no systematic anomalies occur for all expressions and years, so that a good applicability of the results to almost all the operative EU contexts is guaranteed.

3.3.2.7 Step #7 – Performance assessment

Table 3.8 shows the values of the KPIs introduced in Eq. 3.37 to Eq. 3.43 for each correlation curve and considered year. As discussed before, such indices allow to quantitatively measure the fit level of the correlation curves toward the data adopted to develop them.

Table 3.8. Performance assessment for the annual scenario - KPIs.

Year	2004				2005			
	Eq. 3.46	Eq. 3.47	Eq. 3.48	Eq. 3.49	Eq. 3.46	Eq. 3.47	Eq. 3.48	Eq. 3.49
Function								
<i>MAE</i>	0.0609	0.0595	0.0598	0.0607	0.0654	0.0631	0.0634	0.0638
<i>MAPE</i>	0.1502	0.1495	0.1490	0.1561	0.1713	0.1672	0.1652	0.1701
<i>RMSE</i>	0.0796	0.0786	0.0784	0.0793	0.0853	0.0835	0.0830	0.0838
<i>R</i> ²	0.9206	0.9227	0.9229	0.9211	0.9103	0.9141	0.9150	0.9134
<i>t</i> _{stat}	2.11E-12	8.22E-12	3.04E-13	1.0796	6.11E-13	3.37E-12	1.83E-12	0.5968

Year	2006				2007			
	Eq. 3.46	Eq. 3.47	Eq. 3.48	Eq. 3.49	Eq. 3.46	Eq. 3.47	Eq. 3.48	Eq. 3.49
Function								
<i>MAE</i>	0.0656	0.0632	0.0632	0.0638	0.0612	0.0594	0.0593	0.0609
<i>MAPE</i>	0.1604	0.1564	0.1561	0.1594	0.1438	0.1427	0.1426	0.1526
<i>RMSE</i>	0.0836	0.0817	0.0817	0.0821	0.0779	0.0768	0.0766	0.0779
<i>R</i> ²	0.9156	0.9194	0.9194	0.9185	0.9302	0.9321	0.9324	0.9302
<i>t</i> _{stat}	1.69E-12	1.60E-12	1.44E-12	0.5471	2.69E-12	1.02E-12	1.30E-11	1.1262

The logistic curve, i.e. Eq. 3.49, presents, for all scenarios, the worst performances with reference to all the considered indices. In particular, the t_{stat} values clearly highlight the poorness of such a function if adopted to correlate the clearness index to the diffuse fraction. Considering the polynomial functions, i.e. Eq. 3.46 to Eq. 3.48, the third and fourth degree functions outperform the second degree model. Furthermore, the fourth degree function generally outperforms the third degree model. However, for all scenarios, the gap between Eq. 3.47 and Eq. 3.48 results is not significant, i.e. lower than 1.5%, for all the statistical indices. Such reasons lead to consider the third degree polynomial function a good correlating expression between the clearness index and the diffuse fraction for the EU geographical area.

Figure 3.33 compares the waveforms of the following four curves obtained for years 2004 to 2007 and the third degree polynomial function:

$$\hat{K}_d = 1.0098 + 0.1815K - 3.2379K^2 + 1.9962K^3 \quad (3.53)$$

$$\hat{K}_d = 0.9872 + 0.4002K - 3.8346K^2 + 2.4911K^3 \quad (3.54)$$

$$\hat{K}_d = 0.9622 + 0.6713K - 4.3064K^2 + 2.6747K^3 \quad (3.55)$$

$$\hat{K}_d = 0.9959 + 0.3271K - 3.4225K^2 + 1.9999K^3 \quad (3.56)$$

The four curves present very similar waveforms in all the [0,1] range of variation. The maximum gap among them, i.e. the vertical distance between the two farthest curves, is equal to 0.1436. Excluding the regions with $K < 0.1$ or $K > 0.8$, where few of the observed values fall, the maximum gap decreases to 0.0374.

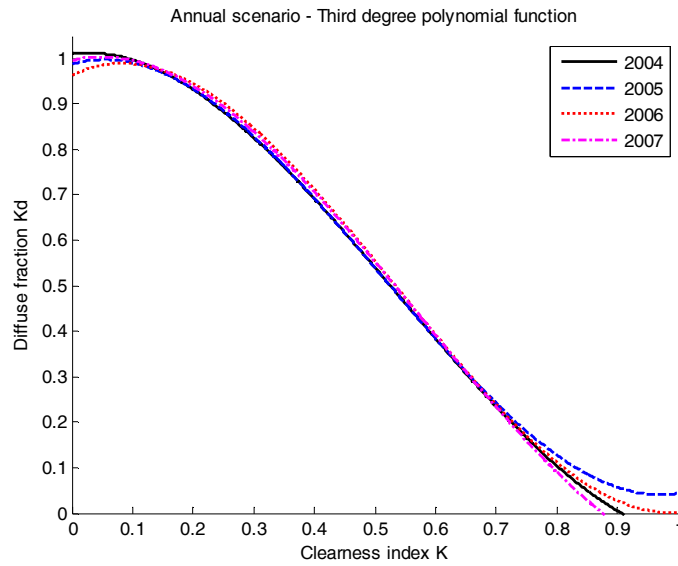


Figure 3.33. Waveform comparison among years, annual scenario.

Results highlight that no relevant differences among years occur. As a consequence, a long-term model is calculated as the average of the four previous models. Its final expression is the following Eq. 3.57.

$$\hat{K}_d = 0.9888 + 0.3950K - 3.7003K^2 + 2.2905K^3 \quad (3.57)$$

3.3.2.8 Step #8 – Seasonality

The seasonal variation effects of the incident solar radiation and, particularly, of its fractions are included in the analysis through the development of two further scenarios, called summer and winter scenarios in the following. The former includes the (K, K_d) couples observed during summer months, i.e. the days from April 1st to September 30th, while the latter focuses on the winter period, i.e. the days from January 1st to March 31st and from October 1st to December 31st.

For each scenario the same approach followed for the annual scenario is developed calculating the best fit curves for the three polynomial expressions and the logistic function. The best fit coefficients and KPIs are computed and compared to study the accuracy of the correlation curves and the similarities among years. The final goals are the proposal of long term models for the summer and the winter scenarios and the comparison of such curves to the annual curves to highlight the dependence of the diffuse fraction of solar radiation on the seasonal variations.

At first, Table 3.9 and Table 3.10 propose the outcomes for the summer scenario.

Table 3.9. Best fit curve coefficients for the summer scenario.

Year	2004				2005			
	Eq. 3.46	Eq. 3.47	Eq. 3.48	Eq. 3.49	Eq. 3.46	Eq. 3.47	Eq. 3.48	Eq. 3.49
<i>a</i>	1.0948	1.0124	1.0332	1.0286	1.1487	1.0189	1.3345	1.1522
<i>b</i>	-0.6630	0.0714	-0.1979	0.0289	-1.1421	0.0324	-3.9215	0.0959
<i>c</i>	-0.8261	-2.6568	-1.5505	6.8166	-0.1698	-3.1633	12.8614	5.0030
<i>d</i>		1.3584	-0.4404			2.2858	-23.7155	
<i>e</i>			1.0076				14.6484	

Year	2006				2007			
	Eq. 3.46	Eq. 3.47	Eq. 3.48	Eq. 3.49	Eq. 3.46	Eq. 3.47	Eq. 3.48	Eq. 3.49
<i>a</i>	1.0957	1.0081	1.0248	1.0242	1.1068	1.0295	0.9331	1.0498
<i>b</i>	-0.7014	0.0620	-0.1514	0.0300	-0.7911	-0.1027	1.1835	0.0394
<i>c</i>	-0.7664	-2.6442	-1.7746	6.7361	-0.6376	-2.3502	-7.7567	6.3267
<i>d</i>		1.3812	-0.0243			1.2661	10.2050	
<i>e</i>			0.7838				-5.0713	

Table 3.10. Performance assessment for the summer scenario - KPIs.

Year	2004				2005			
	Eq. 3.46	Eq. 3.47	Eq. 3.48	Eq. 3.49	Eq. 3.46	Eq. 3.47	Eq. 3.48	Eq. 3.49
<i>MAE</i>	0.0576	0.0571	0.0571	0.0591	0.0624	0.0620	0.0618	0.0621
<i>MAPE</i>	0.1462	0.1460	0.1458	0.1579	0.1399	0.1389	0.1366	0.1391
<i>RMSE</i>	0.0739	0.0735	0.0735	0.0751	0.0803	0.0796	0.0784	0.0797
<i>R²</i>	0.9222	0.9230	0.9231	0.9197	0.8769	0.8792	0.8827	0.8788
<i>t_{stat}</i>	2.20E-12	3.15E-12	1.69E-12	1.2617	3.66E-13	1.02E-12	5.17E-12	0.0724

Year	2006				2007			
	Eq. 3.46	Eq. 3.47	Eq. 3.48	Eq. 3.49	Eq. 3.46	Eq. 3.47	Eq. 3.48	Eq. 3.49
<i>MAE</i>	0.0610	0.0605	0.0605	0.0621	0.0586	0.0581	0.0579	0.0598
<i>MAPE</i>	0.1611	0.1604	0.1602	0.1703	0.1417	0.1419	0.1415	0.1523
<i>RMSE</i>	0.0775	0.0772	0.0771	0.0784	0.0750	0.0747	0.0745	0.0759
<i>R²</i>	0.9119	0.9127	0.9127	0.9098	0.9179	0.9186	0.9190	0.9160
<i>t_{stat}</i>	6.65E-13	2.32E-12	4.17E-13	0.9493	9.8E-13	2.21E-12	1.99E-12	0.8249

Similarly to the annual scenario, the third degree polynomial curve is a good function to correlate the clearness index to the diffuse fraction during summer time. The logistic curve is the last in the rank preceded by the second degree polynomial curve. No relevant differences occur between the third and fourth degree polynomial curves so that the former is preferable to the latter due to its higher simplicity.

For the sake of brevity the graphs for all the studied cases are omitted. They are similar to those proposed for the annual scenario.

On the contrary, a comparison of the obtained curves among years is of high interest. The obtained results suggest to focus the attention on the third degree polynomial function. Figure 3.34 depicts the obtained four third degree polynomial function curves for the period 2004 to 2007.

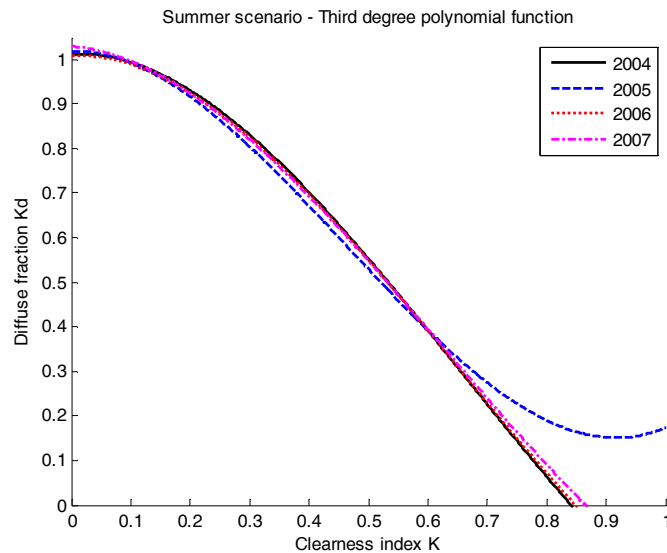


Figure 3.34. Waveform comparison among years, summer scenario.

The waveforms present very similar trends. A partial exception is the 2005 curve that, for the values of the clearness index higher than 0.75, shows an anomalous behavior. This is due to the very few and scattered data observed in such a year in this area, i.e. few clear-sky days. Figure 3.35 presents the filtered 2005 data for the summer period to better understand this evidence.

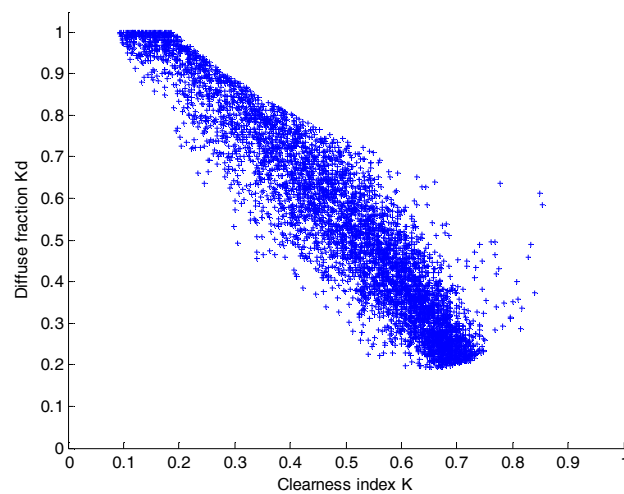


Figure 3.35. (K, K_d) couples for 2005 summer scenario.

Despite this partial exception, affecting high values of the clearness index, rare to be experienced, the results allow to compute a long-term model for the summer scenario. In the

region where the most of the observed data falls the four waveforms are very similar. The maximum gap among the four curves is of 0.3884 in the whole range of variation of K but it reduces to 0.1260 for $K \in [0,0.8]$ and to 0.0491 for $K \in [0,0.7]$. The long-term model is in Eq. 3.58.

$$\hat{K}_d = 1.0172 + 0.0158K - 2.7036K^2 + 1.5729K^3 \quad (3.58)$$

Results for the winter scenario are in Table 3.11 and Table 3.12.

Table 3.11. Best fit curve coefficients for the winter scenario.

Year	2004				2005			
	Eq. 3.46	Eq. 3.47	Eq. 3.48	Eq. 3.49	Eq. 3.46	Eq. 3.47	Eq. 3.48	Eq. 3.49
<i>a</i>	1.1111	0.9573	1.0225	1.0876	1.1047	0.9248	0.9953	1.0682
<i>b</i>	-0.7768	0.8368	-0.1118	0.0455	-0.6644	1.1664	0.1582	0.0342
<i>c</i>	-0.6706	-5.1003	-0.8709	6.1908	-0.7933	-5.7225	-1.3206	6.5333
<i>d</i>		3.5014	-3.7446			3.8307	-3.5340	
<i>e</i>			4.1945				4.1585	

Year	2006				2007			
	Eq. 3.46	Eq. 3.47	Eq. 3.48	Eq. 3.49	Eq. 3.46	Eq. 3.47	Eq. 3.48	Eq. 3.49
<i>a</i>	1.0816	0.9233	0.9780	1.0615	1.0795	0.9557	0.9511	1.0538
<i>b</i>	-0.5212	1.1632	0.3274	0.0319	-0.4979	0.7883	0.8573	0.0287
<i>c</i>	-0.9480	-5.6182	-1.7609	6.5881	-1.0208	-4.5586	-4.8761	6.8635
<i>d</i>		3.7096	-3.0633			2.7926	3.3516	
<i>e</i>			3.9941				-0.3315	

Table 3.12. Performance assessment for the winter scenario - KPIs.

Year	2004				2005			
	Eq. 3.46	Eq. 3.47	Eq. 3.48	Eq. 3.49	Eq. 3.46	Eq. 3.47	Eq. 3.48	Eq. 3.49
<i>MAE</i>	0.0674	0.0630	0.0631	0.0637	0.0767	0.0711	0.0708	0.0715
<i>MAPE</i>	0.1513	0.1443	0.1430	0.1448	0.1780	0.1642	0.1627	0.1639
<i>RMSE</i>	0.0884	0.0850	0.0848	0.0854	0.0991	0.0948	0.0945	0.0950
<i>R²</i>	0.9064	0.9134	0.9139	0.9127	0.8873	0.8968	0.8974	0.8963
<i>t_{stat}</i>	1.40E-12	4.53E-13	7.90E-13	0.0178	1.65E-13	9.15E-13	5.79E-13	0.1767

Year	2006				2007			
	Eq. 3.46	Eq. 3.47	Eq. 3.48	Eq. 3.49	Eq. 3.46	Eq. 3.47	Eq. 3.48	Eq. 3.49
<i>MAE</i>	0.0708	0.0656	0.0654	0.0659	0.0646	0.0612	0.0612	0.0621
<i>MAPE</i>	0.1593	0.1475	0.1468	0.1469	0.1423	0.1355	0.1355	0.1399
<i>RMSE</i>	0.0909	0.0870	0.0868	0.0872	0.0824	0.0802	0.0802	0.0808
<i>R²</i>	0.9014	0.9098	0.9102	0.9094	0.9266	0.9304	0.9304	0.9295
<i>t_{stat}</i>	5.12E-13	3.13E-15	4.67E-13	0.2542	6.95E-13	2.61E-12	6.43E-13	0.4215

Winter scenario is not so different from the previous ones. During winter the clearness index is often low due to few clear-sky days. In the right region of the $K - K_d$ graph low or no values fall so that the correlation curves are erratic. KPIs in Table 3.12 allow to consider the third degree polynomial curve a good correlation function. Similarly to Figure 3.34, Figure 3.36 compares the four obtained waveforms.

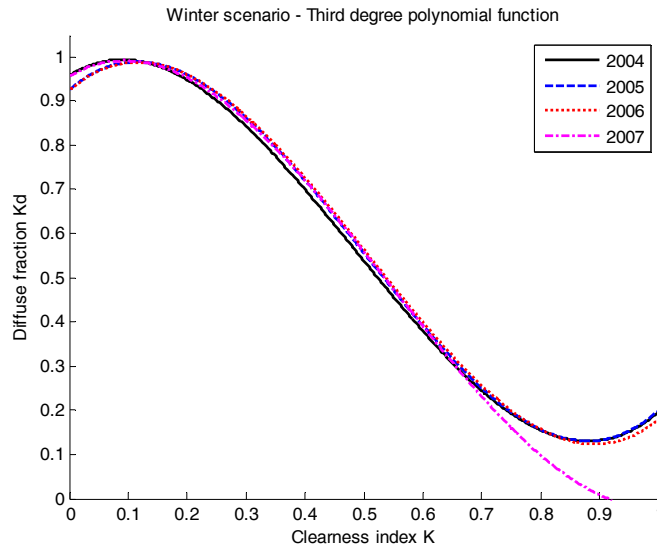


Figure 3.36. Waveform comparison among years, winter scenario.

Neglecting the bottom right area, the four waveforms are comparable (the maximum gap among the curves is equal to 0.2214) and the long-term model for the winter scenario is the following.

$$\widehat{K}_d = 0.9403 + 0.9887K - 5.2499K^2 + 3.4586K^3 \quad (3.59)$$

Finally, the comparison of the long-term models for the annual and seasonal scenarios highlights their differences and the effect of seasonality on the diffuse fraction solar radiation. Figure 3.37 shows Eq. 3.57 to Eq. 3.59 waveforms.

The most evident outcome is the similarity of the three curves in the range $[0.1, 0.8]$ of the clearness index. This is the region where the observed data generally fall. Consequently, seasonal variations do not heavily affect the diffuse fraction values.

Analyzing in detail the aforementioned range, the summer scenario curve, i.e. the red curve of Figure 3.37 is lower than the winter scenario curve, i.e. the black curve of Figure 3.37, while the annual scenario curve is in the middle. Such a trend is coherent. During summer the diffuse radiation is lower than during winter in which the clear-sky days are rare. The annual scenario is intermediate due to the compensation of such seasonal phenomena.

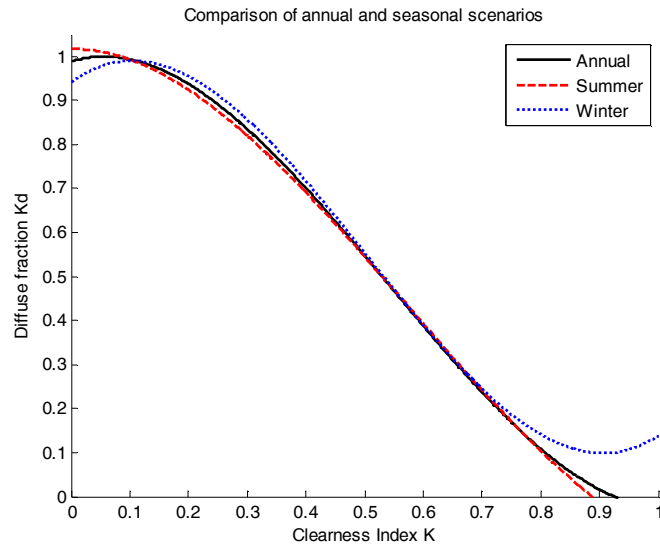


Figure 3.37. Effect of seasonality, comparison of the long-term models.

3.3.2.9 Step #9 – Model validation against independent datasets

Section 3.3.1 highlights the importance of testing correlation models against independent datasets, i.e. adopting data not used for model development. The application of the proposed multi-location model to the previously defined check sites allows such a test measuring the gap between multi-location and single-location models. In such a validation the third degree polynomial function is considered, representing a good correlation curve between K and K_d . Table 3.13 exemplifies the comparative analysis for year 2007 and the three selected check sites. Comparing the values of t_{stat} parameter is not possible due to the different degrees of freedom in single and multi-location models.

Table 3.13. Model validation. Comparative analysis for check sites, year 2007.

	Madrid			Birr			Dresden/klotzsche			
	multi-location	single-location	% gap	multi-location	single-location	% gap	multi-location	single-location	% gap	
<i>MAE</i>	0.0574	0.0535	6.95	0.0586	0.0534	8.76	0.0559	0.0517	7.53	Annual
<i>MAPE</i>	0.2160	0.1769	18.12	0.1133	0.1019	10.04	0.1014	0.1011	0.27	
<i>RMSE</i>	0.0735	0.0714	2.88	0.0772	0.0712	7.84	0.0780	0.0738	5.31	
<i>R</i> ²	0.9296	0.9336	0.43	0.8831	0.9008	1.99	0.9209	0.9290	0.89	
<i>MAE</i>	0.0503	0.0428	14.96	0.0479	0.0469	2.16	0.0519	0.0511	1.63	Summer
<i>MAPE</i>	0.2087	0.1459	30.07	0.0899	0.0888	1.15	0.1101	0.1113	-1.11	
<i>RMSE</i>	0.0625	0.0578	7.57	0.0612	0.0597	2.44	0.0723	0.0715	1.10	
<i>R</i> ²	0.9333	0.9430	1.04	0.9314	0.9347	0.36	0.9219	0.9236	0.19	
<i>MAE</i>	0.0642	0.0594	7.54	0.0767	0.0536	30.18	0.0566	0.0463	18.08	Winter
<i>MAPE</i>	0.2321	0.1918	17.35	0.1471	0.1023	30.44	0.0888	0.0777	12.49	
<i>RMSE</i>	0.0819	0.0784	4.27	0.0971	0.0718	26.09	0.0787	0.0675	14.32	
<i>R</i> ²	0.9271	0.9332	0.66	0.7989	0.8901	11.42	0.8982	0.9253	3.01	

Results highlight a percentage gap between single and multi-location models lower than 20% for all the scenarios, the performance indices and the check sites except for four indices with a gap close to 30%. Particularly critic is the winter scenario for the Birr, Ireland location. This is mainly due to the anomalous dispersion of the registered values of diffuse radiation for such a location, increasing the gap between the multi-location model and the experimental data. However, also for this critic location, acceptable results are obtained.

Finally, adopting the third degree polynomial function and considering the site adopted to calculate the coefficients, single-location models little outperform multi-location models. For any other location, single-location models present a lack of applicability and performances are very poor, e.g. applying the Madrid single-location model to the Birr scenario the values of R^2 are lower than 40% for both annual and seasonal scenarios. On the contrary, the developed multi-location annual and seasonal models, i.e. Eq. 3.57 to Eq. 3.59, adequately fit with datasets from the three check sites, presenting different climatic conditions for the EU area. Their adoption is, consequently, strongly recommended.

3.3.3 Technical note

The proposed procedure for multi-location model development requires an IT expert platform for data collection and processing and the synthesis of the results. A *MatLab*© tool is developed supporting the researcher in the nine phases of the procedure. The main strengths of the system are:

- ✓ the effective interface with the databases for data input and result storage;
- ✓ the flexibility in the definition of the correlation function expressions, i.e. the user can type a custom expression or select among a default list;
- ✓ the availability of specific functions for least square data fitting method;
- ✓ the parallel development of single and multi-location models, annual and seasonal scenarios;
- ✓ the high-quality of the numeric and graphic outputs;
- ✓ the easy-use interfaces;
- ✓ for the programmer, the possibility to easily improve the tool adding further options.

References

- Akinoglu, B.G., (1991). Review of sunshine-based models used to estimate monthly average global solar radiation. *Renewable Energy* 1(3-4):479-497.
- Angus, R.C., Muneer, T., (1993). Sun position for daylight models: precise algorithms for determination. *Lighting Research & Technology* 25(2):81-83.
- Badescu, V., Gueymard, C.A., Cheval, S., Oprea, C., Baci, M., Dumitrescu, A., Iacobescu, F., Milos, I., Rada, C., (2012). Computing global and diffuse solar hourly irradiation on clear sky. Review and testing of 54 models. *Renewable and Sustainable Energy Reviews* 16:1636-1656.
- Bakirci, K., (2009). Models of solar radiation with hours of bright sunshine: a review. *Renewable and Sustainable Energy Reviews* 13:2580-2588.
- Ball, D.W., (2005). The baseline: The solar spectrum. *Spectroscopy* 20(6):1-30.
- Bellocchi, G., Acutis, M., Fila, G., Donatelli, M., (2002). An indicator of solar radiation model performance based on fuzzy expert system. *Agronomy Journal* 94(6):1222-1233.
- Benford, F., Bock, J.E., (1939). A time analysis of sunshine. *Transactions of the Illuminating Engineering Society* 34:200-217.
- Björck, Å., (1997). Numerical methods for least squares problems. Society for Industrial and Applied Mathematics. Amsterdam, The Netherlands.
- Bortolini, M., Gamberi, M., Graziani, A., Manzini, R., Regattieri, A., Santarelli, G., (2011). Multi-location approach to estimate solar energy radiation in the EU countries with a diffuse fraction correlation model. *Proceedings of the XVI Summer School Francesco Turco*, Abano Terme, Italy.
- Bortolini, M., Gamberi, M., Graziani, A., Manzini, R., Mora, C., (2013). Multi-location model for the estimation of the horizontal daily diffuse fraction of solar radiation in Europe. *Energy Conversion & Management* 67:208-216.
- Claywell, R., Muneer, T., Asif, M., (2005). An efficient method for assessing the quality of large solar irradiance datasets. *Journal of Solar Energy Engineering* 127:150-152.

-
- Cooper, P.I., (1969). The absorption of radiation in solar stills. *Solar Energy* 12(3):333-346.
- Duffie, J.A., Beckman, W.A., (2006). *Solar Engineering for Thermal Processes*. 3rd Edition. John Wiley & Sons inc. New York, USA.
- Fritz, S., (1958). Transmission of solar energy through the Earth's clear and cloudy atmosphere. *Transactions of the Conference on Use of Solar Energy* 1:17.
- Geiger, M., Diabaté, L., Ménard, L., Wald, L., (2002). A web service for controlling the quality of measurements of global solar irradiation. *Solar Energy* 73:475-480.
- Gibbas, M.J., Gilbert, C., (2005). A description of the weather source comprehensive global weather observation database. 85th AMS Annual Meeting – Combined Preprints 1167-1172.
- Glahn, H.R., Ruth, D.P., (2003). The new digital forecast database of the national weather service. *Bulletin of the American Meteorological Society* 84(2):195-201.
- Goody, R., (2002). Observing and thinking about the atmosphere. *Annual Review of Energy and the Environment* 27:1-20.
- Gueymard, C.A., (2004). The sun's total and spectral irradiance for solar energy applications and solar radiation models. *Solar Energy* 76:423-453.
- Hottel, H.C., Woertz, B.B., (1942). Performance of flat-plane solar heat collectors. *Transactions of ASME* 64:91.
- Hsu, H., (1998). *Probability, Random Variables and Random Processes*, Schaum's McGraw-Hill. New York, USA.
- Iqbal, M., (1983). *Introduction to solar radiation*, Academic. Toronto, Canada.
- Jamil Ahmad, M., Tiwari, G.N., (2010). Solar radiation models – A review. *International Journal of Energy Research* 35:271-290.
- Jiang, Y., (2009). Computation of monthly mean daily global solar radiation in China using artificial neural networks and comparison with other empirical models. *Energy* 34:1276-1283.

Journée, M., Bertrand, C., (2011). Quality control of solar radiation data within the RMIB solar measurements network. *Solar Energy* 85:72-86.

Khatib, T., Mohamed, A., Sopian, K., (2012). A review of solar energy modeling techniques. *Renewable and Sustainable Energy Reviews* 16:2864-2869.

Kiselman, D., Pereira, T.M.D., Gustafsson, B., Asplund, M., Meléndez, J., Langhans, K., (2011). Is the solar spectrum latitude-dependent? An investigation with SST/TRIPPEL. *Astronomy & Astrophysics* 535:1-9.

Li, H., Lian, Y., Wang, X., Ma, W., Zhao, L., (2011). Solar constant values for estimating solar radiation. *Energy* 36:1785-1789.

Lin, W., Gao, W., Pu, S., Lu, E., (1999). Ranking the overall performance of eight sunshine-based global solar radiation models with a nonparametric statistical procedure. *Energy Conversion & Management* 40:233-241.

Liu, B.Y.H., Jordan, R.C., (1960). The interrelationship and characteristic distribution of direct, diffuse and total solar radiation. *Solar Energy* 4:1-19.

Lu, Y., Khalil, M.A.K., (1996). The distribution of solar radiation in the Earth's atmosphere: the effects of ozone, aerosols and clouds. *Chemosphere* 32(4):739-758.

Mihelić-Bogdanić, A., Budin, R., Filipan, V., (1996). Investigation of solar declination. *Renewable Energy* 7(3):271-277.

Moon, P., (1940). Proposed standard solar radiation curves for engineering use. *Journal of the Franklin Institute* 230(5):583-617.

Müller, M., (1995). Equation of time – problem in astronomy. *Acta Physica Polonica A* 88:S-49.

Munawwar, S., Muneer, T., (2007). Statistical approach to the proposition and validation of daily diffuse irradiation models. *Applied Energy* 84:455-475.

Muneer, T., Munawwar, S., (2006). Improved accuracy models for hourly diffuse solar radiation. *Transaction of the ASME* 128:104-116.

Nijmeh, S., Mamlook, R., (2000). Testing of two models for computing global solar radiation on tilted surfaces. *Renewable Energy* 20:75-81.

Quaschnig, V., (2003). Technology fundamentals: the sun as an energy resource. *Renewable Energy World* 6(5):90-93.

Reindl, D.T., Beckman, W.A., Duffie, J.A., (1990). Diffuse fraction correlations. *Solar Energy* 45(1):1-7.

Ryuji, S., Toshio, Y., Hisashi, K., (1997). Regression of the sun declination and the equation of time for processing observed data of daylight illuminance and solar radiation. *Technology Reports of the Osaka University* 47(2267-2282):111-118.

Seghouani, N., (2006). High resolution spectrum: Towards a new observational strategy. European Space Agency (ESA) – special publication. Noordwijk, The Netherlands.

Spencer, J.W., (1971). Fourier series representation of the position of the sun. *Search* 2(5):172-173.

Steiner, J.J., Minoura, T., Xiong, W., (2005). WeatherInfo: a web-based weather data capture system. *Agronomy Journal* 97(2):633-639.

Stone, R.J., (1993). Improved statistical procedure for the evaluation of solar radiation estimation models. *Solar Energy* 51(4):289-291.

Thekaekara, M.P., (1974). Data on incident solar energy. Supplement to the Proceedings of the Twentieth Annual Meeting of the Institute for Environmental Science 21.

Ulgen, K., Hepbasli, A., (2004). Solar radiation models. Part 1: a review. *Energy Source* 26(5):507-520.

Wenham, S.R., Green, M.A., Watt, M.E., Corkish, R., (2000). *Applied photovoltaics*, 2nd Edition, Earthscan. London, UK.

Whillier, A., (1965). Solar radiation graphs. *Solar Energy* 9:164.

Yorukoglu, M., Celik, A.N., (2006). A critical review on the estimation of daily global solar radiation from sunshine duration. *Energy Conversion & Management* 47:2441-2450.

Younes, S., Claywell, R., Muneer, T., (2006). Quality control of solar radiation data: present status and proposed new approaches. *Energy* 30:1533-1549.

Web - references

European Climate Assessment Dataset project – ECA&D

<http://eca.knmi.nl/>

European Environmental Agency – EEA

<http://www.eea.europa.eu/>

European Solar Radiation Atlas – CEC – Helioclim

<http://www.helioclim.org/esra/>

National Climatic Data Center – NCDC

<http://www.ncdc.noaa.gov/>

National Oceanic and Atmospheric Administration – NOAA

<http://www.noaa.gov/>

Photovoltaic Geographical Information System – PVGIS

<http://re.jrc.ec.europa.eu/pvgis/>

World Meteorological Organization – WMO

<http://www.wmo.int/>

World Radiation Data Center – WRDC

<http://wrdc.mgo.rssi.ru/>

4. *Concentrating solar sector*

Available technologies and the current scenario

The concentrating solar sector deals with technologies and plants producing energy from the solar source through the concentration of the incident radiation. In such plants the specific irradiance on the receiver surface is higher than the punctual local level. This energy sector is far from maturity and the researchers are, still, studying best strategies, technologies and plants to increase the conversion performances.

This chapter provides a description of concentrating solar technologies oriented to the electric and/or thermal power generation. Useful criteria are proposed to classify the existing systems. Furthermore, an analysis is proposed with reference to recent studies considering different areas of application and the main system strengths and weaknesses. The final purpose is to review the sector scenario and to contextualize the description of the bi-axial Fresnel lens solar PV/T prototype provided in the following Chapter 5.

4.1 Solar concentrating principle

Concentrating solar radiation principle is quite simple to understand. Solar rays hitting a generic surface are reflected, or their trajectories are partially deviated, through proper devices to focus them on a smaller area. More properly, solar radiation incident area is called solar collector, while the area in which the concentrated radiation is directed is called solar receiver. Consequently, the incident radiation on the collector is concentrated to the receiver. To measure the concentration level the following key parameter is introduced (Rabl, 1976).

$$CR_g = \frac{A_c}{A_r} \quad (4.1)$$

where A_c is the collector area, A_r is the receiver area and CR_g is the so-called geometric concentration ratio (or geometric concentration factor) measured in Suns. As example, a concentration ratio of 500x, i.e. 500 Suns, means the collector surface is 500 times higher than the receiver surface. A further definition of the concentration ratio refers, directly, to the irradiance fluxes on the collector and the receiver. It is the optic concentration ratio (or optic concentration factor) and its analytic expression in is Eq. 4.2.

$$CR_o = \frac{\frac{1}{A_r} \int I_r dA_r}{I_c} \quad (4.2)$$

CR_o is the ratio between the average concentrated irradiance on the receiver surface and the correspondent irradiance level on the collector surface (supposed uniform on the whole area). Irradiance levels refer to the direct component of solar radiation, the sole that can be usefully converted to heat and/or power in concentrating solar systems.

The concentration ratio represents a distinctive parameter for each concentrating solar plant (Jayarama Reddy, 2012). To concentrate the solar radiation two basic strategies are possible:

- ✓ **Solar reflection** adopting mirrors. In such a strategy the solar collector is a mirror surface reflecting the incident radiation and concentrating it to a focus area, i.e. the receiver, located over the mirror. Adequate collector shapes for such configuration are parabolic. Geometrically, the parabolic shape has the property that, for any line parallel to its axis, the angle between it and the normal surface is equal to the angle between the normal and a line to the focal point. Because of the solar radiation arrives to the Earth through parallel rays and by the Snell law the angle of reflection is equal to the angle of incidence, all the rays parallel to the axis of the parabola are reflected to the focus. Figure 4.1 shows this property, F is the focus;

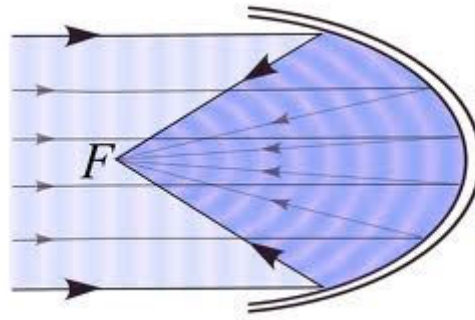


Figure 4.1. Reflection of solar radiation through parabolic mirror.

- ✓ **Solar refraction** adopting lenses. In such a strategy the solar collector is a lens or a set of lenses refracting the incident radiation and concentrating it to a focus area, i.e. the receiver, located under the lens plane. In this configuration a relevant parameter is the so-called focal length expressing the distance over which initially collimated rays are brought to the focus. This length is, consequently, the distance between the collector and the receiver. Figure 4.2 depicts refraction through a Fresnel lens, a typical solution for solar lens collectors.

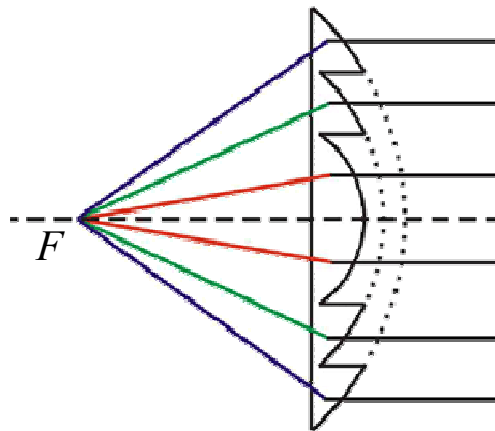


Figure 4.2. Refraction of solar radiation through Fresnel lens.

For both strategies, i.e. solar reflection and refraction, two focus geometries are feasible (Machinda et al., 2011, Ummadisingu & Soni, 2011).

- ✓ **Line-focus geometry.** The solar receiver is continuously distributed on a linear surface;
- ✓ **Point-focus geometry.** The solar receiver is made of a single or a defined number of spot areas.

The focus geometry is the optic parameter most affecting the concentrator plant structure as described in the next section.

4.2 Solar reflection plants

According to the major literature, four basic design typologies of concentrating plants, based on solar reflection, are proposed and installed (Kalogirou, 2004, Hang et al., 2008, Wang et al., 2010, Janjai et al., 2011, Kaygusuz, 2011, Machinda et al., 2011, Pavlović et al., 2012, Pitz-Paal et al., 2012).

- ✓ Parabolic troughs;
- ✓ Parabolic dishes;
- ✓ Solar towers;
- ✓ Linear Fresnel reflectors.

Details about each of them are in the following paragraphs together with notes about the existing plants integrating such typologies. In this context the focus is on medium and large scale power plants.

4.2.1 Parabolic trough systems

Parabolic troughs are line-focus systems. Their collectors are the mirrored surfaces of a linear parabolic concentrator focusing the direct solar radiation to the receiver located along the focal line of the parabola (Figure 4.3).



Figure 4.3. Parabolic trough system, example.

According to SolarPaces' 2009 Annual Report, parabolic trough technology is considered to be a fully mature technology (Richter, 2009). Wide applications of such a design typology are in medium and large scale power solar fields (capacities up to 200MW) integrating an absorber pipe, as solar receiver, flowed by a heat transfer fluid or water in case of direct steam generation. Furthermore, a steam generator unit, power conversion

system and a steam condenser are installed in addition to the solar collector to complete the plant. A basic scheme of such an energy system is in Figure 4.4.

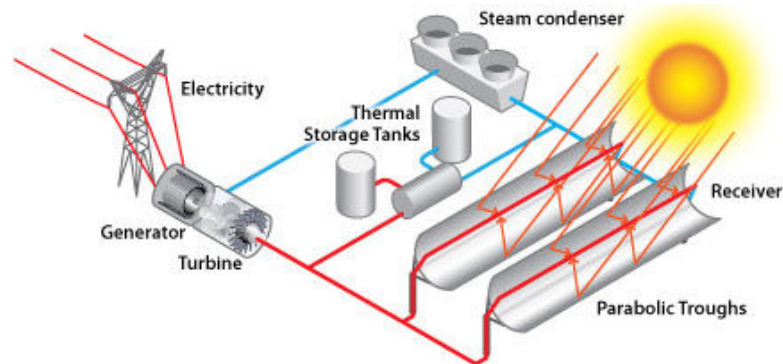


Figure 4.4. Parabolic trough solar plant for power production.

Typical concentration ratios of such plants are $70\div 100\times$, while the operating temperatures achieved are in the range $350\div 550^\circ\text{C}$ with a global electric efficiency of about 15% (Müller-Steinhagen & Trieb, 2004, Ummadisingu & Soni, 2011). To guarantee such performances a single axis tracking technology controlling the solar altitude axis of motion is, generally, integrated.

4.2.2 Parabolic dishes

Parabolic dish reflectors are point-focus collectors that track the Sun in two axes, concentrating the solar radiation to a receiver located on the dish focal point (Figure 4.5).



Figure 4.5. Parabolic dish, example.

The most common applications of such a technology adopt heat engine/generator units, Stirling engines or gas turbines. The fluid or gas in the receiver is heated to about 750°C when the focused beam is incident to the receiver. The engine or turbine is, generally,

fixed to the receiver and it converts the energy stored in the fluid or gas to electrical power. Parabolic dishes present capacities in the range 0.01÷0.4MW and they allow to reach very high concentration ratios, i.e. 1000÷3000x. The annual solar to electric efficiency is higher than for parabolic troughs and it reaches 25÷30% (Müller-Steinhagen & Trieb, 2004, Janjai et al., 2011).

4.2.3 Solar towers

In solar tower plants, the incident sunrays are tracked by large mirrored collectors, called heliostats, properly located and bi-axially oriented (Sánchez & Romero, 2006, Zhang et al., 2009, Convery, 2011, Noone et al., 2012). The heliostats concentrate the energy flux on the receiver mounted on top of a tower where the energy is collected (Figure 4.6).



Figure 4.6. Solar tower, example.

Solar towers are, generally, medium/large scale plants with installed capacities up to 200MW. Typical plant solutions adopt working thermal fluids at high temperatures, i.e. 1500°C, to be used for the generation of electricity as for parabolic troughs. The average solar flux impinging on the receiver is between 200 and 1000kW per m², which facilitates a high working temperature (Kalogirou, 2004). Solar to electric efficiency is in the range of 20÷35%. Heat transfer media includes water/steam, molten salts, liquid sodium and air.

4.2.4 Linear Fresnel reflectors

A linear Fresnel reflector consists of an array of linear mirror strips, behaving as Fresnel lenses, which concentrates light to a fixed receiver mounted on a linear tower support (Figure 4.7).



Figure 4.7. Linear Fresnel reflector, example.

Such a plant design typology presents similarities to parabolic troughs in terms of plant layout and capacity. The average conversion efficiency, for power applications, is smaller than for parabolic collectors and it ranges between 8 and 10% (Müller-Steinhagen & Trieb, 2004, Ummadisingu & Soni, 2011).

4.2.5 Perspectives of solar reflection plants

A wide set of papers compare the technical and economic perspectives of the aforementioned four design typologies of concentrating plants, based on solar reflection, focusing on different geographical regions. Some references are, now, provided. An effective review of concentrating solar power in Europe, the Middle East and North Africa is in Pitz-Pall et al. (2012) presenting the maturity levels of each technology and the trends of plant cost reductions and efficiency improvements. A similar review for the Chinese area is in Wang et al. (2010). Developments of the solar reflection plant sector for the US area are in Alpert et al., (1991) and, more recently, in Taylor (2010). National studies exploring the potential of concentrating solar power through solar reflection plants are in Fluri (2009) for South Africa, Kaygusuz (2011) for Turkey, Pavlović et al. (2012) for Serbia and the Balkans, Ummadisingu & Soni (2011) for India, Al-Badi (2011) for Oman and Janjai et al. (2011) for Thailand. The authors converge to identify concentrating solar reflection as an effective technology to reach fruitfully energetic, environmental and financial benefits and they

encourage the spread of such a technology that, nowadays, is far from expressing its full potential (Kalogirou, 2004, Pitz-Pall, 2012).

Despite solar reflection, applied to large scale plants for power generation through heat or steam production, is the most frequently discussed issue, other technologies received growing attention in the recent past, e.g. solar refraction based plants, CPV plants, i.e. plants adopting PV cells for the conversion of solar radiation to electrical power, and concentrating PV/T plants for heat and power cogeneration. At the same time, the interest in small/medium scale systems grows a lot to convey to a sustainable distributed production of energy. Such aspects are now shortly discussed.

4.3 Solar refraction plants

In refraction plants the solar collector is a lens, or a set of lenses, concentrating the incident radiation on the receiver, generally, located under the lens plane.

Geometric optics widely studies lens properties and their effects on the ray trajectories (Tatum, 2006, Peatross & Ware, 2011). For concentrating purposes, converging lenses are requested. The first solar collectors integrate biconvex or plano-convex converging lenses. This is because a collimated beam of light travelling parallel to the lens axis is focused to a spot on the axis (Figure 4.8).

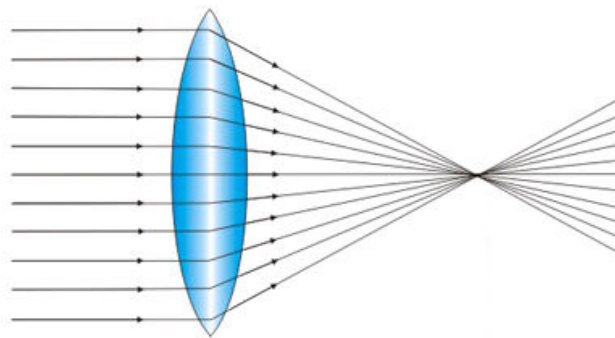


Figure 4.8. Biconvex converging lens.

Strong weaknesses of such lenses are their weight, dimensions and the high focal length. In 1748, G.L. Leclerc starts to investigate how to overcome such troubles and, in 1820, A.J. Fresnel builds the first prototype of a new lens, taking its name, for a lighthouse application. Fresnel lens is a flat optical component with the surface made of several small concentric grooves, approximating by a flat surface the curvature at that position of conventional convex lenses (Sierra & Vázquez, 2004), so that the *excess* non-refractive portions of conventional lenses are removed preserving the focusing profile (Lo & Arenberg,

2006). Figure 4.9 proposes the equivalent Fresnel of a plano-convex lens. The thickness reduction is evident.

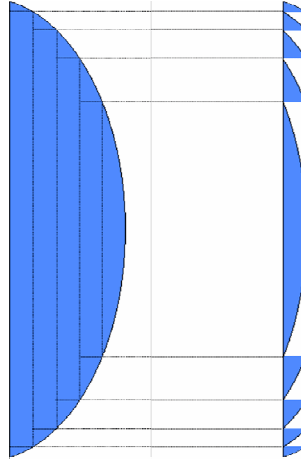


Figure 4.9. Equivalent Fresnel of a plano-convex lens.

Nowadays, Fresnel lenses represent the standard optics for collectors in all solar refraction plants. Two basic configurations of the Fresnel lenses are feasible and they define a same number of refraction plant design typologies.

- ✓ Linear Fresnel lenses;
- ✓ Circular Fresnel lenses.

The former has linear parallel grooves and it focuses the solar radiation on a line, i.e. the receiver should be linear, while the latter presents spotted circular focuses and it is used for point-focus geometry receivers. Models and strategies for lens design and optic properties optimization are proposed by the literature (Leutz et al., 1999).

Developments in concentrating solar energy applications integrating Fresnel lenses are still in progress. The adoption of such a technology to concentrate the solar radiation is more recent than for reflection through mirrors. Xie et al. (2011) fully review this sector presenting an useful classification of the major improvements in concentrating solar energy Fresnel lens systems. The large amount of contributions, both theoretical and experimental, are proposed after the '80s and they consider the so-called non imaging Fresnel lenses, i.e. lenses designed with the specific purpose of concentrating light rather than forming an image. Such a technology is recognized to be very competitive for solar collectors due to the possibility of having high concentration ratios, e.g. higher than 1000x, optical efficiencies, together with light-weight and cost effectiveness due to the adoption of low cost materials, like poly-methyl-methacrylate (PMMA), for lens manufacturing (Deambi & Chaurey, 1992). Such strengths justify the adoption of this concentrating technology for the proposed PV/T solar prototype described in the next chapter.

4.4 Concentrating photovoltaic systems

Concentrating photovoltaic systems adopt PV solar cells to directly convert solar radiation to electrical power energy, without the interaction to any thermal vector, e.g. steam, heat fluids, etc. In such systems, adopting line-focus or point-focus geometries, an array of PV cells is located on the solar receiver and it is lighted by the concentrated solar radiation. Due to the system geometric concentration ratio, the required cell surface is significantly lower than for traditional flat-plane plants because the collection area is replaced with cheaper optical devices, i.e. mirrors or lenses, (Luque & Andreev, 2007, Pérez-Higueras et al., 2011). Low concentration, i.e. 1÷40x, medium concentration, i.e. 40÷300x, and high concentration, i.e. 300÷2000x, CPV systems are studied and tested since the first researches in 1975. A review of the state of the art is in Swanson (2000) critically analyzing current activities, perspectives, strengths and open issues of such solar conversion technology. Particularly challenging opportunities offered by CPV toward flat-plane systems are the following.

- ✓ Superior conversion efficiency levels, i.e. over 20% (Gombert et al., 2010, Pérez-Higueras et al., 2011);
- ✓ Higher annual capacity factor, especially, toward fix plane plants;
- ✓ Low material availability requirements;
- ✓ Less toxic material usage;
- ✓ Ease of recycling;
- ✓ Ease of rapid manufacturing scale-up;
- ✓ High local manufacturing content;
- ✓ Possibility to compete on costs (Yamaguchi & Luque, 1999, Faiman, 2004, McConnell et al., 2005).

Two key issues to make CPV systems competitive are the adoption of efficient solar cells and the proper management of the receiver working temperature.

4.4.1 CPV solar cells

Solar cells are a key component for all PV systems. Great progresses in materials and cell layout, i.e. the position of the photosensitive surface, bonding and wires, by-pass diode, etc., are done together with an increasing miniaturization of cell size. A detailed classification of PV solar cells is in Sharma et al. (1995) and Miles et al. (2005). Figure 4.10 summarizes the major cell typologies and promising frontiers.

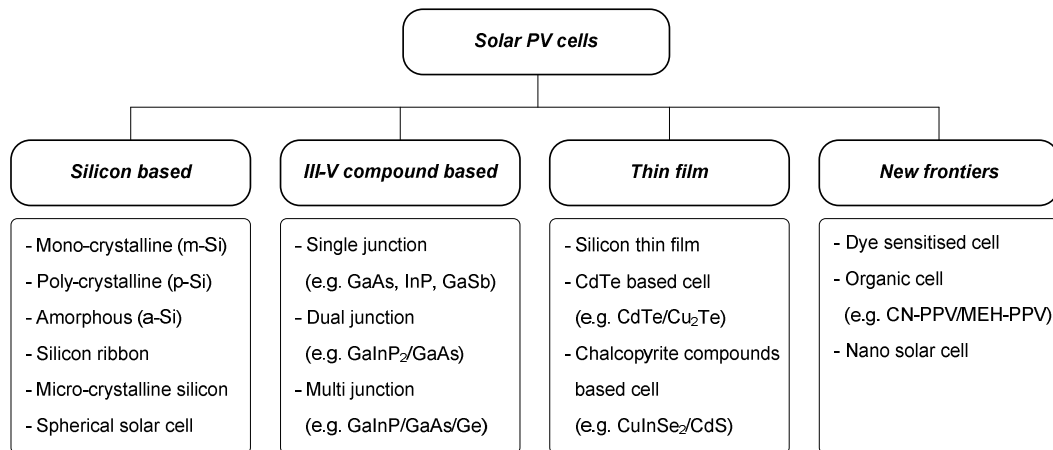


Figure 4.10. Solar PV cell classification.

In CPV systems great attention is paid to guarantee high cell conversion efficiency levels, even tolerating a cost increase for the higher quality of the adopted cells. This is due to the compensation introduced by the low requested receiver surface replaced by the optic collector concentrating the solar radiation. Such reasons explain the great interest in III-V compound based cells for CPV systems (Baur et al., 2007). Despite the cost per Wp of such PV cells is, actually, two times the cost of standard m-Si cells, current best efficiencies are significantly higher, i.e. records are close to 40% (Cotal et al., 2009). From an operative perspective, a solar cell, made of just one material, cannot capture the entire light spectrum but the sole frequency band to which the material is sensible. A multi-junction solar cell is made up of two or more layers of semi-conductor materials, enlarging its working spectrum. Consequently, the overall efficiency is higher than for a single material cell, e.g. silicon cell. From such a perspective, the ideal solar cell should include hundreds of different layers, each one tuned to a small range of light wavelengths, from ultraviolet to infrared. Difficulties in manufacturing limit the number of layers to few units. Nowadays, triple junction PV (TJ-PV) cells represent a standard for multi junction solar cells. The proposed prototype integrates InGa/GaAs/Ge TJ-PV cells.

4.4.2 Cell cooling and heat recovery

In PV systems, only a fraction of the incoming sunlight striking the cell is converted to electrical energy. The remainder of the absorbed energy is converted to thermal energy, i.e. heat, and it causes the temperature to rise unless the heat is efficiently dissipated to the environment. Considering CPV, this phenomenon is critic due to the high light flux concentrated to the small receiver area. Temperatures on the receiver surface can reach hundreds of Celsius degrees, especially in presence of high concentration ratios. As a consequence, unforced heat dissipation, by natural air recirculation, is not sufficient to

maintain reasonable cell temperatures. A receiver cooler is, generally, required. This is also to avoid the cell efficiency degradation due to its high working temperature.

Royne et al. (2005) investigate the cooling of PV cells under concentrated illumination. Their review of such issue points out two strategies for cell cooling:

- ✓ Passive cooling;
- ✓ Active cooling.

Passive cooling transfers heat without using any additional energy. Typical passive coolers are made up of linear fins located on all the available heat sink surfaces to increase the heat exchange area. Such solutions work well at low and medium concentration ratios, i.e. up to 300x, they do not require pipes and other additional circuits and they are cost effective especially for point-focus geometry concentrators. Nevertheless, passive coolers make heat recovery difficult or, even, impossible because of the absence of a cooling circuit and the heat exchange made with air (Cheknane et al., 2006).

On the contrary, active cooling is a type of heat transfer that uses powered devices, such as fans or pumps, to cool a surface, i.e. the cells. It generally requires to install and control a circuit for cooling fluid circulation. Its cost is higher than for passive coolers, the simplicity lower but the performances are, frequently, higher (see Royne et al. (2005) for a comparison between passive and active coolers). Such a cooling strategy fits well with high concentration solar plants, i.e. up to 2000x, linear-focus geometries and it allows to easily collect and to recover heat thanks to the presence of the cooling fluid (Van Kessel et al., 2009, Teo et al., 2012). The prototype described in the next chapter includes an active cooling circuit and heat recovery system using purified water as cooling fluid.

4.5 Smart-grid concept and distributed generation

In the recent years, the energy systems are undergoing a development trend characterized by privatization of the most important energy sectors that turned former monopolies into free-market competitors. Furthermore, community awareness of environmental impact caused by large conventional power plants is growing, together with a greater interest in distributed-generation technologies based upon renewable energy sources and cogeneration (Bakos, 2009). This trend conveys to the so-called smart-grid concept, defined by the Smart Grids European Technology Platform as “an electricity network that can intelligently integrate the actions of all users connected to it – generators, consumers and those that do both, in order to efficiently deliver sustainable, economic and secure electricity supply” (Gharavi & Ghafurian, 2011, Peng & Yan, 2011).

In such a context, renewable energy technologies are emerging as potentially strong competitors due to their intrinsic sustainability, pervasive source availability, delocalized production, matching the producer to the consumer, and the feasibility of small-scale plants.

Small scale plants can be both stand-alone or grid connected to supply local consumers, eventually, using the grid to manage the excesses of production or request through an integrated micro-scale PV distributed generation (Gudimetla et al., 2012).

CPV systems certainly fit with the smart-grid concept and local production especially in presence of a thermal recovery unit that, on one side, provides thermal energy to the local consumer, together with electrical power, and, on the other side, increases the system conversion efficiency, i.e. electric + thermal, making the economic return of the plant positive. Such issues and the related technical solutions are still under development (Borton, 2010). The proposed prototype follows this research path.

References

- Al-Badi, A.H., Malik, A., Gastli, A., (2011). Sustainable Energy usage in Oman – opportunities and barriers. *Renewable and Sustainable Energy Reviews* 15:3780-3788.
- Alpert, D.J., Mancini, T.R., Houser, R.M., Grossman, J.W., James, W., Schissel, P., Carasso, M., Jorgensen, G., Scheve, M., (1991). Solar concentrator development in the United States. *Solar Energy Materials* 24(1-4):307-319.
- Bakos, G.C., (2009). Distributed power generation: a case study of small scale PV power plant in Greece. *Applied Energy* 86:1757-1766.
- Baur, C., Bett, A.W., Dimroth, F., Siefert, G., Meusel, M., Bensch, W., Köstler, W., Strobl, G., (2007). Triple-Junction III-V based concentrator solar cells: perspectives and challenges. *Transactions of the ASME* 129:258-265.
- Borton, D.N., (2010). Distributed industrial scale hybrid solar concentrator photovoltaics and thermal energy. *Proceedings of the 4th International Conference on energy Sustainability – ASME* 431-433.
- Cheknane, A., Benyoucef, B., Chaker, A., (2006). Performance of concentrator solar cells with passive cooling. *Semiconductor Science and Technology* 21:144-147.
- Convery, M.R., (2011). Closed-loop control for power tower heliostats. *Proceeding of SPIE 8108, High and Low Concentrator Systems for Solar Electric Applications VI*.
- Cotal, H., Fetzer, C., Boisvert, J., Kinsey, G., King, R., Hebert, P., Yoon, H., Karam, N., (2009). III-V multijunction solar cells for concentrating photovoltaics. *Energy and Environmental Science* 2:174-192.
- Deambi, S., Chaurey, A., (1992). Fixing the sunshine through photovoltaic concentrators: an overview of recent achievements. *RERIC International Energy Journal* 14(1):1-15.
- Faiman, D., (2004). Terrestrial solar power plants – current perspectives and long term visions. *Proceedings of the 4th International Conference on Solar Power from Space*.
- Fluri, T.S., (2009). The potential of concentrating solar power in South Africa. *Energy Policy* 37:5075-5080.

Gharavi, H., Ghafurian, R., (2011). Smart grid: the electric energy system of the future. Proceedings of the IEEE, Smart grid: the electric energy system of the future 99(6):917-921.

Gombert, A., Heile, I., Wüllner, J., Gerstmaier, T., Van Riesen, S., Gerster, E., Röttger, M., Lerchenmüller, H., (2010). Recent progress in concentrator photovoltaics. Proceedings of SPIE7725, Photonics for Solar Energy Systems III.

Gudimetla, B., Katiraei, F., Romero Agüero, J., Enslin, J.H.R., Alatrash, H., (2012). Integration of micro-scale photovoltaic distributed generation on power distribution systems: dynamic analyses. Proceedings of the IEEE Power Engineering Society Transmission and Distribution Conference.

Hang, Q., Jun, Z., Xiao, Y., Junkui, C., (2008). Prospect of concentrating solar power in China – the sustainable future. Renewable and Sustainable Energy Reviews 12:2505-2514.

Janjai, S., Laksanaboonsong, J., Seesaard, T., (2011). Potential application of concentrating solar power systems for the generation of electricity in Thailand. Applied Energy 88:4960-4967.

Jayarama Reddy, P., (2012). Solar power generation – technology, new concepts & policy. CRC Press - Taylor & Francis Group ed. London, UK.

Kalagirou, S.A., (2004). Solar thermal collectors and applications. Progress in Energy and Combustion Science 30:231-295.

Kaygusuz, K., (2011). Prospect of concentrating solar power in Turkey: the sustainable future. Renewable and Sustainable Energy Reviews 15:808-814.

Leutz, R., Suzuki, A., Akisawa, A., Kashiwagi, T., (1999). Design of a nonimaging Fresnel lens for solar concentrators. Solar Energy 65(6):379-387.

Lo, A., Arenberg, J., (2006). New architecture for space telescopes uses Fresnel lenses. SPIE newsroom – The international Society for Optical Engineering 10.1117/2.1200608.0333.

Luque, A., Andreev, V., (2007). Concentrator photovoltaics. Springer ed. Berlin, Germany.

Machinda, G.T., Chowdhury, S., Arscott, R., Chowdhury, S.P., Kibaara, S., (2011). Concentrating solar thermal power technologies: a review. Proceedings of 2011 Annual IEEE India Conference: Engineering Sustainable Solutions – INDICON – 2011.

McConnell, R., Kurtz, S., Symko-Davies, M., (2005). Concentrator photovoltaic technologies. *Refocus* 6(4):35-39.

Miles, R.W., Hynes, K.M., Forbes, I., (2005). Photovoltaic solar cells: an overview of state-of-the-art cell development and environmental issues. *Progress in Crystal Growth and Characterization of Materials* 51:1-42.

Müller-Steinhagen, H., Trieb, F., (2004). Concentrating solar power – a review of the technology. *Ingenia* 18.

Noone, C.J., Torrilhon, M., Mitsos, A., (2012). Heliostat field optimization: a new computationally efficient model and biomimetic layout. *Solar Energy* 86:792-803.

Pavlović, T.M., Radonjić, I.S., Milosavljević, D.D., Pantić, L.S., (2012). A review of concentrating solar power plants in the world and their potential use in Serbia. *Renewable and Sustainable Energy Reviews* 16:3891-3902.

Peng, L., Ya, G.S., (2011). Clean energy grid-connected technology based on smart grid. *Energy Procedia* 12:213-218.

Pérez-Higueras, P., Muñoz, E., Almonacid, G., Vidal, P.G., (2011). High concentrator photovoltaics efficiencies: present status and forecast. *Renewable and Sustainable Energy Reviews* 15:1810-1815.

Pitz-Paal, R., Amin, A., Bettzuge, M.O., Eames, P., Flamant, G., Fabrizi, F., Holmes, J., Kribus, A., Van der Laan, H., Lopez, C., Novo, F.G., Papagiannakopoulos, P., Pihl, E., Smith, P., Wagner, H.J., (2012). Concentrating solar power in Europe, the Middle East and North Africa: a review of development issues and potential to 2050. *Journal of Solar Energy Engineering* 134:0245011-0245015.

Rabl, A., (1976). Comparison of solar concentrators. *Solar Energy* 18:93-111.

Richter, C., (2009). Solar power and chemical energy systems. *SolaPaces Annual Report 2009*. International Energy Agency (IEA).

Royne, A., Dey, C.J., Mills, D.R., (2005). Cooling of photovoltaic cells under concentrated illumination: a critical review. *Solar Energy Materials and Solar Cells* 86:451-483.

Sánchez, M., Romero, M., (2006). Methodology for generation of heliostat field layout in central receiver systems based on yearly normalized energy surfaces. *Solar Energy* 80:861-874.

Sharma, V.K., Colangelo, A., Spagna, G., (1995). Outlook for high efficiency solar cells to be used with and without concentration. *Energy Conversion and Management* 36(4):239-255.

Sierra, C., Vázquez A.J., (2005). High solar Energy concentration with a Fresnel lens. *Journal of Materials Science* 40:1339-1343.

Swanson, R.M., (2000). The promise of concentrators. *Progress in Photovoltaics: Research and Applications*. 8:93-111.

Taylor, R.W., Davenport, R.L., (2010). Concentrating solar power opportunities. *Proceedings of the World Energy Engineering Congress 1947-1987*.

Teo, H.G., Lee, P.S., Hawlader, M.N.A., (2012). An active cooling system for photovoltaic modules. *Applied Energy* 90:309-315.

Ummadisingu, A., Soni, M.S., (2011). Concentrating solar power – technology, potential and policy in India. *Renewable and Sustainable Energy Reviews* 15:5169-5175.

Van Kessel, T., Abduljabar, A., Khonkar, H., Moumen, N., Sandstrom, R., Al-Saedi, Y., Martin, Y., Guha, S., (2009). Concentrator photovoltaic reliability testing at extreme concentrations up to 2000 suns. *Proceedings of the 34th IEEE Photovoltaic Specialists Conference – PVSC 001020-001023*.

Wang, Z., Li, X., Yao, Z., Zhang, M., (2010). Concentrating solar power development in China. *Journal of Solar Energy Engineering* 132:0212031-0212038.

Xie, W.T., Dai, R.Z., Wang, R.Z., Sumathy, K., (2011). Concentrated solar energy applications using Fresnel lenses: a review. *Renewable and Sustainable Energy Reviews* 15:2588-2606.

Yamaguchi, M., Luque, A., (1999). High efficiency and high concentration in photovoltaics. *IEEE Transactions on Electron Devices* 46(10):2139-2143.

Zhang, H., Wang, Z., Guo, M., Liang, W., (2009). Cosine efficiency distribution of heliostats field of solar thermal power tower plants. *Proceedings of the 2009 Asia-Pacific Power and Energy Engineering Conference – APPEEC*.

Web – references

Peatross, J., Ware, M., (2011). Physics of light and optics. Available on line:

http://optics.byu.edu/BYUOpticsBook_2011c.pdf

Tatum, J.B., (2006). Geometric optics. Available on line:

<http://orca.phys.uvic.ca/~tatum/goptics/goptics.zip>

5. *Concentrating PV/T prototype*

Bi-axial Fresnel solar cogenerator for the distributed production of power and heat

This chapter aim is to introduce the concentrating PV/T prototype designed and developed for the distributed production of electrical power and thermal energy. The plant operates through solar refraction concentrating principle and it presents a point-focus geometry. The maximum geometric concentration ratio is close to 800x. Furthermore, TJ-PV solar cells, designed for medium/high concentration ratios and with an average nominal efficiency of about 30%, are integrated to the receiver for power conversion, while eight non-imaging Fresnel lenses compose the solar collector. Finally, an active cell cooling module allows thermal recovery, i.e. hot water.

The description of the prototype follows a “*general to detail*” approach and a functional perspective. At first, the plant is presented as a whole proposing its general features and the global structure. The seven functional modules are, then, investigated highlighting their role to make the plant working effectively and the choices made for their design and development.

This chapter focuses on the hardware components, i.e. the mechanical, hydraulic and electrical devices, and their integration to the plant postponing the description of the logic of control and monitoring to the following Chapter 6.

In the context of the present Ph.D. dissertation, the developed prototype is studied both itself and it is used to test the further described tracking strategies.

5.1 Purposes and prototype overview

The chapter 4 stresses the growing attention to the distributed generation of energy from renewable sources highlighting the potential of CPV systems in such a field. At the same time, the interest in small scale plant solutions, integrating electrical power generation and thermal energy recovery, increases due to their promising technical, economical and environmental sustainability. The goal is to develop a wide set of atomic local self-producer units in parallel to (and, progressively, in place of) the few big centralized traditional power plants.

In such a context, the proposed PV/T prototype is designed and developed for research purposes and, particularly, to apply the CPV technology to a small plant, including, and managing, a heat recovery unit. Relevant issues to investigate deal with the accuracy in Sun collimation, the electric and thermal conversion efficiencies varying the environmental and operative conditions. In the context of the present dissertation, the comparison among different tracking strategies is, also, of interest.

Before plant description it is just the case to point out the prototypal and experimental connotation of the research project and the developed plant. Improvements, changes and further tests are still required even if a final plant layout solution is already obtained and assembled.

The experimental connotation of such a research activity is confirmed by the support of the Fondazione Cassa di Risparmio di Trento e Rovereto, Italy, through a sponsorship to the *MiSTICo* Project (Micro-Sistemi e Tecnologie Innovative per la COgenerazione da energia solare) focusing on these issues and involving the Universities of Padova, Bologna and Trento together with the Bruno Kessler Foundation - Trento, Italy.

5.1.1 Prototype general features

The concentrating PV/T prototype is a stand-alone plant, designed to be installed at the ground level or on a plane roof facing the Sun during the whole day, e.g. south-oriented location. Actually, such a system is on the south-east oriented plane roof at the University of Bologna – Department of Industrial Engineering laboratories. The installing location geographical coordinates are the following:

- ✓ Latitude $\phi = 44.5136^\circ$ north;
- ✓ Longitude $L = 11.3184^\circ$ east.

The following Figure 5.1 and Figure 5.2 show, respectively, a frontal and back view of the developed prototype. The grey flat surface is the plane roof where the plant is located.



Figure 5.1. Concentrating PV/T prototype, front view.



Figure 5.2. Concentrating PV/T prototype, back view.

The overall dimensions are, approximately, of 1.6×1.7×2m (height) and the weight is of 120kg. The solar conversion system integrates a set of eight 330×330×3mm non-imaging point-focus PMMA Fresnel lenses, with a focal length of 350mm, collecting and concentrating the solar radiation. Such optic elements are fixed to a reticular frame, made of several welded aluminum squared profiles and, together, they compose the solar collector. The solar collector concentrates the incident radiation on an equivalent number of solar receivers located under the lenses. Each of them includes a high efficiency TJ-PV solar cell for electrical power conversion. Each cell is installed on a heat exchanger with the purpose of both cell cooling and thermal recovery. The bi-axial solar tracker represents another relevant module of the designed prototype. Its purpose is to guarantee the highest captation of the solar radiation during the day and it aligns the system position to the current direction of the incident Sun rays. The solar tracker consists of two mechanical actuators able to rotate both the collector and the receiver along the two HCCS solar coordinates, i.e. the azimuthal and zenithal axes of motion, so that the surface of the Fresnel lenses, i.e. the solar collector, is always orthogonal to the direction of the incident radiation. An electronic remote controller implements the algorithms for solar tracking and it includes the required monitoring interfaces. Furthermore, a variable electronic load allows the cells to work at their best conditions, i.e. the maximum power point (MPP), running a MPP tracking algorithm. Finally, a closed-loop hydraulic circuit, integrated to the prototype, allows both the cooling of the cells and the heat recovery by flowing the cooling fluid, i.e. purified water, through the heat exchangers.

Consequently, the following seven functional modules compose the designed solar concentrating prototype:

- ✓ the structural module;
- ✓ the solar collector;
- ✓ the solar receivers;
- ✓ the hydraulic cooling circuit;
- ✓ the electronic variable load;
- ✓ the Sun tracking system (STS);
- ✓ the real-time motion control and monitoring system;

Details about each of them are in the next paragraphs together with a description of the implemented design choices.

5.2 Plant structural module

The prototype structural module, whose purpose is to give stiffness to the whole structure, is made of two elements, i.e. the support base and the vertical pillar, both realized with low-cost structural steel S235. The support base presents a “H” geometry and it is made of four squared 50×50×3mm tubular profiles welded as in Figure 5.3. Furthermore, the air-exposed areas are galvanized to prevent oxidation phenomena. The base perimeter of 1.6×1.0m prevents the tip over of the plant.

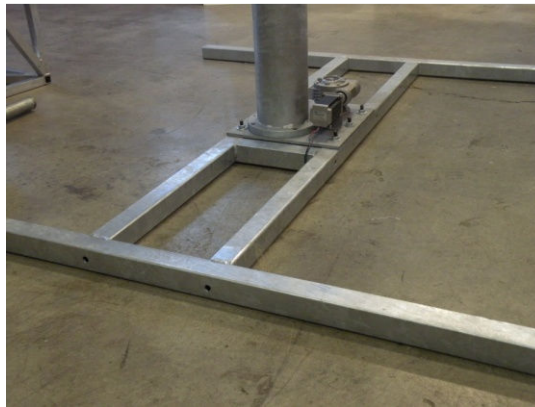


Figure 5.3. Plant structural module: the support base.

The base can directly stand on a flat surface or it allows the installation, at its four corners, of an equivalent number of wheels to facilitate the plant movement during its assembly and the following start-up.

A 320×320mm galvanized steel plate is screwed in the centre of the base and it supports the vertical pillar. Such an element is 1.4m height, with a diameter of 140mm and a thickness of 3mm. The pillar supports the reticular solar collector, integrating the Fresnel lenses and the receivers, thanks to a 1.6m horizontal shaft. Figure 5.1 clearly shows the pillar while the shaft is not immediately visible because it is located inside the solar collection modules. Figure 5.4, taken during the prototype assembly, depicts the horizontal shaft on top of the vertical pillar, together with the zenithal kinematic chain described in the following.

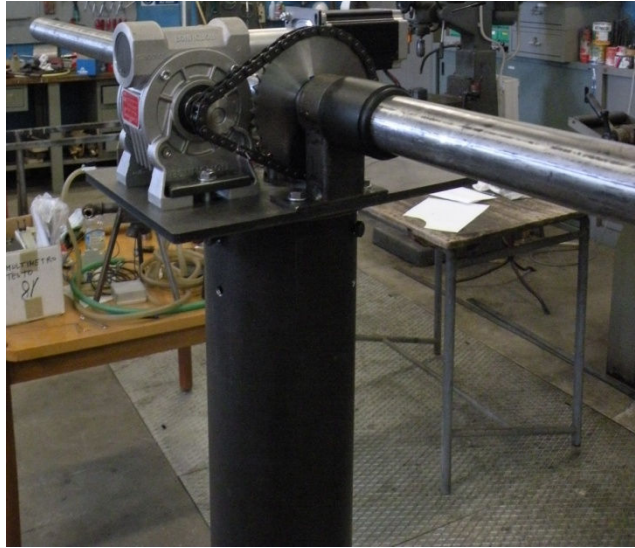
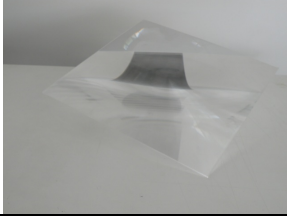


Figure 5.4. Plant structural module: the pillar and the horizontal shaft.

5.3 Solar collector

The designed solar collector detects the incident radiation on a wide surface and concentrates it to a smaller area where the receivers, including the TJ-PV cells, are located. As introduced, eight non-imaging point-focus PMMA Fresnel lenses are used and they represent the key elements of the collector. Their geometric and optic features are summarized in Table 5.1.

Table 5.1. Features of the adopted Fresnel lenses.

Dimensions	330×330mm	
Thickness	3mm	
Focal length	350mm	
Refractive index	1.491	
Groove	1mm	
Abbe number	58	

To properly support and refer the lenses two identical frames are designed, for four lenses each. Such frames are located at the two sides of the pillar and they are in-built with the horizontal shaft. The geometric constraints that need to be considered for the frames design are the lens dimensions and shape, their focal length and the shaft diameter. A picture of the developed frame is in Figure 5.5, while Figure 5.6 depicts the two frames immediately after their assembly to the prototype.

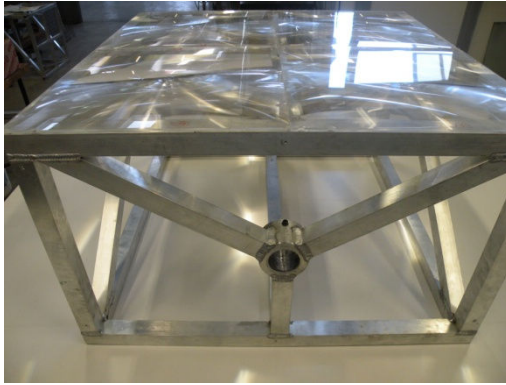


Figure 5.5. Solar collector: Al frame, detail.



Figure 5.6. Solar collector: frames integration.

The reticular frames are built with welded aluminum tubular profiles to join low weight to an acceptable stiffness. Their dimensions are of 666×666mm and the height is of 400mm. Such dimensions fit with a set of 2×2 lenses to be installed on top of each frame thanks to several screwed aluminum sheets (see Figure 5.6) and further fixed with silicone to prevent rain seepage. The lateral surface of each frame includes three profiles welded to create a “Y” configuration around a central ring. Its hole diameter is of 42mm and it fits with the previously introduced horizontal shaft for the collector support and the motion transmission. The shaft and the modules are screwed up so that they are in-built and their movement is coordinated.

Finally, to prevent the rain and the humidity to seep inside the collector from the four lateral surfaces and the bottom of each module, ten metal protection plates are screwed to the tubular profiles. Each of them fits with the lateral/bottom dimensions of the reticular frame. For such protection plates, the adoption of aluminum instead of cheaper plastic materials is required to prevent combustion phenomena in case of the concentrated Sun rays fall out of the receivers in the event of an accident. At last, the adoption of the screws to tighten up the plates to the frames allows to easily remove them if adjustments to the receivers are necessary and/or other devices located inside the collector and under the lens plane need to be manipulated.

5.4 Solar receivers

The solar receiver is the plant functional module, hit by the concentrated radiation, whose purpose is the energy conversion and heat recovery thanks to the solar cells and the cooling fluid. For such reasons the solar receivers represent the key elements of the whole prototype, i.e. the other modules are designed to maximize the solar receiver performances. The description of such a module is split into two sub-sections. The former provides fundamentals about multi-junction PV cell working principle and it introduces the features of

the cells integrated to the plant receivers the latter sub-section describes the layout and the working principle of the heat exchangers, supporting and cooling the cells.

5.4.1 Multi-junction solar cells: fundamentals

To understand the operating principle and the potential strength of multi-junction PV cells the concept of optical band gap needs to be introduced. In PV applications, the optical band gap is an energy range, proper of each material, and it determines the portion of the solar spectrum that the material can absorb. Table 5.2 lists the band gap of some of the most common semi-conductors adopted in the PV sector.

Table 5.2. Energy band gap of the most commonly adopted semi-conductors.

Semi-conductor	Energy Band Gap (eV) at 302K
Silicon (Si)	1.12
Indium Selenide (InSe)	1.3
Gallium Arsenide (GaAs)	1.4
Cadmium Telluride (CdTe)	1.47
Cadmium Selenide (CdSe)	1.7
Gallium Phosphide (GaP)	2.25
Copper Sulfide (CuS)	1.2
Cadmium Sulfide (CdS)	2.25
Germanium (Ge)	0.8
Indium Nitride (InN)	0.9
Gallium Nitride (GaN)	3.4

Considering an ideal single-junction PV cell with a proper band gap E_g and a photon incident on the cell with an energy E_λ equal to

$$E_\lambda = h \cdot \frac{c}{\lambda} \quad (5.1)$$

where:

h is the Planck constant;

c is the speed of light;

λ is the photon wavelength;

two possibility occur. If $E_\lambda < E_g$ the photon is not absorbed and it does not contribute to the PV phenomena. Otherwise, if $E_\lambda \geq E_g$ the photon is absorbed. In such latter case, a portion of energy, equal to E_g , can be converter to electrical power, while the excess is dissipated through heat. As a consequence, a single-junction PV cell is sensible to a specific range of the solar spectrum correspondent to its energy band gap. Because of the energy band gap

depends on the PV cell semi-conductor, to enlarge the sensible range several materials are adopted. Multi-junction solar cells follow such a principle and they integrate several layers of different semi-conductors. The upper layer has the highest band gap, while the lower layers are stacked in descending order of their band gaps. Figure 5.7 shows a 3D scheme of a TJ-PV cell. As explained, the top, middle and bottom sub-cells are in descending order of their energy band gap. The tunnel junctions are added to provide a low electrical resistance and optically low-loss connection between each couple of adjacent sub-cells.

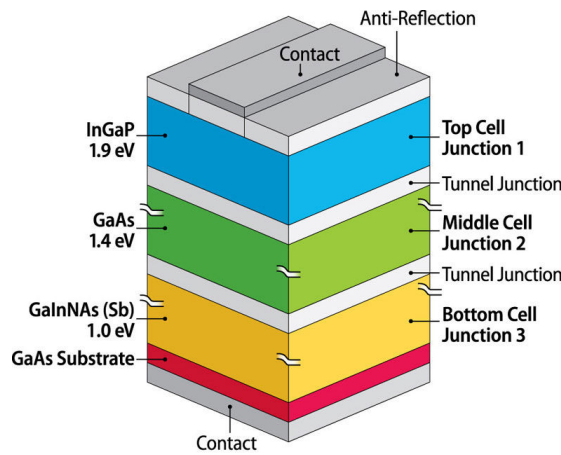


Figure 5.7. Triple-junction solar cell layout, example.

The solar receivers integrated to the prototype include a set of commercial high efficiency TJ-PV cells, specifically designed for concentration plants. The three junctions are made of Indium-Gallium-Phosphide (InGaP), Indium-Gallium-Arsenide (InGaAs) and Germanium (Ge), while the cell layout and electrical features, together with the spectral response, highlighting the sensible wavelengths for each junction, are in the following figures and table.

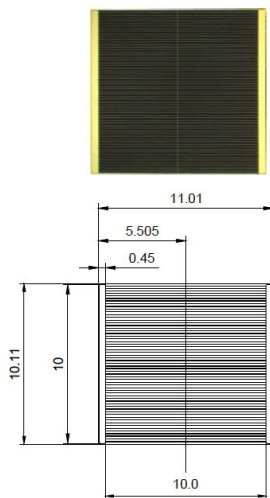


Figure 5.8. PV cell layout.

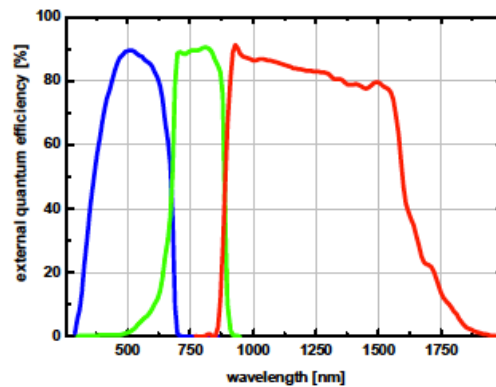


Figure 5.9. PV cell spectral response.

Table 5.3. PV cell electrical features.

Sun concentration	I_{SC} [A]	V_{OC} [V]	I_{MP} [A]	V_{MP} [V]	FF [%]	η [%]
200x	2.740	3.054	2.674	2.687	85.9	35.9
300x	4.114	3.089	4.010	2.702	85.3	36.1
500x	6.838	3.120	6.610	2.710	84.0	35.8
700x	9.533	3.151	9.236	2.681	82.4	35.4
1000x	13.693	3.185	13.301	2.601	79.3	34.6

* measurement conditions: 1.5AM, 1000W/m², 25°C.

(Legend: I_{SC} = short circuit current, V_{OC} = open circuit voltage, I_{MP} & V_{MP} = maximum power point current and voltage, FF = fill factor, η = efficiency)

5.4.2 Receiver layout

As introduced, the receivers are located under the solar collector plane, close to the lens focus points. Each of them integrates the TJ-PV cells (a single cell or a set of four units) fixed on a heat exchanger for cooling and heat recovery. A picture of the receiver (before cell installation) is in Figure 5.10, while the 3D scheme in Figure 5.11 highlights its shape and the cooling fluid inlet and outlets. Overall dimensions of such a units are of 80x80x20(height)mm and they are made of aluminum.

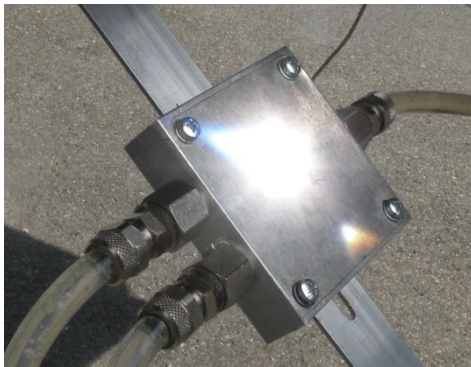


Figure 5.10. Solar receiver, heat exchanger.

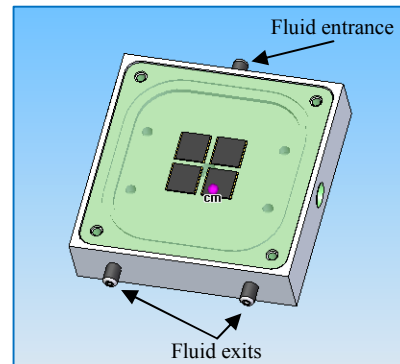


Figure 5.11. Heat exchanger, fluid inlet and outlets.

Particularly, the cold fluid enters the exchangers from a single inlet and flows directly under the PV cell area filling an empty zone milled between the exchanger base and the plate on which the cells are located. Four lateral outlets allow the hot fluid to exit and convey it to the two lateral holes called “fluid exits” in Figure 5.11. Finally, to ease the positioning of the receivers in correspondence of the lens focus points a set of two screws are used and a same number of holes are milled on the bar fixed on the bottom of the reticular frames. The effective positioning of the receivers on the lens focus points can be done manually.

5.5 Hydraulic cooling circuit

The hydraulic circuit, represented in the next Figure 5.12, both cools the TJ-PV cells and it recovers the thermal energy. The circuit deals with two closed loops integrating four heat exchangers each. The cold fluid, thanks to a magnetic driver gear pump, flows through the exchangers, cooling the cells. The flow rate is remotely controlled in the range 500..5000rpm of the gear pump. The hot fluid reaches a brazed fourteen plates heat exchanger for surface heat exchange with the purified water flowing in the second loop and directly feeding the users thanks to a circulation gear pump. In Figure 5.12, for the sake of simplicity, the users are exemplified through a tank. Inlet and outlet temperatures for each exchanger are measured through a set of Pt-100 temperature sensors, while the flow rate is measured through a low volume rotating vane flow meter. Finally, the hydraulic circuit integrates a two liters expansion vessel, two deaerators and a safety valve calibrated to prevent the pressure to grow above 1.5bar.

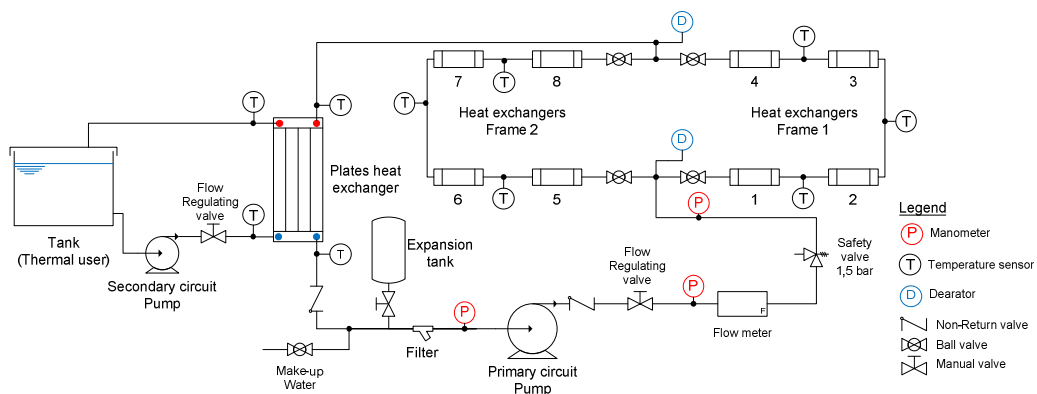


Figure. 5.12. Hydraulic cooling circuit scheme.

In the prototype final layout, except for the heat exchangers located in correspondence of the cell focus points, all the hydraulic devices are placed close to the base of the pillar inside a protection box, as shown in Figure 5.1 and Figure 5.2. The next Figure 5.13 represents a detail of the several components included inside the aforementioned protection box. In addition to the hydraulic devices, the temperature and pressure sensors and the electrical box for signal acquirement and command setting are shown. The overall dimensions of the protection box, including all the major hydraulic circuit components, is of 600x500x300(height)mm and it fits with the width of the support base, described in Section 5.2.

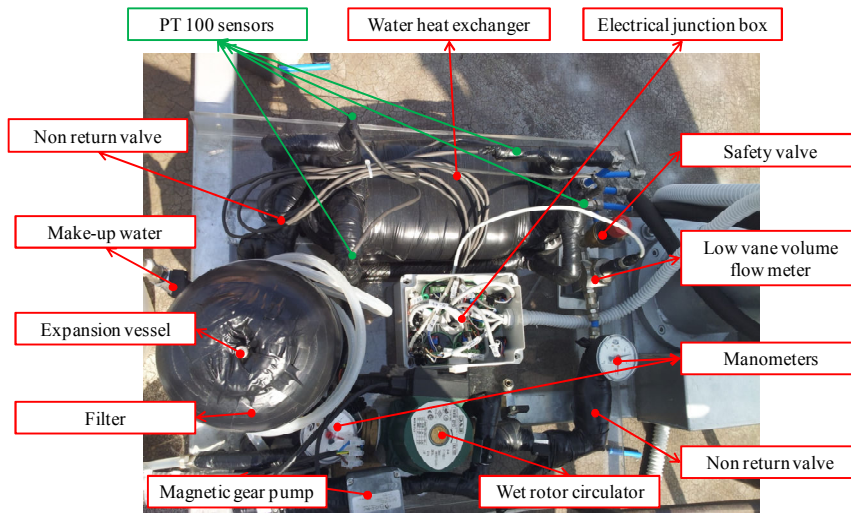


Figure. 5.13. Hydraulic cooling circuit, key elements inside the protection box.

5.6 Electronic variable load

Table 5.3 highlights that the TJ-PV cell working conditions, i.e. the voltage, current, solar irradiation level, cell surface temperature, affect its performances. Among those parameters, some of them are not directly controllable, e.g. the solar irradiation level, while others are, only, partially controllable, e.g. the cell temperature. On the contrary, the electrical parameters can be actively controlled to make the cell working at the maximum power point (MPP), i.e. the couple of values of the current and the voltage maximizing the extracted electrical power. The so called I-V, i.e. current-voltage, and P-V, i.e. power-voltage, curves, typical of each solar cell, clarify such a concept. An illustrative example, not directly referred to the described prototype, is in Figure 5.14.

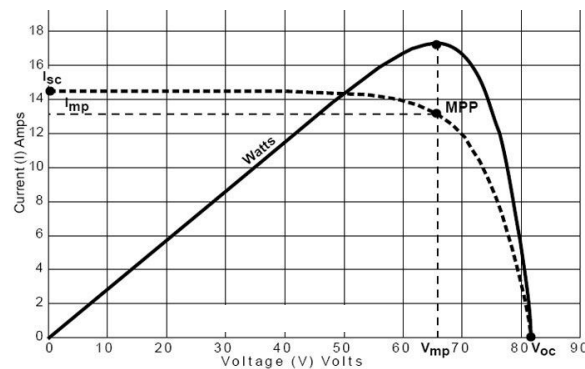


Figure. 5.14. I-V and P-V curves, example.

The MPP is the maximum of the P-V curve, while the couple of values (V_{MP}, I_{MP}) represents the correspondent point on the I-V curve and it identifies the best working conditions maximizing the extracted electrical power. As expected, the MPP varies

continuously during day-time due to the fluctuations of the aforementioned non totally controllable parameters.

The goal of the electronic variable load module is to control the current and the voltage so that the operative working conditions are always close to the MPP. Such a module is composed by a variable load device, manually and/or electronically controllable, and a MPP tracking strategy, i.e. an algorithm to measure and control the current and the voltage variables to maximize the extracted power.

Actually, the developed prototype does not integrate a custom variable load module even if its design and assembly is almost concluded. The preliminary tests to study the cell performances, when they are integrated to the plant, are executed adopting the commercial device represented in Figure 5.15 together with its admissible ranges of control and tolerances.



	Range	Tolerance
Voltage	0..160V	0.1%
Current	0..60A	0.2%
Power	0..400W	0.2%

Figure 5.15. Electronic variable load for MPP tracking.

The adopted device allows a manual control of the electric parameters, through the visible knobs and screen, or can be connected to a remote controller, through the serial unit, for the automatic acquisition and control of the electric variables running a MPP tracking algorithm. Details about the adopted MPP strategy are in the next Chapter 6, together with the description of the prototype control and monitoring platform.

5.7 Sun tracking system

In concentrating solar plants the direct radiation is the only available for the PV conversion process. Consequently, to maximize the solar radiation captation, the accurate collimation between the prototype orientation and the Sun ray direction is required. Due to the apparent motion of the Sun toward the Earth, the solar collector position needs to be continuously checked and changed so that the lens plane is always, approximately, orthogonal to the ray direction.

Single and dual axes tracking systems are, commonly, feasible depending on the number of the controlled axes of motion. Particularly, single axis trackers generally follow the daily East-West Sun trajectory and neglect the Sun rise above the horizon. Dual axes trackers provide a bi-axial motion control along both the two Sun trajectories. In concentrating solar plants, due to the aforementioned possibility to convert the sole direct component of the solar radiation, a bi-axial motion control is generally strongly required. The developed prototype follows such a guide-line.

From the hardware perspective, two independent kinematic mechanisms are developed for the two selected motion axes, i.e. the zenithal and azimuthal axes of motion. Both mechanisms adopt a stepper motor as their actuator. The motors are identical for the two motion axes and they present an holding torque of 3Nm, a phase current of 4.2A DC and an angular step resolution of 1.8 degrees. The last parameter is crucial to guarantee a high accuracy in Sun collimation.

For both motion axes, the actuators are coupled with a gear reducer (gear ratio equal to 100) and, then, with a chain drive motion transmission system (gear ratio equal to 4). As a consequence, the global angular resolution is close to 10^{-3} degrees per step.

The tracking mechanisms are installed in two different positions of the prototype. For the zenithal axis of motion the tracker is on a plate on top of the pillar and it is directly coupled with the horizontal shaft that supports the reticular frames containing the lenses and the receivers. On the contrary, the azimuthal tracker is close to the bottom of the vertical pillar and the transmission of motion is made thanks to a vertical shaft coaxial to the pillar and placed inside it. The next Figure 5.16 and Figure 5.17 show two pictures of the described motion mechanisms, while the vertical shaft for the Azimuthal motion transmission, not directly visible, is in the 3D scheme of Figure 5.18.

Finally, to protect each tracking mechanism from the rain and other atmospheric agents two aluminium capsules are integrated (see Figure 5.1).



Figure 5.16. Zenithal tracking mechanism.

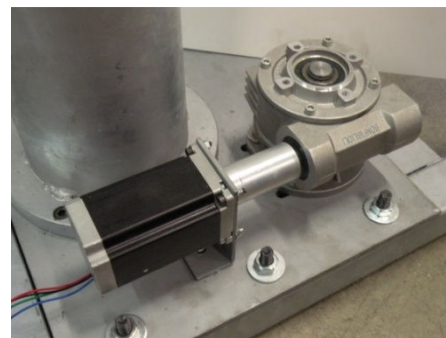


Figure 5.17. Azimuthal tracking mechanism.

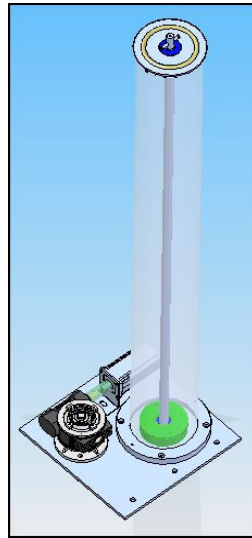


Figure 5.18. Vertical shaft, inside the pillar, for Azimuthal motion transmission.

The developed STS integrates not only the described actuators for motion transmission but, also, a further device, called *solar collimator* in the following, to directly sense the solar irradiation level and drive the algorithms for solar tracking. Figure 5.19 shows a picture of the solar collimator after its integration to the solar collector.

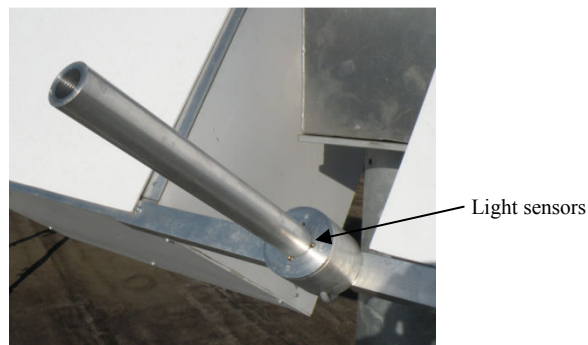


Figure 5.19. Solar collimator integrated to the solar collector.

Such a device is made of two elements: the circular base, integrating four light sensors, and a central 250mm long stem. The collimator is installed so that the base lies on a plane parallel to the solar collector. The operating principle is based on the shadow generated by the central stem. Particularly, if the Sun rays are orthogonal to the base no shadow is generated and the system is correctly oriented. On the contrary, if the Sun rays hit the collimator obliquely a shadow is generated and a misalignment occurs. The four sensors, installed at the corners of two orthogonal diameters of the stem, detect the presence of a shadow decreasing the transduced electrical signal, driving the prototype realignment. A picture of the adopted sensors and of the polar characteristic working curve is in Figure 5.20.

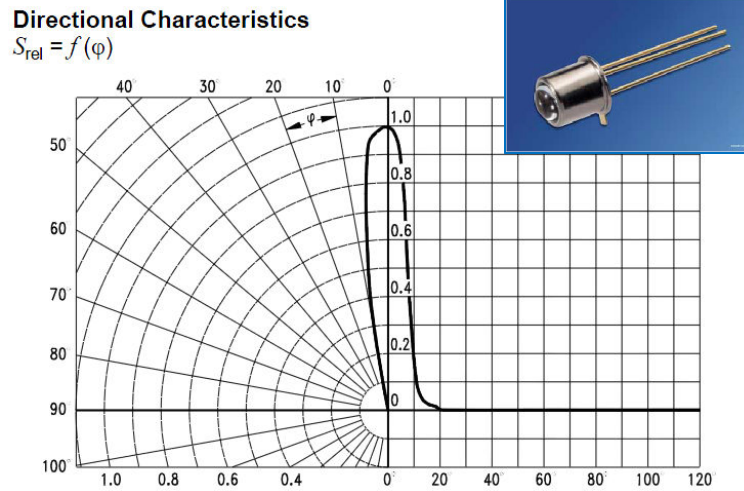


Figure 5.20. Light sensors, picture and polar characteristic curve.

The narrow polar curve of Figure 5.20 generates a relevant decrease of the transduced current signal for low values of the angular gap between the Sun ray direction and the collimator position. If such a gap, called φ in Figure 5.20, is approximately equal to 10° the transduced error decreases of about the 80% of the nominal value. A gap of 20° transduces a null signal. The choice of such sensors allows to increase the accuracy in Sun collimation: low angular misalignments are clearly detected by the control system.

Finally, from an electrical point of view the light sensors work as variable resistors. Given a constant feeding voltage, they reduce or increase the current intensity in function of the illuminance they are exposed to. The electric measurement system is represented in Figure 5.21. The voltage is of 24V and four auxiliary resistors of 1200Ω each are added in series to further reduce the current intensity so that it fits with the $\pm 20\text{mA}$ range of the analog input slot for current data acquisition.

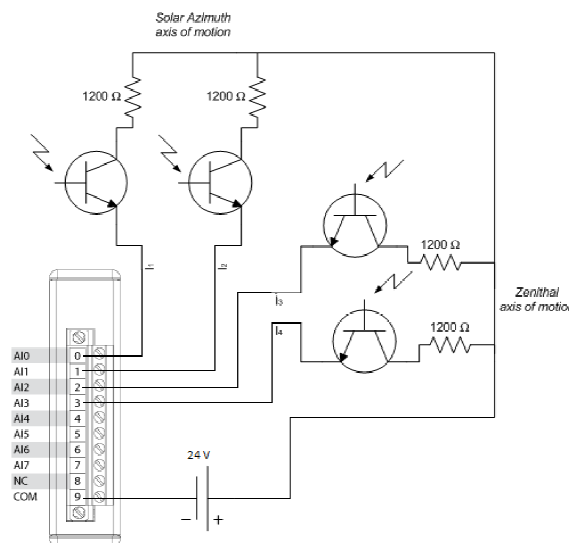


Figure 5.21. Light sensor electrical acquisition circuit.

5.8 Real-time motion control and monitoring system

The developed prototype integrates a real-time remote control and monitoring system for the bi-axial solar tracking and the cyclic measure of both the environmental conditions and the operating parameters. The control and monitoring platform is developed with LabView™ Integrated Development Environment (IDE) and, actually, it runs on a NI C-RIO real-time industrial module. The next Figure 5.22 shows a commented picture of the hardware control board for input and output signal manipulation. In the following, a systematic description is provided.

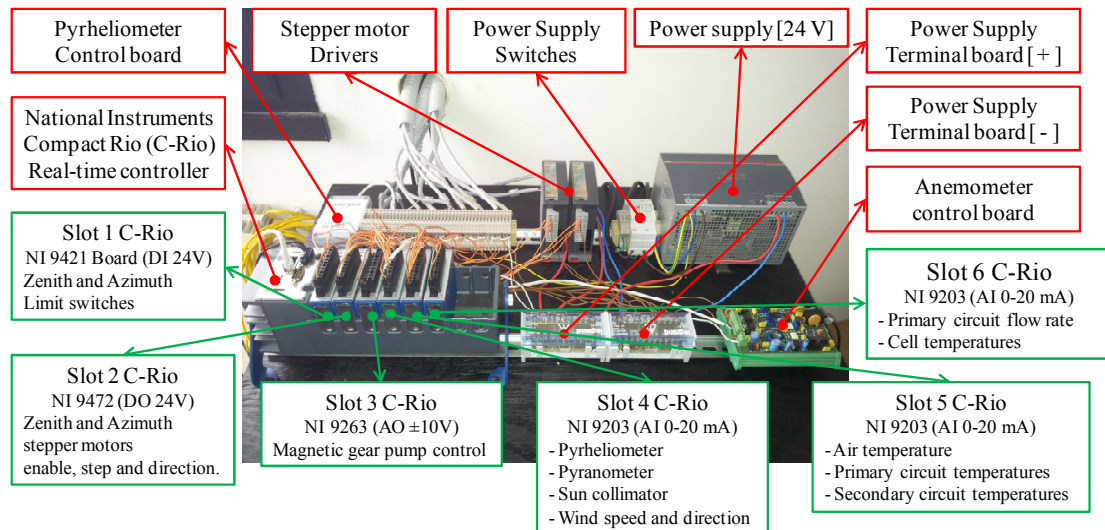


Figure 5.22. Hardware control board.

5.8.1 Power supply unit

Two levels of voltage are required for the complete system control. The grid tension of 220V AC supplies the power devices, i.e. the stepper motors, the gear pumps, the NI C-RIO real-time controller, while a 24V DC voltage supplies the control circuits to acquire and set the control signals. Despite the first voltage level is immediately available from the national grid, to obtain the low voltage level the 24V AC/DC transformer called “Power supply” in Figure 5.22 is required. The switches, installed next to the transformer, control the power supply of the whole board.

5.8.2 Motion control unit

The motion control unit feeds the stepper motors and it manages the light sensor signals for the bi-axial solar tracking, as preliminarily introduced in Section 5.7. The low voltage electrical connections for the signal manipulations are in Figure 5.23.

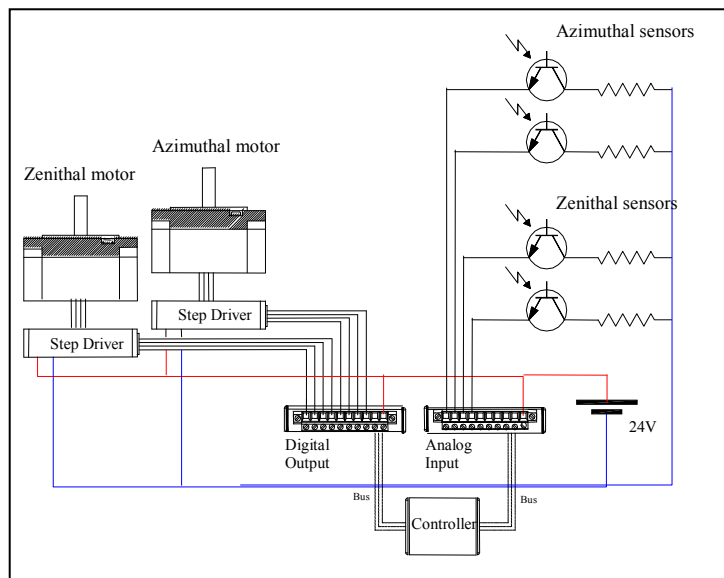


Figure 5.23. Motion control unit circuit.

Each motor is controlled by a step driver that modulates the feeding power through three low voltage digital signals set thanks to the digital output slot connected to the NI C-RIO controller, i.e. the Slot 2 of Figure 5.22. Such signals refer to:

- ✓ enable command: 1 if the motor is enabled, 0 otherwise;
- ✓ direction command: 1 for clockwise driveshaft rotation direction, 0 for counter-clockwise rotation;
- ✓ step command: 1 for single step command, 0 for no step command.

Particularly, to generate a sequence of motor steps, the enable command should be set to 1 and the step signal has to be sequentially switched from 0 to 1. Each switch generates the rotation of the motor shaft of a single step angle. Consequently, for each motion axis, the total number of generated steps is directly correlated to the angular rotation of the solar collector given a *zero* reference position. The right side of Figure 5.23 shows the connections to manage the four signals from the light sensors integrated to the solar collimator and previously described. Such connections are already introduced in Figure 5.21 together with the required analog input slot, i.e. the Slot 4 of Figure 5.22.

Finally, to prevent the solar collector to reach danger positions, generating its tip over or the damage of the electric and hydraulic circuits, two (M)ON-OFF-(M)ON limit switches are provided and their digital signal is acquired by the digital input slot connected

to the NI C-RIO and named Slot 1 in Figure 5.22. Normally, the OFF signal is transduced indicating the system is in an admissible position. If the Azimuthal and/or Zenithal current position reaches a wrong value, e.g. the zenithal angle becomes lower than 0 or higher than 90 degrees, a short shaft hits the limit switch moving it to the momentary ON, i.e. (M)ON, position. The control system detects such a danger condition and it generates the immediate stop of the regular system motion.

5.8.3 Environmental monitoring unit

The knowledge of the profiles of the most important environmental and weather parameters is a crucial data for the performance assessment. In the context of the developed prototype, the following parameters are monitored:

- ✓ the global irradiation on the horizontal surface (in W/m^2);
- ✓ the direct irradiation on a two axis tracked plane (in W/m^2);
- ✓ the air temperature (in Celsius degrees);
- ✓ the wind speed (in km/h) and direction (in degrees from the North).

The solar data are crucial for the prototype performance assessment, the air temperature is relevant for heat recovery and heat dispersion analysis and, finally, the wind speed needs to be controlled to stop the system and move it to a safety position in case of the tip over risk.

Except for the second parameter, requiring a specific device to track the Sun, the other data are measured through three commercial sensors, i.e. a pyranometer, an air temperature thermometer and an anemometer, installed on a separate weather station placed close to the prototype but far from any disturb element, such as heat sources, shadows, etc., and from the ground that, especially during the summer months, irradiates the reflected heat and light. The weather station is visible on top right of Figure 5.1, while a detail is in the next Figure 5.24.



Figure 5.24. Weather station integrating the pyranometer, the air temperature thermometer and the anemometer.

Furthermore, the pyrhelimeter to measure the direct irradiation is installed on a separate commercial tracker and located next to the prototype. A picture of both the measurement device and the tracker is in Figure 5.25. The pyrhelimeter is not directly integrated to the solar collector to prevent the measured data to be affected by the prototype solar collimation accuracy level.



Figure 5.25. Pyrhelimeter for direct solar irradiation measurement.

The operative ranges of the four environmental condition sensors, together with their output signals sent to the control platform, are in the following Table 5.4.

Table 5.4. Features of the four adopted environmental condition sensors.

Sensor	Details	Adopted operative range	Output signal range
Pyranometer	Delta Ohm - LP Pyra 03AC	0..2000W/m ²	4..20mA
	Sensitivity: 17.09mV/(kW/m ²) Impedance: 37.6Ω		
Pyrhelimeter	Kipp & Zonen - CHP1, AMPBOX	0..1600W/m ²	4..20mA
	Sensitivity: 8.03μV/(kW/m ²) Impedance: 30.3Ω		
Air thermometer	Italcoppie Pt-100, Transmitter Accuracy: ±0.12Ω at 0°C	-12..47°C	4..20mA
Anemometer	BitLine - Anemometer, Transmitter	Speed: 0..150km/h	Speed: 4..20mA
	Speed sensitivity: 1km/h Direction sensitivity: 10 degrees	Direction: 0..360degrees	Direction: 4..20mA

The output signals are the same for all the four devices to ease the integration of such sensors to the control platform. The identical ±20mA analog input Slot 4 and Slot 5 are used to acquire them.

5.8.4 Operative condition monitoring unit

The operative condition monitoring unit includes all the sensors integrated to the prototype to cyclically control its key parameters. Two major groups of data are present. The

former group refers to the electrical power conversion efficiency, the latter group refers to the thermal recovery and cell cooling.

As introduced in Section 5.6, the electrical power conversion efficiency strongly depends on the MPP tracking algorithm implemented through the electronic variable load. The voltage and the current levels of the electrical circuit, integrating the TJ-PV cells, are the key parameters affecting the extracted power, given the solar irradiance level and the concentration factor. Because of the adoption of the commercial electronic load represented in Figure 5.15, the correspondent electrical data are immediately available on its screen and, actually, they do not need further sensors and devices for the acquisition.

Considering the thermal parameters, the description of the hydraulic cooling circuit in Section 5.5 and the plant scheme in Figure 5.12 point out the required sensors for the temperature, pressure and flow rate measurement. Despite the pressure manometers are traditional manual sensors, the other devices are connected to the NI C-RIO and the control board. Particularly, ten Pt-100 temperature sensors are installed. They are similar to the air thermometer previously described. Their 4..20mA output signals are acquired through the ten channels of the current analog input Slot 5 and Slot 6. The cooling circuit flow rate is measured through a low volume rotating vane flow meter with an operative range of 0.015..0.7litres/min and a current output signal in the range 4..20mA. The aforementioned Slot 6 manages the load of such a data.

Finally, the $\pm 10V$ analog output Slot 3 is used to control the magnetic gear pump installed in the primary loop of the hydraulic circuit. The speed range is 500..5000rpm. The pump installed in the secondary loop is controllable manually.

5.9 Manufacturing cost analysis

Despite the proposed prototype is at a research stage of its life cycle and, consequently, it is far from an optimized large scale production, a realistic analysis of the rising manufacturing costs is, already, feasible. Such costs represent the initial investment in a solar energy system like the described PV/T concentrator. In particular, a functional cost analysis evaluates the impact of the major module costs on the full production cost. Direct materials and labour costs are computed separately. Table 5.5 resumes the obtained evidences, while the graph in Figure 5.26 shows the incidence of each cost driver on the full manufacturing cost.

Table 5.5. Prototype production cost analysis.

Description	Q.ty		Cost per unit	Total cost
TJ-PV cells	32	u	€ 4.50	€ 144.00
Fresnel lenses	8	u	€ 12.00	€ 96.00
<i>Sun tracking system</i>				
Gear reducer	2	u	€ 73.00	€ 146.00
Chain drive system	2	u	€ 14.00	€ 28.00
Stepper motor	2	u	€ 37.50	€ 75.00
Microstepping driver	2	u	€ 110.00	€ 220.00
				€ 469.00
<i>Support structure</i>				
Galvanized steel structure (base, pillar and shaft)	40	kg	€ 1.40	€ 56.00
Aluminum frames (collector)	8	kg	€ 4.50	€ 36.00
				€ 92.00
<i>Hydraulic circuit</i>				
Circulation pump	1	u	€ 65.00	€ 65.00
Heat exchangers	8	u	€ 1.50	€ 12.00
Plate heat exchanger	1	u	€ 148.00	€ 148.00
Deareator	1	u	€ 8.50	€ 8.50
Expansion vassel	1	u	€ 25.40	€ 25.40
Filter	1	u	€ 13.30	€ 13.30
Piping	1	-	€ 21.00	€ 21.00
				€ 293.20
Direct labor cost	10	h	€ 20.00	€ 200.00
				€ 200.00
<i>Full production cost</i>				€ 1294.20

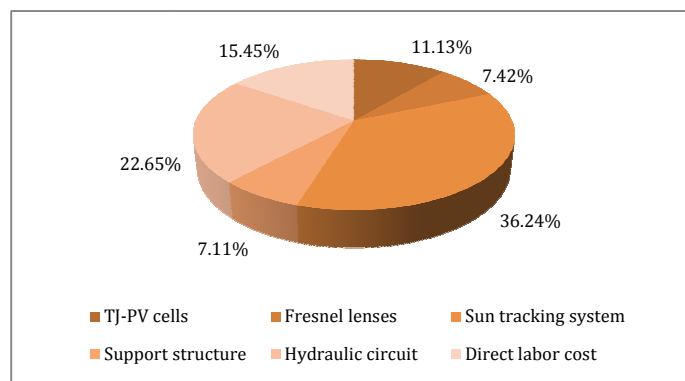


Figure 5.26. Prototype functional cost analysis.

The tracking system and the hydraulic circuit significantly impact on the system global cost. These modules allow to track the Sun and to recover thermal energy and they significantly increase the power and thermal conversion efficiencies and they represent the two key modules that mark the difference between non-concentrating and concentrating PV plants.

5.10 Preliminary field-tests

Despite a wide trial campaign to test the energy performances of the proposed prototype represents a necessary further development, a preliminary set of field-tests are, already, assessed to validate the design prototype and to propose plant improvements. All the tests take place in Bologna, Italy.

The first test focuses on the analysis of the energy conversion performances of a single TJ-PV cell when integrated to the prototype. Several daily tests are done. A significant run refers to July 23, 2012. Figure 5.27 shows the weather conditions of such a day.

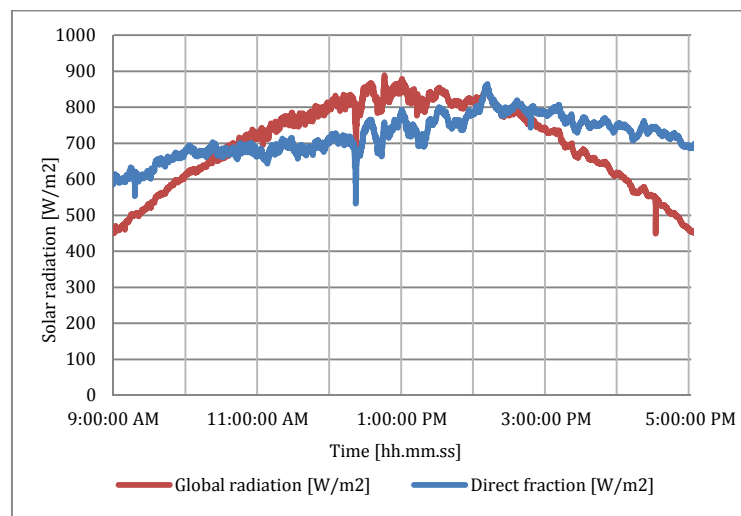


Figure 5.27. Global radiation and direct fraction profiles on July 23, 2012.

The red curve refers to the global radiation on the horizontal plane, while the blue one shows the direct fraction on an optimally oriented surface. Monitored parameters also include the air temperature and the wind speed and direction. During the test, 31.5°C and light wind are measured.

The graph in Figure 5.28 shows the experimental I-V and P-V curves for a single TJ-PV solar cell integrated to the Fresnel lens prototype. The adopted cell extracts a maximum power of 8.7W when irradiated with a 800x concentrated solar radiation. The average global radiation is of 682 W/m², while the cell conversion efficiency is equal to 15.8%.

The second field-test investigates the global electric efficiency of the plant. Eight TJ-PV cells, connected in series, are irradiated with an average concentrated solar power of 652W/m² through the eight Fresnel lenses. The available collecting surface is of 0.648m², while the experienced electrical power is of 65.1W with a correspondent electrical conversion efficiency of about 15.4%.

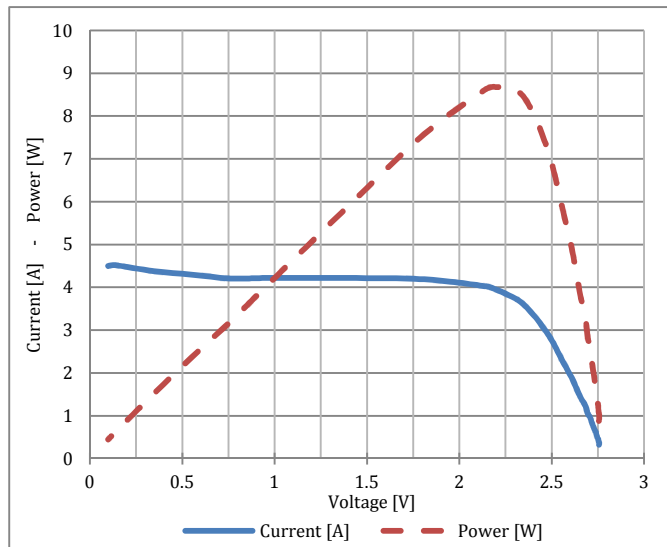


Figure 5.28. Obtained I-V and P-V curves for a single TJ-PV solar cell integrated to the prototype.

Furthermore, a set of daily field-tests, to study both the power and thermal recovery performances, are assessed. In such tests, for the sake of simplicity, only one of the two frames, used as solar collectors, is considered. Consequently, a series of four TJ-PV cells, fixed on a same number of heat exchangers, is adopted. The following Table 5.6 summarizes some of the obtained results.

Table 5.6. Combined heat and power tests.

<i>Test #1</i>			
Power generation		Thermal recovery	
Direct radiation	779 W/m ²	Flow rate	0.252 l/min
Collector area	0.3249 m ²	Inlet temperature	28.2 °C
Incident direct radiation	253.10 W	Outlet temperature	38.3 °C
Produced electrical power	30.70 W	Recovered thermal power	177.57 W
<i>Power conversion efficiency</i>	<i>12.13%</i>	<i>Thermal conversion efficiency</i>	<i>70.16%</i>
<i>Test #2</i>			
Power generation		Thermal recovery	
Direct radiation	740 W/m ²	Flow rate	0.47 l/min
Collector area	0.3249 m ²	Inlet temperature	26.0 °C
Incident direct radiation	240.43 W	Outlet temperature	32.5 °C
Produced electrical power	31.00 W	Recovered thermal power	213.14 W
<i>Power conversion efficiency</i>	<i>12.89%</i>	<i>Thermal conversion efficiency</i>	<i>88.65%</i>

The results suggest two main and independent comments. The former is about the power generation performances, the latter is about thermal recovery.

The experienced electrical conversion efficiency is, generally, lower than the expected values, i.e. the targets are in the cell datasheet. Several causes convey to such a result. Among them the most relevant is the high dispersion of the concentrated radiation around the focus point. As it appears in previous Figure 5.10, the adoption of a single

concentration optics, i.e. the aforementioned Fresnel lenses, is not adequate, by itself, to reduce the width of the concentrated light spot that, generally, is higher than the cell surface. Consequently, a relevant fraction of the concentrated solar radiation does not hit the cell surface, significantly reducing the power conversion efficiency. To overcome such a weakness a secondary optics could be of help. As example, the integration of a low cost plate glass prism, fixed immediately on the cell (Figure 5.29), leads to the enlargement of the concentrated radiation acceptance angle with a foreseeable increase of the number of rays hitting the cell and the improvement of their distribution on the cell area.

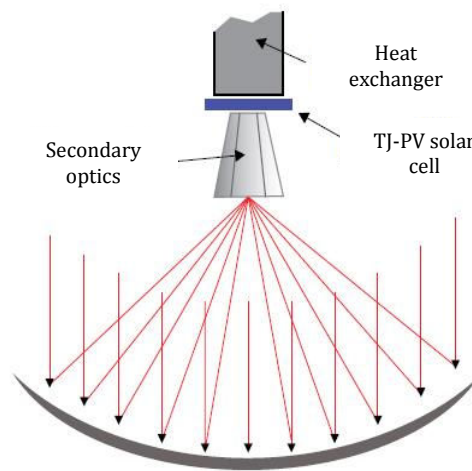


Figure 5.29. Secondary optics, plate glass prism, example.

Considering the thermal recovery performances, the field-tests highlight very good values for such a parameter, i.e. the efficiency is higher than 70%. From a realistic point of view, such performances are affected by two major phenomena. The first is the high air temperature experienced during the tests, preventing the cooling fluid heat dispersion through the pipelines. The latter is related to the aforementioned distribution of the concentrated radiation around the focus point and, particularly, to the rays falling out of the cell surface. Such a fraction of the concentrated radiation is totally available for heat recovery because it directly hits the heat exchanger surface without the cell intermediate surface. The introduction of the secondary optics and other devices/strategies to increase the power conversion efficiency, probably, generates a parallel decrease of the thermal performances. However, the global conversion efficiency trend, i.e. electrical + thermal, should increase.

The described field-tests investigate the energy performances of the proposed prototype. As introduced in the beginning of the present chapter, the described prototype is further adopted to field-test the different tracking strategies described in the next Chapter 6 together with the prototype *software* control platform.

6. *Strategies and platform for concentrating solar plant control*

Approaches for solar tracking and an integrated LabView™ control unit

The present Chapter 6 follows, logically, the previous one as it investigates possible strategies for concentrating solar plant control. Previously, an *hardware perspective* is adopted while, in this chapter, the logic of control and its integration to a *software* unit is analyzed.

Particularly, three main topics are presented. At first, the crucial solar tracking issue is explored by reviewing the literature about the existing STS to propose and test a pool of complementary approaches for motion control, e.g. forward loop and feedback control strategies. The second issue presents an integrated LabView™ control platform to manage and implement the proposed approaches and to fully control a concentrating solar plant. Details about both the user interfaces and the graphic programming modules are provided. Finally, the third issue rapidly reviews the MPP tracking algorithms to optimize the electrical power performances of the PV cells and modules and it presents, in detail, two of them together with a performance preliminary simulation.

The proposed strategies and platform are primarily designed to control the described concentrating PV/T prototype. They are customized to such a plant. Nevertheless, the operating principles and the control approaches are general and can be easily applied to other similar solar systems. Furthermore, the developed control platform allows an ease and effective run of such approaches through an integrated and common environment.

6.1 Solar tracking strategies

The relevance of tracking the Sun to increase the performances of solar concentrators is, already, stressed in the previous pages of the present Ph.D. dissertation. Such a statement is supported by a wide set of studies and papers approaching this issue from different points of view and proposing a very large number of strategies and algorithms to face the solar tracking topic. A review and classification is provided to introduce the proposed and tested set of tracking algorithms. It follows the study summarized in Bortolini et al. (2012).

6.1.1 Literature review

The issue of tracking the Sun to increase the performances of solar energy conversion systems received growing attention since 1962, when the first mechanical tracker is introduced by Finster. In these decades several models, tracking strategies and applications are proposed, tested and, recently, compared to highlight their strengths and weaknesses. Alexandru & Pozna (2008) review the main tracking strategies to optimize the energy efficiency of PV systems while, in 2009, Mousazadeh et al. (2009) present a review of principle and STS to maximize the solar system output. In particular, an effective classification of Sun trackers is possible according to the drivers, i.e. characteristics, listed and described in the following.

- ✓ **Passive vs. Active trackers.** In a passive tracker no electrical actuators are needed. The orientation of the system is realized thanks to a mechanical balance of forces based on the different behavior of specific materials, e.g. Freon, when lighted by the Sun rays. For more details, see Fairbanks & Morse (1972) and Clifford & Eastwood (2004). Active trackers represent the most diffuse technical solutions to face the Sun tracking issue. In these systems, at least a kinematic chain allows the energy plant to change its position according to the relative motion of the Sun so that an accurate collimation is guaranteed;
- ✓ **Number of controlled axes of motion.** Single and dual axes STS are developed. The former tracks the Sun following only one motion trajectory, while the latter includes a second motion axis. As introduced in Chapter 3, the HCCS represents the most diffuse and adopted solar coordinate system even if other possibilities exist (Devies, 1993);
- ✓ **Continuous vs. Step-wise realignment.** In continuous realignment STS the control loop, to check the Sun collimation and to orient the system, is continuously executed

from sunrise to sunset, i.e. the loop period is lower than one minute, while for step-wise STS a discrete and predetermined number of positions is defined and the system changes its orientation few times during the day. As example, Tang & Yu (2010) propose a three position STS including a morning, noon and afternoon orientation;

- ✓ **Control strategy.** Three main strategies can be adopted:
 - *Forward loop.* Motion control is made according to the Sun position calculated applying deterministic or stochastic models, i.e. solar equations, based on the geographic coordinates of the location and the day and time of the year. Details about such models are, already, introduced in Chapter 3;
 - *Feedback control.* A closed-loop algorithm is used to check the collimation error. Light sensors are adopted as transducers and, generally, an electric signal, function of the transduced alignment gap, controls the power signal that feeds the actuators for realignment;
 - *Hybrid strategy.* Both forward loop and feedback control strategies are adopted and properly integrated;
- ✓ **Solar plant.** The literature proposes different Sun tracking strategies and devices. Some of them are general purpose, while the others are designed to be installed to specific solar plants. According to such an issue, an useful distinction is between flat plane and concentrating solar systems.

Considering such drivers, a review of the literature is possible. Only active trackers are considered due to their large popularity if compared to the passive ones. The results of the analysis are presented in the next Table 6.1. Each reference is classified according to the characteristics described before.

The analysis highlights that the most of the solutions adopt a continuous motion algorithm integrating a feedback control strategy on both the two axes of motion. Both flat plane and concentrating solar systems are considered by the literature as plants where STS are convenient to be integrated.

A relevant outcome deals with the adoption of hybrid strategies. Only four references consider this strategy even if the positive effects obtainable by its integration are frequently discussed (Alata et al., 2005, Wu et al., 2008, Vorobiev & Vorobiev 2010). Roth et al. (2004) integrate an automatic closed loop system adopting photo-detectors with a pyrheliometer. A forward loop algorithm is activated if the level of the beam adiation is lower than a defined setpoint, due to bad weather conditions.

Table 6.1. Review and classification of active STS.

# controlled axes		Control strategy			Solar plant		Realignment		Reference
1-axis	2-axes	Forward	Feedback	Hybrid	Flat plane	Concentrator	Continuous	Step-wise	
✓	✓	✓							Alata et al. (2005)
✓		✓			✓		✓		Alexandru & Pozna (2008)
	✓					✓			Al-Jumaily & Al-Kaysi (2005)
✓			✓		✓		✓		Al-Mohamad (2004)
	✓	✓			✓		✓		Al-Naima & Al-Taee (2010)
	✓		✓		✓	✓	✓		Aracil et al. (2006)
	✓		✓			✓	✓		Bakos (2006)
	✓		✓			✓	✓		Bortolini et al. (2010)
	✓		✓				✓		Chen et al. (2002)
✓			✓		✓		✓		Chin et al. (2011)
✓	✓	✓				✓	✓		Chong & Wong (2009)
	✓	✓				✓	✓		Chong & Wong (2010)
	✓	✓					✓		Chong & Tan (2011)
	✓	✓				✓	✓		Davies (1993)
	✓		✓			✓	✓		Edwards (1978)
	✓		✓			✓	✓		Edwards (1981)
	✓	✓				✓	✓		Grena (2008)
	✓	✓					✓		Guo et al. (2011)
✓			✓		✓	✓	✓	✓	Hession & Bonwick (1984)
	✓		✓			✓	✓		Hossian et al. (2008)
✓		✓			✓			✓	Huang et al. (2011)
✓			✓			✓	✓		Kalagirou (1996)
	✓		✓		✓		✓		Kang et al. (2011)
✓			✓		✓		✓		Karimov et al. (2004)
✓			✓		✓		✓		Koyuncu & Balasub. (1991)
	✓		✓		✓		✓	✓	Li & Zhou (2011)
	✓		✓		✓		✓		Lu & Shih (2010)
✓				✓	✓		✓		Luque & Andreev (2007)
	✓		✓		✓	✓	✓		Lynch & Salameh (1990)
	✓	✓			✓		✓		Mashohor et al. (2008)
✓			✓		✓		✓		Mosher et al. (1977)
	✓	✓				✓	✓		Nuwayhid et al. (2001)
✓			✓		✓		✓		Ponniran et al. (2011)
✓			✓		✓		✓		Poulek & Libra (1998)
	✓		✓		✓		✓		Ranganathan et al. (2010)
	✓			✓	✓	✓	✓		Roth et al. (2004)
	✓			✓		✓	✓		Rubio et al. (2007)
	✓		✓		✓		✓		Rumala (1986)
✓			✓		✓		✓		Sefa et al. (2009)
	✓	✓				✓	✓		Seme & Štumberger (2011)
	✓	✓			✓		✓		Shama et al. (2011)
✓			✓			✓		✓	Tang & Wu (2010)
	✓	✓			✓	✓	✓	✓	Vorobiev & Vorobiev (2010)
✓			✓		✓		✓		Wai et al. (2006)
✓			✓		✓			✓	Wu et al. (2008)
	✓			✓		✓	✓		Xie & Guo,Tao & Guo (2010)
	✓		✓		✓		✓		Zhou & Zhu (2010)
	✓		✓		✓	✓	✓		Zogdi & Laplaze (1984)

In Rubio et al. (2007) the electrical power produced by the PV modules is used to control the bi-axial motion, while Luque & Andreev (2007) develop a six-parameter model to estimate the alignment error based both on solar equations and the signal measured by a position sensitive device (PSD). Finally, Tao & Guo (2010) consider a corrective feedback factor, based on the signal transduced by a photo-camera, to update the azimuthal and altitude angles as calculated by the appliance of solar equations.

No contribution integrates a forward loop to a feedback control strategy including, in an easy-use and low cost system, the management of the switch between the two control modes, the daily system switching on and off and the management of danger states, anomalies and bad environmental conditions, e.g. strong wind, thunderstorms, etc.

6.1.2 Proposed solar tracking strategy

The proposed solar tracking strategy aims at the daily management of a concentrating solar plant bi-axial motion. The goal is not only the run of a solar collimation algorithm to make the solar collector orthogonal to the Sun rays but, also, the semi-automatic management of the transient conditions, e.g. sunrise power up and sunset switch off, the detection of danger/critical conditions and, also, the automatic selection of the best tracking strategy among a defined pool of options. This paragraph provides the logic of control to integrate together such purposes. The description is supported by several *flow-charts* proposing the tracking strategy steps, while the most of the notations refer to those introduced in Chapter 3 in which the HCCS is presented.

6.1.2.1 Main control loop

The next Figure 6.1 introduces the *flow-chart* diagram representing the overall structure of the proposed control strategy for solar tracking.

The algorithm, iterated cyclically, firstly calculates the current solar time, t , expressed in hours, as proposed in Eq. 3.5. The value of the solar time leads to the preliminary selection of the control action, function of the specific moment of the day. In particular, the following periods are considered:

- ✓ **Stop at sunset.** At night-time the system automatically stops and it moves the plant to a defined safety position (SP), e.g. leeward, generally identified by the presence of two micro-switches, one for each motion axis;

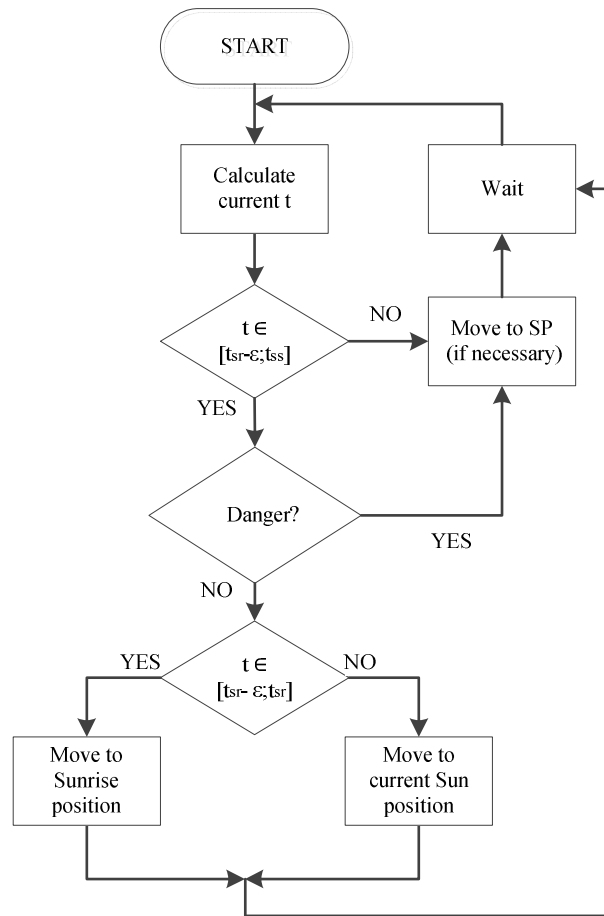


Figure 6.1. Main control loop, flow-chart.

- ✓ **Preliminary positioning before sunrise.** Few minutes before sunrise, i.e. $t \in [t_{sr} - \varepsilon, t_{sr}]$, the controller aligns the plant to the daily sunrise position, i.e. Azimuthal angle equals to Az_{sr} and altitude angle equals to zero. After that, the plant is oriented correctly to begin, without delays, the daily solar tracking;
- ✓ **Daily tracking.** During day-time, i.e. from sunrise to sunset, the controller moves the system to the current position of the Sun so that solar collimation is guaranteed. Further details about the motion control strategies are provided in the next paragraphs;
- ✓ **Danger conditions.** In presence of a danger, e.g. strong lateral wind, pouring rain, etc., the controller detects such a condition thanks to proper sensors, e.g. anemometer, and it immediately stops the normal solar tracking procedure moving the plant to the previously defined SP since the danger finishes and the normal tracking can be restarted. Generally, the system reboot is done manually after an inspection to check the presence of anomalies.

Finally, the wait block in the diagram of Figure 6.1 allows to control the frequency of execution of the whole algorithm, i.e. loop timing.

6.1.2.2 Day-time solar tracking approach

During day-time the STS have to guarantee Sun collimation by reducing the angular displacement between the ray direction and the normal vector to the solar collection area. Adopting the HCCS, such a displacement is split into two angular gaps, i.e. the Azimuthal and Altitude (or Zenithal) gaps, that need to be controlled and reduced to fit with a defined range of tolerance.

An effective and easy method to guarantee solar collimation is through the so-called *on-off controller* that allows two states for the actuators, only: activated and non activated. Consequently, the controller manages a boolean variable to feed or not to feed the actuators. In the former case, the system rotates reducing the alignment gap, while in the latter case the system maintains its position. The two axes of motion, i.e. Azimuth and solar Altitude, are independent and controlled separately (but simultaneously). Furthermore, the rotation direction, clockwise or counter clockwise, is defined considering the sign of the angular gap. Conventionally, to reduce a positive alignment gap a clockwise rotation is required and to reduce a negative alignment gap a counter clockwise rotation is required. The following time dependent diagram summarizes the *on-off controller* operating principle for a generic axis of motion and considering the two possible motion directions.

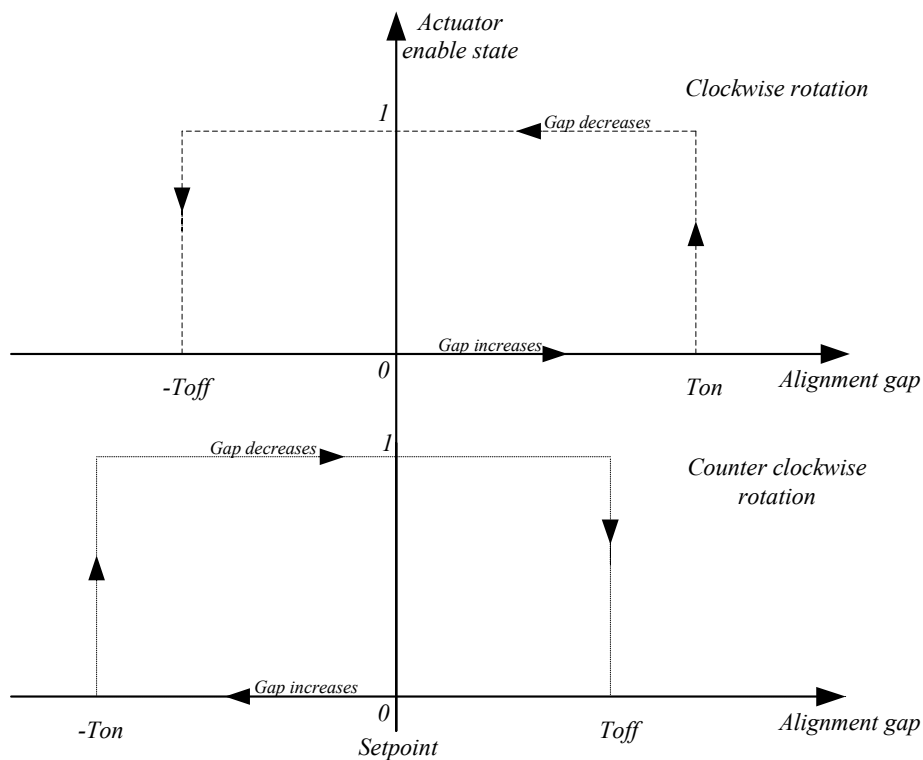


Figure 6.2. *On-off controller* operating principle.

An acceptable value for the switch on limit, T_{on} , is not lower than the actuator minimum rotation angle and not higher than 0.5 ± 1 degrees in order to orient the plant accurately. The switch off limit, T_{off} , can be set to 0, i.e. the setpoint value, or, more properly, to a lower or upper value, depending on the rotation direction, to move the plant few fractions of degree *in advance* with respect to the Sun current position. In such a way, the actuators are less stressed and the accuracy in solar collimation does not decrease significantly.

The described tracking approach fits very well with the STS and the motion control unit described in Section 5.7 and Section 5.8.2. The stepper motor digital enable and direction signals allow to manage both the state and rotation direction of the solar collector for both motion axes.

Furthermore, the *on-off controller* operating principle can be integrated to both forward loop and feedback control strategies, or even a mix of both, simply modifying the approach adopted to compute the alignment gap. In a forward loop control algorithm the gap is assessed *a priori*, while in a feedback control algorithm the gap is from the sensor transduced signals. In the following a forward loop control, a feedback control and an innovative hybrid control strategy are discussed.

6.1.2.3 Forward loop bi-axial control strategy

The proposed forward loop control strategy allows to follow Sun trajectories during day-time in accordance with the astronomic solar equations introduced in Eq. 3.7 and Eq. 3.8. Such equations allow to compute the current value of the Sun position expressed through the couple (Az, Alt) . At each iteration, the algorithm calculates the current position of the Sun and it compares the (Az, Alt) values to the current position of the energy plant. For each axis of motion, the alignment gap is defined as the difference between the Sun position and the plant position calculated counting the number of steps from a defined *zero* position and multiplying the result by the actuator angular resolution. If such a gap, in one or both of the axes of motion, is out of a given tolerance, i.e. the aforementioned limit T_{on} , the STS moves the system to the current Sun position until the T_{off} limit is reached. As usual, the alignment gap sign defines the rotation direction.

The main advantage of such a strategy of control is its independence from the specific environmental conditions. The solar equations are not affected by the specific weather conditions and they allow to control the plant motion even during variable or partially cloudy days without interferences and temporary noises. On the contrary, the accuracy in Sun collimation of such an approach cannot be as accurate as expected due to the

uncertainty of solar equations and the presence of mechanical lashes that create a further gap between the calculated and the effective plant position. To face these weaknesses, without a high increase of the STS cost, a feedback control strategy can be adopted and integrated.

6.1.2.4 Feedback bi-axial control strategy

The adopted strategy for the feedback control is based on the current signals transduced by the four light sensors integrated to a solar collimator similar to the system described in previous Section 5.7. These sensors, two for each motion axis, are located at the four vertex of two orthogonal diameters as in the scheme of Figure 6.3.

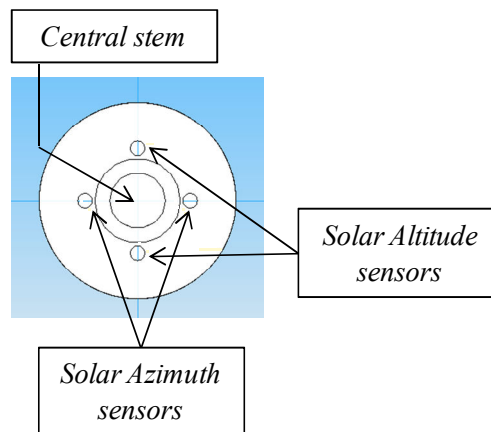


Figure 6.3. Scheme of a solar collimator, sensors for shadow detection.

If the Sun rays are not orthogonal to the solar collimator base the central stem generates a shadow that partially or totally covers one or more sensors reducing their transduced current signals. The difference between the measured current levels for each couple of sensors is directly correlated to the alignment gap on the correspondent motion axis. The higher such a value, the higher the misalignment is.

The next Figure 6.4 proposes the *flow-chart* diagram of the proposed feedback control strategy. It refers to the Azimuthal axis of motion. A similar approach is developed for the solar Altitude axis. At first, the two current signals transduced by the correspondent light sensors, called Az_1 and Az_2 in the following, are acquired and their difference E_{Az} is calculated. Such a data is directly correlated to the angular alignment gap.

The strategy enables the actuator if the absolute value of E_{Az} is higher than a defined switch on limit, i.e. T_{on} , and, at the same time, the actuator is actually off. Motion direction, clockwise or counter clockwise, is set in accordance with the sign of E_{Az} . Otherwise, if the gap

E_{AZ} is lower than the switch off limit $-T_{off}$ (or higher than T_{off} depending on the direction of motion) and, at the same time, the actuator is currently activated, it is switched off.

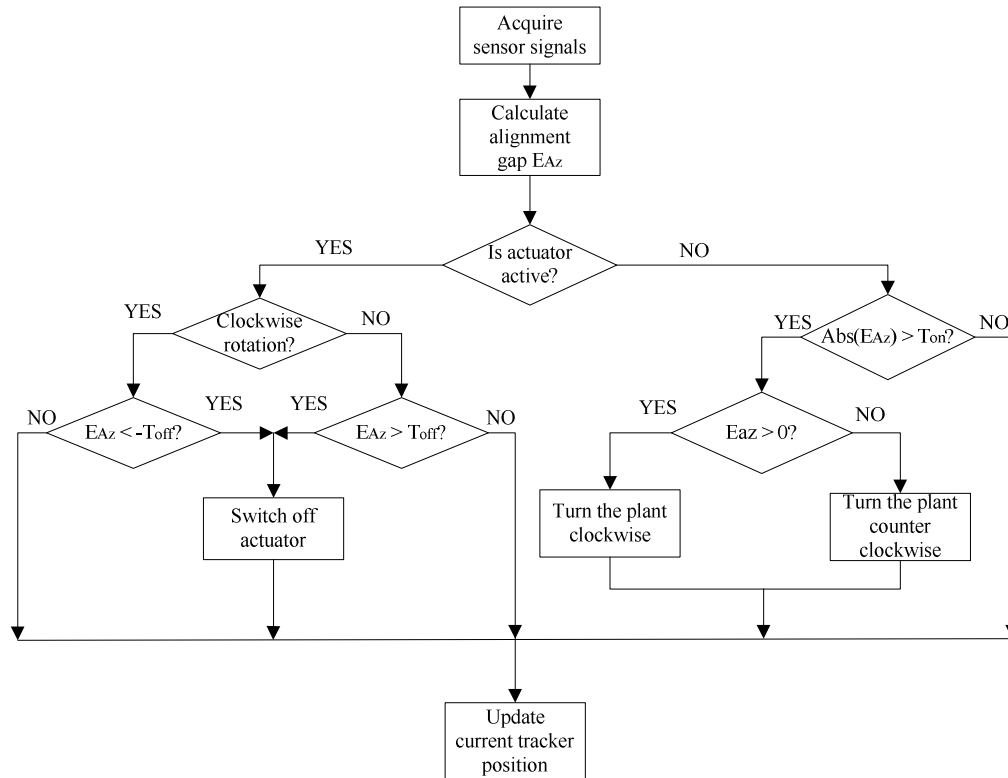


Figure 6.4. Feedback control strategy, flow-chart for the Azimuthal axis of motion.

Finally, the new plant position is calculated updating the previous value and considering the rotation angle together with the direction of motion.

The feedback control strategy is strongly depend on the environmental conditions. The presence of clouds or reflective surfaces can affect the algorithm performances. Furthermore, a high misalignment between the solar collector and the Sun rays is critic because the four transduced signals have very low intensity to drive the plant toward the Sun. On the contrary, in presence of clear sky days and for small alignment gaps the feedback strategy outperforms the other approaches and, particularly, the forward loop strategy described in the previous paragraph.

In conclusion, the proposed forward loop and feedback strategies are complementary in their strengths and weaknesses. The former is more steady but it presents a lower accuracy level without a relevant STS cost increase, the latter is less steady but it is more accurate.

The following innovative hybrid strategy tries to join the strengths of the two described approaches to increase the system tracking accuracy with any environmental condition and alignment gap between the plant and the Sun position.

6.1.2.5 Hybrid bi-axial control strategy

According to the recent literature (Xie & Guo, 2010), forward and feedback control strategies present complementary strengths and weaknesses. As a consequence, their effective integration allows to significantly increase the tracking accuracy and the energy conversion performances of solar modules and plants.

Generally, an hybrid strategy for solar tracking implements a switching procedure between forward and feedback control algorithms as a function of the environmental conditions and the current system position. Depending on these factors, the opportunity to switch from forward loop to feedback control or *vice-versa* is considered. The next Figure 6.5 proposes the *flow-chart* diagram of the proposed switching procedure. The algorithm is based on the four signals transduced by the same sensors adopted for the feedback control strategy and described in the previous paragraphs. Basically, if at least one of the four devices is directly illuminated, i.e. the correspondent transduced electrical signal is higher than a defined setpoint, the feedback control module is activated and the associate algorithm is executed. Otherwise, the forward loop module is used to track the Sun.

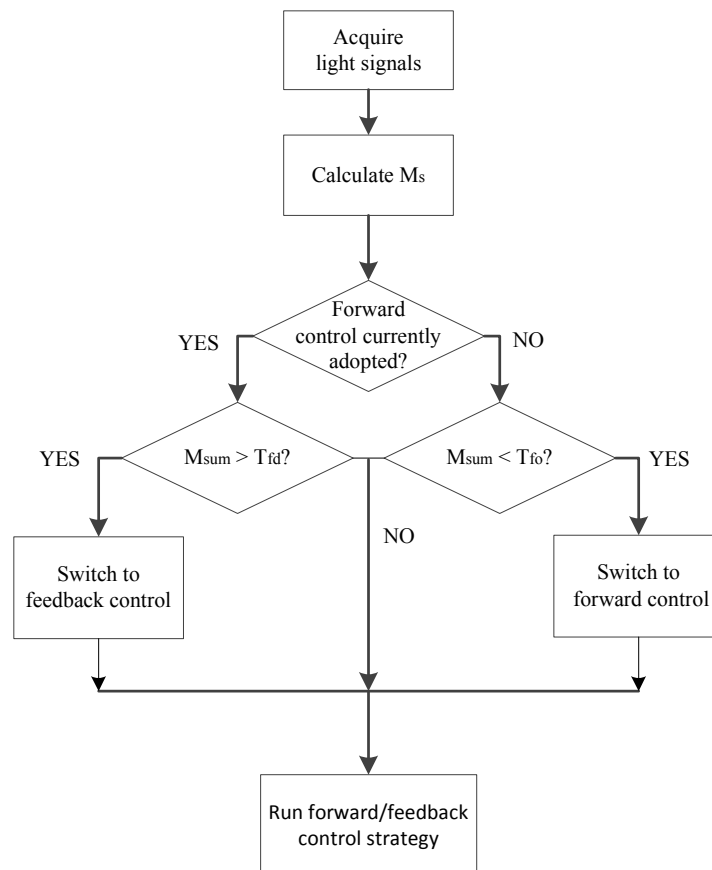


Figure 6.5. Hybrid control strategy, flow-chart of the switching procedure.

The decisional parameter adopted to evaluate the opportunity to switch between the two control modules is defined as follows:

$$M_s = \max\{Az_1 + Az_2, Alt_1 + Alt_2\} \quad (6.1)$$

where Az_1, Az_2, Alt_1, Alt_2 indicate the transduced signals for both azimuthal and zenithal axes of motion.

The feedback control module is run to align the system to the current Sun position if M_s is higher than a defined setpoint, called T_{fd} . Otherwise, if M_s is lower than the setpoint T_{fo} and the feedback control module is run, the switch to the forward loop module occurs. The values of the setpoint T_{fd} and T_{fo} need to be defined according to the output signal range of the adopted light sensors and must prevent an oscillatory behaviour of the system, i.e. the cyclical switch between the two control modules. Finally, when the control strategy is selected the correspondent algorithm is run in accordance with the procedures described in the previous paragraphs.

The introduced strategy defines three regions on the (t, M_s) plane according to the next Figure 6.6.

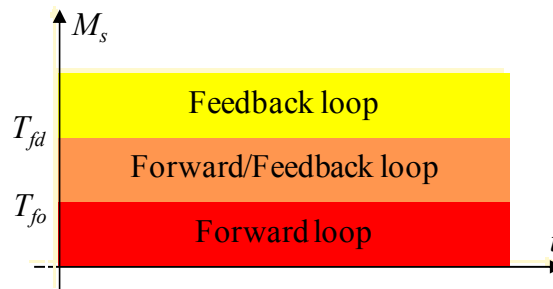


Figure 6.6. Best tracking strategy as a function of M_s .

In the intermediate region, i.e. $T_{fo} < M_s < T_{fd}$, the current tracking strategy is still run until the lower or upper limit is reached. Such a region avoids the continuous switch between the forward loop and feedback strategies.

The described strategies for bi-axial solar tracking are implemented in a LabView™ control platform to be easily interfaced to the real-time motion control and monitoring system described in Section 5.8. Details about the developed *software* are, now, provided. Such a platform is adopted to fully control the previously described concentrating PV/T prototype and, particularly, to test the accuracy of the proposed tracking strategies.

6.2 LabView™ platform for PV/T prototype control

The developed platform for the PV/T prototype control provides the required *software* algorithms and interfaces to run the proposed tracking strategies, to control the prototype functional devices, e.g. the hydraulic cooling circuit, and to monitor both the environmental and operative conditions.

Details about the *hardware* platform, integrating the NI-CRIO controller are, already, provided before. The *software* interfaces, developed with LabView™ graphical programming language, are now described from a *final user* perspective and neglecting, for the sake of brevity, the most of the details and technicalities about the coding of the wide set of instructions. The description follows a functional structure introducing the six functional panels integrated to the platform. Particularly, the following units are commented in the next paragraphs:

- ✓ the command & control panel;
- ✓ the geo-coordinates & time panel;
- ✓ the alarm panel;
- ✓ the sensors & setpoint panel;
- ✓ the environmental condition panel;
- ✓ the cooling circuit panel.

6.2.1 Command & control panel

The command & control panel depicted in Figure 6.7 allows the final users to select the tracking strategy, to manage the most of the actuators and, particularly, the stepper motors and the hydraulic pump. Furthermore, the sampling frequencies for all the installed sensors can be set. Particularly, from the top left and moving clockwise, the panel provides:

- ✓ the *mode* selector to set and check the tracking strategy to adopt. Five options are possible:
 - manual: the user directly decides the opportunity to change the plant position together with the rotation direction. Such an option is very useful during the plant assembly, test and preliminary run;
 - closed loop: the feedback bi-axial control strategy is run;
 - open loop: the forward loop bi-axial control strategy is run;
 - hybrid: the hybrid bi-axial control strategy is run;
 - danger state: a danger condition occurs, an inspection and further reboot are necessary;

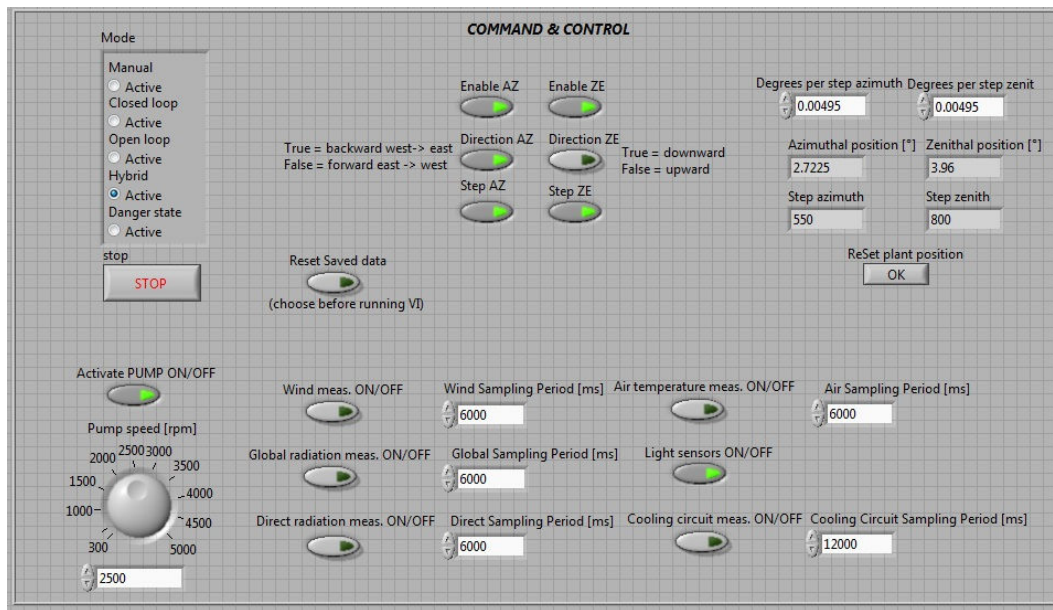


Figure 6.7. LabView™ platform, command & control panel.

- ✓ the six stepper motor buttons, three for each actuator. They allow to set or check the enable, direction and step signals. Particularly, when the manual control mode is run such buttons are used as controls to enable and disable the two actuators. In all the other control modes such buttons are used as indicators to monitor, also remotely, the state of the stepper motors;
- ✓ the plant current position indicators to set the angular resolution for the Azimuthal and Zenithal kinematic chains and to check the current plant position expressed as the angular displacement from the *zero* reference position;
- ✓ the sensor switching on buttons and sampling period set controls to enable/disable the several sensors installed on-board and to specify the temporal gap between two consecutive samples;
- ✓ the cooling circuit pump activation and set of its speed. As specified, only one of the two circulation pumps is remotely controllable. The secondary loop pump is controllable manually, only;
- ✓ the stop button to switch off the whole plant;
- ✓ the reset saved data button to delete the previously saved data about the prototype performances and environmental conditions.

6.2.2 Geo-coordinates & time panel

The effective control of the prototype requires to know the data about the location where the plant is installed and the time of the day. As example, such parameters are crucial to compute the current value of the Azimuthal and solar Altitude angles through the

aforementioned astronomic solar equations. The solar time drives, also, the main control loop described in the *flow-chart* of Figure 6.1. The geo-coordinates & time panel provides such information. It is represented in Figure 6.8.

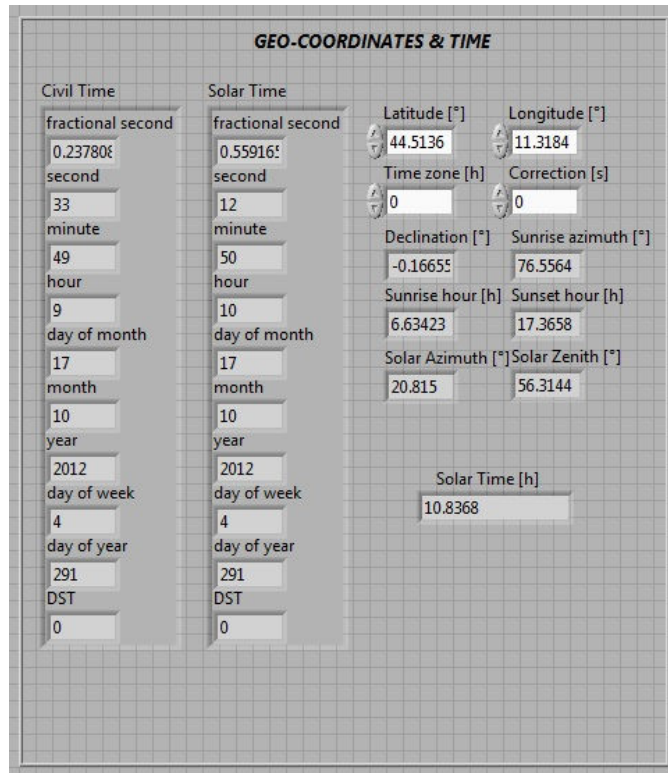


Figure 6.8. LabView™ platform, geo-coordinates & time panel.

The current standard civil time, t_{std} , and the correspondent solar time, t , are shown together with the sunrise and sunset hours, $t_{sr/ss}$, the sunrise azimuthal angle, Az_{sr} , and the daily solar declination δ . Furthermore, the solar azimuth and zenith angles, representing the current Sun position, are calculated at each iteration of the main control loop. To correctly compute such parameters the user needs to preliminary set the latitude, the longitude and the time zone of the location where the prototype is installed.

A final remark is about the system time synchronization. The NI-CRIO controller remotely gets, via FTP and NTP, the universal time from an international reference centre to guarantee the accuracy of such a crucial data.

6.2.3 Alarm panel

The alarm panel in Figure 6.9 is made of four boolean indicators normally set to zero, i.e. the color white. They are switched to the value one, i.e. the color red, to alert the user that a critic event occurs.

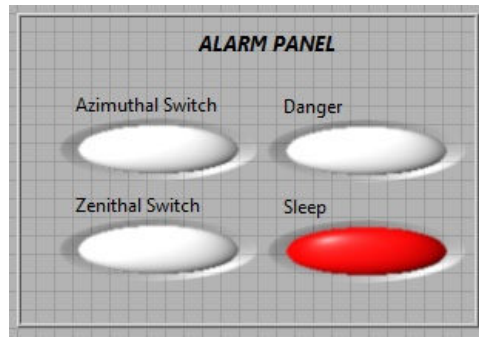


Figure 6.9. LabView™ platform, alarm panel.

Particularly, the two indicators on the left side of the panel monitor the position of the solar collector. If the position, for one or both the motion axes, is out of the admissible range the limit switches described in Section 5.8.2 are activated, the plant motion immediately stopped and the correspondent indicator switched from the color white to the danger color red. The *Danger* indicator on the top right is activated when the environmental conditions are critic, e.g. a strong wind is measured by the anemometer. In such a condition the prototype is stopped and the SP is promptly reached. Finally, the *Sleep* indicator is activated during night-time, i.e. $t \notin [t_{sr} - \varepsilon, t_{ss}]$, to inform the user that the prototype is sleeping and it is waiting for the next sunrise. Such indicator is not, properly, an alarm (no anomaly occurs) but an useful information to the user that, otherwise, can not immediately understand why the prototype seems not to track the Sun correctly.

6.2.4 Sensors & setpoint panel

The sensors & setpoint panel includes data related to the described bi-axial solar tracking strategies. A snapshot is in Figure 6.10. The top four numerical indicators show the light sensor signals. *Sensor 1* and *sensor 2* are for the zenithal motion axis, while *sensor 3* and *sensor 4* are for the azimuthal axis (see Figure 6.3). The correspondent gaps are shown below. Such values are the key parameters to run the feedback control strategy described in previous Section 6.1.2.4.

Furthermore, the following two boxes allow the user to set the required limits, T_{on} , T_{off} , T_{fd} and T_{fo} to mark the difference between the working states for both the feedback and hybrid control strategies. Finally, for the last strategy, the current value of the parameter M_s , introduced in Eq. 6.1, is proposed and two boolean indicators show which of the two control strategies, i.e. *hybrid-open* and *hybrid-closed*, is actually run.

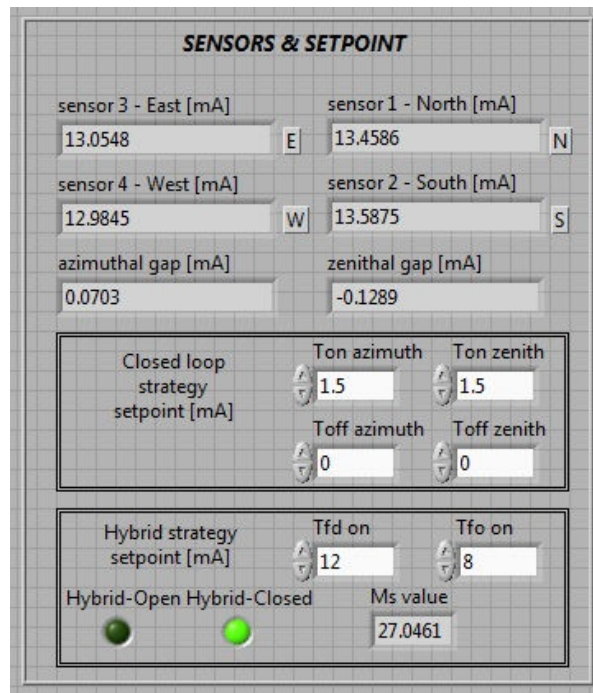


Figure 6.10. LabView™ platform, sensors & setpoint panel.

6.2.5 Environmental condition panel

The environmental condition panel provides information about the current weather conditions. The data are measured by the three sensors installed on the weather station depicted in Figure 5.24 and by the pyrheliometer of Figure 5.25.

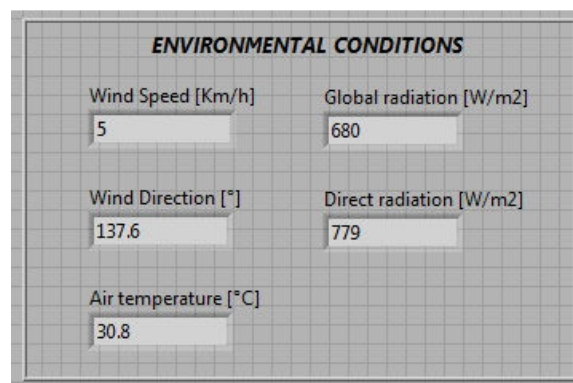


Figure 6.11. LabView™ platform, environmental condition panel.

The sampling period is independent for each sensor and is controllable through the control & command panel. Details about the data measurement chain and the data saving procedure are provided in the following.

6.2.6 Cooling circuit panel

The cooling circuit panel in Figure 6.12 shows the current temperatures, flow rate and recovered heat. It refers to one of the two modules composing the solar collector. The most of the data refers to the primary loop, i.e. the closed loop hydraulic circuit cooling the TJ-PV cells, even if the secondary loop heat exchanger inlet and outlet temperatures are provided. In fact, the primary loop is totally integrated to the prototype, while the secondary loop configuration, flow rate and dispersions depend on the thermal user features.

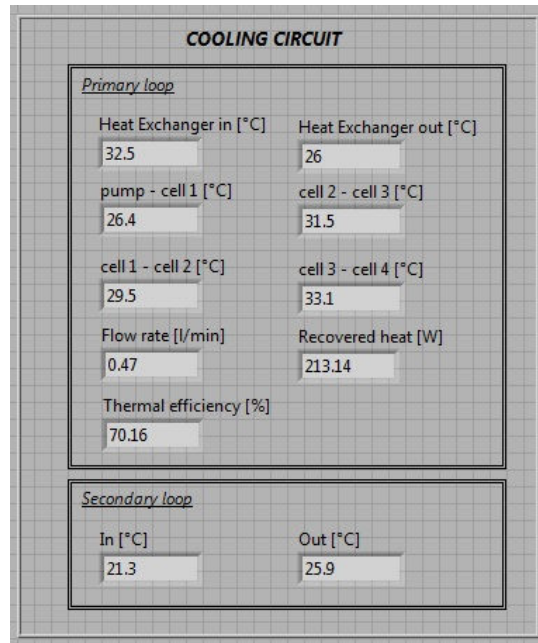


Figure 6.12. LabView™ platform, cooling circuit panel.

The temperatures in six relevant points of the primary loop are measured through a same number of Pt-100 temperature sensors installed before and after each PV cell heat exchanger and before and after the brazed plates heat exchanger located in the protection box and allowing the heat exchange between the primary and secondary loops.

6.2.7 Field-data acquisition procedure

At the end of the description of the developed functional panels for the PV/T prototype control, the field-data acquisition procedure is, now, presented. Both the control algorithms and the monitoring units require the acquisition of several data from the field through a wide set of sensors. In the previous paragraphs great attention is paid to the description of both the sensors and their electrical connection to the *hardware* control board, together with the discussion of the correspondent indicators on the *software* platform. On

the contrary, few attention is paid on how each field-data is measured to guarantee a reliable acquisition.

Each measured data is not the result of a single sample because of the relevant risk of its distortion due to the presence of environmental noise. Assessing multiple measures and calculating the average of the obtained values allows to reduce the random biases affecting the measured data due to the compensation effect principle. Such a strategy is adopted for all the acquired signals. Particularly, each measured data comes from a sequence of five samples. The sampling period is one-fifth of the sampling period the user set in the control & command panel, while the measured data is the average of the five sampled values.

An example of such a procedure is in the next Figure 6.13 and it refers to the air temperature signal. Such a figure provides, also, an example of the LabView™ graphical programming language adopted for the *software* platform development.

At first the auxiliary variable *Sum T air* is set to zero. The second frame is made of a *for loop structure* iterated five times. Each iteration acquires a sample from the field, i.e. the current signal from the *AIO* physical slot, and converts it to the correspondent temperature value. Such a value is added to the aforementioned variable *Sum T air*. Between each iteration and the next one a *wait block* of one fifth of the sampling period is added. Finally, the result of the ratio between *Sum T air* and five, i.e. the number of samples, is assigned to the *Air temperature* indicator shown to the user on the environmental condition panel.

6.2.8 Data saving and download

The measured data about environmental and operative conditions need to be saved for further analyses. The developed *software* platform temporarily stores each data in a custom two column matrix. The first column contains the timestamp, while the second column records the correspondent data. Such matrixes are saved on the NI C-RIO controller hard disk and can be downloaded from a remote laptop by the net. In such a way the controller works autonomously and a connection is necessary for downloading the data, only.

Such a working approach is further used for the LabView™ *software*. The program code is developed on a host laptop and then uploaded to the NI C-RIO and run through its processor, totally excluding the auxiliary laptop except for the user command set and the prototype monitoring.

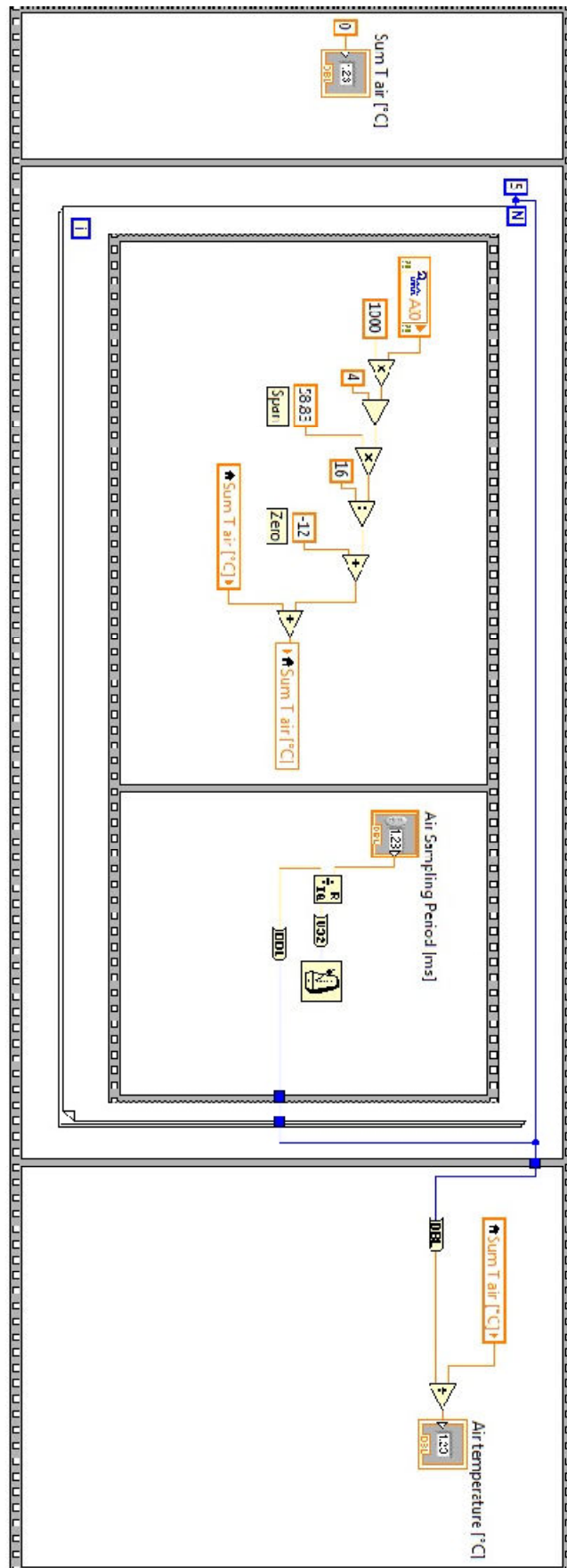


Figure 6.13. Field-data acquisition procedure, example.

6.3 Solar tracking strategy field-test

The proposed tracking strategies, described in Section 6.1 and integrated to the platform presented in Section 6.2., are field-tested to experimentally investigate their performances in solar collimation. The solar collimator described in Section 5.7, integrated to the PV/T prototype, is used for the tests.

The adopted approach to measure the alignment accuracy between the Sun ray direction and the solar collector position follows the scheme of Figure 6.14.

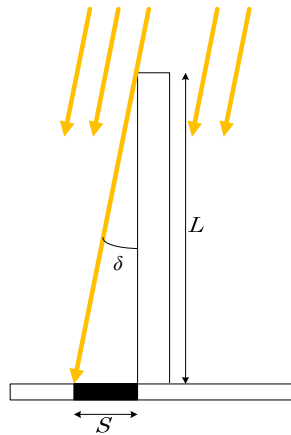


Figure 6.14. Misalignment measurement strategy.

The measure of the shadow length, S , generated by the solar collimator stem on the base allows the estimation of the angular alignment gap through the following Eq. 6.2.

$$\delta = \tan^{-1} \left(\frac{S}{L} \right) \quad (6.2)$$

The presence of a set of concentric circles on the base helps the measure process.

The Figure 6.15 and the Figure 6.16 show two pictures of the aforementioned shadow when the forward loop and feedback loop strategies are run.



Figure 6.15. Forward loop strategy shadow.



Figure 6.16. Feedback strategy shadow.

As already introduced, the forward loop is less accurate, i.e. $\delta \approx 2^\circ$, than the feedback strategy, i.e. $\delta < 1^\circ$. For such a reason, the hybrid strategy runs the latter control algorithm for an accurate collimation if no critic weather conditions are present.

6.4 MPP tracking algorithms

The LabView™ platform for PV/T prototype control described in Section 6.2 does not include a panel for the electrical parameter control and the MPP tracking. As introduced in Section 5.6, such functions are implemented manually through the described electronic variable load. Their integration to the *hardware* and *software* platforms represents a necessary further development of the proposed research.

Focusing on the MPP tracking, a preliminary study reviews the possible algorithms able to guarantee the PV cells always work close to their MPP extracting the maximum electrical power available at the current environmental conditions, i.e. the non controllable parameter.

In the recent past, the literature widely discusses the MPP tracking issue proposing a relevant set of algorithms and approaches. Considering the renewable energy field, characterized by the variability of the energy source, the key issue pointed out by several authors deals with the necessity to develop dynamic algorithms able to track the MPP that continuously varies its position on the *power-voltage* or *power-current* plane.

For the wind renewable sector, an interesting survey is proposed by Abdullah et al. (2012), while for the solar PV sector several reviews are developed. In 2006, Salas et al. (2006) propose a survey of MPP tracking algorithms and classify them into two main groups: the so-called *quasi seeks* methods, also called indirect, open-loop and off-line methods, and the *true seeking* methods, also called direct and closed-loop methods. Particularly, the indirect methods are based on the use of a database that includes the parameters and the data such as the curves typical of the PV generator for different irradiances and temperatures, or they consider the mathematical functions obtained from field data to estimate the MPP. On the contrary, the direct methods include those methods that use the PV voltage and/or current measurements to track the MPP. They are independent from the *a priori* knowledge of the PV generator characteristics. Recently, similar reviews are proposed enlarging the set of algorithms. Xiao et al. (2011), Ishaque & Salam (2013) and Reza Raisi et al. (2013) present relevant contributions in such a direction together with effective overviews of the topic.

Furthermore, a parallel research area focuses on the comparison among different MPP tracking methods considering several PV applications and environmental conditions. As example, Barchowsky et al. (2011) test MPP tracking methods under different cloudiness levels assessing the stability and quality of the algorithms. Ngan & Tan (2011) compare direct and indirect methods and, then, focus on the frequently adopted *Perturb & Observe* algorithm testing it under clear sky and cloudy conditions. Finally, Subudhi & Pradhan

(2013) propose an useful reference comparison grid about the strengths and weaknesses of 25 algorithms taken from the literature.

Basically, the MPP is the maximum of the P - V curve. Such a curve is different varying the irradiance level.

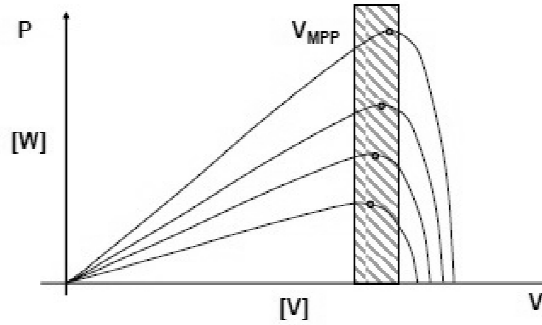


Figure 6.17. P-V curves for different irradiance levels.

Analytically, the MPP verifies the maximum condition

$$\left. \frac{dP}{dV} \right|_{MPP} = 0 \quad (6.3)$$

or, equivalently,

$$\left. \frac{dP}{dI} \right|_{MPP} = 0 \quad (6.4)$$

considering the P - I curve.

The aforementioned open-loop methods consider *a priori* correlations between the MPP (V_{MP} , I_{MP}) and other relevant parameters like the open circuit voltage, V_{OC} , and the short circuit current, I_{SC} . As example, for the most of the PV cells and modules the MPP range of variation is not so wide (see Figure 6.17) and it is almost proportional to both the open loop voltage and the short circuit current. Empirical correlations are deduced.

$$V_{MP} = k_v \cdot V_{OC} \quad k_v \in [0.75, 0.85] \quad (6.5)$$

$$I_{MP} = k_i \cdot I_{SC} \quad k_i \in [0.85, 0.95] \quad (6.6)$$

The cyclical sense of V_{OC} or I_{SC} allows to estimate the MPP and to set the correspondent voltage and current levels to the PV cell circuit.

The most of the open-loop methods are, evidently, very easy and low-costing but present a set of systematic biases undermining their effectiveness, e.g. their strong dependence on both the PV cell or module features and environmental conditions, the load disconnecting requirement to sense the open circuit voltage or the short circuit current, etc.

To overcome such weaknesses the closed-loop methods are introduced. In the context of the present Ph.D. dissertation, two basic algorithms are discussed: the *perturb & observe* algorithm and the *incremental conductance* algorithm.

6.4.1 Perturb & observe algorithm

The *perturb & observe* algorithm is an iterative method of obtaining the MPP. It measures the PV array characteristics and, then, it perturbs the working point of the PV system to encounter the change direction. The algorithm perturbs the voltage or current, indifferently. If the effect of the k^{th} perturbation is a power increase the $(k+1)^{\text{th}}$ perturbation is identical to the previous one, otherwise, such a perturbation is in the opposite direction. The following *flow-chart* clarifies the algorithm steps considering voltage perturbations.

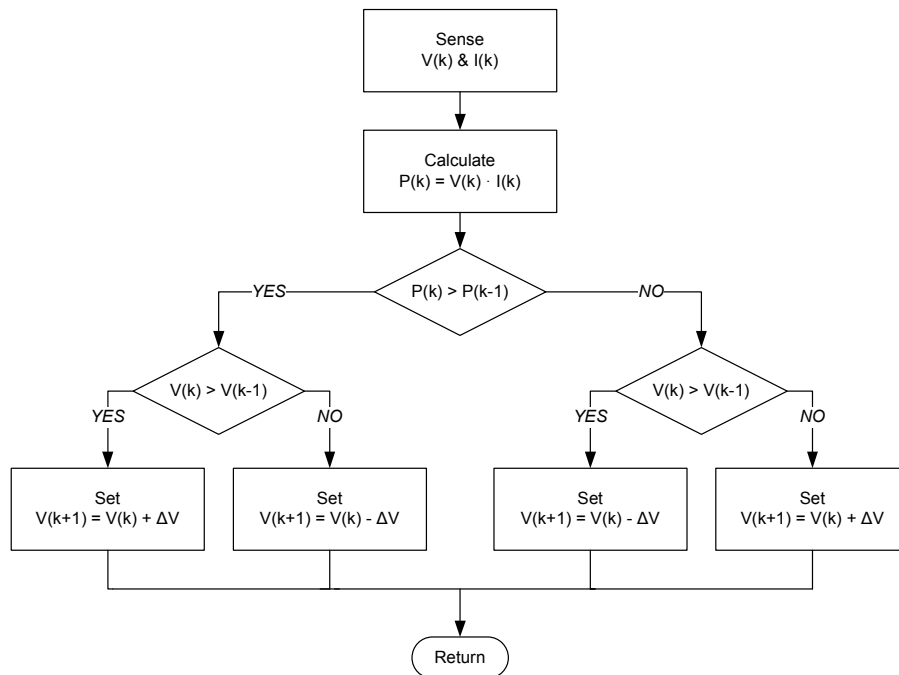


Figure 6.18. *Perturb & observe* algorithm.

The introduced perturbation, represented by ΔV , is added or subtracted to the current voltage level depending on the effect, on the extracted power, of the previous one. The left side of the *flow-chart* shows a perturbation equal to the previous one due to power increase, while the right side of the *flow-chart* shows the change of the perturbation sign due to power decrease.

An intrinsic weakness of the proposed algorithm is the presence of a limit cycle in the neighborhood of the MPP, i.e. the occurrence of a cyclical oscillation of the voltage around V_{MP} . This is due to the adopted fixed incremental step that decreases the algorithm

noise sensibility but that it introduces the aforementioned limit cycle. To face such a problem an accuracy tolerance range on the power level can be of help.

6.4.2 Incremental conductance algorithm

The *incremental conductance* algorithm is based on the following equations.

Eq. 6.3 states

$$\left. \frac{dP}{dV} \right|_{MPP} = 0 \quad (6.7)$$

and

$$P = V \cdot I \quad (6.8)$$

Thus,

$$\left. \frac{d(V \cdot I)}{dV} \right|_{MPP} = \left(I + V \cdot \frac{dI}{dV} \right) \Big|_{MPP} = 0 \quad (6.9)$$

and, finally, for the MPP

$$\frac{I}{V} + \frac{dI}{dV} = 0 \quad \rightarrow \quad \frac{dI}{dV} = -\frac{I}{V} \quad (6.10)$$

The absolute and incremental conductances are the same but of opposite sign. Furthermore, the slope of the PV power curve is positive on the left of the MPP and negative on the right. Analytically,

$$\begin{cases} \frac{dP}{dV} = 0 \rightarrow \frac{dI}{dV} = -\frac{I}{V} \text{ at MPP} \\ \frac{dP}{dV} > 0 \rightarrow \frac{dI}{dV} > -\frac{I}{V} \text{ left of MPP} \\ \frac{dP}{dV} < 0 \rightarrow \frac{dI}{dV} < -\frac{I}{V} \text{ righth of MPP} \end{cases} \quad (6.11)$$

Such considerations drive the algorithm for MPP tracking. Its *flow-chart* is in Figure 6.19. The left side of the *flow-chart* represents the three conditions of Eq. 6.11, while the right side is added to prevent deadlocks.

Finally, due to the discrete increment ΔV the *incremental conductance* algorithm is affected by a limit cycle in the neighborhood of the MPP. Similarly, to the *perturb & observe* method, the introduction of an accuracy tolerance range prevents a periodic oscillation behavior around the MPP.

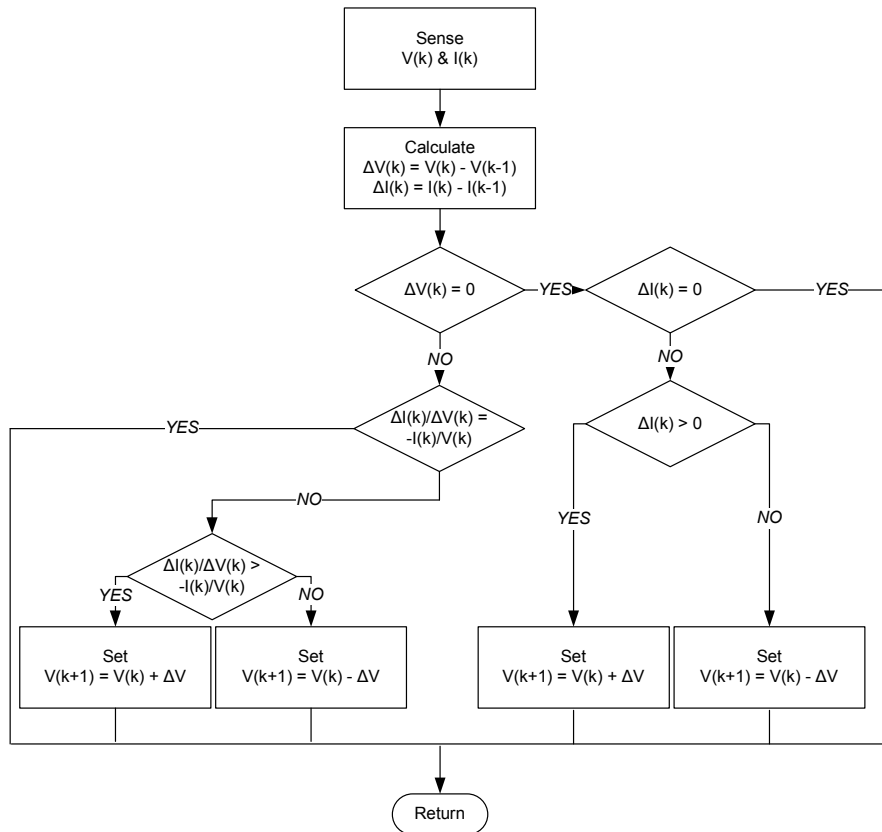


Figure 6.19. Incremental conductance algorithm.

Several other algorithms exist even if they are more complex than the presented two methods. A comparison among them is always possible in terms of the wasted power or, similarly, by computing the algorithm efficiency, η .

$$\eta = \frac{1}{n} \sum_{i=1}^n \frac{P_i}{P_i^{max}} \quad (6.12)$$

Given $i = 1, \dots, n$ samples, the efficiency is the mean value of the ratio between the extracted power, P_i , and the maximum solar power, P_i^{max} . The higher such a value, the higher the algorithm performance is. Good algorithms present $\eta > 90\%$, generally. The literature includes the *perturb & observe* and *incremental conductance* algorithms among the effective methods for the most of the operative scenarios (Subudhi & Pradhan, 2013).

Despite the full development of a MPP module for the developed PV/T prototype represents a necessary further development, the *perturb & observe* method is indirectly adopted for the preliminary field-tests described in Section 5.10. The electronic variable load introduced in Section 5.6 provides the voltage, current and power levels directly on the screen so that the user can, manually, change one of the first two parameters to track the MPP. As example, if a small increase of the voltage level generates a power increase the user further increase the voltage since a power decrease occurs. Such a way of operating is in accordance with the *perturb & observe* algorithm.

Finally, a preliminary test, out of the *software* control platform, to simulate the MPP *perturb & observe* algorithm behavior is, already, developed in LabView™ environment.

6.4.3 LabView™ simulation of *perturb & observe* algorithm

The simulation reproduces the effect of the *perturb & observe* algorithm on a virtual PV module. For the sake of brevity, the equations about the equivalent electric circuit for the PV module are neglected. The simulation input is the short circuit current, I_{SC} , affected by the solar irradiance level, and the incremental step ΔV . The output deals with the voltage, current and power instantaneous values and profiles. The following Figure 6.20 shows the result of a 100 iteration run considering $I_{SC} = 2.5A$.

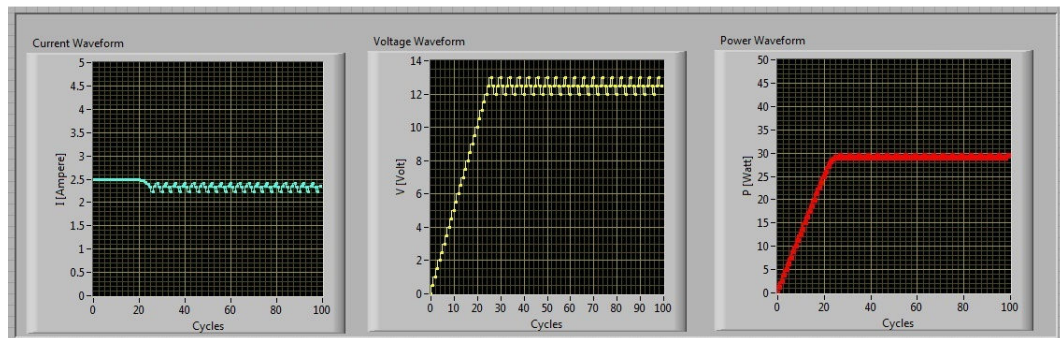


Figure 6.20. *Perturb & observe* algorithm, LabView™ simulation.

The waveforms after the initial transient state, i.e. the first 20 cycles, are regular and they clearly highlights the aforementioned limit cycle in the neighborhood of the MPP. For the run scenario the maximum power is close to 30W. The absence of environmental noises makes the trend perfectly regular.

Finally, the effect of the variation of the irradiance level is visible changing the I_{SC} during the run. The following Figure 6.21 shows the effect of a variation from 2.5A to 4.0A of the short circuit current, i.e. a solar irradiance increase.

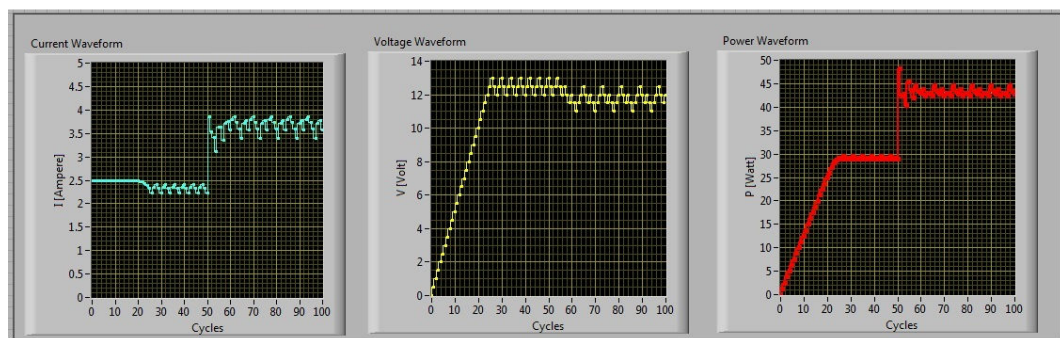


Figure 6.21. Effect on the PV cell electrical parameters of the environmental condition change.

The extracted power increases from 30W to 44W, while the current and voltage profiles change accordingly. The simulation highlights the effectiveness of the *perturb & observe* algorithm in the MPP tracking. The I_{sc} change introduces a short transient state in which the algorithm tracks the system to the new MPP neighborhood.

The proposed simulation, adopted to test the *perturb & observe* algorithm in the LabView™ environment will be followed, as a future development, by the integration of the proposed logic of control to the described prototype platform to complete and fully field-test it.

References

- Abdullah, M.A., Yatim, A.H.M., Tan, C.W., Saidur, R., (2012). A review of maximum power point tracking algorithms for wind energy systems. *Renewable and Sustainable Energy Reviews* 16:3220-3227.
- Alata, M., Al-Nimr, M.A., Qaroush, Y., (2005). Developing a multipurpose sun tracking system using fuzzy control. *Energy Conversion and Management* 46:1229-1245.
- Alexandru, C., Pozna, C., (2008). Different tracking strategies for optimizing the energetic efficiency of a photovoltaic system. *Proceedings of the AQTR'08* 3:434-439.
- Al-Jumaily, K.E.J., Al-Kaysi, M.K.A., (1998). The study of the performance and efficiency of flat linear Fresnel lens collector with sun tracking system in Iraq. *Renewable Energy* 14(1-4):41-48.
- Al-Mohamad, A., (2004). Efficiency improvements of photo-voltaic panels using a sun-tracking system. *Applied Energy* 79:345-354.
- Al-Naima, F.M., Al-Tae, B.R., (2010). An FPGA Based Stand-alone Solar Tracking System. *Proceedings of EnergyCon'10* 513-518.
- Aracil, C., Quero, J.M., Castañer, L., Osuna, R., Franquelo, L.G., (2006). Tracking system for solar power plants. *Proceedings of IECON'06* 3024-3029.
- Bakos, G.C., (2006). Design and construction of a two-axis Sun tracking system for parabolic trough collector (PTC) efficiency improvement. *Renewable Energy* 31:2411-2421.
- Barchowsky, A., Parvin, J.P., Reed, G.F., Korytowski, M.J., Grainger, B.M., (2011). A comparative study of MPPT methods for distributed photovoltaic generation. *Proceedings of the Innovative Smart Grid Technologies - IEEE PES* 1-7.
- Bortolini, M., Gamberi, M., Accorsi, R., Manzini, R., Mora, C., Regattieri, A., (2010). Sun tracking system and testing for solar energy conversion systems. *Proceedings of the XV Summer School "Francesco Turco"* 257-262.
- Bortolini, M., Gamberi, M., Graziani, A., Manfroni, M., Manzini, R., (2012). Hybrid strategy for bi-axial solar tracking system. *Journal of Control Engineering and Technology* 2(4):130-142.

Chen, Y.T., Chong, K.K., Lim, C.S., Lim, B.H., Tan, K.K., Aliman, O., Bligh, T.P., Tan, B.K., Ismail, G., (2002). Report of the first prototype of non-imaging focusing heliostat and its application in high temperature solar furnace. *Solar Energy* 72(6):531-544.

Chin, C.S., Babu, A., McBride, W., (2011). Design, modeling and testing of a standalone single axis active solar tracker using MATLAB/Simulink. *Renewable Energy* 36:3075-3090.

Chong, K.K., Wong, C.W., (2009). General formula for on-axis sun-tracking system and its application in improving tracking accuracy of solar collector. *Solar Energy* 83:298-305.

Chong, K.K., Wong, C.W., (2010). Open-loop azimuth-elevation sun-tracking system using on-axis general sun-tracking formula for achieving tracking accuracy of below 1 mrad. *Proceedings of PVSC'10* 3019-3024.

Chong, K.K., Tan, M.H., (2011). Range of motion study for two different sun-tracking methods in the application of heliostat field. *Solar Energy* 85:1837-1850.

Clifford, M.J., Eastwood, D., (2004). Design of a novel passive solar tracker. *Solar Energy* 77:269-280.

Davies, P.A., (1993). Sun-tracking mechanism using equatorial and ecliptic axes. *Solar Energy* 50(6):487-489.

Edwards, B.P., (1978). Computer based sun following system. *Solar Energy* 21:491-496.

Edwards, B.P., (1981). A computational alignment method for paraboloidal collectors. *Solar Energy* 26:121-125.

Fairbanks, J.W., Morse, F.H., (1972). Passive solar array orientation devices for terrestrial application. *Solar Energy* 14:67-79.

Grena, R., (2008). An algorithm for the computation of the solar position. *Solar Energy* 82:462-470.

Guo, M., Wang, Z., Zhang, J., Sun, F., Zhang, X., (2011). Accurate altitude-azimuth tracking angle formulas for a heliostat with mirror-pivot offset and other fixed geometrical errors. *Solar Energy* 85:1091-1100.

- Hession, P.J., Bonwick, W.J., (1984). Experience with a sun tracker system. *Solar Energy* 32(1):3-11.
- Hossain, E., Muhida, R., Ali, A., (2008). Efficiency Improvement of Solar Cell Using Compound Parabolic Concentrator and Sun Tracking System. *Proceedings of Electrical Power and Energy Conference*.
- Huang, B.J., Ding, W.L., Huang, Y.C., (2011). Long-term field test of solar PV power generation using one-axis 3-position sun tracker. *Solar Energy* 85:1935-1944.
- Ishaque, K., Salam, Z., (2013). A review of maximum power point tracking techniques of PV system for uniform insolation and partial shading condition. *Renewable and Sustainable Energy Reviews* 19:475-488.
- Kalogirou, S.A., (1996). Design and construction of a one-axis sun-tracking system. *Solar Energy* 57(6):465-469.
- Kang, D., Martínez, E.A., Chaparro, E., (2011). Solar Tracker System Based on a Digital Heuristic Controller. *Proceedings of Trondheim Power Tech'11*.
- Karimov, K.S., Saqib, M.A., Akhter, P., Ahmed, M.M., Chattha, J.A., Yousafzai, S.A., (2004). A simple photo-voltaic tracking system. *Solar Energy Materials and Solar Cells* 87:49-59.
- Koyuncu, B., Balasubramanian, K., (1991). A microprocessor controlled automatic sun tracker. *IEEE Transaction on Consumer Electronics* 37(4):913-917.
- Li, Z.M., Zhou, R., (2011). Sun tracker design based on AVR. *Proceedings of APPEEC'11*.
- Lu, H.C., Shih, T.L., (2010). Fuzzy System Control Design with Application to Solar Panel Active Dual-Axis Sun Tracker System. *Proceedings of SCM'10* 1878-1883.
- Luque, A., Andreev V., (2007). *Concentrator Photovoltaics*. Springer ed. Berlin, Germany.
- Lynch, W.A., Salameh, Z.M., (1990). Simple electro-optically controlled dual-axis sun tracker. *Solar Energy* 45(2):65-69.
- Mashohor, S., Samsudin, K., Noor, A.M., Rahman, A.R.A., (2008). Evaluation of generic algorithm based solar tracking system for photovoltaic panels. *Proceedings of ICSET'08* 269-273.

- Mosher, D.M., Boese, R.E., Soukup, R.J., (1977). The advantages of sun tracking for planar silicon solar cells. *Solar Energy* 19:91-97.
- Mousazadeh, H., Keyhani, A., Javadi, A., Mobli, H., Abrinia, K., Sharifi, A., (2009). A review of principle and sun-tracking methods for maximizing solar systems output. *Renewable and Sustainable Energy Reviews* 13:1800-1818.
- Ngan, M.S., Tan, C.W., (2011). A study of maximum power point tracking algorithms for stand-alone photovoltaic systems. *IEEE Applied Power Electronics Colloquium* 22-27.
- Nuwayhid, R.Y., Mrad, F., Abu-Said, R., (2001). The realization of a simple solar tracking concentrator for university research applications. *Renewable Energy* 24:207-222.
- Ponniran, A., Hashim, A., Munir, H.A., (2011). A design of single axis sun tracking system. *Proceedings of PEOCO'11* 107-110.
- Poulek, V., Libra, M., (1998). New solar tracker. *Solar Energy Materials and Solar Cells* 51:113-120.
- Ranganathan, R., Mikhael, W., Kutkut, N., Batarseh, I., (2010). Adaptive sun tracking algorithm for incident energy maximization and efficiency improvement of PV panels. *Renewable Energy* 36:2623-2626.
- Reza Reisi, A., Moradi, M.H., Jamasb, S., (2013). Classification and comparison of maximum power point tracking techniques for photovoltaic system: a review. *Renewable and Sustainable Energy Reviews* 19:433-443.
- Roth, P., Georgiev, A., Boudinov, H., (2004). Design and construction of a system for sun-tracking. *Renewable Energy* 29:393-402.
- Rubio, F.R., Ortega, M.G., Gordillo, F., López-Martínez, M., (2007). Application of a new control strategy for sun tracking. *Energy Conversion and Management* 48:2174-2184.
- Rumala, S.S.N., (1986). A shadow method for automatic tracking. *Solar Energy* 37(3):245-247.
- Salas, V., Olías, E., Barrado, A., Lázaro, A., (2006). Review of the maximum power point tracking algorithms for stand-alone photovoltaic systems. *Solar Energy Materials & Solar Cells* 90:1555-1578.

Sefa, I., Demirtas, M., Çolak, I., (2009). Application of one-axis sun tracking system. *Energy Conversion and Management* 50:2709-2718.

Seme, S., Štumberger, G., (2011). A novel prediction algorithm for solar angles using solar radiation and differential evolution for dual-axis sun tracking purposes. *Solar Energy* 85:2757-2770.

Shama, F., Roshani, G.H., Ahmadi, A., Roshani, S., (2011). A novel and experimental study for a two-axis sun tracker. *Proceedings of APPEEC'11*.

Subudhi, B., Pradhan, R., (2012). A comparative study on maximum power point tracking techniques for photovoltaic power systems. *IEEE Transactions on Sustainable Energy* 4(1):89-98.

Tang, R., Yu, Y., (2010). Feasibility and optical performance of one axis three positions sun-tracking polar-axis aligned CPCs for photovoltaic applications. *Solar Energy* 84:1666-1675.

Tao, Y., Guo, W., (2010). Study on tracking strategy of automatic sun-tracking system based on CPV Generation. *Proceedings of ISDEA'10* 506-509.

Vorobiev, P., Vorobiev, Y., (2010). Automatic sun tracking solar electric system for applications on transport. *Proceedings of CCE'10* 66-70.

Wai, R.J., Wang, W.H., Lin, J.Y., (2006). Grid-connected photovoltaic generation system with adaptive step-perturbation method and active sun tracking scheme. *Proceedings of IECON'06* 224-228.

Wu, C.S., Wang, Y.B., Liu, S.Y., Peng, Y.C., Xu, H.H., (2008). Study on automatic sun-tracking technology in PV generation. *Proceedings of DRPT'08* 2586-2591.

Xiao, W., Elnosh, A., Khadkikar, V., Zeineldin, H., (2011). Overview of maximum power point tracking technologies for photovoltaic power systems. *Proceedings of 37th Annual Conference on IEEE Industrial Electronics Society* 3900-3905.

Xie, Y., Guo, W., (2010). The design of ARM-based automatic sun tracking system. *Proceedings of ISDEA'10* 608-611.

Zhou, Y., Zhu, J., (2010). Application of fuzzy logic control approach in a microcontroller-based sun tracking system. *Proceedings of ICIE'10* 161-164.

Zogbi, R., Laplaze, D., (1984). Design and construction of a sun tracker. *Solar Energy* 33(3-4):369-372.

7. *Concentrating solar simulator*

Ray-tracing model and Monte Carlo simulation for the solar simulator reflector design

In laboratory analyses and optic experimental studies, solar simulators are widely adopted devices to artificially reproduce the emission spectrum of the Sun. Their use allows to study the effect of the solar radiation on both materials and components, e.g. PV materials, solar PV cells etc., under controlled conditions.

This chapter focuses on such devices and it investigates the effective design of the ellipsoidal reflector for a single source concentrating solar simulator. A ray-tracing model, combined to a Monte Carlo simulation, is proposed to study the reflector geometric shape maximizing the target incident radiation and optimizing the radiative incident flux distribution. The developed approach includes the main physical and optic phenomena affecting the light rays from the source to the target area and it is based on the geometrical optic theory. Furthermore, the adoption of Monte Carlo simulation allows to simulate a wide set of configurations to identify the mirror reflector best shape.

A realistic case study, focusing on the design of a small scale solar simulator, is presented to apply the proposed approach. Details about the most relevant outcomes are provided to support the further reflector purchase and the future solar simulator assembly.

7.1 Solar simulator overview

Solar simulators provide a luminous flux approximating natural sunlight spectrum. Their basic structure includes a metal support frame, one or more light sources, e.g. high flux arc lamps with power supplier and igniter are frequently adopted, and a reflective surface to properly orient the emitted rays to light the target area. Several system geometries are developed, for both micro and macro applications. As example, Figure 7.1 shows a large scale, high flux, seven sources solar simulator prototype concentrating the solar radiation on a small surface located in front of the reflectors, i.e. in the position where the picture is taken.



Figure 7.1. High flux solar simulator, example.

Furthermore, Figure 7.2 depicts a single source small scale commercial solar simulator for laboratory tests. A 3D layout, highlighting the system components, is in Figure 7.3. Such a system is compact and can be located on the laboratory desk to study small targets, e.g. $100 \times 100 \text{ mm}$.



Figure 7.2. Small scale commercial solar simulator.

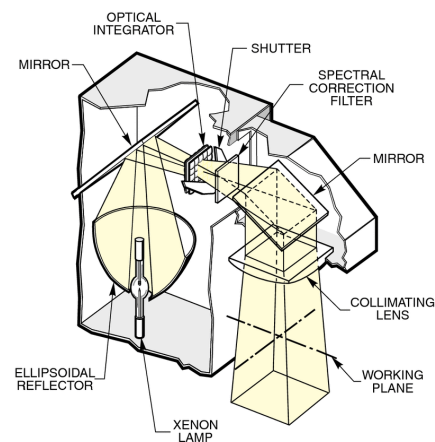


Figure 7.3. 3D layout and components.

Such devices include ellipsoidal mirrors as the reflective surface. The reflector shape allows the system to generate a concentrated or non-concentrated light beam. Particularly, non concentrating solar simulators present parabolic reflectors, while concentrating solar simulators include ellipsoidal reflectors. This is due to the geometric properties of such quadric surfaces. In parabolic shapes, a straight stream is generated from a source located on the focus point, while the rays emitted from an ellipsoid focus point are concentrated to the other focus. Figure 7.4 clarifies such geometric properties. The yellow spot represents the light source.

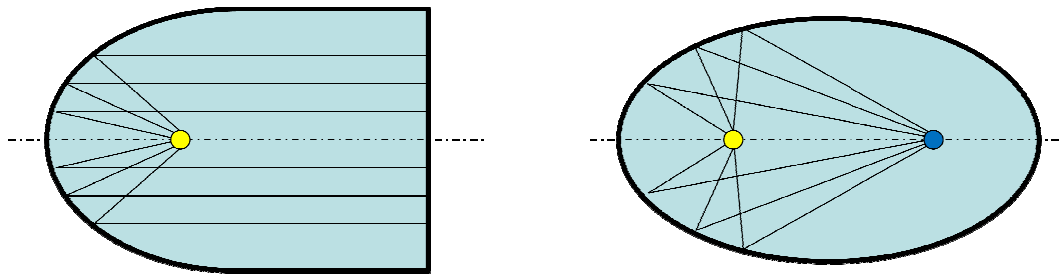


Figure 7.4. Geometric properties of parabolic and ellipsoidal surfaces.

The relevance of solar simulators, in laboratory tests and analyses, is frequently discussed by the recent literature presenting several applications for a wide set of research fields. Petrash et al. (2007) both review the topic and describe a 11,000 suns high-flux solar simulator. Domínguez et al. (2008), Domínguez et al. (2009), Pravettoni et al. (2010), Rehn and Hartwig (2010), Hussain et al. (2011) and Meng et al. (2011a) present different studies about the design and development of high flux solar simulators applied to both concentrating and non-concentrating PV systems. Amoh (2004) and Meng et al. (2011b) describe the design of solar simulators to test multi-junction solar cells for terrestrial and space applications. Kreuger et al. (2011) develop a 45kW solar simulator for high-temperature solar thermal and thermo-chemical researches, while Codd et al. (2010) present a low cost high flux simulator to study the optic melting and light absorption behavior of molten salts. All these contributions focus on the relevance of the proper design of the system to achieve high performances in both the flux intensity and its uniform distribution on the target area. The mirror reflective surface represents a crucial component to gain such purposes. An accurate shape design and simulation of the physical and optic properties is essential to the effective simulator construction (Johnston, 1995).

Ray-tracing algorithms combined to Monte Carlo analyses are recognized as effective approaches to analytically study the geometrical optic phenomena that occur in solar simulators. They allow to test different configurations of the reflective surface and to compare the system performances (Petrash et al., 2007, Chen et al., 2010, Ota & Nishioka, 2010, Cooper & Steinfeld, 2011).

In this chapter, such a strategy is adopted to design the ellipsoidal reflector of a small scale concentrating solar simulator. The following paragraphs provide details about the developed ray-tracing model and further describe its application to a realistic case study for the reflector shape design of a small scale solar simulator based on an OSRAM XBO® 3000W/HTC OFR Xenon short arc lamp. The obtained results are, finally, commented.

7.2 Ray-tracing model

Previous paragraph states that, in geometrical optics, the foci of an ellipsoid of revolution are conjugate points. If no distortion effects occur, each ray emitted by a punctiform source located in one of the foci passes through the other after a single specular reflection. According to such a principle, the concentrating solar simulators are designed. The light source, reproducing the Sun emission spectrum, and the target area, e.g. the studied material or component, are located at the foci of an ellipsoidal mirror reflective surface.

Considering experimental contexts, the following conditions and phenomena contribute to reduce the global system radiation transfer efficiency, i.e. the ratio between the light flux that reaches the target and the global emitted flux:

- ✓ the finite area of the emitting light source;
- ✓ the absorption phenomena due to the presence of the light source quartz bulb, the source electrodes and the reflective surface;
- ✓ the deviation and distortion phenomena due to the specular dispersion errors of the reflective surface;
- ✓ the losses due to the rays falling out of the reflector shape.

Such conditions affect all the operative contexts and cannot be neglected in the solar simulator design. Their impact in reducing the system performances is strongly correlated to the features of the emitting source, the target shape and, particularly, to the reflector shape and characteristics. Given a configuration of the source, the reflector and the target surface, the proposed ray-tracing approach analytically studies the ray trajectories, predicting the global transfer performances. The *flow-chart* in Figure 7.5 summarizes the step sequence of the proposed approach highlighting the stages in which the losses in transfer efficiency occur.

According to the major literature (Petrash et al., 2007, Domínguez et al., 2008, Kreuger et al., 2011) the light source is assumed to emit isotropic radiation uniformly from its surface. Consequently, the emission point, P_0 , is randomly located on the whole source

surface. The incident ray direction vector, \mathbf{v} , is defined according to the Lambert's cosine law distribution, as in Eq. 7.1 (Steinfeld (1991)).

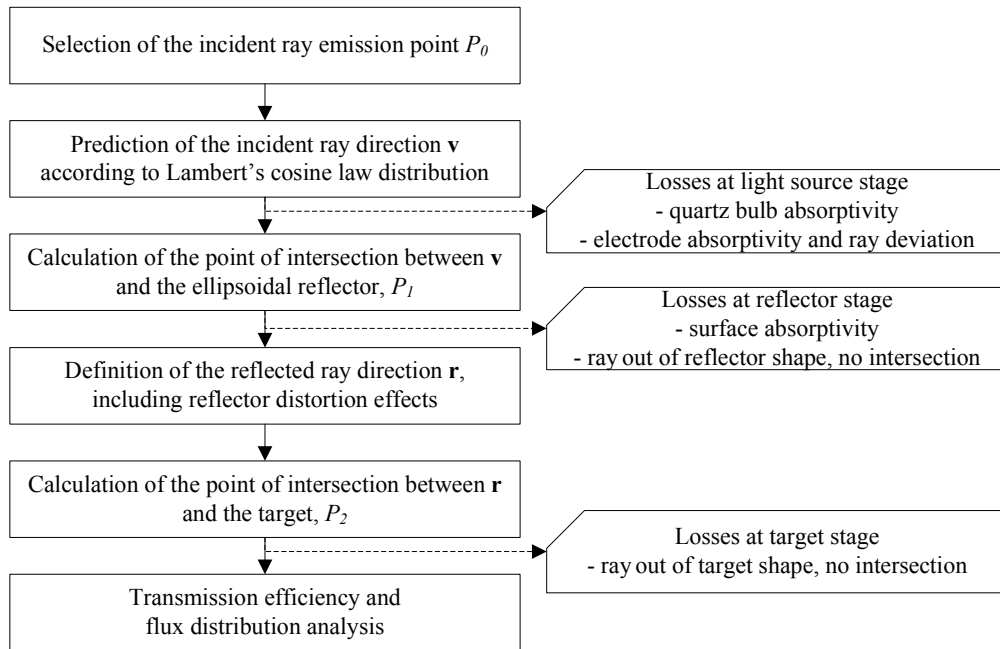


Figure 7.5. Ray-tracing model, flow-chart.

$$\mathbf{v} \times \mathbf{n} = \cos(\sin^{-1}\sqrt{U}) = \sqrt{1-U} \quad (7.1)$$

where \mathbf{n} is the normal direction to the emitting surface, in P_0 , and U a random number drawn from a $[0,1]$ uniform distribution. Proper quartz bulb and electrodes absorption phenomena are considered by introducing two coefficients, i.e. the bulb and the electrodes absorption coefficients, that reduce the emitted radiation and decrease the system transfer efficiency, i.e. the losses at the light source stage.

For each emitted ray, the point of intersection with the ellipsoidal surface, P_1 , is computed. If P_1 falls out of the surface shape or it falls in the hole necessary to install the light source, the ray is lost and the process finishes. Otherwise, two possibilities occur. Generally, the mirror reflects the ray but, in few cases, an absorption phenomenon occurs and the ray is not reflected at all. In such a circumstance, modeled considering a proper absorption coefficient, the process ends, i.e. the losses at the reflector stage.

Considering the reflected rays, their direction, \mathbf{r} , needs to be estimated. Distortion effects, caused by the specular dispersion errors of the reflective surface, affect \mathbf{r} vector. As widely discussed by Cooper & Steinfeld (2011), geometric surface errors modify the normal vector, \mathbf{k} , to the ellipsoid surface. The authors identify two angular components of such a dispersion error, i.e. the azimuthal angular component, θ_{err} , and the circumferential component, φ_{err} . By applying the, so called, Rayleigh method they outline proper expressions to estimate such angular errors.

$$\theta_{err} = \sqrt{2} \cdot \sigma_{err} \cdot \sqrt{-\ln U} \quad (7.2)$$

$$\varphi_{err} = 2\pi U \quad (7.3)$$

where σ_{err} is the standard deviation of the dispersion azimuthal angular error distribution, including all distortion effects, and U is a random number drawn from a [0,1] uniform distribution. As a consequence, to estimate the direction of \mathbf{k} , in the point of intersection P_1 , the theoretic normal vector \mathbf{k}' needs to be twofold rotated with rotation angles equal to θ_{err} and, then, $\varphi_{err} \cdot \theta_{err}$ rotation is around a vector orthogonal to a plane parallel to the major ellipse semi-axis, while the second rotation is around \mathbf{k}' . The normal direction to the reflective surface, in P_1 , allows to calculate the reflected ray direction, \mathbf{r} , according to Eq. 7.4 (Steinfeld, 1991).

$$\mathbf{r} = \mathbf{v} - 2 \cdot (\mathbf{k} \times \mathbf{v}) \times \mathbf{k} \quad (7.4)$$

The intersection between \mathbf{r} and the plane where the target lies allows to calculate the coordinates of the common point P_2 . If P_2 is inside the target area the ray correctly hits the target, otherwise the ray is lost and the transfer efficiency decreases, i.e. the losses at the target stage. Such a study does not consider multiple reflection phenomena.

Finally, the distance and mutual position between P_2 and the ellipsoid focus point allows to study the radiative incident flux distribution on the target area.

7.2.1 Analytic model

In the following the key equations of the developed ray-tracing model are proposed in accordance with the procedure of Figure 7.5. For the sake of simplicity, some details are neglected to avoid unnecessary redundancies. All the equations refer to a 3D Cartesian coordinate system with the origin of axes on the reflector ellipsoid center (Figure 7.6).

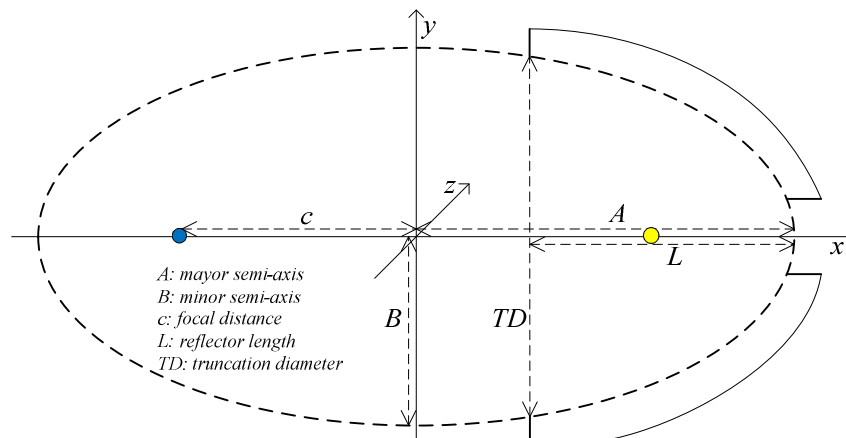


Figure 7.6. Ray-tracing model Cartesian coordinate system and notations.

The ellipsoid equation is the following:

$$\frac{x^2}{A^2} + \frac{y^2+z^2}{B^2} = 1 \quad (7.5)$$

and the focal distance c is:

$$c = \sqrt{A^2 - B^2} \quad (7.6)$$

Each light ray emission point, $P_0(x_0, y_0, z_0)$, is randomly distributed on the light source surface assumed to be a sphere centered on the focus point $(c, 0, 0)$. Such a sphere equation is the following:

$$(x - c)^2 + y^2 + z^2 = r^2 \quad (7.7)$$

where r is the sphere ray.

The emitted ray is identified by the vector $\mathbf{v}(v_x, v_y, v_z)$ defining its direction. To calculate such a vector the Lambert's cosine law distribution, defined in Eq. 7.1, is used. Analytically, the components of the normal vector \mathbf{n} to the emitting surface, in P_0 , are as follows.

$$\mathbf{n} = \begin{bmatrix} \frac{x_0 - c}{\|\mathbf{n}\|} \\ \frac{y_0}{\|\mathbf{n}\|} \\ \frac{z_0}{\|\mathbf{n}\|} \end{bmatrix} \quad (7.8)$$

Such a vector needs to be twofold rotated in the 3D space. The former rotation is around an axis lying on the $x = 0$ plane and the rotation angle, α , is in accordance with Eq. 7.1. The latter rotation is around the vector \mathbf{n} and the rotation angle β is random in the $[0, 2\pi]$ range. To face such rotations the so-called *Rodrigues' rotation formula* is used twice.

Given an unit vector $\mathbf{t}(t_x, t_y, t_z)$ and an angle of rotation ω , the ω radians rotation of the generic vector \mathbf{w} , around the direction identified by \mathbf{t} , is \mathbf{w}' , with

$$\mathbf{w}' = (\mathbf{I} \cos \omega + [\mathbf{t}]_{\times} \sin \omega + (1 - \cos \omega) \mathbf{t} \cdot \mathbf{t}^T) \cdot \mathbf{w} \quad (7.9)$$

$$\mathbf{I} = \begin{bmatrix} 1 & 0 & 0 \\ 0 & 1 & 0 \\ 0 & 0 & 1 \end{bmatrix} \quad \text{and} \quad [\mathbf{t}]_{\times} = \begin{bmatrix} 0 & -t_z & t_y \\ t_z & 0 & -t_x \\ -t_y & t_x & 0 \end{bmatrix} \quad (7.10)$$

Applying two times the *Rodrigues' rotation formula* and neglecting the comment of all the boring mathematic technicalities the result of the twofold rotations of \mathbf{n} is the incident vector \mathbf{v} .

$$\mathbf{v} = \begin{bmatrix} \frac{y_0^2 \cos \beta \sin \alpha + z_0^2 \cos \beta \sin \alpha + c \sqrt{y_0^2 + z_0^2} \cos \alpha - x_0 \sqrt{y_0^2 + z_0^2} \cos \alpha}{r \sqrt{y_0^2 + z_0^2}} \\ \frac{(-z_0 y_0^2 + 2c x_0 z_0 - x_0^2 z_0 - z_0^3 - c^2 z_0) \sin \alpha \sin \beta + (-c y_0 + x_0 y_0) r \sin \alpha \cos \beta + y_0 r \sqrt{y_0^2 + z_0^2} \cos \alpha}{r^2 \sqrt{y_0^2 + z_0^2}} \\ \frac{(y_0 z_0^2 - 2c x_0 y_0 + x_0^2 y_0 + y_0^3 + c^2 y_0) \sin \alpha \sin \beta + (-c z_0 + x_0 z_0) r \sin \alpha \cos \beta + z_0 r \sqrt{y_0^2 + z_0^2} \cos \alpha}{r^2 \sqrt{y_0^2 + z_0^2}} \end{bmatrix} \quad (7.11)$$

Furthermore, the parametric equation of the line where the emitted ray lies is the following:

$$P = P_0 + \kappa \mathbf{v} \quad \kappa \in \mathbb{R} \quad (7.12)$$

The intersection between such a line and the ellipsoid defined in Eq. 7.5 provides the coordinates of the two common points. Between them, $P_1(x_1, y_1, z_1)$ is chosen according to the position of P_0 so that the two points lie in the same semi-space identified by the x and z axes. The solving equation providing z_1 is the following.

$$A^2 z_1^2 = A^2 B^2 - B^2 \left(x_0 + \frac{(z_1 - z_0) v_x}{v_z} \right)^2 - A^2 \left(y_0 + \frac{(z_1 - z_0) v_y}{v_z} \right)^2 \quad (7.13)$$

Then,

$$x_1 = x_0 + \frac{(z_1 - z_0) v_x}{v_z} \quad (7.14)$$

$$y_1 = y_0 + \frac{(z_1 - z_0) v_y}{v_z} \quad (7.15)$$

To calculate the reflected ray direction, \mathbf{r} , the previously introduced vector \mathbf{k} is necessary to apply Eq. 7.4. Similarly to \mathbf{v} , \mathbf{k} is obtained from the twofold rotation of the vector \mathbf{k}' , i.e. the theoretic normal vector to the ellipsoid in P_1 , considering the previously introduced θ_{err} and φ_{err} rotation angles. The *Rodrigues' rotation formula* allows such rotations.

The components of the theoretic normal vector \mathbf{k}' to the ellipsoid, in P_1 , are as follows:

$$\mathbf{k}' = \begin{bmatrix} \frac{B^2 x_1}{\|\mathbf{k}'\|} \\ \frac{A^2 y_1}{\|\mathbf{k}'\|} \\ \frac{A^2 z_1}{\|\mathbf{k}'\|} \end{bmatrix} \quad (7.16)$$

while, the final components of \mathbf{k} (k_x, k_y, k_z) are in Eq. 7.17.

$$\mathbf{k} = \begin{bmatrix} \frac{B^2 x_1 \cos \theta_{err} \sqrt{y_1^2 + z_1^2 - A^2 (y_1^2 + z_1^2)} \sin \theta_{err} \cos \varphi_{err}}{\sqrt{y_1^2 + z_1^2} \sqrt{B^4 x_1^2 + A^4 (y_1^2 + z_1^2)}} \\ \frac{(A^2 \cos \theta_{err} \sqrt{y_1^2 + z_1^2} + B^2 x_1 \sin \theta_{err} \cos \varphi_{err}) y_1}{\sqrt{y_1^2 + z_1^2} \sqrt{B^4 x_1^2 + A^4 (y_1^2 + z_1^2)}} \\ \frac{(A^2 \cos \theta_{err} \sqrt{y_1^2 + z_1^2} + B^2 x_1 \sin \theta_{err} \cos \varphi_{err}) z_1}{\sqrt{y_1^2 + z_1^2} \sqrt{B^4 x_1^2 + A^4 (y_1^2 + z_1^2)}} \end{bmatrix} \quad (7.17)$$

Finally, the components of the reflected ray \mathbf{r} (r_x, r_y, r_z) are in Eq. 7.18

$$\mathbf{r} = \begin{bmatrix} v_x - 2v_x k_x^2 - 2v_y k_x k_y - 2v_z k_x k_z \\ v_y - 2v_y k_y^2 - 2v_x k_x k_y - 2v_z k_y k_z \\ v_z - 2v_z k_z^2 - 2v_x k_x k_z - 2v_y k_y k_z \end{bmatrix} \quad (7.18)$$

The parametric equation of the line where the reflected ray lies is the following:

$$P = P_1 + \kappa \mathbf{r} \quad \kappa \in \mathbb{R} \quad (7.19)$$

The last step of the ray-tracing model deals with the calculation of P_2 , i.e. the point of intersection between the reflected ray and the target. In the proposed model the target surface is assumed to lie on the $x = -c$ plane. Consequently, the coordinates of $P_2(x_2, y_2, z_2)$ are as follows.

$$x_2 = -c \quad (7.20)$$

$$y_2 = y_1 - \frac{x_1 + c}{r_x} r_y \quad (7.21)$$

$$z_2 = z_1 - \frac{x_1 + c}{r_x} r_z \quad (7.22)$$

Finally, the following conditions complete the ray-tracing model:

- ✓ the quartz bulb, electrodes and reflector absorptivity is considered through three coefficients. As example, if the reflector absorptivity coefficient is $\psi \in [0,1]$ a generic light ray is reflected with a probability of $1 - \psi$. Consequently, drawing a random number ψ' from a $[0,1]$ uniform distribution if $\psi' < \psi$ the ray is absorbed, if $\psi' \geq \psi$ the ray is reflected;
- ✓ the incident ray falls out of the reflector shape if P_1 does not lie on the truncated ellipsoid. Particularly, if $x_1 < A - L$ the ray is lost, otherwise it hits the reflector and it is reflected or absorbed;
- ✓ the incident ray falls in the hole necessary to install the light source if $|y_1| \leq D/2$ and $|z_1| \leq D/2$, where D is the hole diameter. If such a condition occurs the ray is lost;

- ✓ the reflected ray hits the $m \times n$ rectangular target if $|y_2| \leq m/2$ and $|z_2| \leq n/2$, otherwise the ray is lost.

7.2.2 Model parameters: summary

The proposed ray-tracing model considers several geometric and optic parameters. A list of them, classified according to the physical component they belong to, is summarized in the following.

Parameters belonging to the light source (generally an high flux arc lamp):

- ✓ shape and dimensions;
- ✓ emission light spectrum;
- ✓ emission surface shape and dimensions, e.g. sphere, cylinder, etc.;
- ✓ emission direction distribution;
- ✓ absorption coefficients of quartz bulb and electrodes (if present);
- ✓ interference angle of electrodes (if present).

Parameters belonging to the ellipsoidal reflector:

- ✓ reflector shape, identified by the two ellipsoid semi-axes or by the major semi-axis and the truncation diameter;
- ✓ reflector length, i.e. the distance between the vertex, on the major axis, and the longitudinal truncation section;
- ✓ absorption coefficient;
- ✓ standard deviation of the dispersion azimuthal angular error distribution, previously called σ_{err} .

Parameters belonging to the target surface:

- ✓ shape, e.g. circular, squared, rectangular;
- ✓ dimensions;
- ✓ relative position toward the ellipsoid.

For a given a set of such parameters, the geometric and optic features of the solar simulator are univocally identified and the ray-tracing approach can be applied to study the system performances through the simulation of a large number of light rays, i.e. Monte Carlo simulation. Furthermore, varying one or several parameters the best configuration of the system can be identified.

7.2.3 Performance indices

The effectiveness of a solar simulator is, mainly, assessed in terms of target incident radiation level and radiative incident flux distribution. Considering the proposed ray-tracing model and Monte Carlo simulation the following data are of interest:

- ✓ N , number of emitted rays;
- ✓ N_A , number of rays absorbed by the light source;
- ✓ N_H , number of rays lost due to the presence of the hole used to install the light source;
- ✓ N_L , number of rays falling out of the reflector shape;
- ✓ N_R , number of rays absorbed by the mirror reflector;
- ✓ N_T , number of reflected rays hitting the target;
- ✓ N_O , number of reflected rays that do not hit the target;

Furthermore, the following key performance indices highlight the impact of the reflector features on the solar simulator global performances.

- ✓ losses due to the reflector shape, i.e. ellipsoid shape, hole and truncation diameters;

$$\xi_1 = \frac{N_H + N_L}{N - N_A} \quad (7.23)$$

- ✓ losses due to the optic and distortion effects caused by the reflector surface errors;

$$\xi_2 = \frac{N_R + N_O}{N - N_A - N_H - N_L} \quad (7.24)$$

- ✓ global reflector transfer efficiency;

$$\eta = (1 - \xi_1) \cdot (1 - \xi_2) = \frac{N_T}{N - N_A} \quad (7.25)$$

- ✓ statistical distribution of the reflected rays on the target surface, i.e. the mean distance, M_D , and standard deviation, σ_D , between P_2 and the ellipsoid focus point $(-c, 0, 0)$.

7.3 Realistic case study

The following case study provides an empirical application of the described ray-tracing approach integrated to Monte Carlo simulation.

A single source small scale concentrating solar simulator is investigated. Particularly, the effective design of the ellipsoidal reflector is analyzed. Both the emitting source and the target area features are assumed constant, while several configurations of the reflector shape, corresponding to different sets of the parameters introduced in Section 7.2.2, are tested and performances compared.

The considered emitting source is a commercial OSRAM XBO® 3000W/HTC OFR Xenon short arc lamp (OSRAM, 2012) with a luminous flux of 130,000 lumen and an average luminance of 85,000 cd/cm². Other relevant data about the shape of the considered high flux lamp are summarized in Table 7.1 and shown in Figure 7.7.

Table 7.1. Key features of the emitting source shape. Refer to Figure 7.7 for notations.

Light source parameters		
Lamp length (overall)	l_1	398mm
Lamp length	l_2	350mm
Lamp cathode length	a	165mm
Electrode gap (cold)	e_0	6mm
Bulb diameter	d	60mm
Electrode interference angles	ϑ_1	30°
	ϑ_2	20°

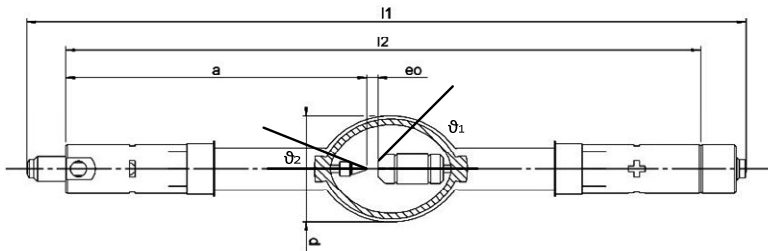


Figure 7.7. High flux emitting source, structure and notations.

The target surface is squared, side length of 50 mm, and it lies on the $x = -c$ plane.

Considering the ellipsoidal mirror reflector, the next Table 7.2 summarizes the tested scenarios providing the ranges of variation and the incremental steps for four of the parameters defining the reflector shape and the optic features. Notations refer to Figure 7.6.

Table 7.2. Tested configurations for the ellipsoidal reflector.

	Reflector Parameters [mm]		
	<i>min value</i>	<i>max value</i>	<i>step</i>
<i>A</i>	200	1000	100
<i>TD</i>	100	2 <i>A</i>	50
σ_{err}	0.005	0.01	0.005
<i>L</i>	$A - \sqrt{A^2 - TD^2/4}$	<i>A</i>	50

Particularly, the truncation diameter *TD* allows to compute the ellipsoid minor semi-axis *B*.

$$B = \frac{A \cdot TD}{2\sqrt{L(2A-L)}} \quad (7.26)$$

For all the other parameters constant values are assumed. Particularly, the light source sphere ray is of 0.5mm, the quartz bulb and reflector absorption coefficient is 4% and the electrodes absorption coefficient is 98%. Finally, for each of the 3840 tested configurations $N = 500,000$ light rays are simulated and performances collected.

7.3.1 Results and discussion

The Table 7.3 shows a subset of the obtained results presenting the twenty best and worst scenarios. In addition to the previous notations, ε indicates the ellipsoidal reflector eccentricity, defined as in Eq. 7.27 and included in the [0,1] range.

$$\varepsilon = \sqrt{1 - B^2/A^2} \quad (7.27)$$

Figure 7.8 shows the radiative flux map for the best scenario. The squared dashed line identifies the target area whereas all dots inside the square are the rays that correctly hit the target, while the other dots are the rays causing the losses at the target stage.

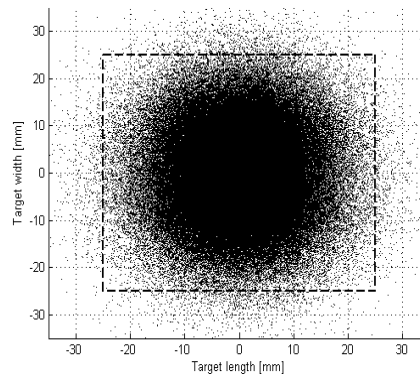


Figure 7.8. Radiative flux map for the best scenario.

Table 7.3. Multi-scenario analysis results. Twenty best and worst scenarios.

Rank	A	TD	Q _{err}	L	B	ε	N _A	%	N _H	%	N _L	%	N _R	%	N _T	%	N _O	%	ξ ₁	ξ ₂	η	M _D	Q _D
1	600	650	0.005	600	325	0.841	65506	13.10%	5585	1.12%	6771	1.35%	16942	3.39%	401501	80.30%	3695	0.74%	2.844%	4.889%	92.407%	8.284	6.387
2	700	700	0.005	700	350	0.866	65885	13.17%	6287	1.26%	719	0.14%	16935	3.39%	399723	79.94%	10471	2.09%	1.614%	6.416%	92.073%	9.867	7.265
3	700	750	0.005	700	375	0.844	65477	13.10%	2107	0.42%	5849	1.17%	17211	3.44%	399732	79.95%	9624	1.92%	1.831%	6.291%	91.993%	9.622	7.147
4	600	600	0.005	600	300	0.866	65943	13.19%	13355	2.67%	702	0.14%	16782	3.36%	399052	79.81%	4166	0.83%	3.239%	4.988%	91.955%	8.521	6.205
5	600	700	0.005	600	350	0.812	65936	13.19%	1491	0.30%	13675	2.74%	16838	3.37%	398989	79.80%	3071	0.61%	3.494%	4.753%	91.919%	8.077	7.453
6	500	550	0.005	500	275	0.835	65626	13.13%	12034	2.41%	7907	1.58%	16699	3.34%	396935	79.33%	799	0.16%	4.591%	4.222%	91.381%	6.918	5.108
7	500	600	0.005	500	300	0.800	65623	13.12%	4064	0.81%	16235	3.25%	16688	3.34%	396752	79.35%	638	0.13%	4.673%	4.184%	91.338%	6.705	5.281
8	700	800	0.005	700	400	0.821	65424	13.08%	499	0.10%	11629	2.33%	17004	3.40%	396659	79.33%	8785	1.76%	2.791%	6.105%	91.275%	9.462	7.226
9	600	650	0.005	550	326	0.839	65174	13.03%	5308	1.06%	13451	2.69%	16698	3.34%	395752	79.15%	3617	0.72%	4.314%	4.883%	91.014%	8.298	6.631
10	700	700	0.005	650	351	0.865	65824	13.16%	6088	1.22%	5619	1.12%	16789	3.36%	395000	79.00%	10680	2.14%	2.696%	6.502%	90.977%	9.868	7.868
11	700	750	0.005	650	376	0.844	65819	13.16%	1925	0.39%	11180	2.24%	16775	3.36%	394742	78.95%	9559	1.91%	3.018%	6.254%	90.916%	9.661	12.983
12	600	600	0.005	550	301	0.865	65393	13.08%	13003	2.60%	6290	1.26%	16493	3.30%	394753	78.95%	4068	0.81%	4.439%	4.951%	90.830%	8.508	6.197
13	800	800	0.005	800	400	0.866	65306	13.06%	2336	0.47%	744	0.15%	17232	3.45%	394171	78.83%	20211	4.04%	0.709%	8.675%	90.678%	11.228	8.321
14	600	750	0.005	600	375	0.781	65675	13.14%	286	0.06%	21051	4.21%	16654	3.33%	393652	78.73%	2682	0.54%	4.913%	4.682%	90.635%	7.923	10.472
15	800	850	0.005	800	425	0.847	65715	13.14%	659	0.13%	5146	1.03%	17002	3.40%	392244	78.45%	3148	0.63%	5.184%	8.395%	90.321%	11.004	8.655
16	600	700	0.005	550	351	0.811	65720	13.14%	1407	0.28%	21106	4.22%	16375	3.28%	392244	78.45%	3148	0.63%	5.184%	4.741%	90.321%	8.074	6.300
17	700	850	0.005	700	425	0.795	65720	13.14%	211	0.04%	17598	3.52%	16642	3.33%	392119	78.42%	7710	1.54%	4.101%	5.847%	90.292%	9.232	10.141
18	700	650	0.005	650	326	0.885	65836	13.17%	13360	2.67%	584	0.12%	16704	3.34%	391884	78.38%	11632	2.33%	3.212%	6.743%	90.262%	10.109	7.391
19	700	650	0.005	700	325	0.886	65749	13.15%	13333	2.67%	512	0.10%	16895	3.38%	391933	78.39%	11578	2.32%	3.188%	6.773%	90.255%	10.112	7.375
20	500	500	0.005	500	250	0.866	65937	13.12%	24369	4.87%	722	0.14%	16449	3.29%	391887	78.38%	976	0.20%	5.776%	4.257%	90.213%	7.188	6.463
3821	600	450	0.005	50	563	0.346	65447	13.09%	35	0.01%	409130	81.83%	1016	0.20%	24347	4.87%	25	0.01%	94.158%	4.100%	5.603%	53.826	4427
3822	600	450	0.01	50	563	0.346	65927	13.19%	23	0.00%	408554	81.71%	1053	0.21%	22152	4.43%	2291	0.46%	94.126%	13.116%	5.103%	128.611	23924
3823	1000	850	0.005	100	975	0.222	65157	13.03%	11	0.00%	411962	82.39%	897	0.18%	21134	4.27%	629	0.13%	94.741%	6.672%	4.908%	92.488	5811
3824	800	500	0.005	50	718	0.440	65429	13.09%	22	0.00%	412160	82.43%	911	0.18%	21118	4.22%	360	0.07%	94.848%	5.677%	4.860%	43.496	2531
3825	900	800	0.01	100	873	0.243	65717	13.14%	11	0.00%	406282	81.26%	1085	0.22%	20798	4.16%	6107	1.22%	93.555%	25.695%	4.789%	383.653	150438
3826	1000	1050	0.01	150	997	0.082	66030	13.21%	8	0.00%	406182	81.24%	1177	0.24%	20351	4.07%	6252	1.25%	93.599%	26.742%	4.689%	199.142	7646
3827	900	500	0.01	50	761	0.535	65500	13.10%	23	0.00%	407282	81.46%	1145	0.23%	17951	3.59%	8099	1.62%	93.741%	33.992%	4.131%	58.225	2676
3828	1000	500	0.01	50	801	0.599	65804	13.16%	12	0.00%	403926	80.79%	1218	0.24%	17887	3.58%	11153	2.23%	93.031%	40.885%	4.120%	28.040	65
3829	800	500	0.01	50	718	0.440	65880	13.18%	27	0.01%	411665	82.33%	937	0.19%	16543	3.31%	4948	0.99%	94.834%	26.240%	3.811%	75.963	5461
3830	1000	550	0.005	50	881	0.474	66168	13.23%	12	0.00%	415741	83.15%	730	0.15%	16257	3.25%	1092	0.22%	95.833%	10.078%	3.747%	53.311	5468
3831	1000	850	0.01	100	975	0.222	65330	13.07%	12	0.002%	412098	82.42%	871	0.17%	15910	3.18%	5779	1.16%	94.810%	29.477%	3.660%	256.684	37704
3832	700	500	0.005	50	674	0.272	65630	13.13%	19	0.004%	419413	83.88%	589	0.12%	14309	2.86%	40	0.01%	96.561%	4.211%	3.294%	71.500	12637
3833	900	550	0.005	50	837	0.368	65966	13.20%	18	0.004%	420144	84.03%	543	0.11%	12947	2.59%	362	0.07%	96.808%	6.533%	2.983%	55.009	2629
3834	700	500	0.01	50	674	0.272	65828	13.17%	14	0.003%	418994	83.80%	585	0.12%	12729	2.55%	1850	0.37%	96.507%	16.056%	2.932%	100.957	3266
3835	1000	550	0.01	50	881	0.474	65808	13.16%	16	0.003%	416421	83.28%	687	0.14%	11242	2.25%	5826	1.17%	95.911%	36.683%	2.589%	91.629	6668
3836	900	550	0.01	50	837	0.368	65775	13.16%	16	0.003%	420351	84.07%	558	0.11%	9775	1.96%	3525	0.71%	96.809%	29.463%	2.251%	135.650	13985
3837	1000	600	0.005	50	961	0.277	65848	13.17%	8	0.002%	427627	85.53%	269	0.05%	6052	1.21%	196	0.04%	98.499%	7.135%	1.394%	101.737	18564
3838	800	550	0.005	50	790	0.156	65524	13.10%	11	0.002%	428332	85.67%	236	0.05%	5867	1.17%	30	0.01%	98.588%	4.337%	1.350%	87.917	8513
3839	800	550	0.01	50	790	0.156	65207	13.04%	7	0.001%	428814	85.76%	251	0.05%	4882	0.98%	839	0.17%	98.626%	18.252%	1.123%	195.014	16000
3840	1000	600	0.01	50	961	0.277	65586	13.12%	11	0.002%	427651	85.53%	296	0.06%	4658	0.93%	1798	0.36%	98.446%	31.013%	1.072%	226.342	40309

The values of the global transfer efficiency vary from 92.407% of the best scenario to 1.072% of the worst case. Consequently, a first relevant outcome of the analysis is the heavily influence of the reflector design on the solar simulator performances.

Considering the best scenarios, the ξ_1 and the ξ_2 loss indices have values lower than 9%, while the large amount of the rays are concentrated close to the target, i.e. the mean distance between the rays and the ellipsoid focus point, M_D , is close to 10mm and standard deviation, σ_D , is included between [5,13]mm. On the contrary, the main cause for the performance decrease are the losses due to the reflector shape. With reference to the worst scenarios, high values of ξ_1 , greater than 93%, are always experienced while ξ_2 does not present a regular trend. The main reason for such losses is the critic length of the reflector, i.e. the parameter L . All worst scenarios present very small values for such a parameter, e.g. 50 or 100mm, so that a great number of the emitted rays are lost because they do not hit the mirror reflector. The very high value of the number of rays falling out of the reflector shape, N_L , included between the 80% and 86%, clearly highlights the main cause for the global transfer efficiency decrease.

Furthermore, the standard deviation of the dispersion azimuthal angular error distribution, σ_{err} , represents another relevant parameter affecting the global performances of the system. As expected, the lower σ_{err} , the higher the global transfer efficiency values are. However, to reduce the standard deviation error an increase of the reflector production costs is necessary because of the major accuracy required during reflector manufacturing and mirror surface treatments. The graph in Figure 7.9 correlates the reflector length to the global transfer efficiency for the two simulated values of σ_{err} , i.e. 0.005mm and 0.01mm. The obtained values are listed in Table 7.4.

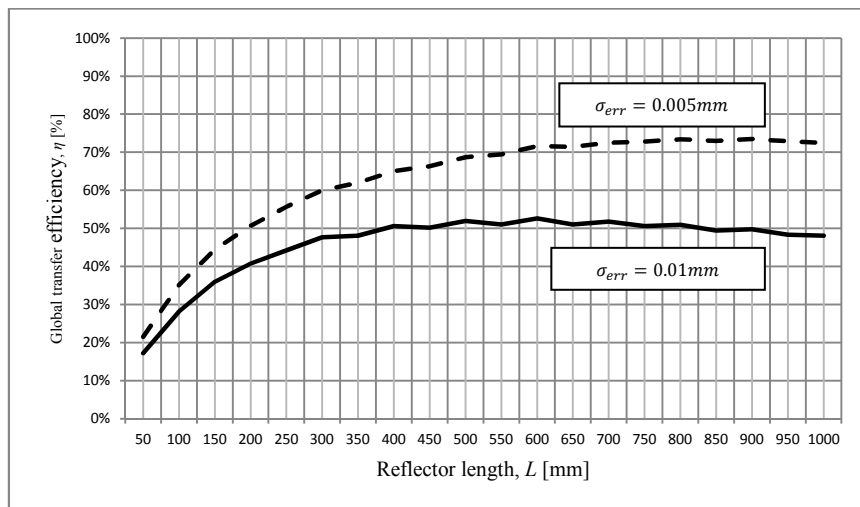


Figure 7.9. Correlation between the reflector length and global transfer efficiency for the two values of σ_{err} .

Table 7.4. Dependence of η on the L and σ_{err} values.

L [mm]	η [%]		
	$\sigma_{err} = 0.005\text{mm}$	$\sigma_{err} = 0.01\text{mm}$	gap
50	21.468%	17.227%	4.241%
100	35.103%	28.149%	6.954%
150	44.465%	35.948%	8.517%
200	50.718%	40.766%	9.952%
250	55.610%	44.188%	11.423%
300	60.049%	47.626%	12.423%
350	61.918%	48.110%	13.808%
400	65.090%	50.614%	14.476%
450	66.357%	50.201%	16.156%
500	68.722%	51.918%	16.804%
550	69.477%	51.042%	18.435%
600	71.596%	52.595%	19.002%
650	71.427%	50.988%	20.440%
700	72.510%	51.780%	20.730%
750	72.834%	50.592%	22.241%
800	73.403%	50.979%	22.425%
850	72.976%	49.454%	23.521%
900	73.467%	49.773%	23.694%
950	72.867%	48.299%	24.569%
1000	72.506%	48.039%	24.466%

The results, for the two tested values of the standard deviation of the dispersion azimuthal angular error distribution, present similarities in the waveforms. Low values of the reflector length are associated to very poor performances, i.e. $\eta < 30\%$. Optimal conditions are, respectively, for a reflector length of 800mm and $\sigma_{err} = 0.005\text{mm}$ and of 600mm for $\sigma_{err} = 0.01\text{mm}$. A significant performance increase occurs for values of L included in [50,450]mm range, while for the higher values of the reflector length, i.e. $L > 500$ mm, the global transfer efficiency presents comparable values. Finally, considering the gap between the performances in the trends identified by the two values of σ_{err} , an increase, from 4.241% to 24.466%, occurs. High values of σ_{err} have a crucial impact on the global transfer efficiency in presence of high values of L . Long reflectors force the emitted rays to sweep out long trajectories from the source to the mirror and, then, from the mirror to the target. An error, caused by anomalies in the mirror surface, generates an angular deviation of the ray path. Such a deviation is amplified by the distance between the mirror and the target. Consequently, if L increases the standard deviation of the dispersion azimuthal angular error distribution must have low values not to significantly reduce η .

Another relevant parameter for the effective mirror reflector design is the ellipsoid eccentricity, ε , defined in previous Eq. 7.27. It identifies the mutual position of the vertices and the foci. If ε is equal to 0 the ellipsoid is a sphere, i.e. $A = B$, while values of ε between 0 and 1 are for eccentric geometries. If $\varepsilon = 1$ the ellipsoid degenerates into a plane and the foci

lay upon the vertices on the major axis. Developed analysis highlights a range of optimal values for the ellipsoid eccentricity, to maximize the global transfer efficiency, included between 0.75 and 0.9, as represented in Figure 7.10 showing the graph correlating the ellipsoidal mirror eccentricity to the values of η . Each dot represents one of the 3840 simulated scenarios.

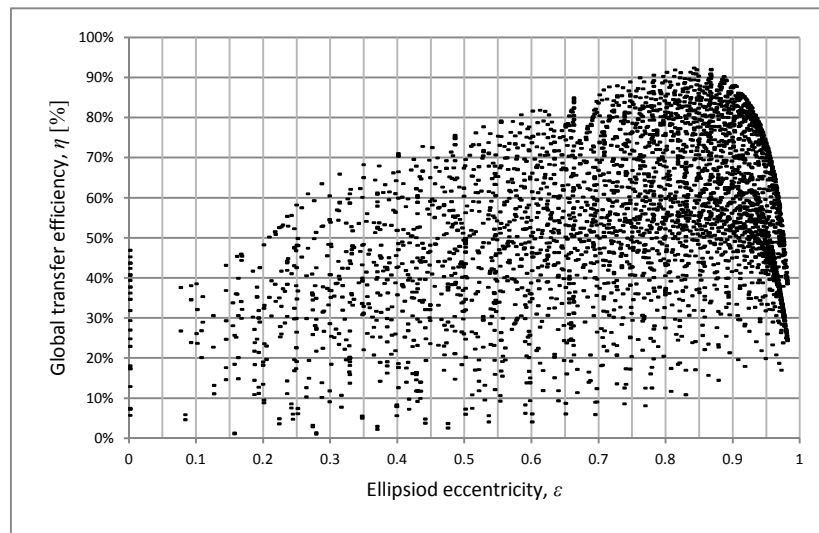


Figure 7.10. Correlation between the ellipsoid eccentricity and the global transfer efficiency.

Such outcome may be in contrast with the major literature (Steinfeld & Fletcher, 1988, Steinfeld, 1991) suggesting low values of ϵ to maximize the reflector global transfer efficiency. On the contrary, in the proposed analysis, values of the eccentricity close to zero generate the worst performances. A reasonable explanation for such an evidence lies in the adopted reflector modeling approach. The literature ray-tracing models and related results approximate the reflector to an ellipsoid of revolution neglecting both the truncation section, i.e. the parameter TD , and the hole necessary to install the light source. The proposed ray-tracing approach includes such two elements to provide a realistic and accurate description of the physical system. The presence of the aforementioned elements significantly modifies the geometric and optic features of the solar simulator introducing the so-called losses at the reflector stage that significantly contribute to the global transfer efficiency decrease, especially for the scenarios where L and ϵ assume low values. In fact, if ϵ is low the foci are located far from the vertices and close to the geometrical center of the ellipsoid. In such a circumstance, the light source, located on one ellipsoid focus point, juts out from the reflector profile and a large number of the emitted rays do not hit the reflector surface. The lower the reflector length, the higher such losses are.

In eccentric reflectors, the light source is close to the ellipsoid major axis vertex and a lower number of rays is lost. However, very high values of ϵ , i.e. $\epsilon > 0.9$, cause an increase of the losses and a decrease of η . This is due to the presence of the hole for the light source installation. A focus point located close to the reflector vertex increases the value of N_H , i.e.

the number of rays lost due to the presence of the hole used to install the light source, so that, in such a case, the global transfer efficiency decreases. The optimal values for the reflector eccentricity are in the [0.75,0.9] range.

7.3.2 Future developments

The developed ray-tracing model and Monte Carlo simulation drives the concentrating solar simulation design. For the investigated realistic case study, an effective shape for the ellipsoidal reflector is identified. Such a result is used as a benchmark to compare several commercial shapes, while the ray-tracing model allows to simulate their performances. Figure 7.11 shows the purchased reflector.

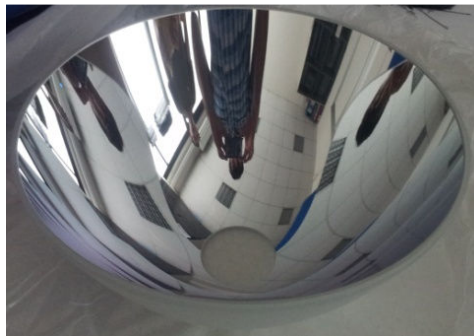


Figure 7.11. Purchased ellipsoidal reflector.

Its geometrical features are the following: $A = 489.7\text{mm}$, $B = 422.5\text{mm}$, $L = 600\text{mm}$ and $TD = 650\text{mm}$. Such dimensions are close to the best of the simulated scenarios. The appliance of the proposed ray-tracing model to such an ellipsoid shape leads to a value of the global reflector transfer efficiency close to 84%.

The major future development of the present study deals with the assembly of a concentrating solar simulator prototype based on the purchased reflector and the aforementioned light source to field-test and validate the case study results and, then, to study the optic performances of different components like the TJ-PV cells integrated to the PV/T prototype described in the previous chapters.

References

- Amoh, H., (2004). Design for multi-solar simulator. Proceedings of SPIE – The International Society for Optical Engineering 5520:192-199 Denver (Colorado, USA).
- Chen, C.F., Lin, C.H., Jan, H.T., (2010). A solar concentrator with two reflection mirrors designed by using a ray tracing method. *Optik* 121:1042-1051.
- Codd, D.S., Carlson, A., Rees, J., Slocum, A.H., (2010). A low cost high flux solar simulator. *Solar Energy* 84:2202-2212.
- Cooper, T., Steinfeld, A., (2011). Derivation of the angular dispersion error distribution of mirror surfaces for Monte Carlo ray-tracing applications. *Journal of Solar Energy Engineering* 133(4) 44501 1-4.
- Domínguez, C., Antón, I., Sala, G., (2008). Solar simulator for concentrator photovoltaic systems. *Optics express* 16(19):14894-14901.
- Domínguez, C., Askins, S., Antón, I., Sala, G., (2009). Characterization of five CPV module technologies with the Helios 3198 solar simulator. *IEEE* 1004-1008.
- Hussain, F., Othman, M.Y.H., Yatim, B., Ruslan, H., Sopian, K., (2011). Fabrication and irradiance mapping of low cost solar simulator for indoor testing of solar collector. *Journal of Solar Energy Engineering* 133(4) 44502 1-4.
- Johnston, G., (1995). On the analysis of surface error distributions on concentrated solar collectors. *Transactions of the ASME* 117:294-296.
- Kruger, K.R., Davidson, J.H., Lipiński, W., (2011). Design of a new 45kWe high-flux solar simulator for high-temperature solar thermal and thermo-chemical research. *Journal of Solar Energy Engineering* 133(4) 11013 1-8.
- Meng, Q., Wang, Y., Zhang, L., (2011a). Irradiance characteristics and optimization design of a large-scale solar simulator. *Solar Energy* 85:1758-1767.
- Meng, Q., Wang, Y., (2011b). Testing and design of a low-cost large scale solar simulator. Proceedings of SPIE – The International Society for Optical Engineering 8128 San Diego (California, USA).

Ota, Y., Nishioka, K., (2010). 3-dimensional simulator for concentrator photovoltaic modules using ray-trace and circuit simulator. Proceedings of the 35th IEEE Photovoltaic Specialists Conference, PVSC 2010 3065-3068 Honolulu (Hawaii, USA).

Petrash, J., Coray, P., Meier, M., Brack, M., Häberling, P., Wullemin, D., Steinfeld, A., (2007). A novel 50kW 11.000 suns high-flux solar simulator based on an array of xenon arc lamps. Journal of Solar Energy Engineering 129:405-411.

Pravettoni, M., Galleano, R., Dunlop, E.D., Kenny, R.P., (2010). Characterization of a pulsed solar simulator for concentrator photovoltaic cell calibration. Measurement Science and Technology 21:1-8.

Renh, H., Hartwig, U., (2010). A solar simulator design for concentrating photovoltaics. Proceedings of SPIE – The International Society for Optical Engineering 7785 San Diego (California, USA).

Steinfeld, A., Fletcher, E.A., (1988). Solar energy absorption efficiency of an ellipsoidal receiver-reactor with specularly reflecting walls. Energy 13(8):609–614.

Steinfeld, A., (1991). Exchange factor between two spheres placed at the foci of a specularly reflecting ellipsoidal cavity. International Communications in Heat and Mass Transfer 18:19-26.

Web - reference

OSRAM company website

<http://www.osram.com>

8. *Conclusions*

Nowadays, the renewable energy sources present a great potential for a sustainable and low carbon development and to spread the energy access to a wider group of people, now excluded. However, to display such a potential, progresses in politics, economy, management and technology are, still, required.

The present Ph.D. dissertation aim is to study and to propose innovative models, approaches, strategies and prototypes to face the challenges related to the renewable source development with a specific focus on the solar source that presents an enormous potential in terms of energy availability.

The research path, summarized in the present dissertation, firstly proposes an overview of the open challenges related to the energy issues reviewing the key indicators frequently discussed to highlight the role played by energy and renewable sources in the current global scenario (*Chapter 1*). Starting from such a background, the dissertation considers the energy mix and it proposes a preliminary analytic optimization model to face its dynamic, i.e. time-dependent, definition in order to meet the demand targets and to include a higher incidence of energy from the renewable sources. Furthermore, focusing on the solar energy, the assessment of the economic feasibility of distributed small and medium size PV plants in Europe is proposed (*Chapter 2*). Results confirm the strong potential of such a source and the parallel necessity to improve the current PV technologies to make solar plants fully self-sustainable. Consequently, the Ph.D. research investigates the innovative solar concentrating technology as a potential alternative to traditional flat plane modules. Due to the possibility, for such plants, to convert only the direct component of the solar radiation, a deep analysis of the solar components is proposed, reviewing the fundamentals about solar energy prediction models and discussing an innovative multi-location model to estimate the components of the solar radiation given the incident global irradiation level and the values of the clearness index (*Chapter 3*). A short review of the solar concentrating sector is proposed (*Chapter 4*) to introduce the designed and developed Fresnel lens concentrating prototype for the electrical power production, through high efficiency multi-junction solar

cells located on the lens focus point, and the heat recovery thanks to the adoption of a cooling circuit and a set of heat exchangers. A functional description of the physical modules integrated to the prototype, highlighting their connections and contribution to guarantee the whole plant working correctly, is done (*Chapter 5*). Furthermore, the outcomes of a preliminary field-test to study the energy performances of the system are proposed. Results highlight good thermal performances, i.e. the measured thermal conversion efficiency is higher than 70%, while improvements in the electric conversion efficiencies are, still, required. They mainly deal to the increase of the optic performances to reduce the fraction of the concentrating radiation that falls out of the PV cell surface. The introduction of a secondary optics is proposed as an effective approach to face such a weakness. The following section of the dissertation (*Chapter 6*) focuses on the bi-axial solar tracking strategies to accurately align the solar collector to the Sun rays. Forward loop and feedback strategies are discussed and an innovative hybrid approach is presented and field-tested adopting the proposed prototype. Details about the LabView™ *software* platform for motion control and system monitoring are, further, provided together with a short review of the maximum power point tracking algorithms to let the PV cells working at their best conditions. Finally, the last part of the Ph.D. dissertation (*Chapter 7*), investigates the effective design of concentrating solar simulators, known as useful and frequently adopted devices to artificially reproduce the Sun light spectrum. A ray-tracing model, integrated to a Monte Carlo simulation, is proposed to face the effective ellipsoidal reflector design. A single source system is focused. A realistic case study, based on a commercial Xenon arc lamp, is presented to both apply the proposed approach and to drive the reflector purchase for the future simulator assembly.

8.1 Future developments

Starting from the topics investigated in the present Ph.D. dissertation a set of future developments are encouraged to continue and expand the research on the described models, approaches, strategies and prototypes.

With reference to the models proposed in the first part of the dissertation (*Chapter 2* and *Chapter 3*) their continuous update to include the most recent data could be of interest. In particular, the economic model to assess the feasibility of PV plants is applicable to further geographical contexts and it requires to take into account the evolution in the support schemes to the PV sector. Furthermore, considering the multi-location model to estimate the diffuse component of solar radiation, an enlargement to further climatologic indices is possible to study if they affect the accuracy in the solar component prediction. In addition, the inclusion of recent data, i.e. from year 2008, is possible to check the proposed models

against other sets of experimental parameters. Considering the PV/T prototype described in *Chapter 5* and *Chapter 6* the aforementioned improvements in the concentrating optics are necessary before an extensive trial campaign to study the plant energy performances. The complete integration of the maximum power point functional module, described in the dissertation, to both the *hardware* and *software* platforms contributes to the plant optimization and fine-tuning. Finally, the assembly and test of the single source solar simulator prototype introduced in *Chapter 7* leads to the ray-tracing model experimental validation.

Such a list of future developments points out some of the open issues coming from the topics investigated in the Ph.D. research path and that can drive the future studies.

The final goal of all efforts is the grew up of a *sustainable culture* for a *sustainable living planet!*